ANALYTICAL AND NUMERICAL STUDY OF QUANTUM IMPURITY SYSTEMS IN THE INTERMEDIATE AND STRONG COUPLING REGIMES

DISSERTATION ZUR ERLANGUNG DES DOKTORGRADES DER NATURWISSENSCHAFTEN
(DR. RER. NAT.) DER FAKULTÄT FÜR PHYSIK
DER UNIVERSITÄT REGENSBURG

vorgelegt von
Davide Mantelli aus
Genua, Italien

im Jahr 2016

Promotionsgesuch eingereicht am: 08.06.2016

Die Arbeit wurde angeleitet von: Prof. Dr. Milena Grifoni

Prüfungsausschuss:
Vorsitz: Prof. Dr. Dieter Weiss
Erstgutachter: Prof. Dr. Milena Grifoni
Zweitgutachter: Prof. Dr. Kalus Richter
Weiterer Prüfer: Prof. Dr. Vladimir Braun

Termin Promotionskolloquium: 21.07.2016

To my family,

Contents

Abstract

In this thesis we deal with the description of quantum impurity systems. In order to achieve such an aim, we exploit in the first part of this work the Reduced Density Matrix (RDM) formalism, in the second one the Density Matrix-Numerical Renormalization Group (DM-NRG) method.
The first half of the thesis deals with the derivation and the application of out-of-equilibrium and non-perturbative approximations for the dynamics of the Single Impurity Anderson Model (SIAM) in the perturbative, intermediate coupling and Kondo cross-over regimes. In this part of the thesis, the main aim is to develop new technical tools useful to extend the RDM formalism from the well established perturbative regime to the intermediate and, in the future, to the strong coupling regimes.

In this part, we analyse the advantages and drawbacks of the so-called Dressed Second Order (DSO), Dressed DSO (DDSO) and the Resonant Tunnelling Approximation (RTA). In the DSO we include processes capable to describe the broadening of the Coulomb blockade peaks but the DSO itself, as the RTA, is not capable to describe the Kondo resonance width properly. In the DDSO we propose a prescription to solve this issue and to describe properly the exponential dependence of the Kondo resonance width. However, in the DDSO the vertex corrections are not included and this yields a spurious conductance peak in the empty orbital regime (Coulomb valley with zero electrons). For this reason we turn our attention to the inclusion of the vertex corrections within the RTA framework.

In the second part, we describe transport and thermodynamic properties of carbon-nanotubes (CNTs) based quantum dots using the DM-NRG method. We present results on the spectral function and the linear conductance in cooperation with Cătălin Paşcu Moca and Gergely Zaránd from the Universities of Oradea and Budapest, respectively. In order to model the CNTs we consider an extended Anderson Hamiltonian. Exploiting such an Hamiltonian we study the crossover from the SU(4) to the SU(2) Kondo effect.

We demonstrate numerically and analytically that the Kondo temperature scales inversely with respect to the SU(4)-symmetry breaking parameter Δ, tending to the Kondo temperature of the SU(2) Kondo effect in the large Δ limit. Furthermore we study the CNT quantum dot in the presence of a parallel and perpendicular (with respect to the CNT axis) magnetic field. We find necessary conditions to observe the so-called "Kondo revivals" for specific values of the magnetic field.

In the final part of this thesis, we model a real world device realised by Jean-Pierre Cleuziou, Ngoc-Viet Nguyen and Wolfgang Wernsdorfer in Grenoble by means of the previously studied Hamiltonian. For this system we search for the best set of parameters to reproduce the experimentally measured linear conductance and we study the underlying Kondo state evaluating the CNT added entropy and specific heat.

Introduction

DURING the last two decades the development in the fabrication of mesoscopic systems [1–3] made experimentally accessible the verification of new intriguing fundamental physics. Of particular interest are the so-called quantum dots [4, 5], since they are the perfect candidate to explore the interplay between single particle and many-body [6, 7] physics in a controlled way.

Quantum dots may be fabricated by shaping two-dimensional electron gases (2DEGs) in heterostructures [8, 9], such as GaAs-AlGaAs, exploiting the quantum well formed at the boundary between the two different semiconductors. Such 2DEGs can be furthermore confined by means of metallic contacts (gates), that can be defined on the top of the heterostructure (see Fig.1), obtaining a zero dimensional quantum dot. Moreover, additional metallic contacts (source and drain) can be used for transport measurements. On the other hand, one can also consider quantum dots fabricated by contacting one-dimensional objects such as semiconductor nano-wires [10, 11] or, as we will see in the second part of this thesis, carbon nanotubes [12]. Finally, it is also possible to obtain quantum dots contacting zero-dimensional objects such as fullerene molecules [13] or ultra-small metallic grains [14] to metallic leads. Such devices, whose length is comparable with the average free path of the carriers, are the ideal playground to test quantum transport theories and they are of great interest from the quantum computational point of view.

In quantum dots it is possible to confine an integer number of charges in the device by tuning, by means of an external applied gate voltage, electron by electron the charge in the dot. Since the quantum dots are zero dimensional objects, they show a set of discrete energy levels and for this reason they are often regarded as artificial "atoms". In contrast to real atoms, quantum dots are much easier to tune and they offer experimentally the opportunity to investigate fundamental physics such as single electron tunnelling or the phenomenon of the Coulomb blockade [4, 5, 16], the evolution of the dot

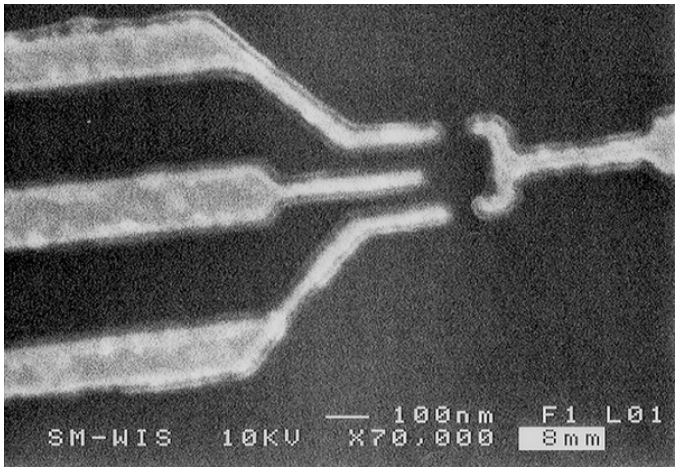

Figure 1: Scanning electron microscope image of a 2DEG quantum dot. There are four gate electrodes (white regions). Source and drain contacts at the top and bottom are not shown. Adapted with permission form Ref. [15].

single particle energy states in an external magnetic field [5, 17], the interplay between the quantum dot and the contacts with a shaped density of states, as in the case of superconducting [18, 19] or ferromagnetic leads [20], or the formation of many-body resonances due to the hybridisation with the external leads.

It was indeed in this context that the Kondo effect [22], experimentally well known since the 1930s and theoretically explained in the 1960s, was revived [15, 21, 23–26]. In the 1934 de Haas, de Boer and van den Berg experimentally found that some "pure" metallic materials, such as gold, silver and copper, showed an increasing resistance when cooling the material down to very low temperatures (red solid line in Fig.2 left panel). Such a behaviour was puzzling since the resistance in a usual metal lowers as one decreases the temperature and then saturates to a value related to the number of impurities in the metal (see blue solid line in Fig.2 left panel). This happens because the electrons can travel more easily through the material as the number of thermally excited phonons decreases. In contrast, in a superconductor (see green solid line in Fig.2 left panel), the resistance drops as one lowers the temperature below the critical superconducting temperature as a manifestation of the formation of a coherent many-body state. No theoretical description for this apparently contradictory measurement was found until, in 1964, Jun Kondo found a consistent justification [27]. From the theoretical point of view the resistance in a material is due to scattering processes that hinder the motion of the conduction electrons. Calculating the probability to scatter against some magnetic impurity centres with a perturbative approach, Jun Kondo showed that the second order term of this expansion was not decreasing at lower temperatures, yielding instead

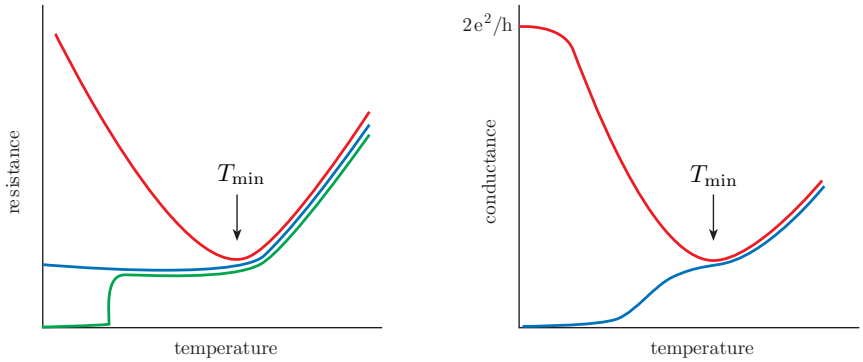

Figure 2: (Left) temperature dependence of the resistivity in a normal metal (blue solid line), a superconducting material (green solid line) and in a metal with magnetic impurities (red solid line). (Right) conductance temperature dependence in an Anderson quantum dot tuned in a state with a net spin (red solid line) or tuned in a state with zero net spin (blue solid line). Adapted from [21].

a logarithmic divergence in the zero temperature limit. Kondo's theory described correctly the presence of a minimum in the conductance of the material and its upturn as the temperature is furthermore decreased. Indeed it turned out that these "pure" metals were actually contaminated with magnetic impurities such as chromium, magnesium and iron. The Kondo effect is a many-body effect that arises when a magnetic impurity couples strongly to a non-magnetic material. When the spin of such a magnetic impurity interacts with the ones of the surrounding electrons anti-ferromagnetically, it is screened by the spins of the surrounding electrons forming a singlet bound state [22] which traps the itinerant electrons.

In quantum dots the Kondo effect manifests itself in the opposite manner (see right panel in Fig.2) due to the intrinsic geometry of the system [28]. If the quantum dot is tuned into a state with a net spin (red solid line in the right panel in Fig.2), lowering the temperature, the conductance of the quantum dot increases reaching its maximum in the zero temperature limit [25] (in Fig.2 we are considering a single impurity and the maximum conductance is $2e^2/h$). In contrast if the dot is tuned in a state with zero net spin, the conductance lowers for decreasing temperatures [25] since the Kondo effect is absent. In this context the dot plays the role of the impurity. Having in mind all the above considerations, this may lead to the Kondo effect (see Fig.3) if the dot is tuned in the so-called localized moment regime [22], i.e. when the Anderson quantum dot is populated by an electron, and the environment temperature is lower than the Kondo one [22].

The Kondo temperature (T_{K}) is a many-body energy scale related to the binding energy of the Kondo singlet. As we will see in detail, it depends

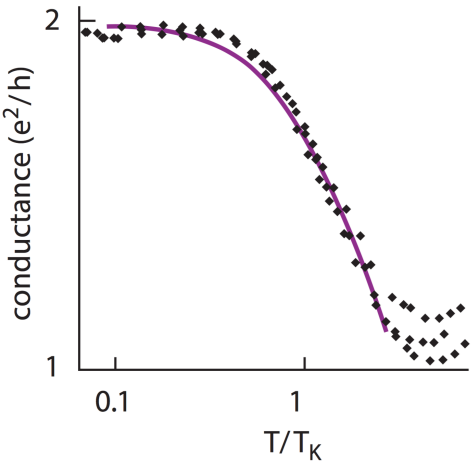

Figure 3: Temperature dependence of the measured conductance in a 2DEG quantum dot. Here the temperature is normalised to the Kondo one and the data are presented for different gate values in the localised moment regime. Adapted from [21].

exponentially on the parameters of the quantum dot and it fully characterises the cross-over between a formed Kondo singlet [21, 25], in the strong coupling regime for temperatures $T/T_{\rm K} \ll 1$, and the "melted" Kondo singlet, in the weak coupling regime for $T/T_{\rm K} \gg 1$ (as we depicted in the right panel in Fig.2). The same holds true considering the applied bias voltage (eV) [15, 29] or magnetic field [15, 30] ($\mu_{\rm B} g_{\rm s} B/2$). Whenever the corresponding energy scale exceeds the Kondo binding energy ($eV/(k_{\rm B}T_{\rm K}) \gg 1$ or $(\mu_{\rm B} g_{\rm s} B/2)/(k_{\rm B}T_{\rm K}) \gg 1$) the Kondo singlet breaks down and the conductance is strongly suppressed.

In Fig.3 we show the measured temperature dependence of the conductance for different gate values in the localised moment regime (data adapted from Ref. [5]). It is clear that the conductance reaches its maximum for $T/T_{\rm K} \ll 1$, as we previously mentioned. Moreover, in Fig.3 it is easy to notice another peculiar characteristics of the Kondo effect. Indeed, as we will see in detail in this thesis, normalising the temperature to the Kondo one all the experimental points fall onto each other, i.e. the linear conductance temperature dependence is universal with respect to the ratio $T/T_{\rm K}$ [22]. This remarkable experimental result shows that the aforementioned theoretical predictions can be indeed experimentally verified in quantum dot systems.

In this thesis, the Kondo effect will play an important role since we will consider Hamiltonian models, i.e. the Anderson or the extended Anderson model, that are known to show an anti-ferromagnetic behaviour if tuned in the proper regime [31]. In order to describe the transport characteristics of such systems, many diverse techniques have been introduced in the literature. In this thesis we will consider two approaches in order to capture this many-

body physics: the Reduced Density Matrix (RDM) formalism [32–35], and the Numerical Renormalization Group (NRG) method introduced by Wilson in the 1970s [36].

The thesis is divided into two parts. In the first part we describe the quantum dot dynamics within the RDM framework. The RDM formalism is an out-of-equilibrium master equation approach [37], i.e. one derives a system of differential equations for the elements of the reduced density matrix of the system that is governed by the rates of exchange between pairs of dot states.

We organise this part as follows:

Chapter 1: Transport properties of an interacting quantum dot. In this Chapter we will introduce the density matrix formalism, the Hamiltonian of the system and some tools, such as the diagrammatic technique, to evaluate the time evolution of a statistical mixture. At the end of this Chapter we will show a perturbative application of this formalism considering the single impurity Anderson model up to second order in the tunnelling energy of coupling.

Chapter 2: Beyond the perturbative theory. Here we will develop new diagrammatic tools to capture non perturbative effects in the transport characteristics of the system. Thus we will obtain the expression for the rates in the so-called dressed second order (DSO) approximation. We will benchmark the DSO against known properties in the weak and intermediate coupling regimes. We will discuss the issue regarding the scaling exponent in the DSO expression for the Kondo temperature. Moreover we will propose a prescription to solve this problem dressing the DSO self-energy in the Dressed-DSO (DDSO) approximation. We will analyse the advantages and drawbacks of the DDSO and we will move our discussion to the inclusion of the vertex corrections in the theory in the next Chapter.

Chapter 3: The Resonant tunnelling approximation. In this Chapter we will include the so-called vertex corrections in the theory extending the DSO along the lines of the Resonant Tunnelling Approximation (RTA) presented in Ref. [38]. In contrast to the DSO, the RTA takes into account all the processes up to fourth order. Thus it is not possible to "dress" the second order master equation as in the case of the DSO and DDSO, rather the vertex corrections must be further included. To this extent we shall start from a formally exact master equation for the RDM and retain a specific sub-set of diagrams which include tunnelling processes to all order. Moreover, in this Chapter, we will link our formalism to the one of the Green functions showing that a diagrammatic expression for the Green functions may be found. Then we will compare the transport characteristics within the RTA with the ones we have obtained in the DSO and DDSO approximations.

In the second part of this thesis, we describe transport and thermodynamic properties of a carbon nanotube based quantum dot with the Density Matrix-Numerical Renormalization Group (DM-NRG) method:

Chapter 4: DM-NRG study of the Kondo effect in a CNT. In this Chapter we will model the CNT quantum dot with an extended Anderson impurity model. Then we will analyse the symmetries of the system and introduce the general scheme to obtain the transport characteristics from the DM-NRG procedure. Then we will present our results, considering firstly the system in the absence of a magnetic field. We will study the linear conductance, the spectral function and the behaviour of the Kondo temperature as a function of the so-called Kramers pairs splitting. Then we will turn our discussion to the inclusion of a finite magnetic field and we will discuss the conditions to be fulfilled in order to observe the so-called "Kondo revivals". Finally we will describe the transport characteristics of a real world device fabricated by the group of Jean-Pierre Cleuziou in Grenoble, exploiting the model we studied in the Chapter. The experimentally measured linear conductance will be compared to the theoretical predictions using the extended Anderson model for CNTs.

Publications

Large parts of the chapters have been published in:

1. Davide Mantelli, Cătălin Paşcu Moca, Gergely Zaránd and Milena Grifoni. *Kondo effect in a carbon nanotube with spin-orbit interaction and valley mixing: A DM-NRG study.* Physica E: Low-dimensional Systems and Nanostructures **77**, 180 (2016).

2. Michael Niklas, Sergey Smirnov, Davide Mantelli, Magdalena Margańska, Ngoc-Viet Nguyen, Wolfgang Wernsdorfer, Jean-Pierre Cleuziou and Milena Grifoni. *Blocking transport resonances via Kondo entanglement in quantum dots.* Accepted for publication in Nature Communications.

Part I

Transport across quantum dot systems within the Reduced Density Matrix (RDM) framework

CHAPTER 1

Transport properties of an interacting quantum dot

In this Chapter we consider the transport properties of a quantum dot coupled to leads and to a gate terminal (see Fig.1.1). We want to derive the current, the average number of particles in the system and the conductance as a function of the applied voltages: source, drain and gate voltages. We will deal with the perturbative approach, whereas in Chap.2 we will present non perturbative methods to study this system. We will first introduce (Sect.1.1) the notation and the formalism that we have adopted, we will then derive (Sect.1.2) the main transport quantities of the quantum dot in the second order perturbation theory.

1.1 Introduction to the formalism

In order to study the transport properties of a quantum dot we introduce the Hamiltonian of the system and the formalism that we have adopted: *the Reduced Density Matrix (RDM) approach* [39, 40]. In this Chapter we follow mainly Refs. [40] and [41].

1.1.1 The density operator

In quantum mechanics the largest set of eigenvalues corresponding to mutual commuting operators of a system yields the *"maximum available information"* we can obtain from the measurement of the system itself. Thus, if a set $\{\hat{Q}_1, \ldots, \hat{Q}_n\}$ is composed of independent operators $\hat{Q}_i$ such that

$$\left[\hat{Q}_i, \hat{Q}_j\right] = 0, \quad \forall\, i, j,$$

the corresponding set of eigenvalues $\{q_1, \ldots, q_n\}$ completely specify the state vector of the system,

$$|\psi\rangle = |q_1, \ldots, q_n\rangle \,, \tag{1.1}$$

if and only if n is the largest number of independent and simultaneously measurable variables. The choice of this complete set of commuting operators is not unique. Indeed the state $|\psi\rangle$ can be also specified giving the amplitudes a_n which identify the state in terms of the eigenbasis $\{|\phi_n\rangle\}$:

$$|\psi\rangle = \sum_n a_n \, |\phi_n\rangle \,, \qquad\qquad \langle\psi \,|\, \psi\rangle = \sum_n |a_n|^2 = 1, \tag{1.2}$$

where ϕ_n is an n-dimensional index formed by one of the possible sets of n independent observables. From the physical point of view, $|a_n|^2$ represents the probability that a measurement gives the state $|\phi_n\rangle$. The states (Eq.(1.1)), specified by the largest set of the eigenvalues of the system, are said **pure states** because they are the states of maximum knowledge. It is not necessary that the system is in such state. Indeed the system can be found in a *superposition of such pure states*, called **mixed state**. Such mixed states can be described by stating that the system has certain probabilities $W_1, \ldots, W_N$ of being in the pure states $|\psi_1\rangle \,, \ldots, |\psi_N\rangle$:

$$|\Psi\rangle = \sum_n W_n \, |\psi_n\rangle \,, \qquad\qquad \sum_n W_n = 1, \qquad\qquad 0 \leq W_n \leq 1. \tag{1.3}$$

This means that the system is in a statistical mixture and, if such a state is achieved, the result of a measurement on the observable $\hat{Q}_i$ will be a variety of eigenvalues of this operator. The average over all the measurements is given by the expectation value

$$\left\langle \hat{Q}_i \right\rangle = \langle\Psi| \, \hat{Q}_i \, |\Psi\rangle = \sum_n W_n \, \langle\psi_n| \, \hat{Q}_i \, |\psi_n\rangle \,. \tag{1.4}$$

In literature the *density operator* is often introduced,

$$\hat{\rho} = \sum_n W_n \, |\psi_n\rangle\langle\psi_n| = \sum_{n,m,m'} W_n a_{m'}^{(n)} a_m^{(n)*} \, |\phi_{m'}\rangle\langle\phi_m| \,, \tag{1.5}$$

in order to rewrite the average in Eq.(1.4) as follows:

$$\begin{aligned} \left\langle \hat{Q}_i \right\rangle &= \sum_{n,m,m'} W_n a_{m'}^{(n)} a_m^{(n)*} \left\langle \phi_m \,\middle|\, \hat{Q}_i \,\middle|\, \phi_{m'} \right\rangle = \\ &= \mathsf{Tr} \left\{ \sum_{n,m,m'} W_n a_{m'}^{(n)} a_m^{(n)*} \, |\phi_{m'}\rangle\langle\phi_m| \, \hat{Q}_i \right\} = \mathsf{Tr} \left\{ \hat{\rho} \hat{Q}_i \right\} . \end{aligned} \tag{1.6}$$

Moreover the matrix elements of the density matrix in the generic eigenbasis $\{|\phi_i\rangle\}$ read:

$$\langle\phi_i|\,\hat{\rho}\,|\phi_j\rangle = \rho_{ij} = \sum_n W_n a_i^{(n)} a_j^{(n)*}.$$

Then the diagonal elements,

$$\rho_{ii} = \sum_n W_n |a_i^{(n)}|^2,$$

represent the probability to find the system in the eigenstate $|\phi_i\rangle$. It follows they have to observe the *normalization condition*

$$\sum_i \rho_{ii} = 1. \tag{1.7}$$

They are called *populations* and, since $W_n \geq 0$, they are real and positive as a probability has to be (i.e. $\hat{\rho}$ is a positive defined operator). The non diagonal elements (ρ_{ij}) are called *coherences* since they quantify a sort of correlation between the state $|\phi_i\rangle$ and $|\phi_j\rangle$. The probability to find the system in the statistical mixture $|\Psi\rangle$ can be written as

$$W(\Psi) \overset{\text{def}}{=} \langle\Psi|\,\hat{\rho}\,|\Psi\rangle = \sum_n W_n \left\|\langle\psi_n\,|\,\Psi\rangle\right\|^2.$$

In the end, directly from the definition of Eq.(1.5), it can be proved that

$$\mathsf{Tr}\left\{\hat{\rho}^2\right\} \leq \mathsf{Tr}\left\{\hat{\rho}\right\} = 1,$$

where the equality holds only for pure states. The density operator plays a central role in the transport theory since all the information on the behaviour of a quantum mechanical system can be expressed in terms of expectation values of a certain operator. As we will see, all the relevant quantities, such as the occupation probability of the states in the dot (*populations*), the current of particles through the quantum dot and the conductance will be directly linked to this operator.

1.1.2 The Hamiltonian

We consider a quantum dot in the context of the Anderson model. The Hamiltonian of such a model can be written without loss of generality as follows:

$$\hat{H}_{\text{tot}} = \hat{H}_{\text{RS}} + \hat{H}_{\text{T}} + \hat{H}_{\odot}. \tag{1.8}$$

The Hamiltonian

$$\hat{H}_{\text{RS}} = \sum_{l,\sigma,\mathbf{k}} \varepsilon_{l,\sigma,\mathbf{k}}\, \hat{c}^{\dagger}_{l,\sigma,\mathbf{k}} \hat{c}_{l,\sigma,\mathbf{k}}, \tag{1.9}$$

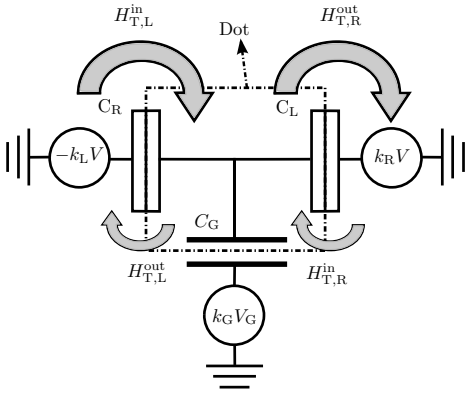

Figure 1.1: Scheme of a quantum dot coupled to leads and to a gate terminal. The dot is linked to all the terminals through the capacitances $C_{\rm G}$, $C_{\rm L}$ and $C_{\rm R}$. The transport of electrons from the source to the drain can be achieved with tunnelling events from and to the dot. We have reported the terms of the total Hamiltonian responsible for the tunnelling events: $H^{\rm in/out}_{{\rm T},l}$ with $l = {\rm R/L}$. In the figure we have assumed proportional coupling to the leads and the gate terminal via the dimensionless constants $k_{\rm G}$ and k_l.

is the one of the reservoirs: source (left lead, $l = {\rm L}$) and drain (right lead, $l = {\rm R}$). We assume they are well described by a Fermi liquid model since they are macroscopic objects: $\varepsilon_{l,\sigma,\mathbf{k}}$ is the bare energy-wave number relation in the l-lead. Here we have introduced the *second quantization* fermionic annihilation operator $\hat{c}_{l,\sigma,\mathbf{k}}$ of an electron in the l-lead with spin $\sigma =\uparrow,\downarrow$. As usual, the hermitian conjugated operator $\hat{c}^\dagger_{l,\sigma,\mathbf{k}}$ is such that:

$$\left\{\hat{c}_{l_1,\sigma_1,\mathbf{k}_1}, \hat{c}^\dagger_{l_2,\sigma_2,\mathbf{k}_2}\right\} = \delta_{l_1,l_2}\,\delta_{\sigma_1,\sigma_2}\,\delta_{\mathbf{k}_1,\mathbf{k}_2}. \tag{1.10}$$

The leads are described by *the grand-canonical density operator* [42]

$$\hat{\rho}_l = \frac{\exp\left[-\beta\left(\hat{H}_l - \mu_l \hat{N}^{\rm RS}_l\right)\right]}{\mathcal{Z}_l}, \qquad l = {\rm R,L} \tag{1.11}$$

where $\mathcal{Z}_l = \mathsf{Tr}_l\left\{\exp[-\beta(\hat{H}_l - \mu_l \hat{N}^{\rm RS}_l)]\right\}$ is *the partition function* of the corresponding lead and $\beta = 1/k_{\rm B}T$, with $k_{\rm B}$ equal to the Boltzmann constant. Moreover, we have introduced the particle number operator $\hat{N}^{\rm RS}_l = \sum_{l,\sigma,\mathbf{k}} \hat{c}^\dagger_{l,\sigma,\mathbf{k}}\hat{c}_{l,\sigma,\mathbf{k}}$ and the chemical potential $\mu_{l={\rm R,L}}$. The dependence

on the bias is captured as

$$\mu_{\mathrm{R}} = \mu_0 - ek_{\mathrm{R}}V, \tag{1.12a}$$
$$\mu_{\mathrm{L}} = \mu_0 + ek_{\mathrm{L}}V, \tag{1.12b}$$

where e is the modulus of the electron charge, μ_0 is the Fermi level of the system, V is the bias potential and k_l is the asymmetry parameter for the voltage drop such that the total difference of potential between the left and the right lead is exactly V. This can be achieved requiring:

$$\sum_{l=\mathrm{L,R}} k_l = 1. \tag{1.13}$$

Moreover, the density matrix of both the reservoirs reads

$$\hat{\rho}_{\mathrm{RS}} = \hat{\rho}_{\mathrm{R}} \otimes \hat{\rho}_{\mathrm{L}}.$$

The tunnelling Hamiltonian,

$$\hat{H}_{\mathrm{T}} = \sum_{l=\mathrm{L,R}} \hat{H}_{\mathrm{T},l} = \sum_{l,\sigma,\mathbf{k}} \left(T_{l,\sigma,\mathbf{k}}\, \hat{d}^{\dagger}_{\sigma} \hat{c}_{l,\sigma,\mathbf{k}} + T^{*}_{l,\sigma,\mathbf{k}}\, \hat{c}^{\dagger}_{l,\sigma,\mathbf{k}} \hat{d}_{\sigma} \right), \tag{1.14}$$

describes the coupling between the quantum dot and the leads via the $T_{l,\sigma,\mathbf{k}}$: *the tunnelling matrix coefficients* (TMCs). The first term ($H^{\mathrm{in}}_{\mathrm{T},l}$) allows electrons with spin σ and wave-number $\mathbf{k}$ to tunnel into the dot from the l-lead, the second term ($H^{\mathrm{out}}_{\mathrm{T},l}$) to tunnel out into the l-lead with spin σ and wave-number $\mathbf{k}$. For simplicity we assume energy independent TMCs and, in the absence of ferromagnetic or superconducting leads, it is a good approximation to consider them as *spin independent*. These simplifications correspond to the hypothesis of *proportional coupling to the leads* and then the TMCs read:

$$T_{l,\sigma,\mathbf{k}} = \sqrt{\kappa_l} E_{\mathrm{T}}, \tag{1.15a}$$
$$\sum_{l} \kappa_l = 1, \tag{1.15b}$$

where E_{T} is the tunnelling energy of coupling of the dot with the leads and κ_l is the asymmetry parameter in the *coupling energies*. It is, a priori, different from k_l defined in Eq.(1.13). However, in the perfectly symmetric case, it reads:

$$\kappa_l = k_l = \frac{1}{2},$$

since the sums in Eqs.(1.13) and (1.15b) must be equal to one. The quantum dot Hamiltonian is

$$\hat{H}_{\odot} = \hat{H}^{(0)}_{\odot} - ek_{\mathrm{G}}V_{\mathrm{G}}\hat{N}, \tag{1.16a}$$
$$\hat{H}^{(0)}_{\odot} = U\, \hat{d}^{\dagger}_{\uparrow}\hat{d}_{\uparrow}\hat{d}^{\dagger}_{\downarrow}\hat{d}_{\downarrow} + \sum_{\sigma} \bar{E}_{\sigma}\hat{d}^{\dagger}_{\sigma}\hat{d}_{\sigma}, \tag{1.16b}$$

with $\hat{d}_\sigma^\dagger$ and $\hat{d}_\sigma$ denoting the fermionic annihilation and creation operator of the electron in the dot with spin σ, and $\hat{N} = \sum_\sigma \hat{d}_\sigma^\dagger \hat{d}_\sigma$ the number operator. We have defined $\hat{H}_\odot^{(0)}$ as the Hamiltonian of an isolated quantum dot in the Anderson model, while the second term of $\hat{H}_\odot$ in Eq.(1.16a) describes the effect of the gate terminal. We have introduced the dimensionless constant k_G, in analogy with k_l, to incorporate the effects of the experimental set-up. Experimentally the typical gate voltage range is of the order of some Volts while the bias one is in the range of the millivolts. This is due to the fact that $k_\mathrm{G} \ll k_l$. Here, in the totally symmetric case, we will fix, by convention, $k_\mathrm{G} = 1/2$, keeping in mind that in the experiments it is a free parameter. In Eq.(1.16b) we have introduced the interaction between particles via the constant U, while E_σ is the energy of the state with spin σ. In the Anderson model the Fock space of the quantum dot is

$$\mathcal{H}_\odot = \{|0\rangle, |\uparrow\rangle, |\downarrow\rangle, |2\rangle\},$$

where the total spin in the state $|2\rangle$ is zero. Having few states it is not difficult to diagonalize $\hat{H}_\odot$ of Eq.(1.16b) in the following form

$$\hat{H}_\odot^{(0)} = \sum_\nu \bar{E}_\nu \, |\nu\rangle\langle\nu|,$$

where $\nu = 1, \uparrow, \downarrow, 2$, while $\bar{E}_\nu$ is the energy of the corresponding state:

$$\bar{E}_0 = 0, \qquad \bar{E}_2 = U + \sum_\sigma \bar{E}_\sigma. \tag{1.17a}$$

Often in literature the on-site energy E_d is introduced. Thus the spin dependent energies read

$$\bar{E}_{\uparrow,\downarrow} = E_\mathrm{d} \pm \Delta(B), \tag{1.18}$$

where $\Delta(B) = \mu_\mathrm{B} g_\mathrm{s} B/2$. Here μ_B is the Bohr magnetic moment, $g_\mathrm{s} = 2$ is the Landè spin g-factor and B is the amplitude of the applied magnetic field fixing the z-quantization axis. We can also include the effect of the gate voltage as follows:

$$\hat{H}_\odot = \sum_\nu E_\nu \, |\nu\rangle\langle\nu|,$$

where $E_\nu = \bar{E}_\nu - n_\nu e k_\mathrm{G} V_\mathrm{G}$. Concluding the considerations about the Hamiltonian of the system, it is often useful to split $\hat{H}_\mathrm{tot} = \hat{H}_0 + \hat{H}_\mathrm{T}$, where $\hat{H}_0$ is the principal part $\hat{H}_0 = \hat{H}_\odot + \hat{H}_\mathrm{RS}$ and $\hat{H}_\mathrm{T}$ is the tunnelling Hamiltonian in Eq.(1.14).

1.1.3 Time evolution of a statistical mixture

Let us now consider the time evolution of a statistical mixture described by the state vector $|\Psi(t)\rangle$. Let us suppose that at a certain initial time t_0 the system is in the state $|\Psi(t_0)\rangle$ and the density operator is

$$\hat{\rho}(t_0) = \sum_n W_n |\psi_n(t_0)\rangle\langle\psi_n(t_0)| .$$

Because the states change in time, from Eq.(1.5), it follows

$$\begin{aligned}\hat{\rho}(t) &= \sum_n W_n |\psi_n(t)\rangle\langle\psi_n(t)| \\ &= \hat{U}(t,t_0)\,\hat{\rho}(t_0)\,\hat{U}^\dagger(t,t_0) .\end{aligned} \tag{1.19}$$

Here we have introduced the unitary time evolution operator $\hat{U}(t,t_0)$. This operator is such that

$$|\psi_n(t)\rangle = \hat{U}(t,t_0)\,|\psi_n(t_0)\rangle , \tag{1.20}$$

and it completely determines the time evolution of the system. In order to obtain the analytic expression of such an operator we have to consider the Schrödinger equation

$$i\hbar\frac{\partial}{\partial t}|\psi_n(t)\rangle = \hat{H}_{\text{tot}}(t)\,|\psi_n(t)\rangle . \tag{1.21}$$

Now, substituting Eq.(1.20) into Eq.(1.21), we have the following differential equation

$$i\hbar\frac{\partial}{\partial t}\hat{U}(t,t_0) = \hat{H}_{\text{tot}}(t)\,\hat{U}(t,t_0) , \tag{1.22}$$

with initial condition $\hat{U}(t_0,t_0) = \mathbb{1}$, since $|\psi(t_0)\rangle = \hat{U}(t_0,t_0)\,|\psi(t_0)\rangle$. Solving this equation (that in general for time dependent Hamiltonians is not trivial), the time evolution of the system and of the observables is determined. Furthermore, we can derive a differential equation also for the density matrix differentiating Eq.(1.19) and using Eq.(1.22). The result is the so-called *Liouville-Von Neumann equation* and reads:

$$i\hbar\dot{\hat{\rho}}(t) = \left[\hat{H}_{\text{tot}}(t)\,,\hat{\rho}(t)\right] , \tag{1.23}$$

with proper initial condition depending on the physical situation. Here we have indicated the derivative with respect to time of the density matrix with $\dot{\hat{\rho}}(t)$. We can rewrite Eq.(1.23) introducing the *Liouville superoperator*

$$\hat{\mathcal{L}}_i(t)\,\hat{X}_i \overset{\text{def}}{=} \frac{\left[\hat{H}_i(t)\,,\hat{X}_i\right]}{\hbar}, \tag{1.24}$$

in a more compact form

$$\dot{\hat{\rho}}(t) = -i\hat{\mathcal{L}}_{\text{tot}}(t)\,\hat{\rho}(t) . \tag{1.25}$$

Interaction picture In the following we will consider the interaction picture. Thus it is convenient to partition the Hamiltonian as follows

$$\hat{H} = \hat{H}_0 + \Theta(t - t_0)\,\hat{H}_{\mathrm{T}},$$

where $\Theta(t - t_0)$ is the Heaviside-function, $\hat{H}_0$ is the Hamiltonian of the two reservoirs plus the one of the dot, and $\hat{H}_{\mathrm{T}}$ describes the interaction between the dot and the leads, as we have defined in Sect.1.1.2. We want to stress that $\hat{H} = \hat{H}_{\mathrm{tot}}(t)$ for $t \geq t_0$, while, for $t < t_0$, the dot and the leads are completely decoupled. Here we have supposed that the interaction between the leads and the dot starts at a certain arbitrary time t_0. In this case the most efficient procedure is to switch from the Schrödingier picture we have adopted to the interaction one. From now on operators and states of the system without any subscript are to be intended in the Schrödinger picture, whereas we will labelled them, in the interaction picture, with the subscript I. In this picture both state vector and operators evolve with respect to time [42]. In particular, the states in the interaction picture read

$$|\psi_n(t)\rangle_{\mathrm{I}} \stackrel{\mathrm{def}}{=} \hat{U}_0^{\dagger}(t, t_0)\,|\psi_n(t)\rangle\,, \tag{1.26a}$$

$$i\hbar\frac{\partial}{\partial t}\hat{U}_0(t, t_0) = \hat{H}_0\hat{U}_0(t, t_0)\,, \tag{1.26b}$$

while the remaining part of the time evolution, for $t > t_0$, gives

$$|\psi_n(t)\rangle_{\mathrm{I}} = \hat{U}_{\mathrm{I}}(t, t_0)\,|\psi_n(t_0)\rangle_{\mathrm{I}}\,, \tag{1.27a}$$

$$i\hbar\frac{\partial}{\partial t}\hat{U}_{\mathrm{I}}(t, t_0) = \hat{H}_{\mathrm{T,I}}(t)\,\hat{U}_{\mathrm{I}}(t, t_0)\,. \tag{1.27b}$$

From Eqs.(1.26) and (1.27) we can deduce that $\hat{U}_{\mathrm{I}}(t, t_0) = \hat{U}_0^{\dagger}(t, t_0)\,\hat{U}(t, t_0)$. Notice that since in our case $\hat{H}$ is not time dependent for $t > t_0$, we have

$$\hat{U}(t, t_0) = e^{-\frac{i}{\hbar}\left(\hat{H}_0 + \hat{H}_{\mathrm{T}}\right)(t - t_0)},$$

where

$$\left[\hat{H}_0, \hat{H}_{\mathrm{T}}\right] \stackrel{\mathrm{def}}{=} \hat{C} \neq \mathbb{0}, \qquad \left[\hat{C}, \hat{H}_{\mathrm{T}}\right] \neq \mathbb{0}, \qquad \left[\hat{C}, \hat{H}_0\right] \neq \mathbb{0}. \tag{1.28}$$

Because $\hat{H}_{\mathrm{T}}$ and $\hat{H}_0$ do not commute with each other, using the Baker-Campbell-Hausdorff relation, the proper time evolution operator should be

$$\begin{aligned}\hat{U}(t, t_0) &= e^{-\frac{i}{\hbar}\hat{H}_0(t - t_0)}e^{-\frac{i}{\hbar}\hat{H}_{\mathrm{T}}(t - t_0)}e^{\hat{Z}} \\ &\simeq e^{-\frac{i}{\hbar}\hat{H}_0(t - t_0)}e^{-\frac{i}{\hbar}\hat{H}_{\mathrm{T}}(t - t_0)} + \Theta(t - t_0)\,\mathcal{O}\left(\hat{H}_{\mathrm{T}}\right).\end{aligned}$$

Here $\hat{Z}$ is a complicated function of commutators as in Eq.(1.28). Moreover, in Eq.(1.27), we have indicated with $\hat{H}_{\mathrm{T,I}}(t)$ the time evolution of the tunnelling Hamiltonian in the interaction picture

$$\hat{H}_{\mathrm{T,I}}(t) = \hat{U}_0^{\dagger}(t, t_0)\,\hat{H}_{\mathrm{T}}\hat{U}_0(t, t_0) \tag{1.29}$$

It is also useful to define the density matrix in the interaction picture as

$$\begin{aligned}\hat{\rho}_{\mathrm{I}}(t) &\stackrel{\mathrm{def}}{=} \sum_i W_i \left|\psi_i(t)\right\rangle_{\mathrm{I}\ \mathrm{I}}\left\langle\psi_i(t)\right| \\ &= \hat{U}_{\mathrm{I}}(t,t_0)\,\hat{\rho}_{\mathrm{I}}(t_0)\,\hat{U}_{\mathrm{I}}^{\dagger}(t,t_0)\,. \end{aligned} \tag{1.30}$$

This, remembering Eq.(1.26), Eq.(1.27) and differentiating Eq.(1.30), demonstrates that, in this picture, the density matrix evolves only with respect to the interaction Hamiltonian:

$$\dot{\hat{\rho}}_{\mathrm{I}}(t) = -i\hat{\mathcal{L}}_{\mathrm{T,I}}(t)\,\hat{\rho}_{\mathrm{I}}(t)\,, \tag{1.31a}$$

$$\hat{\rho}_{\mathrm{I}}(t_0) = \hat{\rho}(t_0)\,. \tag{1.31b}$$

Here we have imposed the continuity of the density operator for $t = t_0$ as initial condition (Eq.(1.31b)). Formally it is possible to integrate the *Liouville-von Neumann* equation in the interaction picture obtaining

$$\hat{\rho}_{\mathrm{I}}(t) = \hat{\rho}_{\mathrm{I}}(t_0) - i\int_{t_0}^{t} \hat{\mathcal{L}}_{\mathrm{T,I}}(\tau)\,\hat{\rho}_{\mathrm{I}}(\tau)\;d\tau. \tag{1.32}$$

This is an integral equation for the time evolved density matrix. The method commonly adopted is to insert Eq.(1.32) in Eq.(1.31). This yields

$$\dot{\hat{\rho}}_{\mathrm{I}}(t) = -i\hat{\mathcal{L}}_{\mathrm{T,I}}(t)\,\hat{\rho}_{\mathrm{I}}(t_0) - \int_{t_0}^{t} \hat{\mathcal{L}}_{\mathrm{T,I}}(t)\,\hat{\mathcal{L}}_{\mathrm{T,I}}(\tau)\,\hat{\rho}_{\mathrm{I}}(\tau)\;d\tau. \tag{1.33}$$

Iterating this procedure we can obtain a power series identifying the evolution of the density operator, the so-called *Dyson-series*, that is formally written as

$$\hat{\rho}_{\mathrm{I}}(t) = \hat{\mathsf{T}}\exp\left(-i\int_{t_0}^{t} d\tau\,\hat{\mathcal{L}}_{\mathrm{T,I}}(\tau)\right)\hat{\rho}_{\mathrm{I}}(t_0)\,. \tag{1.34}$$

Here we have introduced the time ordering super-operator $\hat{\mathsf{T}}$ that imposes the right time sequence of the Liouville super-operator when we expand the exponential $(t,\ldots,t_n,\ldots,\tau,t_0)$. This expression is the starting point for all order perturbation theory (in the energy of coupling to the leads E_{T}) and for introducing the concept of Feynmann diagrams. Initially we will deal only with a second order approximation of Eq.(1.33). However, in a second step we will address non perturbative corrections to the density matrix operator and then, in a certain sense, we will recover some parts of the series in Eq.(1.34).

1.1.4 The reduced density matrix

As we have already discussed in Sect.1.1.2, our system is formed by the leads and the dot. Without the tunnelling Hamiltonian they would be completely independent having separated Hilbert spaces $\mathcal{H}_{\mathrm{RS}} = \{|\phi_i\rangle\}$, for the leads, and $\mathcal{H}_{\odot} = \{|\varphi_j\rangle\}$, for the dot. Before the interaction is turned on the two systems are in the pure states $|\phi_i\rangle$ and $|\varphi_j\rangle$, then the combined system state is represented by the state vector

$$|\Psi(t)\rangle = |\phi_\alpha(t)\rangle \otimes |\varphi_\beta(t)\rangle, \qquad t < t_0. \tag{1.35}$$

At a certain time t_0 the interaction between these two systems is turned on and the state vector evolves driven by the time evolution operator determined by the composite space. For $t \geq t_0$ Eq.(1.35) is no more valid because the system is in a mixed state:

$$|\Psi(t)\rangle = \sum_{i,j} a_{i,j}(t) |\phi_i(t)\rangle \otimes |\varphi_j(t)\rangle, \qquad t \geq t_0,$$

where $|a_{i,j}(t)|^2$ is the probability to find the dot in the state $|\varphi_j(t)\rangle$ and the leads in $|\phi_i(t)\rangle$. Since we are interested only in the properties of the dot we want to construct the relevant density operator characterizing the dot: the so-called *reduced density matrix* (RDM). Let us consider an operator $\hat{Q}$ acting only on the space of the dot. Then, being $\hat{\rho}$ the density matrix of the whole system, the expectation value of such an operator reads

$$\begin{aligned}\left\langle \hat{Q} \right\rangle &\stackrel{\text{def}}{=} \mathsf{Tr}\left\{\hat{\rho}(t)\hat{Q}\right\} \\ &= \sum_{i',j'}\sum_{i,j}\left[\langle\phi_i\varphi_j|\hat{\rho}(t)\left|\phi_{i'}\varphi_{j'}\right\rangle\langle\phi_{i'}|\phi_i\rangle\left\langle\varphi_{j'}\right|\hat{Q}|\varphi_j\rangle\right].\end{aligned} \tag{1.36}$$

This suggests us to introduce the **reduced density matrix**

$$\hat{\rho}_{\odot} \stackrel{\text{def}}{=} \sum_i \langle\phi_i|\hat{\rho}(t)|\phi_i\rangle = \mathsf{Tr}_{\mathrm{RS}}\{\hat{\rho}(t)\}. \tag{1.37}$$

This allows us to rewrite Eq.(1.36) as

$$\left\langle \hat{Q} \right\rangle = \mathsf{Tr}\left\{\hat{\rho}(t)\hat{Q}\right\} = \mathsf{Tr}_{\odot}\left\{\hat{\rho}_{\odot}(t)\hat{Q}\right\},$$

highlighting the fact that $\hat{\rho}_{\odot}(t)$ contains only informations about the dot.

Time evolution of the reduced density matrix In the previous Section we have seen that a closed system evolves according to the Liouville-von Neumann equation (Eq.(1.25)). In particular a pure state of the whole system, evolving in time, will not become a mixed one. In our case only the dot and

leads together can be considered isolated; hence a pure state of the dot is allowed to evolve in a mixture during the time evolution. Indeed the system "dot" itself is said to be an **open system**, being allowed to exchange particles and energy with the leads that are unobserved. In this case the evolution of the dot cannot be determined via the Liouville equation but we have to address the problem with the RDM. Combining Eq.(1.37), stating that the reduced density matrix is the trace over the leads degrees of freedom of the density matrix itself, and Eq.(1.25) we get the right differential equation for an open system:

$$\dot{\hat{\rho}}_{\odot}(t) = -i\mathsf{Tr}_{\mathrm{RS}}\left\{\hat{\mathcal{L}}_{\mathrm{tot}}(t)\,\hat{\rho}(t)\right\}, \tag{1.38a}$$

$$\hat{\rho}(t_0) = \hat{\rho}_{\odot}(t_0)\otimes\hat{\rho}_{\mathrm{RS}}(t_0). \tag{1.38b}$$

Here the initial condition (Eq.(1.38b)) we have chosen imposes that the leads and the dot are completely *uncorrelated* for $t < t_0$. Taking the same trace over the leads' degrees of freedom of Eq.(1.33) we can obtain also the Liouville equation for the RDM in the interaction picture:

$$\dot{\hat{\rho}}_{\odot,\mathrm{I}}(t) = -i\mathsf{Tr}_{\mathrm{RS}}\left\{\hat{\mathcal{L}}_{\mathrm{T,I}}(t)\,\hat{\rho}_{\mathrm{I}}(t_0)\right\} - \int_{t_0}^{t}\mathsf{Tr}_{\mathrm{RS}}\left\{\hat{\mathcal{L}}_{\mathrm{T,I}}(t)\,\hat{\mathcal{L}}_{\mathrm{T,I}}(\tau)\,\hat{\rho}_{\mathrm{I}}(\tau)\right\}d\tau. \tag{1.39}$$

We want to point out that at this stage no approximation was considered and Eqs.(1.39) and (1.38a) are both exact to all orders in $\hat{H}_{\mathrm{T,I}}$.

The generalized master equation In the previous paragraph we have obtained the Liouville equation for the RDM in the interaction picture (Eq.(1.39)) with the corresponding initial condition Eq.(1.38b). Let us assume furthermore that the leads are so extended that they will be always in thermal equilibrium, independent of the energy and the particles they exchange with the dot. This is a realistic assumption since they have so many degrees of freedom that they can rearrange themselves on a time scale much smaller than the time scale of the dynamics of the dot. Mathematically we are taking the limit of infinite volumes of the leads (assuming it exists) and then the leads have no dynamics in comparison to the time scale of the dot:

$$\hat{\rho}_l(t) = \lim_{V\to\infty}\hat{\rho}_l(t_0), \qquad l = \mathrm{R},\mathrm{L}$$

where $\hat{\rho}_l(t_0)$ is defined in Eq.(1.11). Then the time evolution of the whole system is determined up to first order in the tunnelling by the time evolution of the RDM:

$$\hat{\rho}_{\mathrm{I}}(t) = \hat{\rho}_{\odot}(t)\otimes\hat{\rho}_{\mathrm{RS}}(t_0) + \mathcal{O}\left(\hat{H}_{\mathrm{T}}\right), \qquad \forall t. \tag{1.40}$$

After all these consideration let us further develop the differential equation for the RDM (Eq.(1.39)). As stated in Eq.(1.14), the tunnelling Hamiltonian is bilinear in the dot and leads creation-annihilation operators. Moreover, since $[\hat{H}_{\odot}, \hat{H}_{\mathrm{RS}}] = 0$, considering Eq.(1.29) the tunnelling Hamiltonian in the interaction picture reads:

$$\begin{aligned}\hat{H}_{\mathrm{T,I}}(t) &= \hat{U}^{\dagger}_{\mathrm{RS}}(t,t_0)\,\hat{U}^{\dagger}_{\odot}(t,t_0)\,\hat{H}_{\mathrm{T}}(t)\,\hat{U}_{\mathrm{RS}}(t,t_0)\,\hat{U}_{\odot}(t,t_0)\\ &= \sum_{l,\sigma,\mathbf{k}} T_{l,\sigma,\mathbf{k}} \hat{d}^{\dagger}_{\mathrm{I},\sigma}(t)\,\hat{c}_{\mathrm{I},l,\sigma,\mathbf{k}}(t) + \mathrm{h.c.},\end{aligned} \tag{1.41}$$

where

$$\hat{c}_{l,\sigma,\mathbf{k}}(t) = \hat{U}^{\dagger}_{\mathrm{RS}}(t,t_0)\,\hat{c}_{l,\sigma,\mathbf{k}}(t_0)\,\hat{U}_{\mathrm{RS}}(t,t_0)\,, \tag{1.42a}$$

$$\hat{d}^{\dagger}_{\sigma}(t) = \hat{U}^{\dagger}_{\odot}(t,t_0)\,\hat{d}^{\dagger}_{\sigma}(t_0)\,\hat{U}_{\odot}(t,t_0)\,. \tag{1.42b}$$

Since in the tunnelling Hamiltonian $\hat{c}_{l,\sigma,\mathbf{k}}(t)$ and $\hat{c}^{\dagger}_{l,\sigma,\mathbf{k}}(t)$ appear separately, using Wick's theorem, from Eq.(1.39) we deduce

$$\mathsf{Tr}_{\mathrm{RS}}\left\{\hat{\mathcal{L}}_{\mathrm{I,T}}(t)\,\hat{\rho}_{\mathrm{I}}(t_0)\right\} = \mathbb{0},$$

and then it results

$$\dot{\hat{\rho}}_{\odot,\mathrm{I}}(t) = -\int_{t_0}^{t} \mathsf{Tr}_{\mathrm{RS}}\left\{\hat{\mathcal{L}}_{\mathrm{T,I}}(t)\,\hat{\mathcal{L}}_{\mathrm{T,I}}(\tau)\,\hat{\rho}_{\mathrm{I}}(\tau)\right\} d\tau. \tag{1.43}$$

Being interested in a second order approximation of Eq.(1.43), we can use Eq.(1.40) and introduce the *Kernel super-operator*:

$$\hat{\mathcal{K}}^{(2)}_{\mathrm{I}}(t,\tau)\,\hat{X}_i = -\mathsf{Tr}_{\mathrm{RS}}\left\{\hat{\mathcal{L}}_{\mathrm{T,I}}(t)\,\hat{\mathcal{L}}_{\mathrm{T,I}}(\tau)\,\hat{X}_i\,\hat{\rho}_{\mathrm{RS}}(t_0)\right\}, \tag{1.44}$$

acting on a generic operator $\hat{X}_i$ in the i-picture. This allows us to adsorb the Liouville super-operator and to recast Eq.(1.43) in a more compact form:

$$\dot{\hat{\rho}}_{\odot,\mathrm{I}}(t) = \int_{t_0}^{t} \hat{\mathcal{K}}^{(2)}_{\mathrm{I}}(t,\tau)\,\hat{\rho}_{\odot,\mathrm{I}}(\tau)\,d\tau. \tag{1.45}$$

Here we have introduced the superscript (2) to stress the fact that the super-operator in Eq.(1.44) as well as the differential equation for the reduced density matrix in Eq.(1.45) are correct up to the second order in the energy of coupling with the leads. In general, if this procedure is iterated to all orders in the coupling with the leads, similarly to Eq.(1.45), the exact equation can be found

$$\dot{\hat{\rho}}_{\odot,\mathrm{I}}(t) = \int_{t_0}^{t} \hat{\mathcal{K}}_{\mathrm{I}}(t,\tau)\,\hat{\rho}_{\odot,\mathrm{I}}(\tau)\,d\tau,$$

whose super-operator $\hat{\mathcal{K}}_{\mathrm{I}}(t,\tau)$ is a *power series* in the tunnelling Hamiltonian:

$$\hat{\mathcal{K}}_{\mathrm{I}}(t,\tau) = \sum_{i=1}^{\infty} \hat{\mathcal{K}}_{\mathrm{I}}^{(2i)}(t,\tau).$$

Thus far this is only a formal writing of the Kernel super-operator, but in the following (Sects.2.1 and 3), it will be further clarified and it will be of crucial importance. This integro-differential equation is known as *generalized master equation* (GME). Since we are interested in the stationary properties of the dot the proper condition to be imposed on the RDM is

$$\lim_{t\to\infty} \dot{\hat{\rho}}_{\odot}(t) = 0.$$

Then we have to back-transform Eq.(1.45) to the Schrödinger picture. To this purpose, since $\hat{H}_0$ is time-independent we can solve Eq.(1.26b) and we obtain the following relation

$$\begin{aligned}\dot{\hat{\rho}}_{\odot}(t) &= \frac{\partial}{\partial t}\left[\hat{U}_0(t,t_0)\,\hat{\rho}_{\odot,\mathrm{I}}(t)\,\hat{U}_0^{\dagger}(t,t_0)\right] \\ &= -\frac{i}{\hbar}\left[\hat{H}_0,\hat{\rho}_{\odot}(t)\right] + e^{-\frac{i}{\hbar}\hat{H}_0(t-t_0)}\dot{\hat{\rho}}_{\odot,\mathrm{I}}(t)\,e^{\frac{i}{\hbar}\hat{H}_0(t-t_0)}.\end{aligned}$$

Substituting Eq.(1.45) into the previous relation we arrive at the *GME for the RDM*

$$\dot{\hat{\rho}}_{\odot}(t) = -\frac{i}{\hbar}\left[\hat{H}_0,\hat{\rho}_{\odot}(t)\right] + \int_{t_0}^{t} \hat{\mathcal{K}}^{(2)}(t,\tau)\,\hat{\rho}_{\odot}(\tau)\,d\tau, \tag{1.46}$$

where $\hat{\mathcal{K}}^{(2)}(t,\tau)$ is the kernel operator in the Schrödinger picture:

$$\begin{aligned}&\hat{\mathcal{K}}^{(2)}(t,\tau)\left[\hat{\rho}_{\odot}(\tau)\right] = \\ &= e^{-\frac{i}{\hbar}\hat{H}_{\odot}(t-t_0)}\left(\hat{\mathcal{K}}_{\mathrm{I}}^{(2)}(t,\tau)\left[e^{\frac{i}{\hbar}\hat{H}_{\odot}(\tau-t_0)}\hat{\rho}_{\odot}(\tau)\,e^{-\frac{i}{\hbar}\hat{H}_{\odot}(\tau-t_0)}\right]\right)e^{\frac{i}{\hbar}\hat{H}_{\odot}(t-t_0)}.\end{aligned} \tag{1.47}$$

Here we have used $\hat{U}_{\odot}(t-t_0)$ since we have traced out the leads degrees of freedom. Since, in our case, no time-dependent perturbation is applied to the system, it can be demonstrated (App.A.1) that

$$\hat{\mathcal{K}}^{(2)}(t,\tau) = \hat{\mathcal{K}}^{(2)}(t-\tau). \tag{1.48}$$

This fact is of crucial importance. Indeed, it states that Eq.(1.46) acquires a convolutive form. Taking the limit for the steady state we obtain

$$\lim_{t\to+\infty} \dot{\hat{\rho}}_{\odot}(t) = -\frac{i}{\hbar}\left[\hat{H}_0,\hat{\rho}_{\odot}^{\infty}\right] + \lim_{t\to+\infty}\int_{t_0}^{t} \hat{\mathcal{K}}^{(2)}(t-\tau)\,\hat{\rho}_{\odot}(\tau)\,d\tau, \tag{1.49}$$

where we have supposed the existence of a stationary density matrix that we have indicated with $\hat{\rho}_{\odot}^{\infty} = \lim_{t\to+\infty} \hat{\rho}_{\odot}(t)$. In order to further recast the above equation let us introduce the Laplace transform as

$$\mathscr{L}\left\{\hat{X}(t)\right\} \stackrel{\text{def}}{=} \hat{X}(\lambda) = \int_0^{+\infty} \hat{X}(t) \exp(-\lambda t)\, dt$$

and define

$$\hat{\varrho}(t) \stackrel{\text{def}}{=} \int_{t_0}^{t} \hat{\mathcal{K}}^{(2)}(t-\tau)\, \hat{\rho}_{\odot}(\tau)\, d\tau.$$

Since the Laplace transform of a convolution integral, in the dual space, is the product of the transformed two functions we are integrating, this term reads

$$\mathscr{L}\{\hat{\varrho}(t)\} = \hat{\varrho}(\lambda) = \hat{\mathcal{K}}^{(2)}(\lambda)\, \hat{\rho}_{\odot}(\lambda).$$

Therefore, using the *final value theorem*,

$$\lim_{t\to+\infty} \hat{\varrho}(t) = \lim_{\lambda\to 0} \lambda \hat{\varrho}(\lambda), \tag{1.50}$$

applied to Eq.(1.49), we find

$$\dot{\hat{\rho}}_{\odot}^{\infty} = \mathbb{0} = -\frac{i}{\hbar}\left[\hat{H}_0, \hat{\rho}_{\odot}^{\infty}\right] + \left(\lim_{\lambda\to 0} \hat{\mathcal{K}}^{(2)}(\lambda)\right) \hat{\rho}_{\odot}^{\infty}, \tag{1.51}$$

because the limit of a product is the product of the limits if they exist. Moreover we have applied one more time the final value theorem stating $\hat{\rho}_{\odot}^{\infty} = \lim_{\lambda\to 0} \lambda \hat{\rho}_{\odot}(\lambda)$. The first term of Eq.(1.51) accounts for the coherent dynamics of the isolated system, whereas the second describes all processes due to tunnelling in or out of the dot. In general this is a system of coupled deferential equations that, in the stationary limit, reduces itself to a linear system of equations. We can see this explicitly taking the matrix elements with respect to the many-body eigenstates of $\hat{H}_0$:

$$\mathbb{0}_{b'}^{b} = -\frac{i}{\hbar} \sum_{a,a'} \delta_{a,b}\delta_{a',b'} (E_a - E_{a'})\, \rho_{a'}^{a} + \sum_{a,a'} K_{b',a'}^{b,a}(\lambda = 0)\, \rho_{a'}^{a}, \tag{1.52}$$

with

$$\hat{\rho}_{\odot}^{\infty} = \sum_{a,a'} \rho_{a'}^{a} \left|a\right\rangle\!\left\langle a'\right|, \tag{1.53a}$$

$$K_{b',a'}^{b,a}(\lambda = 0) \stackrel{\text{def}}{=} \left\langle b \middle| \hat{\mathcal{K}}^{(2)}(\lambda = 0)\left[\left|a\right\rangle\!\left\langle a'\right|\right] \middle| b' \right\rangle. \tag{1.53b}$$

Here we have used the square brackets to stress the fact that the kernel super-operator acts first on the density operator and afterwards the matrix

elements are taken. As we have discussed in Sect.1.1.1 the diagonal elements of the density matrix represent the probability of finding the system in a certain state. Thus, they must observe the *normalization condition* Eq.(1.7). This condition is required to solve the system in Eq.(1.52) because it is under-determined due to the following sum-rule:

$$\sum_{b} K^{b,a}_{b,a'} = 0 \quad \forall a, a'. \tag{1.54}$$

This sum-rule will become particularly evident once we will have introduced the *diagrammatic language* in the following.

Current through the dot As we have already pointed out in Sect.1.1.1 every expectation value of an observable can be written tracing out the observable itself times the density matrix (Eq.(1.4)). In particular we can define the average current flowing through the quantum dot as the variation in time of the average number of particles in the left or right lead:

$$I_l(t) = \mathsf{Tr}\left\{\hat{I}_l(t_0)\,\hat{\rho}(t)\right\} = \mathsf{Tr}\left\{\hat{U}^{\dagger}_{\mathrm{I}}(t,t_0)\,\hat{I}_{l,\mathrm{I}}(t)\,\hat{U}_{\mathrm{I}}(t,t_0)\,\hat{\rho}(t_0)\right\},$$

with $\hat{I}_{l,\mathrm{I}}(t)$ the current operator defined via

$$\begin{aligned}\hat{I}_{l,\mathrm{I}}(t) &\overset{\text{def}}{=} -e\dot{\hat{N}}_{l,\mathrm{I}}(t) = -i\frac{e}{\hbar}\left[\hat{H}_{\mathrm{I,T},l}(t), \hat{N}^{\mathrm{RS}}_{l,\mathrm{I}}(t)\right] \\ &= -i\frac{e}{\hbar}\sum_{\sigma,\mathbf{k}}\left[T_{l,\sigma,\mathbf{k}}\hat{d}^{\dagger}_{\sigma,\mathrm{I}}(t)\,\hat{c}_{l,\sigma,\mathbf{k},\mathrm{I}}(t) - T^{*}_{l,\sigma,\mathbf{k}}\hat{c}^{\dagger}_{l,\sigma,\mathbf{k},\mathrm{I}}(t)\,\hat{d}_{\sigma,\mathrm{I}}(t)\right].\end{aligned} \tag{1.55}$$

Here $\hat{N}^{\mathrm{RS}}_{l} = \sum_{\sigma,\mathbf{k}}\hat{c}^{\dagger}_{l,\sigma,\mathbf{k}}\hat{c}_{l,\sigma,\mathbf{k}}$ is the number operator in the l-lead. Comparing the expression of the current operator (Eq.(1.55)) and the one of the tunnelling Hamiltonian (Eq.(1.14)) we can notice that they differ, beside a pre-factor, in the sign of the out-tunnelling process with respect to the quantum dot. This will be very important in the next Section about the diagrammatic rules. Repeating the same steps of the previous paragraph we can recast this expectation value in a form similar to Eq.(1.46):

$$I_l(t) = \mathsf{Tr}_{\odot}\left\{\int_{t_0}^{t}\hat{\mathcal{K}}^{(2)}_{I_l}(t-\tau)\,\hat{\rho}^{\mathrm{I}}_{\odot}(\tau)\,d\tau\right\}, \tag{1.56a}$$

$$\hat{\mathcal{K}}^{(2)}_{\mathrm{I},I_l}(t-\tau)\,\hat{\rho}(\tau) = -i\mathsf{Tr}_{\mathrm{RS}}\left\{\hat{I}_{\mathrm{I},l}(t)\,\hat{\mathcal{L}}_{\mathrm{T,I}}(\tau)\,\hat{\rho}_{\odot,\mathrm{I}}(\tau)\otimes\hat{\rho}_{\mathrm{RS}}(t_0)\right\}, \tag{1.56b}$$

where we switched again to the interaction picture. Here we have introduced the *current Kernel* $\hat{\mathcal{K}}^{(2)}_{\mathrm{I},I_l}(t-\tau)$ that differs from the one of Eq.(1.44), besides the pre-factor, in the fact that the first Liouville super-operator has to be substituted with $\hat{I}_{\mathrm{I},l}(t)$. This is the only difference between the derivation of

Eq.(1.46) and Eq.(1.56). Indeed, due to the presence of $\hat{I}_{\mathrm{I},l}(t)$, now we have an odd number of Liouville superoperators in the final expression. In the end we can take the stationary limit also for the current, in the same way we have reported for the RDM. It results in

$$\lim_{t\to+\infty} I_l(t) = \mathsf{Tr}_{\odot}\left\{\hat{\mathcal{K}}_{I_l}(\lambda=0)\,\hat{\rho}_{\odot}^{\infty}\right\} = \sum_{a,a'}\sum_{b}\left(\hat{\mathcal{K}}_{I_l}(\lambda=0)\right)_{b',a'}^{b\ ,a}\rho_{a'}^{a}, \tag{1.57}$$

where we have defined

$$\hat{\mathcal{K}}_{I_l}(\lambda=0) \overset{\text{def}}{=} \lim_{\lambda\to 0}\mathscr{L}\left\{\hat{\mathcal{K}}_{I_l}(t)\right\}.$$

1.1.5 Diagrammatic analysis

In this Section we want to introduce a very useful tool to directly deduce the Kernel components $K_{b',a'}^{b\ ,a}(\lambda=0)$: *the diagrammatic technique*. To this purpose we will follow the same steps as in Ref. [40]. This method was introduced by Gerd Schön, Herbert Schoeller and Jürgen König [33, 38, 43–45] and it allows us to reformulate the GME (Eq.(1.52)) in a graphical language. As S. Koller has shown in Refs. [40] and [46], there is a one-to-one correspondence between diagrams and Kernel analytical expressions. The starting point of this method is the time evolution of the total density matrix in Eq.(1.34). Considering the trace of the full density matrix with respect to the leads degrees of freedom and expanding the Liouville super-operator definition, for dot's states $|b(t)\rangle$ and $|b'(t)\rangle$, we have

$$\begin{aligned}
\rho_{b'}^{b}(t) &= \langle b(t)|\,\mathsf{Tr}_{\mathrm{RS}}\left\{\hat{\rho}(t_0)\right\}|b'(t)\rangle \\
&= \sum_{a,a'}\rho_{a'}^{a}(t_0)\,\mathsf{Tr}_{\mathrm{RS}}\Big\{\Big\langle b_{\mathrm{I}}(t)\Big|\,\hat{\mathsf{T}}^{(+)}e^{-\frac{i}{\hbar}\int_{t_0}^{t}d\tau\,\hat{H}_{\mathrm{T,I}}(\tau)}\Big|a(t_0)\Big\rangle\,\hat{\rho}_{\mathrm{RS}}(t_0) \\
&\quad \Big\langle a'(t_0)\Big|\,\hat{\mathsf{T}}^{(-)}e^{\frac{i}{\hbar}\int_{t_0}^{t}d\tau\,\hat{H}_{\mathrm{T,I}}(\tau)}\Big|b'_{\mathrm{I}}(t)\Big\rangle\Big\} = \qquad (1.58a)\\
&= \sum_{a,a'}\Pi_{b',a'}^{b\ ,a}(t,t_0)\,\rho_{a'}^{a}(t_0), \qquad (1.58b)
\end{aligned}$$

where $\hat{\mathsf{T}}^{(+)}$ is the time ordering super-operator. Expanding the exponents in Eq.(1.58a), it orders the operators in such a way that every operator lies on the right of operators to later times ($t>\tau_n>\tau_{n-1}>\cdots>\tau_0>t_0$). $\hat{\mathsf{T}}^{(-)}$ is the anti-time ordering super-operator and its effect is the opposite one. Here we have written the initial RDM as $\hat{\rho}_{\mathrm{I},\odot}(t_0)=\sum_{a,a'}\rho_{a'}^{a}(t_0)\,|a(t_0)\rangle\langle a'(t_0)|$. Moreover, often in literature, the reduced propagator

$$\begin{aligned}
\Pi_{b',a'}^{b\ ,a}(t,t_0) = \mathsf{Tr}_{\mathrm{RS}}\Big\{&\Big\langle b_{\mathrm{I}}(t)\Big|\,\hat{\mathsf{T}}^{(+)}e^{-\frac{i}{\hbar}\int_{t_0}^{t}d\tau\,\hat{H}_{\mathrm{T,I}}(\tau)}\Big|a(t_0)\Big\rangle\,\hat{\rho}_{\mathrm{RS}}(t_0) \\
&\Big\langle a'(t_0)\Big|\,\hat{\mathsf{T}}^{(-)}e^{\frac{i}{\hbar}\int_{t_0}^{t}d\tau\,\hat{H}_{\mathrm{T,I}}(\tau)}\Big|b'_{\mathrm{I}}(t)\Big\rangle\Big\}
\end{aligned} \tag{1.59}$$

is introduced. It is responsible for the time evolution of the RDM from the initial time t_0 to the final one t. Such a propagator is the exact version of the second order Kernel super-operator in Eq.(1.44). Considering the Taylor

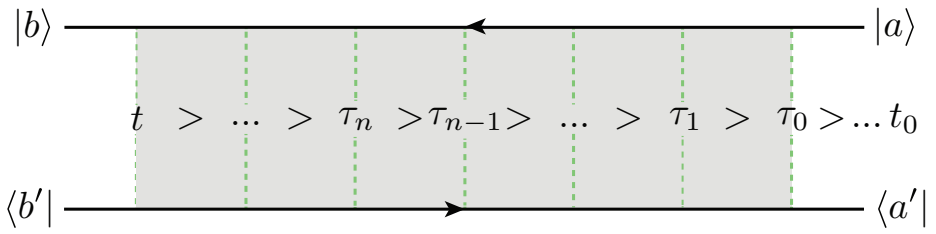

Figure 1.2: Time ordering in a diagrammatic representation of one contribution to the RDM time evolution. Here time evolves from the initial time t_0, on the right, to the final one t, on the left.

expansion of the exponentials in terms of the tunnelling Hamiltonian, one can arrive at the afore-mentioned graphical language. Indeed, from Eq.(1.58a), we can understand that, in order to describe the time evolution of the RDM, we need two time lines evolving in opposite directions, the first connecting the state $|b(t)\rangle \leftarrow |a(t_0)\rangle$ while the second $\langle b'(t)| \rightarrow \langle a'(t_0)|$, because of the time and anti-time ordering super-operators (Fig.1.2). Intuitively one can understand this difference thinking that bra states evolve in the opposite direction with respect to the physical time because they belong to the dual space [42]. In literature these time lines are often called *Keldysh contours*. In the diagram the physical time grows from right to left[1]in such a way that $|a(t_0)\rangle$, $\langle a'(t_0)|$ are said *initial states*. Indeed they represent the initial state of the RDM (see Eq.(1.58a)), and $|b'(t)\rangle$, $\langle b(t)|$ are said *final states*. As depicted in Fig.1.2, in the between of the first event in τ_0 and the final one in t several tunnelling events in (or out) the dot may occur (shaded area). These are represented (see Tab.1.1) with fermion lines (grey lines) connecting the upper and the lower contour and two vertexes on the contours themselves. Vertexes are placed along the time-line in precise points, labelled with increasing time indexes from the right to the left, corresponding to the time at which the event, annihilation or creation of a particle in the dot or in the leads, occurs. As we have already pointed out the strength of this technique is that we can directly deduce the analytic contribution of the Kernel super-operator Laplace transform from these diagrams with simple rules (App.A.3.1). In order to understand deeply these rules let us split the tunnelling Hamiltonian into an in-tunnelling (+) and out-tunnelling (−)

[1]Notice that in Ref. [38] another convention was used, i.e. time grows form left to right.

components

$$\hbar^{-1}\hat{H}_{\mathrm{T,I}}(\tau_i) = \hat{A}_i^{+} + \hat{A}_i^{-}, \qquad \text{with} \quad \hat{A}_i^{p} \stackrel{\text{def}}{=} \sum_{\mathbf{j}} \hat{D}^{p}_{\mathrm{I},i,\mathbf{j}} \hat{C}^{\bar{p}}_{\mathrm{I},i,\mathbf{j}}, \tag{1.60}$$

where $\mathbf{j} = (l, \sigma, \mathbf{k})$ and $p = +/-$. Here $\hat{D}^{p}_{\mathrm{I},i,\mathbf{j}}$ and $\hat{C}^{\bar{p}}_{\mathrm{I},i,\mathbf{j}}$ are the time evolution, in the interaction picture, of the operators in the Schrödinger one:

$$\hat{D}^{p}_{\mathrm{I},i,\mathbf{j}} = \hat{U}_0^{\dagger}(\tau_i, t_0)\, \hat{D}^{p}_{\mathbf{j}} \hat{U}_0(\tau_i, t_0), \tag{1.61a}$$

$$\hat{C}^{p}_{\mathrm{I},i,\mathbf{j}} = \hat{U}_0^{\dagger}(\tau_i, t_0)\, \hat{C}^{p}_{\mathbf{j}} \hat{U}_0(\tau_i, t_0). \tag{1.61b}$$

We have introduced the p-index in such a way that the expression of $\hat{H}_{\mathrm{T}}$ in Eq.(1.14) and Eq.(1.60) coincides if

$$\hat{D}^{+}_{l,\sigma,\mathbf{k}} = \hbar^{-1}\hat{d}^{\dagger}_{\sigma}, \tag{1.62a}$$

$$\hat{C}^{-}_{l,\sigma,\mathbf{k}} = T_{l,\sigma,\mathbf{k}}\, \hat{c}_{l,\sigma,\mathbf{k}}, \tag{1.62b}$$

$$\hat{D}^{-}_{l,\sigma,\mathbf{k}} = \left(\hat{D}^{+}_{l,\sigma,\mathbf{k}}\right)^{\dagger}, \tag{1.62c}$$

$$\hat{C}^{+}_{l,\sigma,\mathbf{k}} = \left(\hat{C}^{-}_{l,\sigma,\mathbf{k}}\right)^{\dagger}. \tag{1.62d}$$

Expanding the Kernel definition in Eq.(1.44) in terms of the ones introduced in Eq.(1.60) we find

$$\hat{\mathcal{K}}^{(2)}_{\mathrm{I}}(t,\tau)\, \hat{\rho}_{\mathrm{I},\odot}(t) = -\sum_{p_0,p_1} \mathsf{Tr}_{\mathrm{RS}} \left\{ \left[\hat{A}^{p_1}_{1}, \left[\hat{A}^{p_0}_{0}, \hat{\rho}_{\mathrm{I},\odot}(\tau) \otimes \hat{\rho}_{\mathrm{RS}} \right] \right] \right\}. \tag{1.63}$$

Here we have imposed $t = \tau_1$ and $\tau = \tau_0$.

General structure of the Kernel superoperator components In the following we will analyse the most general Kernel component of order $2n$ in the coupling to the leads. However, if the reader is interested just in the second order approximation, it is enough to consider Eq.(1.63) to obtain all the terms in Tab.1.1. Then one can consider the diagrammatic rules presented the next paragraph to understand the mapping between the second order diagrams and Kernel components.
In general, considering a Kernel of the order $2n$, we have to impose $\tau_n = t$ and $\tau_0 = \tau$. As it is shown for the second order in App.A.1 (Eq.(A.3)) it is possible to evaluate the multiple commutators and recast Eq.(1.63) in the sum of terms with the following structure:

$$\prod_{\alpha=1}^{n} \left\langle \hat{C}^{p^{(0)}_{\alpha}}_{\mathrm{I},t^{(0)}_{\alpha},\mathbf{j}^{(0)}_{\alpha}} \hat{C}^{p^{(1)}_{\alpha}}_{\mathrm{I},t^{(1)}_{\alpha},\mathbf{j}^{(1)}_{\alpha}} \right\rangle_{\mathrm{RS}} \left\langle b \left| \prod_{\beta=1}^{n_{\mathrm{L}}} \hat{D}^{\bar{p}^{\mathrm{L}}_{\beta}}_{\mathrm{I},t^{\mathrm{L}}_{\beta},\mathbf{j}^{\mathrm{L}}_{\beta}} \right| a \right\rangle$$

$$\left\langle a \left| \hat{\rho}_{\mathrm{I},\odot}(\tau) \right| a' \right\rangle \left\langle a' \left| \prod_{\gamma=1}^{n_{\mathrm{R}}} \hat{D}^{\bar{p}^{\mathrm{R}}_{\gamma}}_{\mathrm{I},t^{\mathrm{R}}_{\gamma},\mathbf{j}^{\mathrm{R}}_{\gamma}} \right| b' \right\rangle. \tag{1.64}$$

Here we have defined $n_{\rm L}+n_{\rm R}=2n$. Moreover we introduced the n dimensional vectors $\mathbf{p}^{(0)}$ and $\mathbf{p}^{(1)}$, whose components $p_\alpha^{(0)}=\pm$ and $p_\alpha^{(1)}=\pm$ specifies whether the corresponding operator is a creation $(+)$ or annihilation $(-)$ process. Accordingly we defined the n dimensional time and quantum numbers vectors

$$\mathbf{t}^{(0/1)}=\left\{\, t_\alpha^{(0/1)},\, \alpha=1,\dots,n\,\right\},$$
$$\mathbf{j}^{(0/1)}=\left\{\, \mathbf{j}_\alpha^{(0/1)},\, \alpha=1,\dots,n\,\right\},$$

correspondingly. Here $t_\alpha^{(0/1)}\in\{0,\dots,n-1\}$ fixes the time-label (Fig.1.2) and $\mathbf{j}_\alpha^{(0/1)}=(l_\alpha,\sigma_\alpha,\mathbf{k}_\alpha)$ specifies the quantum numbers associated to the α-th tunnelling process. In general $t_\alpha^{(0)}\neq t_\alpha^{(1)}$ and $\mathbf{j}_\alpha^{(0)}\neq\mathbf{j}_\alpha^{(1)}$, allowing all the possible combinations between the operators $\hat{C}^{p_\alpha^{(0)}}_{{\rm I},t_\alpha^{(0)},\mathbf{j}_\alpha^{(0)}}$ and $\hat{C}^{p_\alpha^{(1)}}_{{\rm I},t_\alpha^{(1)},\mathbf{j}_\alpha^{(1)}}$. Because of the average value in Eq.(1.64), we have that Wick theorem imposes

$$\left\langle \hat{C}^{p_\alpha^{(0)}}_{{\rm I},t_\alpha^{(0)},\mathbf{j}_\alpha^{(0)}}\hat{C}^{p_\alpha^{(1)}}_{{\rm I},t_\alpha^{(1)},\mathbf{j}_\alpha^{(1)}}\right\rangle_{\rm RS}\propto\delta_{\mathbf{j}_\alpha^{(0)}\mathbf{j}_\alpha^{(1)}}\delta_{p_\alpha^{(0)},\bar{p}_\alpha^{(1)}}. \tag{1.65}$$

Thus we have only n degrees of freedom in the choice of both $p_\alpha^{(0)}$ and $p_\alpha^{(1)}$. The same holds true for $\mathbf{j}_\alpha^{(0)}$ and $\mathbf{j}_\alpha^{(1)}$. We will specify the missing proportionality coefficient in Eq.(1.65) in the following. Furthermore, in Eqs.(1.64) and (1.65) we have defined the left (L) and right (R) vectors

$$\mathbf{p}^{\rm L}=\left\{\, p_\beta^{\rm L},\, \beta=1,\dots,n_{\rm L}\,\right\},\qquad \mathbf{p}^{\rm R}=\left\{\, p_\gamma^{\rm R},\, \gamma=1,\dots,n_{\rm R}\,\right\},$$
$$\mathbf{t}^{\rm L}=\left\{\, t_\beta^{\rm L},\, \beta=1,\dots,n_{\rm L}\,\right\},\qquad \mathbf{t}^{\rm R}=\left\{\, t_\gamma^{\rm R},\, \gamma=1,\dots,n_{\rm R}\,\right\},$$
$$\mathbf{j}^{\rm L}=\left\{\, \mathbf{j}_\beta^{\rm L},\, \beta=1,\dots,n_{\rm L}\,\right\},\qquad \mathbf{j}^{\rm R}=\left\{\, \mathbf{j}_\gamma^{\rm R},\, \gamma=1,\dots,n_{\rm R}\,\right\}.$$

They are a recombination of the $\mathbf{p}^{(0/1)}$, $\mathbf{t}^{(0/1)}$ and $\mathbf{j}^{(0/1)}$ vectors we have discussed above. Furthermore because of the Wick theorem we have $\sum_\gamma p_\gamma^{\rm R}+\sum_\beta p_\beta^{\rm L}=0$.

Let us consider a second order example ($n=1$). In order to obtain the operator in the first row of Tab.1.1 we have to choose $n_{\rm L}=n_{\rm R}=1$,

$$\left\{\begin{array}{l} p_1^{(0)}=+,\\ p_1^{(1)}=-,\end{array}\right.\longrightarrow\left\{\begin{array}{l} p_1^{\rm R}=+,\\ p_1^{\rm L}=-,\end{array}\right.\quad\text{and}\quad\left\{\begin{array}{l} t_1^{(0)}=0,\\ t_1^{(1)}=1,\end{array}\right.\longrightarrow\left\{\begin{array}{l} t_1^{\rm R}=0,\\ t_1^{\rm L}=1.\end{array}\right.$$

Moreover we can consider also the term in the third row. As in the previous case $n=2$ and $\alpha=1$. In contrast, since we have two dot operators on the left ($n_{\rm L}=2$) and zero on the right ($n_{\rm R}=0$) of the RDM, in this case we have

$$\left\{\begin{array}{l} p_1^{(0)}=-,\\ p_1^{(1)}=+,\end{array}\right.,\longrightarrow\left\{\begin{array}{l} p_1^{\rm L}=-,\\ p_2^{\rm L}=+,\end{array}\right.\quad\text{and}\quad\left\{\begin{array}{l} t_1^{(0)}=0,\\ t_1^{(1)}=1,\end{array}\right.\longrightarrow\left\{\begin{array}{l} t_1^{\rm L}=0,\\ t_2^{\rm L}=1.\end{array}\right.$$

Diagrammatic rules Eq.(1.64) give us the opportunity to explain the missing step to construct uniquely the diagrams in Tab.1.1. Indeed every quantum dot operator standing on the left of the RDM creates a vertex at t^{L}_{β} on the upper contour, while each quantum dot operator on the right creates a vertex at t^{R}_{γ} on the lower contour. In each vertex the number of particles in the dot changes by ± 1. As we have already pointed out, these vertexes are connected through fermion lines whose directions are fixed pointing to the vertex of the creation operator: $p^{\mathrm{L}}_{\beta} = p^{\mathrm{R}}_{\gamma} = +$. Moreover, each fermion line acquires the indexes l_α, σ_α and an energy $\varepsilon_\alpha = \varepsilon(\mathbf{k}_\alpha)$, that are specified by $\mathbf{j}^{\mathrm{L}}_{\beta}(\mathbf{j}^{\mathrm{R}}_{\gamma})$.

The result of the afore-mentioned rules to construct a diagram is shown in Tab.1.1. Let us compare the first half of Tab.1.1 and the second one. It is possible to notice that the Kernel components that are hermitian conjugated, from the diagrammatic point of view, can be obtained one from the other upon applying a reflection of the fermion lines with respect to a line cutting the graph in its half and reversing their directions. This rule is known in literature as the **mirror rule** [40, 47]. Moreover, the terms in Tab.1.1 are not separable in smaller independent events, this means that all the processes we have reported are **irreducible**. From the diagrammatic point of view this is equivalent to say that in the time interval between τ_0 and τ_1 it is *not* possible to separate the diagram in two independent parts without cutting the fermion line. This fact, obvious for the second order Kernel, will be important when we will consider terms of the Kernel beyond the second order approximation (see Ref. [40] for the fourth order approximation).

GME in the diagrammatic language. Since we have shown a one-to-one correspondence between the components of the density matrix time evolution (Eq.(1.58a)) and diagrams, we can also connect the diagrams to the analytical expression of the Kernel Laplace transform $K^{b\,,a}_{b',a'}$ $(\lambda = 0)$ (see Eq.(1.52)). Then the GME of Eq.(1.52) can be rewritten symbolically as

$$\mathbb{O}^{b}_{b'} = -\frac{i}{\hbar}\sum_{a,a'}\delta_{a,b}\delta_{a',b'}\left(E_a - E_{a'}\right)\rho^{a}_{a'} + \sum_{a,a'}\left(\begin{array}{l} |b\rangle \longleftarrow |a\rangle \\ \langle b'| \longrightarrow \langle a'| \end{array}\right)\rho^{a}_{a'},$$

In order to further clarify this point, let us consider the analytical expression of the Kernel Laplace transform super-operator from Eq.(1.47)

$$\left(\hat{\mathcal{K}}^{(2)}\right)^{b\,,a}_{b',a'} = \lim_{\lambda\to 0}\int_0^{+\infty} e^{-\lambda\tau'} e^{\frac{i}{\hbar}(E_a - E_{a'})(t-\tau')} e^{-\frac{i}{\hbar}(E_b - E_{b'})t} \cdot \left\langle b\middle|\hat{\mathcal{K}}^{(2)}_{\mathrm{I}}\left(t, t-\tau'\right)\left[|a\rangle\left\langle a'\right|\right]\middle|b'\right\rangle d\tau'. \quad (1.66)$$

$\hat{\mathcal{K}}_{\mathrm{I}}^{(2)}(t,\tau)\left[\hat{\rho}_{\mathrm{I},\odot}(\tau)\right]$	Diagram
$+\left\langle \hat{C}^{+}_{\mathrm{I},0,\mathbf{j}_1}\hat{C}^{-}_{\mathrm{I},1,\mathbf{j}_1}\right\rangle_{\mathrm{RS}}\left(\hat{D}^{+}_{\mathrm{I},1,\mathbf{j}_1}\hat{\rho}_{\mathrm{I},\odot}(\tau)\,\hat{D}^{-}_{\mathrm{I},0,\mathbf{j}_1}\right)$	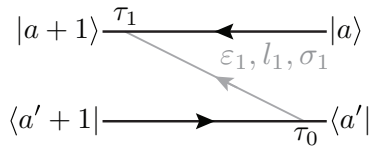
$+\left\langle \hat{C}^{-}_{\mathrm{I},0,\mathbf{j}_1}\hat{C}^{+}_{\mathrm{I},1,\mathbf{j}_1}\right\rangle_{\mathrm{RS}}\left(\hat{D}^{-}_{\mathrm{I},1,\mathbf{j}_1}\hat{\rho}_{\mathrm{I},\odot}(\tau)\,\hat{D}^{+}_{\mathrm{I},0,\mathbf{j}_1}\right)$	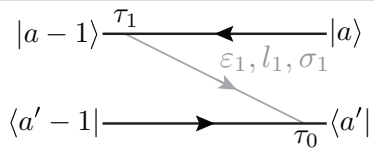
$-\left\langle \hat{C}^{-}_{\mathrm{I},0,\mathbf{j}_1}\hat{C}^{+}_{\mathrm{I},1,\mathbf{j}_1}\right\rangle_{\mathrm{RS}}\left(\hat{D}^{+}_{\mathrm{I},0,\mathbf{j}_1}\hat{D}^{-}_{\mathrm{I},1,\mathbf{j}_1}\hat{\rho}_{\mathrm{I},\odot}(\tau)\right)$	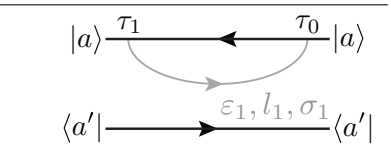
$-\left\langle \hat{C}^{+}_{\mathrm{I},0,\mathbf{j}_1}\hat{C}^{-}_{\mathrm{I},1,\mathbf{j}_1}\right\rangle_{\mathrm{RS}}\left(\hat{D}^{-}_{\mathrm{I},0,\mathbf{j}_1}\hat{D}^{+}_{\mathrm{I},1,\mathbf{j}_1}\hat{\rho}_{\mathrm{I},\odot}(\tau)\right)$	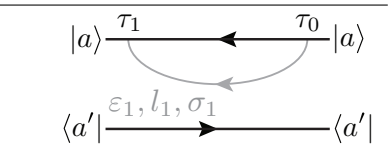
$+\left\langle \hat{C}^{-}_{\mathrm{I},1,\mathbf{j}_1}\hat{C}^{+}_{\mathrm{I},0,\mathbf{j}_1}\right\rangle_{\mathrm{RS}}\left(\hat{D}^{+}_{\mathrm{I},0,\mathbf{j}_1}\hat{\rho}_{\mathrm{I},\odot}(\tau)\,\hat{D}^{-}_{\mathrm{I},1,\mathbf{j}_1}\right)$	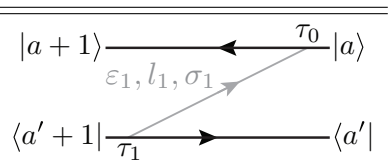
$+\left\langle \hat{C}^{+}_{\mathrm{I},1,\mathbf{j}_1}\hat{C}^{-}_{\mathrm{I},0,\mathbf{j}_1}\right\rangle_{\mathrm{RS}}\left(\hat{D}^{-}_{\mathrm{I},0,\mathbf{j}_1}\hat{\rho}_{\mathrm{I},\odot}(\tau)\,\hat{D}^{+}_{\mathrm{I},1,\mathbf{j}_1}\right)$	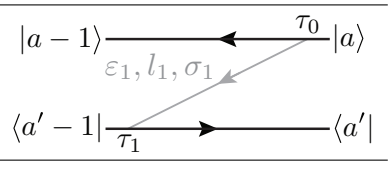
$-\left\langle \hat{C}^{+}_{\mathrm{I},1,\mathbf{j}_1}\hat{C}^{-}_{\mathrm{I},0,\mathbf{j}_1}\right\rangle_{\mathrm{RS}}\left(\hat{\rho}_{\mathrm{I},\odot}(\tau)\,\hat{D}^{+}_{\mathrm{I},1,\mathbf{j}_1}\hat{D}^{-}_{\mathrm{I},0,\mathbf{j}_1}\right)$	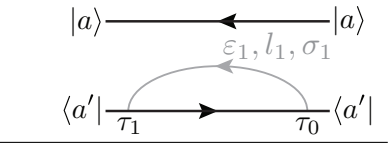
$-\left\langle \hat{C}^{-}_{\mathrm{I},1,\mathbf{j}_1}\hat{C}^{+}_{\mathrm{I},0,\mathbf{j}_1}\right\rangle_{\mathrm{RS}}\left(\hat{\rho}_{\mathrm{I},\odot}(\tau)\,\hat{D}^{-}_{\mathrm{I},1,\mathbf{j}_1}\hat{D}^{+}_{\mathrm{I},0,\mathbf{j}_1}\right)$	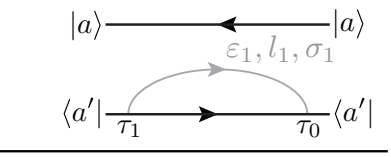

Table 1.1: All second order components of the Kernel: on the left we have reported the analytical form, on the right we have shown the correspondent diagram. We have divided the table with respect to hermitian conjugated terms. A component of the Kernel is always the sum of a given term and its hermitian conjugated, as it is possible to understand from Eq.(1.63).

Here we have performed the Laplace transform with respect to the variable $\tau' = t - \tau$ and we have substituted $t - t_0 \to t$, $\tau - t_0 \to \tau$. As we have demonstrated in App.A.1, the Kernel super-operator in the Schrödinger picture is dependent only on this time difference, therefore no time dependence t is left in the final expression of $\left(\hat{\mathcal{K}}^{(2)}\right)^{b\,,a}_{b',a'}$. This is further highlighted in App.A.2 where we perform the calculation of the Kernel component directly from Eq.(1.66). Using the expression of $\hat{\mathcal{K}}^{(2)}_{\mathrm{I}}(t, t-\tau')$, see Tab.1.1, we can decompose it in terms of the dot and leads operators:

$$\sum_{\mathbf{k}} \left\langle \hat{C}^{p}_{\mathrm{I},t_1,\mathbf{j}} \hat{C}^{\bar{p}}_{\mathrm{I},t_2,\mathbf{j}} \right\rangle_{\mathrm{RS}} \prod_{\beta=1}^{n_{\mathrm{L}}} \hat{D}^{\bar{p}^{\mathrm{L}}_{\beta}}_{\mathrm{I},t^{\mathrm{L}}_{\beta},\mathbf{j}^{\mathrm{L}}_{\beta}} |a\rangle\langle a'| \prod_{\gamma=1}^{n_{\mathrm{R}}} \hat{D}^{\bar{p}^{\mathrm{R}}_{\gamma}}_{\mathrm{I},t^{\mathrm{R}}_{\gamma},\mathbf{j}^{\mathrm{R}}_{\gamma}} = \tag{1.67}$$

$$= \frac{1}{\hbar^2} \int_{-\infty}^{+\infty} d\varepsilon\, \bar{\alpha}_{l,\sigma}(\varepsilon)\, f^{p}_{l}(\varepsilon) e^{p\frac{i}{\hbar}\varepsilon(\tau_{t_1}-\tau_{t_2})}\cdot$$

$$\prod_{\beta=1}^{n_{\mathrm{L}}} e^{\frac{i}{\hbar}\hat{H}_{\odot}\tau_{t^{\mathrm{L}}_{\beta}}} \hat{d}^{\bar{p}^{\mathrm{L}}_{\beta}}_{\sigma^{\mathrm{L}}_{\beta}} e^{-\frac{i}{\hbar}\hat{H}_{\odot}\tau_{t^{\mathrm{L}}_{\beta}}} |a\rangle\langle a'| \prod_{\gamma=1}^{n_{\mathrm{R}}} e^{\frac{i}{\hbar}\hat{H}_{\odot}\tau_{t^{\mathrm{R}}_{\gamma}}} \hat{d}^{\bar{p}^{\mathrm{R}}_{\gamma}}_{\sigma^{\mathrm{R}}_{\gamma}} e^{-\frac{i}{\hbar}\hat{H}_{\odot}\tau_{t^{\mathrm{R}}_{\gamma}}},$$

where $f^{+}_{l}(\varepsilon) = f(\beta\varepsilon - \beta\mu_l) = (1 + e^{\beta\varepsilon+\beta\mu_l})^{-1}$ is the Fermi function for the l-lead and $f^{-}_{l}(\varepsilon) = 1 - f^{+}_{l}(\varepsilon)$. In Eq.(1.67) we have recast the sum as an integral over the energy $\varepsilon = \varepsilon(\mathbf{k})$. We have assumed that the leads are large enough to consider $\mathbf{k}$ as a continuous variable: mathematically we have performed the limit of infinite volumes of the leads. Furthermore, to achieve the final expression in Eq.(1.67), we have introduced

$$\bar{\alpha}_{l,\sigma}(\varepsilon) = \iint_{\{\varepsilon=\varepsilon_{l,\sigma}(\mathbf{k})\}} \frac{Z_l \left|T_{l,\sigma,\mathbf{k}}\right|^2}{\|\boldsymbol{\nabla}\varepsilon_{l,\sigma}(\mathbf{k})\|}\, dS, \tag{1.68}$$

where Z_l is the number of states per unit of volume in a quantum of $\mathbf{k}$-space, i.e. considering periodic boundary conditions $Z_l = 1/(2\pi)^3$. In the case of energy independent TMCs Eq.(1.68) reads

$$\bar{\alpha}_{l,\sigma}(\varepsilon) = \left|T_{l,\sigma}\right|^2 \bar{\rho}_{l,\sigma}(\varepsilon), \tag{1.69}$$

where $\bar{\rho}_{l,\sigma}(\varepsilon)$ is the density of state of the l-lead with spin σ. As long as we are not interested in the effects due to the density of state we will assume the following analytical form

$$\bar{\rho}_{l,\sigma}(\varepsilon) = \rho_{l,\sigma} L(\varepsilon, W, l), \qquad L(\varepsilon, W, l) = \frac{W^2}{(\varepsilon-\mu_l)^{2+}W^2}, \tag{1.70}$$

where $\rho_{l,\sigma}$ is a constant density of state and W is a finite cut-off to ensure that the density of state tend to zero at high energy ($W \gg$ all energies of the

system). We have judged this approximation more physical than assuming a flat density of state for every energy. Moreover this cut-off will assure the convergence of every step in the following. For shortness in the notation we will also use

$$\alpha_{l,\sigma} \overset{\text{def}}{=} \|T_{l,\sigma}\|^2 \rho_{l,\sigma} = \|T_{l,\sigma}\|^2 \rho_{l,\sigma} \lim_{W\to+\infty} L(\varepsilon, W, l) .$$

In conclusion it can be shown that the expression for the Kernel elements splits into a sum of the products of the TMCs, the constant density of state $\rho_{l,\sigma}$ and an energy dependent function (see Eq.(A.12)). The same result can be obtained directly from the diagrams, in a much faster way, with the rules explained in App.A.3.

Diagrams for the current Kernel In Sect.1.1.4 we have demonstrated that the equation governing the current operator through the dot (Eq.(1.56)) and the one describing the time evolution of the RDM (Eq.(1.46)) are very similar. For this reason the diagrams contributing to $\hat{\mathcal{K}}_{I_l}(\lambda = 0)$ are a subclass of the one for $\hat{\mathcal{K}}(\lambda = 0)$. Indeed, as we have pointed out in Sect.1.1.4, the two super-operators differ one from the other in the substitution of the first Liouville super-operator with the current operator. Because of this we have to apply the following modifications to obtain the right contributions for the current super-operator:

1- (t-vertex position) Because $\hat{I}_l$ is an operator, and not a super-operator, it does not involve commutators. Then *the vertex corresponding to the time t has to lie on the upper contour*: first half of Tab.1.1;

2- (Direction of the last fermion line) *The sign of the diagrams with the fermion line pointing away from the t-vertex has to be inverted* because the tunnelling Hamiltonian and the current operator differ up to the sign of the out-tunnelling contribution (compare Eq.(1.55) and Eq.(1.14));

3- (Lead index) Since $\hat{I}_l$ is composed by operators of the l-lead, in the final expression for the current in the asymptotic limit, *we have not to sum over the index l* that labels the fermion line leading to the t-vertex.

Alternatively, because of the cyclic property of the trace, we can take into account all the diagrams with the fermion line pointing towards the t-vertex that lies on the upper contour (first and fourth rows of Tab.1.1) and the one with the fermion line pointing away from the same vertex lying on the lower contour (sixth and seventh rows of Tab.1.1). Also in this case we have to change the sign to the diagrams pointing away from the t-vertex.

1.2 The second order

At this stage we have all the material necessary to obtain all the physical quantities of interest such as the *populations*, the *current* flowing through the dot and the *differential conductance* as a function of the applied voltages. The latter two quantities can in turn be visualized in the so-called *stability diagram* of the quantum dot. In this Section we will consider only processes of the second order in the coupling energy to the leads (E_{T} in Eq.(1.15)). As we will see in detail this theory is suitable for small ratios $E_{\mathrm{T}}/k_{\mathrm{B}}T \ll 1$.

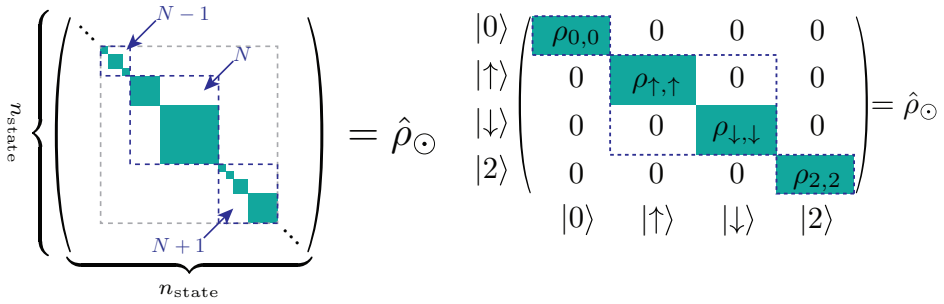

(a) *Sketch of a generic RDM.* (b) *Anderson RDM.*

Figure 1.3: Structure scheme of the RDM: if a quantum number is conserved during tunnelling, it acquires a block diagonal structure in which only certain elements are not zero. (a) In a generic RDM the first block (blue dashed) corresponds to charge conservation, while the others (green) are due to conservation of the spin or other quantum numbers. Here we have reported only the sectors corresponding to the $N-1$, N and $N+1$ charges (grey dashed) in the system but this sketch it is also valid for the other sectors. All the elements that are not reported are supposed to be zero. (b) We have reported the RDM in the Anderson model we have chosen.

Coherences Let us consider Eq.(1.52). In general, the RDM, given n_{state} states in the dot, has dimensionality n_{state}^2. Fortunately there exist some *selection rules* that allow us to set to zero certain elements of the RDM. Indeed, if the initial RDM is diagonal with respect to the charge number $\langle a' \,|\, \hat{\rho}_{\odot}(t_0) \,|\, a\rangle \propto \delta_{N_a,N_{a'}}$ and the charge number is conserved, whenever two states, $|a\rangle$ and $|a'\rangle$, differ by this quantum number then the corresponding coherence $\langle a' \,|\, \hat{\rho}_{\odot}^{\infty} \,|\, a\rangle = 0$. In our case we find

$$\left[\hat{N}_{\sigma}, \hat{H}_{\odot}\right] = 0, \qquad \left[\hat{N}_{\sigma,l}^{\mathrm{RS}}, \hat{H}_{\mathrm{RS}}\right] = 0, \qquad \left[\hat{N}_{\sigma}^{\mathrm{RS}} + \hat{N}_{\sigma}, \hat{H}_{\mathrm{I}}\right] = 0,$$

where $\hat{N} = \sum_{\sigma} \hat{N}_{\sigma}$ is the dot number operator with spin σ, $\hat{N}_{\sigma,l}^{\mathrm{RS}}$ is the one for the electrons in the l-lead and $\hat{N}_{\sigma}^{\mathrm{RS}} = \sum_{l} \hat{N}_{\sigma,l}^{\mathrm{RS}}$. This means that the total

number of particles (charge) in the system is conserved and the number of electrons per spin species ($\hat{N}_\sigma^{\mathrm{RS}} + \hat{N}_\sigma$) cannot evolve in time. For this reason the reduced density matrix in the asymptotic limit acquires a block diagonal form as we can appreciate in Fig.1.3(a) and 1.3(b). We have represented the conservation of the charge with (blue) dashed blocks and the one of the others generic quantum numbers with (green) squares. In Fig.1.3(b) we have reported the RDM relevant in our case with the same convention for the colours as in the figure on the left. We want to stress that the spin conservation is a model dependent condition. Indeed, in order to break the spin conservation, it is sufficient to generalize the tunnelling Hamiltonian by allowing spin flip processes during the tunnelling

$$\hat{H}_{\mathrm{T}} = \sum_{l,\mathbf{k},\sigma,\sigma_1} T_{l,\sigma,\sigma_1,\mathbf{k}}\, \hat{d}^\dagger_{\sigma_1} \hat{c}_{l,\mathbf{k},\sigma} + \mathrm{h.c.}.$$

This is necessary, for example, in case of polarized electrodes. However we will not consider this case in the following. We will take into account $\hat{H}_{\mathrm{T}}$ as in Eq.(1.14) and then, in the Anderson model, the RDM reads

$$\hat{\rho}^\infty_\odot = \sum_\nu \rho^\nu_\nu \left|\nu\right\rangle\!\left\langle\nu\right| \stackrel{\mathrm{def}}{=} \sum_\nu \rho_\nu \left|\nu\right\rangle\!\left\langle\nu\right|.$$

Moreover, as it is easy to understand from Tab.1.1, for the second order the GME, from Eq.(1.52), reads

$$\begin{cases} \mathbb{0}^0_0 = K^{0,0}_{0,0}\rho^0_0 + \sum_\sigma K^{0,\sigma}_{0,\sigma}\rho^\sigma_\sigma + K^{0,2}_{0,2}\rho^2_2, \\ \mathbb{0}^\sigma_\sigma = K^{\sigma,0}_{\sigma,0}\rho^0_0 + \sum_{\sigma_1} K^{\sigma,\sigma_1}_{\sigma,\sigma_1}\rho^{\sigma_1}_{\sigma_1} + K^{\sigma,2}_{\sigma,2}\rho^2_2, \\ \mathbb{0}^2_2 = K^{2,0}_{2,0}\rho^0_0 + \sum_\sigma K^{2,\sigma}_{2,\sigma}\rho^\sigma_\sigma + K^{2,2}_{2,2}\rho^2_2, \end{cases} \tag{1.71}$$

where, for shortness in the notation, we have indicated $K^{b,a}_{b,a}(\lambda = 0)$ with $K^{b,a}_{b,a}$.

Gain and loss relations Let us consider Eq.(1.71). Using the sum-rule we have mentioned in Eq.(1.54) we have

$$\begin{cases} \mathbb{0}^0_0 = -\left(\sum_\sigma K^{\sigma,0}_{\sigma,0} + K^{2,0}_{2,0}\right)\rho^0_0 + \sum_\sigma K^{0,\sigma}_{0,\sigma}\rho^\sigma_\sigma + K^{0,2}_{0,2}\rho^2_2, \\ \mathbb{0}^\sigma_\sigma = K^{\sigma,0}_{\sigma,0}\rho^0_0 - \left(K^{0,\sigma}_{0,\sigma} + K^{\bar\sigma,\sigma}_{\bar\sigma,\sigma} + K^{2,\sigma}_{2,\sigma}\right)\rho^\sigma_\sigma + K^{\sigma,\bar\sigma}_{\sigma,\bar\sigma}\rho^{\bar\sigma}_{\bar\sigma} + K^{\sigma,2}_{\sigma,2}\rho^2_2, \\ \mathbb{0}^2_2 = K^{2,0}_{2,0}\rho^0_0 + \sum_\sigma K^{2,\sigma}_{2,\sigma}\rho^\sigma_\sigma - \left(K^{0,2}_{0,2} + \sum_\sigma K^{\sigma,2}_{\sigma,2}\right)\rho^2_2. \end{cases} \tag{1.72}$$

This sum-rule represents the conservation of the total probability. Indeed, considering it for the state $a = a' = 0$ we have

$$\underbrace{K^{0,0}_{0,0}}_{\text{loss}} = -\sum_{\sigma} \underbrace{K^{\sigma,0}_{\sigma,0}}_{\text{gain}} - \underbrace{K^{2,0}_{2,0}}_{\text{gain}} .$$

As we can notice, what is a "*loss*" in the first equation for ρ^0_0, is a "*gain*" in the second for ρ^σ_σ, and in the third one for ρ^2_2. Here we mean *loss* when the process decreases the probability to find the state $|a\rangle$, and *gain* when the probability is increased.

1.2.1 Second order analytic expression for the rates and the populations

We have now all the ingredients to evaluate the Kernel elements. To this purpose let us consider $K^{\sigma,0}_{\sigma,0}$. In Tab.1.1 it is not hard to understand that only diagrams with a fermion line connecting the opposite contours can contribute to this term. Following the *diagrammatic rules* explained in App.A.3, we can directly obtain its integral form

$$K^{\sigma,0}_{\sigma,0} = \sum_{l,\mathbf{k}} \left(\begin{array}{c} |\sigma\rangle \xleftarrow{E_\sigma\ \tau_0} |0\rangle \\ \langle\sigma| \xrightarrow[\tau_1\quad E_0]{\varepsilon,l,\sigma} \langle 0| \end{array} + \begin{array}{c} |\sigma\rangle \xleftarrow{\tau_1\ E_0} |0\rangle \\ \langle\sigma| \xrightarrow[E_\sigma\quad \tau_0]{\varepsilon,l,\sigma} \langle 0| \end{array} \right)$$

$$= \sum_l \frac{i}{\hbar} \lim_{\eta\to 0} \int_{-\infty}^{+\infty} d\varepsilon \frac{f^+_l(\varepsilon)\,\bar{\alpha}_{l,\sigma}(\varepsilon)}{\varepsilon + E_0 - E_\sigma + i\eta} + \text{h.c.}.$$

We can now perform the integration as we have shown in App.A.5. Recognising that it fulfils the definition of the function $Y^p_d(\bar{\mu}^{i,j}_l)$ in App.A.2, it reads

$$K^{\sigma,0}_{\sigma,0} = -\sum_l \alpha_{l,\sigma} Y^+_+\left(\bar{\mu}^{\sigma,0}_l\right) + \text{h.c.} = \frac{2\pi}{\hbar}\sum_l \alpha_{l,\sigma} f^+_l(E_{\sigma 0}),$$

where we have introduced the notation $E_{ij} \overset{\text{def}}{=} E_i - E_j$. We can obtain the analytic expression for all the other Kernel components in the same way, finally obtaining:

$$K^{0,\sigma}_{0,\sigma} = \frac{2\pi}{\hbar}\sum_l \alpha_{l,\sigma} f^-_l(E_{\sigma 0}), \tag{1.73}$$

$$K^{2,\sigma}_{2,\sigma} = \frac{2\pi}{\hbar}\sum_l \alpha_{l,\sigma} f^+_l(E_{2\sigma}), \tag{1.74}$$

$$K^{\sigma,2}_{\sigma,2} = \frac{2\pi}{\hbar}\sum_l \alpha_{l,\sigma} f^-_l(E_{2\sigma}). \tag{1.75}$$

It is worth to notice that Kernel components with initial and final states reversed differ only because of the sign in the Fermi function exponent since they refer to processes that are in opposite direction in the energy space. All the other components are zero up to the second order, since it is not possible to connect, on the contours, the corresponding states with only one fermion line. In literature the rates ($\Gamma^{\pm}_{l,ij}$) are often introduced: they represent the average number of transitions per unit of time between the state $|j\rangle \to |i\rangle$ because of the tunnelling of an electron from the l-lead. In our case, for the second order GME, they are defined as

$$\Gamma^{\pm}_{l,\sigma 0} \overset{\text{def}}{=} \frac{2\pi}{\hbar}\alpha_{l,\sigma} f_l^{\pm}\left(E_{\sigma 0}\right), \qquad \Gamma^{\pm}_{l,2\sigma} \overset{\text{def}}{=} \frac{2\pi}{\hbar}\alpha_{l,\sigma} f_l^{\pm}\left(E_{2\sigma}\right). \tag{1.76}$$

We can also recast the GME in Eq.(1.72) in terms of these rates obtaining:

$$\begin{cases} 0 = -\sum_{l,\sigma}\Gamma^{+}_{l,\sigma 0}\rho^0_0 & +\sum_{l,\sigma}\Gamma^{-}_{l,\sigma 0}\rho^{\sigma}_{\sigma}, \\ 0 = \sum_{l}\Gamma^{+}_{l,\sigma 0}\rho^0_0 & -\sum_{l}\left(\Gamma^{-}_{l,\sigma 0}+\Gamma^{+}_{l,2\sigma}\right)\rho^{\sigma}_{\sigma} & +\sum_{l}\Gamma^{-}_{l,2\sigma}\rho^2_2, \\ 0 = & \sum_{l,\sigma}\Gamma^{+}_{l,2\sigma}\rho^{\sigma}_{\sigma} & -\sum_{l,\sigma}\Gamma^{-}_{l,2\sigma}\rho^2_2. \end{cases} \tag{1.77}$$

Here we have aligned with respect to the columns in order to highlight the afore-mentioned sum-rule: indeed the sum over a column is always equal to zero. Because of this restriction, the Kernel for the Anderson model is a linear operator of rank three or less, in case some further symmetries are imposed on the system. Then, choosing three equations from the system in Eq.(1.77) and the normalization condition $\sum_\nu \rho^\nu_\nu = 1$, we can determine the populations of the system:

$$\begin{pmatrix} \rho^0_0 \\ \rho^{\uparrow}_{\uparrow} \\ \rho^{\downarrow}_{\downarrow} \\ \rho^2_2 \end{pmatrix} = \frac{1}{\bar{N}} \begin{pmatrix} \sum_\sigma \Gamma^{-}_{\bar\sigma 0}\Gamma^{-}_{2\bar\sigma}\left(\Gamma^{-}_{\sigma 0}+\Gamma^{+}_{2\sigma}\right) \\ \sum_\sigma \left(\Gamma^{+}_{\uparrow 0}\Gamma^{-}_{\downarrow 0}\Gamma^{-}_{2\sigma}+\Gamma^{+}_{2\downarrow}\Gamma^{-}_{2\uparrow}\Gamma^{+}_{\sigma 0}\right) \\ \sum_\sigma \left(\Gamma^{+}_{\downarrow 0}\Gamma^{-}_{\uparrow 0}\Gamma^{-}_{2\bar\sigma}+\Gamma^{+}_{2\uparrow}\Gamma^{-}_{2\downarrow}\Gamma^{+}_{\bar\sigma 0}\right) \\ \sum_\sigma \Gamma^{+}_{\bar\sigma 0}\Gamma^{+}_{2\bar\sigma}\left(\Gamma^{-}_{\sigma 0}+\Gamma^{+}_{2\sigma}\right) \end{pmatrix}, \tag{1.78}$$

where we have introduced

$$\bar{N} = \sum_\sigma \Big[\Gamma^{-}_{2\sigma}\left(\Gamma^{-}_{\uparrow 0}\Gamma^{+}_{\downarrow 0}+\Gamma^{-}_{\downarrow 0}\Gamma_{\uparrow 0}\right) + \Gamma^{-}_{\sigma 0}\left(\Gamma^{-}_{2\sigma}+\Gamma^{+}_{\bar\sigma 0}\right)\Gamma^{+}_{2\bar\sigma} + \\ + \Gamma^{+}_{\sigma 0}\left(\Gamma^{-}_{2\uparrow}\Gamma^{+}_{2\downarrow}+\Gamma_{2\downarrow}\Gamma^{+}_{2\uparrow}\right)\Big] \tag{1.79}$$

Moreover we have adopted the following conventions

$$\Gamma^{\pm}_{ab} \overset{\text{def}}{=} \sum_l \Gamma^{\pm}_{l,ab}, \qquad \Gamma_{ab} \overset{\text{def}}{=} \Gamma^{+}_{ab} + \Gamma^{-}_{ab}.$$

It is important to notice that if *no magnetic* field is applied to the system and $E_\uparrow = E_\downarrow = E_1$ then the *rates do not depend on the spin index* and the *populations with opposite spin are equal*. Indeed, imposing this further constraint on the solution of Eq.(1.78), we obtain a much simpler form of the populations

$$\begin{pmatrix} \rho_0^0 \\ \rho_\uparrow^\uparrow \\ \rho_\downarrow^\downarrow \\ \rho_2^2 \end{pmatrix} = \frac{1}{\Gamma_{21}^- \Gamma_{10} + \Gamma_{10}^+ \Gamma_{21}} \begin{pmatrix} \Gamma_{10}^- \Gamma_{21}^- \\ \Gamma_{10}^+ \Gamma_{21}^- \\ \Gamma_{10}^+ \Gamma_{21}^- \\ \Gamma_{10}^+ \Gamma_{21}^+ \end{pmatrix}, \tag{1.80}$$

where $\Gamma_{10}^{+(-)} = \Gamma_{\uparrow 0}^{+(-)} = \Gamma_{\downarrow 0}^{+(-)}$ and $\Gamma_{21}^{+(-)} = \Gamma_{2\uparrow}^{+(-)} = \Gamma_{2\downarrow}^{+(-)}$.

1.2.2 Analytic expression of the current

We want now to derive the current flowing out of the l-lead. To achieve this purpose we have to consider the modification to the diagrammatic rules we have presented at the end of Sect.1.1.5. Let us consider Eq.(1.57). As we have already mentioned $\rho_{a'}^a \propto \delta_{a,a'}$ in the stationary limit. Then we have to evaluate

$$I_l \stackrel{\text{def}}{=} \lim_{t \to +\infty} I_l(t) = \sum_{a,b} \left(\hat{\mathcal{K}}_{I_l} \right)_{b,a}^{b,a} \rho_a^a.$$

Here we have omitted the limit with respect to λ for shortness in the notation. In order to further clarify how to evaluate in practice the current, let us consider one of the traces we have to sum up in the previous equation:

$$\begin{aligned} \mathsf{Tr}\left\{ \hat{\mathcal{K}}_{I_l} \left[|0\rangle\langle 0| \right] \right\} &= e \sum_{\sigma,\mathbf{k}} \Bigg(- \quad + \Bigg) \\ &= e \sum_{\sigma,\mathbf{k}} \Bigg(\quad + \Bigg) \\ &= e \sum_{\sigma} \left[\sum_{\mathbf{k}} 2\mathsf{Re} \left\{ \right\} \right] \\ &= e \sum_{\sigma} \Gamma_{l,\sigma 0}^{+}. \end{aligned}$$

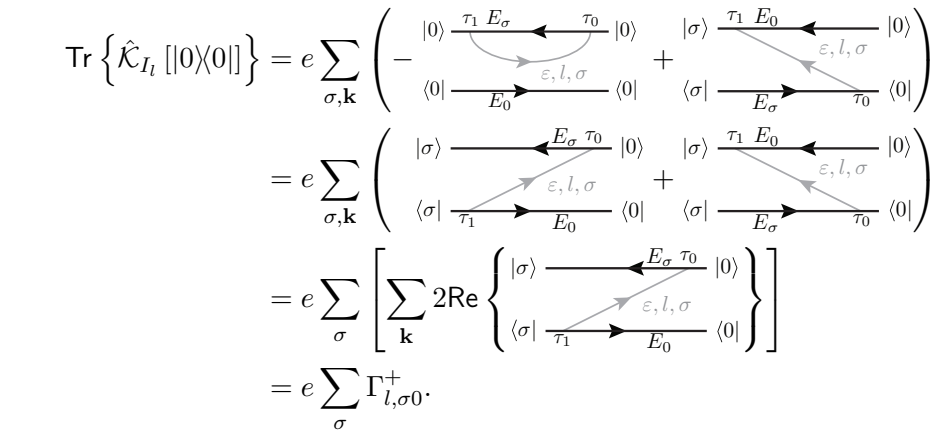

As we can notice we have considered only diagrams with the last vertex on the upper contour, as the first rule for the current Kernel imposes. Moreover we exploited the relation

$$\left(\hat{\mathcal{K}}_{I_l} \right)_{0,0}^{0,0} = - \left(\hat{\mathcal{K}}_{I_l} \right)_{\sigma,0}^{\sigma,0}$$

to rewrite the first diagram in term of the one in the second line. This is indeed a general fact that, shifting the leftmost vertex from the upper to the lower contour and keeping the states time evolution unaltered, the diagrammatic rules produce only a change of sign in the analytical contribution of the corresponding diagram. Finally, we have recognized that the resulting diagram is the same whose contribution we have evaluated in the previous paragraph. The calculation of the other contributions is completely analogous. We hence find

$$I_l = e\sum_\sigma \left[\Gamma^+_{l,\sigma 0}\rho^0_0 + \left(\Gamma^+_{l,2\sigma} - \Gamma^-_{l,\sigma 0}\right)\rho^\sigma_\sigma - \Gamma^-_{l,2\sigma}\rho^2_2\right]. \tag{1.81}$$

Having already written the population in terms of the rates (Eq.(1.78)) the previous equation completely identifies the stationary current through the dot. Unfortunately the explicit expression in the presence of a magnetic field is not very user-friendly. If we do not consider the spin asymmetric case then the current, written in terms of the rates, reads

$$I_l = \frac{2e}{N}\left(\Gamma^-_{21}, \Gamma^+_{10}\right)\begin{pmatrix}\Gamma^+_{l,10}\Gamma_{\bar{l},10} - \Gamma_{l,10}\Gamma^+_{\bar{l},10}\\ \Gamma_{l,21}\Gamma^-_{\bar{l},21} - \Gamma_{\bar{l},21}\Gamma^-_{l,21}\end{pmatrix},$$

where $N = \Gamma^-_{21}\Gamma_{10} + \Gamma^+_{10}\Gamma_{21}$. Here it is worth to notice that substituting $l \to \bar{l}$ and vice versa we have $I_l = -I_{\bar{l}}$: this means that there is no charge accumulation in the dot in the stationary limit. Moreover if we consider the case of *proportional tunnelling* (see Eq.(1.15)) the expression for the current further simplifies

$$I_l = \frac{2e}{1+\frac{\Gamma_{21}\Gamma^+_{10}}{\Gamma^-_{21}\Gamma_{10}}}\left(\kappa_{\bar{l}}\Gamma^+_{l,10} - \kappa_l\Gamma^+_{\bar{l},10}\right) - \frac{2e}{1+\frac{\Gamma^-_{21}\Gamma_{10}}{\Gamma_{21}\Gamma^+_{10}}}\left(\kappa_{\bar{l}}\Gamma^-_{l,21} - \kappa_l\Gamma^-_{\bar{l},21}\right), \tag{1.82}$$

since $\alpha_{\sigma,l} = \kappa_l\alpha\delta_{\sigma,\bar{\sigma}}$. In literature is often introduced the energy

$$\Gamma \overset{\text{def}}{=} 2\pi\alpha \tag{1.83}$$

to measure the coupling to the leads. Even if this is a bit confusing, since we have labelled with $\Gamma^\pm_{l,ij}$ the rates so far, we will adopt the same convention, keeping clear in mind that $[\Gamma/\hbar] = [\text{sec}^{-1}]$, due to $[\Gamma] = [\text{eV}]$. The coefficients of the two terms in Eq.(1.82) can be nicely interpreted considering the average number of particle in the dot

$$\langle N\rangle = \mathsf{Tr}_\odot\left\{\hat{N}\hat{\rho}_\odot\right\} = \sum_n n\rho^n_n = \frac{2}{1+\frac{\Gamma^-_{21}\Gamma_{10}}{\Gamma_{21}\Gamma^+_{10}}}.$$

It is now clear that the second term in Eq.(1.82) represents the current due to the average number of electrons, while, considering a dot fully occupied,

the first coefficient coincides with the average number of holes:

$$\langle N_{\rm h}\rangle = 2 - \langle N\rangle = \frac{2}{1+\frac{\Gamma_{21}\Gamma^{+}_{10}}{\Gamma^{-}_{21}\Gamma_{10}}}.$$

They, indeed, contribute with opposite sign. Since the *differential conductance* is the derivative of the current (I_l) with respect to the bias potential (V see Eq.(1.12)) and the analytical form is not compact, usually, it is computed numerically.

In the following we will adopt this strategy: we will evaluate the populations from the analytical expression or performing the time evolution of the density operator numerically, then we will compute the current through the dot from the analytical expression (Eq.(1.81)) and, in the end, we will calculate the differential conductance numerically.

1.2.3 Stability diagram in the second order approximation

In Fig.1.4 and 1.5 we show the populations of the dot (Fig.1.4a), the current through the left junction (Fig.1.4b) and the conductance of the system (Fig.1.5). From the left to the right, in Fig.1.4, we have considered the effect of the temperature on the populations and the current of the dot. In Fig.1.5 we have plotted the same effect on the conductance. From the left to the right and from the top to the bottom, we decreased the temperature up to the regime in which the second order approximation can be considered a suitable one (in Fig.1.5(d) we have $\Gamma \simeq 3k_{\rm B}T$).

It is worth to give a physical explanation of the results we reported in the above figures. To this end we can summarize all the possible processes, contributing to the current flowing through the dot, as the one populating the dot ($N \to N+1$) and the one depopulating it ($N+1 \to N$). Let us assume that the chemical potential of the L-lead is higher ($\mu_{\rm L} = \mu_0 + eV/2$) than the one of the R-lead ($\mu_{\rm R} = \mu_0 - eV/2$), where $e > 0$ is the modulus of the electron charge. Since the current is flowing from the left to the right lead we have that, on average, the left lead is populating the dot and the right one is depopulating it. Considering the energy conservation for the processes that takes place in the left junction ($N \to N+1$) we have

$$\text{initial energy:}\quad E_{\rm L} + E_N, \qquad \text{final energy:}\quad E_{\rm L} - \varepsilon_{{\rm L},\sigma,\mathbf{k}} + E_{N+1},$$

where E_N is the energy of the dot in the state with N particles and, assuming that all the states in the leads with energy lower than the chemical potential are occupied, we have $E_{\rm L} = \sum_{\mathbf{k}} \varepsilon_{{\rm L},\sigma,\mathbf{k}}\Theta(\mu_{\rm L} - \varepsilon_{{\rm L},\sigma,\mathbf{k}})$, i.e. the electrons in the L-lead have to be chosen from the Fermi sea: $\varepsilon_{{\rm L},\sigma,\mathbf{k}} \leq \mu_{\rm L}$. Then the conservation of energy during the in-tunnelling process imposes

$$E_N = E_{N+1} - \varepsilon_{{\rm L},\sigma,\mathbf{k}} \geq E_{N+1} - \mu_0 - \frac{eV}{2}. \tag{1.84}$$

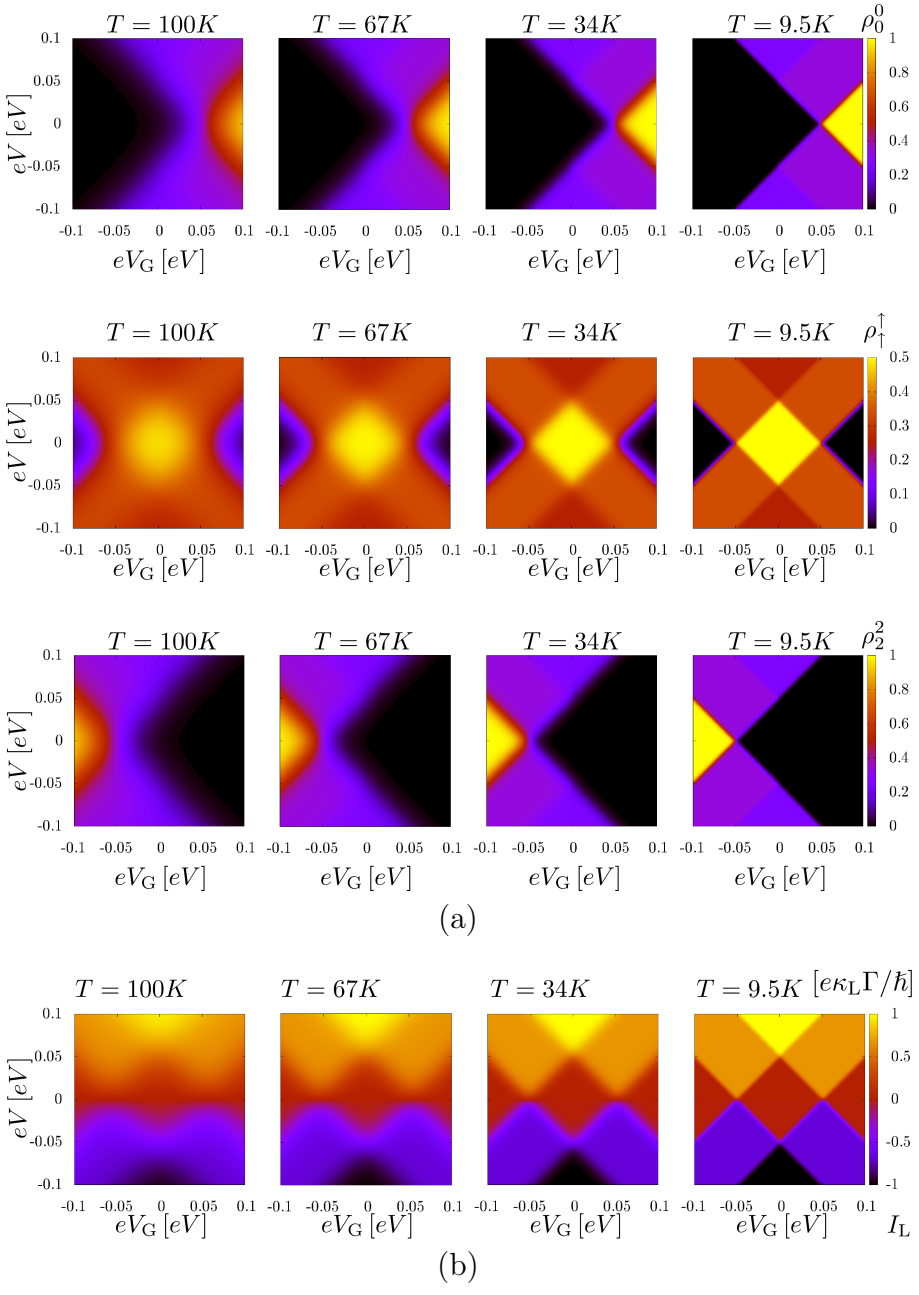

Figure 1.4: (a) Populations of the dot in the Anderson model as a function of the gate and bias voltages (in the absence of a magnetic field $\rho_\uparrow^\uparrow = \rho_\downarrow^\downarrow$). (b) Current through the L-lead tunnelling junction $I_R = -I_L$ ($\kappa_l = k_l = 1/2$, $l = R, L$). In both cases we show four different coloured plots showing the temperature dependence of the corresponding quantity. Here we have chosen $E_{10} = 1\,\text{meV}$, the interaction parameter $U = 50\,\text{meV}$ and the Fermi level $\mu_0 = \bar{E}_1 + U/2$ in such a way that the plot is centred around zero.

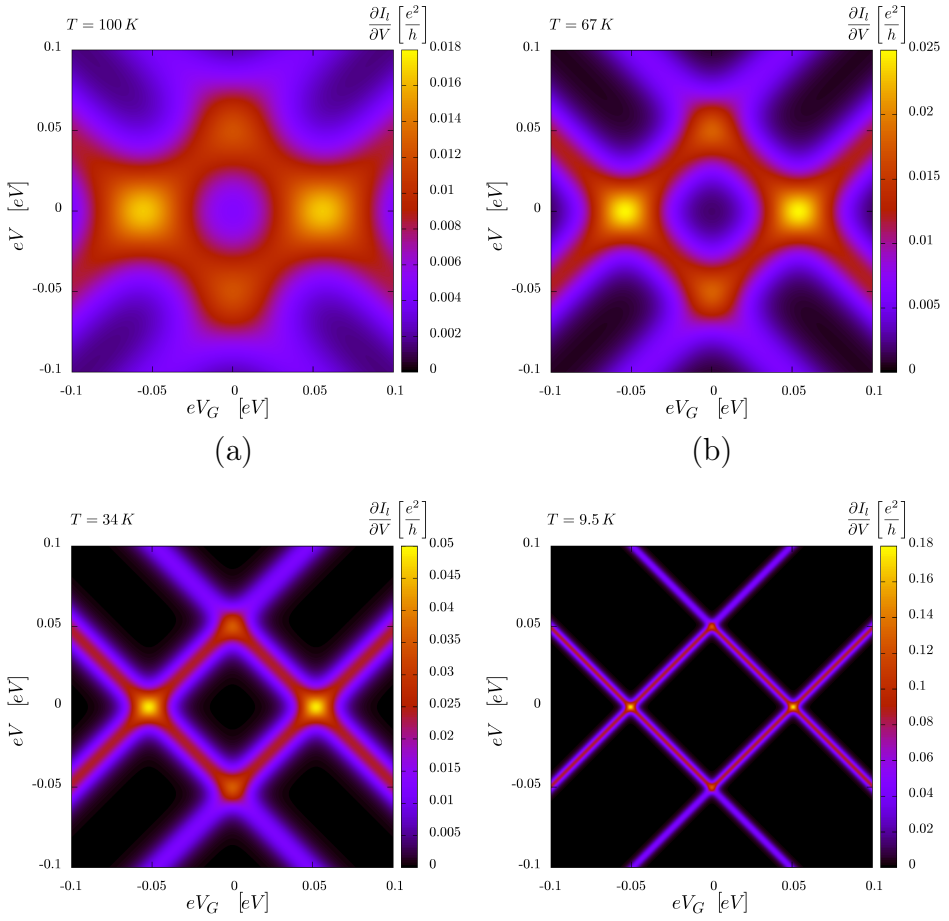

Figure 1.5: Stability diagram: differential conductance of the quantum dot in the Anderson model as a function of the gate and bias voltages. We have chosen the same parameters in Figs.1.4 and we have specified $\alpha_{l,\sigma} = 0.042\,meV$. From (a)→(d) we have decreased the temperature in the region in which the *second order theory* can be considered valid: $T > \Gamma/k_{\rm B} \simeq 3\,{\rm K}$.

The same kind of argument can be presented for the out-tunnelling process in the R-lead, giving the energy conservation condition

$$E_{N+1} = E_N + \varepsilon_{\mathrm{R},\sigma,\mathbf{k}} \geq E_N + \mu_0 - \frac{eV}{2}. \tag{1.85}$$

We can interpret Eqs.(1.84) and (1.85) as conditions identifying the regions, in the source-drain and gate voltage plane, in which the transport of current is allowed:

$$E_{N+1} - E_N - \mu_0 \leq \frac{eV}{2} \qquad N \to N+1 : \text{ Source}, \tag{1.86a}$$

$$E_{N+1} - E_N - \mu_0 \geq -\frac{eV}{2} \qquad N+1 \to N : \text{ Drain}. \tag{1.86b}$$

In the spin symmetric Anderson model Eqs.(1.86) read:

$$\begin{cases} \dfrac{eV}{2} \geq \bar{E}_1 - e\dfrac{V_\mathrm{G}}{2} - \mu_0 & 0 \to 1 : \text{ Source}, \\ -\dfrac{eV}{2} \leq \bar{E}_1 - e\dfrac{V_\mathrm{G}}{2} - \mu_0 & 1 \to 0 : \text{ Drain}, \end{cases} \tag{1.87a}$$

$$\begin{cases} \dfrac{eV}{2} \geq \bar{E}_1 + U - e\dfrac{V_\mathrm{G}}{2} - \mu_0 & 1 \to 2 : \text{ Source}, \\ -\dfrac{eV}{2} \leq \bar{E}_1 + U - e\dfrac{V_\mathrm{G}}{2} - \mu_0 & 2 \to 1 : \text{ Drain}. \end{cases} \tag{1.87b}$$

The two systems of equations split the bias-gate plane in nine regions symmetrically with respect to $V = 0$. In Fig.1.6 we show the sketch of this subdivision. We have depicted in grey the regions in which current cannot flow, in white and in light-blue the ones in which $I_l \neq 0$. The boarders of these regions are determined considering the equalities from the inequalities in Eqs.(1.87). This defines four straights in the bias-gate plane (green dashed lines). Notice that we attached the type of transition ($i \to j$: D(S)) to each straight in this plane. For each inequality we indicated with red arrows the bias-gate plane subregion in which the corresponding inequality is satisfied (the red arrow is pointing to the region in which the inequality holds true). Let us consider the region labelled with B in Fig.1.6. The first equation in Eqs.(1.87a) and the second one in Eqs.(1.87b) are satisfied, whereas the second in Eqs.(1.87a) and the first one in Eqs.(1.87b) do not hold true. Hence we have

$$\text{Source} : |0\rangle \to |1\rangle \nrightarrow |2\rangle\,,$$
$$\text{Drain} : |0\rangle \nleftarrow |1\rangle \leftarrow |2\rangle\,,$$

where we marked with a simple arrow an allowed transition and with a marked arrow a forbidden one. Both the Source and the Drain are feeding the state $|1\rangle$. Then, when it is filled (see Fig.1.4b), the current cannot flow

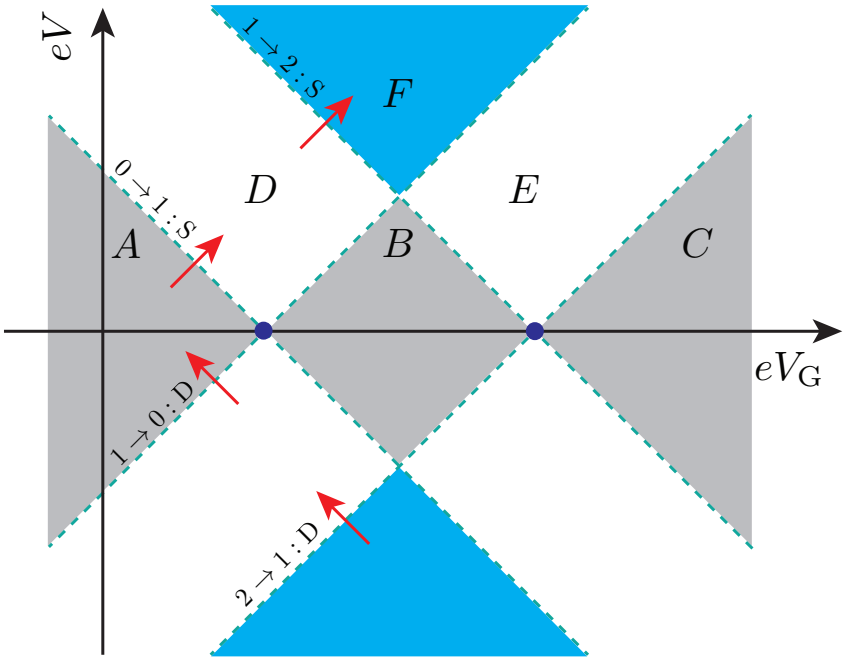

Figure 1.6: Sketch of the source-drain and gate voltages plane subdivision (from $A \to F$) as it follows from Eqs.(1.87). We show (green dashed) the resonance condition for a specific transition reported close to the corresponding straight, the charge degeneracy points (blue dots), the region in which the current is not allowed to flow (grey). In the other regions (light-blue and white), $I_l \neq 0$. The red arrows point towards the bias-gate plane region satisfying the corresponding inequalities. The leftmost charge degeneracy point corresponds to $eV_G/2 = E_1 - \mu_0$ and the rightmost one to $eV_G/2 = E_1 - \mu_0 + U$.

and $\rho_1^1 = \rho_\uparrow^\uparrow + \rho_\downarrow^\downarrow = 1$ (see Fig.1.4a). Conversely, if we consider the region D, we have

$$\begin{aligned} \text{Source} &: |0\rangle \to |1\rangle \nrightarrow |2\rangle\,, \\ \text{Drain} &: |0\rangle \leftarrow |1\rangle \leftarrow |2\rangle\,. \end{aligned}$$

Here the Drain is depopulating the state $|1\rangle$, whereas the Source is feeding it. This allows current to flow. Finally in the region F we have

$$\begin{aligned} \text{Source} &: |0\rangle \to |1\rangle \to |2\rangle\,, \\ \text{Drain} &: |0\rangle \leftarrow |1\rangle \leftarrow |2\rangle\,. \end{aligned}$$

In this case the current is also flowing but its intensity is twice larger than in the region D (see Fig.1.4b) since the Source is populating *all* the states that the Drain is depopulating. Thus the system is tuned in a condition where two "channels" are contributing to the transport of current in contrast to the previous case where only one "channel" was contributing.

This analysis can be extended to all the other regions leading to the sketch in Fig.1.6 that describes the simulations reported in Fig.1.4b. Usually the region labelled with B is called *Coulomb diamond* [3] because the interaction (U) opens up this region that otherwise would not be visible. In the Anderson model we have only one Coulomb diamond since only four states are available in the Hilbert space of the dot. In general, increasing the number of states in the model of the dot, the number of diamonds increases. Moreover the blue dots are the so-called *charge degeneracy points*. Indeed, in the rightmost one, for example, the probabilities to find the states $|\uparrow\rangle$, $|\downarrow\rangle$ and $|2\rangle$ are equal and such that $\rho_{\uparrow}^{\uparrow} = \rho_{\downarrow}^{\downarrow} = \rho_2^2 = 1/3$.

Usually the target of the experimentalists is the differential conductance (Fig.1.5) since it shows more clearly all the considerations we have explained so far.

CHAPTER 2

Beyond the perturbative theory

In this Chapter we consider the physical observables related to a quantum dot non perturbatively with respect to the coupling energy to the leads. We will present non perturbative approaches to the transport through an Anderson quantum dot: in Section 2.1 we will introduce the so-called *dressed second order theory* [41] (DSO), in Sect.2.2 we will show a proposal to extend the DSO by dressing its Nucleus.

2.1 The dressed second order (DSO)

So far we have calculated the lowest order current through the Anderson quantum dot. In this Section we want to capture effects beyond this perturbative theory considering an infinite series of higher order diagrams (with respect to E_{T}) [41]. This series is selected by allowing the RDM to be non diagonal, between the final and initial time, up to a certain degree in order to extend the temperature range of validity of our theory and to capture new interesting low energy effects. In the second order, considering the first diagram of Tab.1.1 with $|a\rangle = |a'\rangle = 0$, for example, the time-line of the RDM during the whole process reads:

$$|\sigma_1\rangle\langle\sigma_1| \leftarrow |0\rangle\langle\sigma_1| \leftarrow |0\rangle\langle 0| \,.$$

This means that we are considering a matrix element characterised by off-diagonal elements up to one electron excitation. If we consider all the diagrams of Tab.1.1 we can understand that, in the second order, only *single charge* or *single hole* excitation are found. It is natural to try to extend the classical second order theory by considering higher order diagrams with off-diagonal elements up to one excitation. In the DSO, this is achieved

considering diagrams such as the ones in Figs.2.1. These diagrams are formed by a *main fermion line* (delimited by the first (in τ_0) and the last tunnelling event (in τ_{2n-1} if n fermion lines are present)), that connects the two opposite contours, and other fermion lines whose corresponding tunnelling events occur between the ones delimiting the main one. The fermion lines connecting the latter tunnelling events, i.e. the fermion lines "under the main one", describe quantum fluctuations in the dot: in the sense that the state on the single contour is conserved considering only these processes. In order to further clarify this crucial point let us consider the diagram in Fig.2.1(b). Its time line is

$$|\sigma\rangle\langle\sigma| \leftarrow |\sigma\rangle\langle 0| \leftarrow |\sigma\rangle\langle\sigma| \leftarrow |\sigma\rangle\langle 0| \leftarrow |0\rangle\langle 0|\,.$$

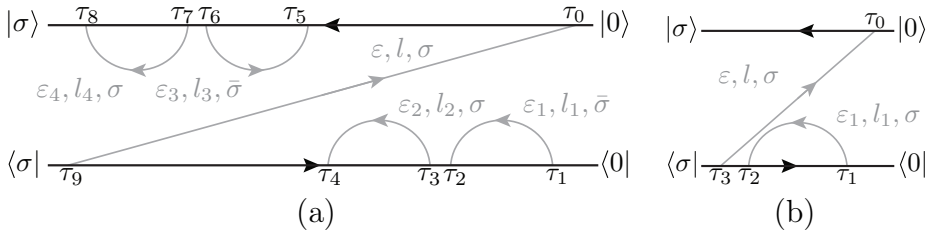

Figure 2.1: Examples of diagrams included in the DSO theory.

As it is clear from the previous equation the state that enters in τ_1 is the same that is re-established in τ_2 (analogously for τ_i and τ_{i+1} with $1 \leq i \leq 7$ for Fig.2.1(a)) and this means that the state on the single contour (upper or lower separately) is conserved. In the DSO the *main fermion line is dressed by all the possible combinations of a set of independent, irreducible and state contour conserving diagrams that defines the Nucleus ($\mathcal{N}$) of the dressing*. In this theory the equations for the populations, the current and the conductance, that we have derived for the second order, still hold true, whereas the analytical form of the rates changes. Then, in order to capture the effects of these quantum fluctuations, we have to learn how to re-write the rate for the DSO theory.

Rates in the DSO In this perspective, as we have shown in detail in App.A.4, we have derived "*new diagrammatic rules*" to write directly the integral form of all the rates. In the DSO a single rate is due to the series of all the possible combinations of the diagrams belonging to the *Nucleus of the dressing* ($\mathcal{N}$) under the main fermion line (see Fig.2.1(a) for an example of a typical term of the series). As first we have to choose the elements of the Nucleus. The diagrams that guarantee to have the closest form of the RDM to the diagonal one are "bubbles" (one fermion line either above or below the main fermion line). Notice that, considering the notation in App.A.4.1

this corresponds to $n = 2$ and $n_{\text{int}} = 0$ for all the elements in $\mathcal{N}$. Let us now consider the dressing of the diagram in the fifth row of of Tab.1.1, the Nucleus of the dressing reads:

$\mathcal{N} =$ 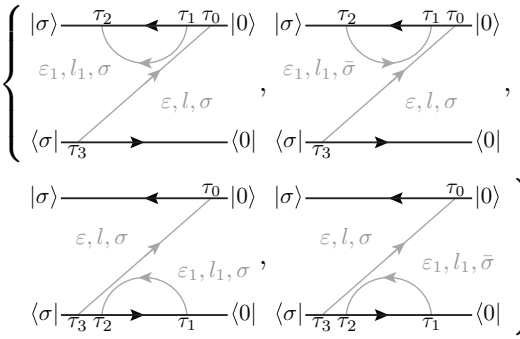

(2.1)

Here it is clear that the dimension of this set is $N = 4$. Then, following the afore-mentioned new diagrammatic rules (App.A.4), we directly obtain the integral form of the "dressed diagram". Symbolically we write (see Eq.(A.20))

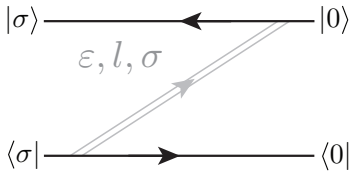

$$= \frac{i}{\hbar} \lim_{\eta \to 0} \int_{-\infty}^{+\infty} d\varepsilon \, \frac{\bar{\alpha}_{l,\sigma}(\varepsilon) f_l^+(\varepsilon)}{\varepsilon - E_{\sigma 0} + i\eta - \Sigma^{\sigma 0}(\varepsilon)}, \tag{2.2a}$$

$$\Sigma^{ij}(\varepsilon) = \sum_{k=1}^{4} a_k^{ij}(\varepsilon). \tag{2.2b}$$

$\Sigma^{ij}(\varepsilon)$ will play an important role in the following and we shall refer to it as the *self-energy* in the DSO theory. The self-energy is a complex function of the real variable ε, and it is expressed in terms of the contribution $(a_k^{\sigma 0}(\varepsilon))$ of the diagram in $\mathcal{N}$ that we have reported (using Eq.(A.22)) in Tab.2.1: on the left we show the diagram with the corresponding cut determining the denominators for the integral form on the right. As we have already shown for the second order we can write directly the corresponding rate from Eq.(2.2a):

$\Gamma^+_{l,\sigma 0} = \sum_{\mathbf{k}}$ 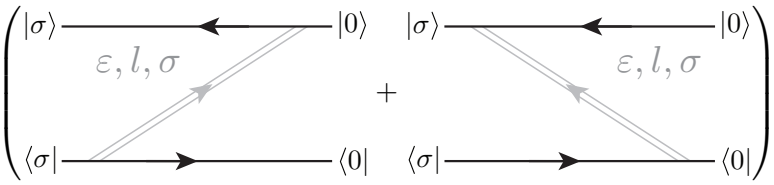

$$= \frac{2\Gamma}{h} \kappa_l \mathsf{Re} \left\{ i \lim_{\eta \to 0} \int_{-\infty}^{+\infty} d\varepsilon \, \frac{f_l^+(\varepsilon) L(\varepsilon, W, l)}{\varepsilon - E_{\sigma 0} + i\eta - \Sigma^{\sigma 0}(\varepsilon)} \right\}.$$

Diagram	Integral form
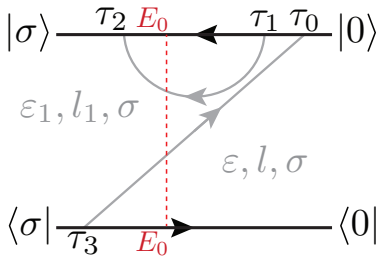	$a_1^{\sigma 0}(\varepsilon) = \sum_{l_1} \int_{-\infty}^{+\infty} d\varepsilon_1 \frac{\bar{\alpha}_{l_1,\sigma}(\varepsilon_1) f_{l_1}^{-}(\varepsilon_1)}{-\varepsilon_1 + \varepsilon + i\eta}$
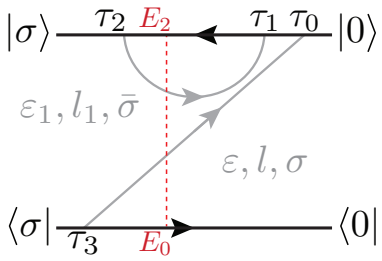	$a_2^{\sigma 0}(\varepsilon) = \sum_{l_1} \int_{-\infty}^{+\infty} d\varepsilon_1 \frac{\bar{\alpha}_{l_1,\bar{\sigma}}(\varepsilon_1) f_{l_1}^{+}(\varepsilon_1)}{\varepsilon_1 + \varepsilon - E_{20} + i\eta}$
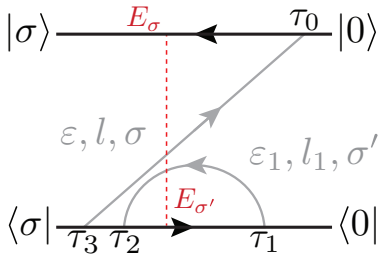	$a_{3/4}^{\sigma 0}(\varepsilon) = = \sum_{l_1} \int_{-\infty}^{+\infty} d\varepsilon_1 \frac{\bar{\alpha}_{l_1,\sigma'}(\varepsilon_1) f_{l_1}^{+}(\varepsilon_1)}{-\varepsilon_1 + \varepsilon - E_{\sigma\sigma'} + i\eta}$

Table 2.1: Summary table of the integral contribution related to the elements of the dressing Nucleus: on the left we show the diagram with the cut (red dashed line) that determines the denominator of the integral expression on the right. Here we have grouped the diagrams with the "$(\bar{\sigma})\sigma$-bubble" ($a_{3/4}^{\sigma 0}(\varepsilon)$) in the last row.

Diagram	Integral form
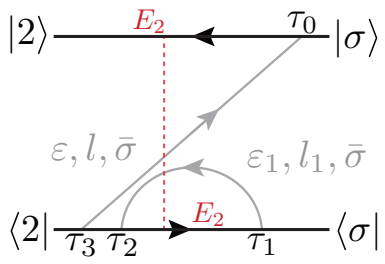	$a_1^{2\sigma}(\varepsilon) = \sum_{l_1} \int_{-\infty}^{+\infty} d\varepsilon_1 \frac{\bar{\alpha}_{l_1,\bar{\sigma}}(\varepsilon_1) f_{l_1}^{+}(\varepsilon_1)}{-\varepsilon_1 + \varepsilon + i\eta}$
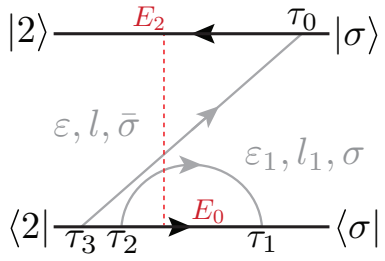	$a_2^{2\sigma}(\varepsilon) = \sum_{l_1} \int_{-\infty}^{+\infty} d\varepsilon_1 \frac{\bar{\alpha}_{l_1,\sigma}(\varepsilon_1) f_{l_1}^{-}(\varepsilon_1)}{\varepsilon_1 + \varepsilon - E_{20} + i\eta}$
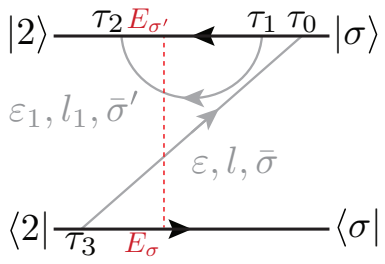	$a_{3/4}^{2\sigma}(\varepsilon) =$ $= \sum_{l_1} \int_{-\infty}^{+\infty} d\varepsilon_1 \frac{\bar{\alpha}_{l_1,\bar{\sigma}'}(\varepsilon_1) f_{l_1}^{-}(\varepsilon_1)}{-\varepsilon_1 + \varepsilon - E_{\sigma'\sigma} + i\eta}$

Table 2.2: Summary table of the integral contribution related to the elements of the dressing Nucleus for the rate $\Gamma_{\sigma 2}^{\pm}$: on the left we show the diagram with the cut (red dashed line) that determines the denominator of the integral expression on the right. Here we have reported the diagrams with the "$(\bar{\sigma})\sigma$-bubble" ($a_{3/4}^{\sigma 0}(\varepsilon)$) together (last row). We want to stress the strong similarity between the expression of $a_k^{\sigma 0}(\tilde{\varepsilon})$ and $a_k^{2\sigma}(\tilde{\varepsilon})$.

Following the same steps for the backward pointing diagrams with $|a\rangle = |a'\rangle = |\sigma\rangle$ and for the diagrams describing the transition $|\sigma\rangle \leftrightarrow |2\rangle$ it's easy to see that:

$$\Gamma^{\pm}_{l,\sigma 0} = \frac{2\Gamma}{h}\kappa_l \mathsf{Re}\left\{ i \lim_{\eta\to 0} \int_{-\infty}^{+\infty} d\varepsilon \, \frac{f_l^{\pm}(\varepsilon)\, L(\varepsilon, W, l)}{\varepsilon - E_{\sigma 0} + i\eta - \Sigma^{\sigma 0}(\varepsilon)} \right\}, \tag{2.3a}$$

$$\Gamma^{\pm}_{l,2\sigma} = \frac{2\Gamma}{h}\kappa_l \mathsf{Re}\left\{ i \lim_{\eta\to 0} \int_{-\infty}^{+\infty} d\varepsilon \, \frac{f_l^{\pm}(\varepsilon)\, L(\varepsilon, W, l)}{\varepsilon - E_{2\sigma} + i\eta - \Sigma^{2\sigma}(\varepsilon)} \right\}. \tag{2.3b}$$

The expression of the $a_k^{2\sigma}(\varepsilon)$ are obtained analogously (see Tab.2.2). Performing numerically the integrations we have in Eqs.(2.3) allows us to obtain numerically all the physical informations we are searching for. To this purpose it is convenient to derive an analytical form of the self-energy, recognizing that the integration defining the elements of the Nucleus $a_k^{\sigma 0/2\sigma}(\varepsilon)$ is of the same kind of the one we have studied in App.A.5. The result of such an integration is reported in Tab.2.3. However attention must be paid to the limits we consider. Indeed, for the Anderson model in the limit of infinite

$\dfrac{a_1^{\sigma 0/2\sigma}(\tilde{\varepsilon})}{(\Gamma/2\pi)}$	$\displaystyle\sum_l \kappa_l L\left(\tilde{\varepsilon}, \tilde{W}, l\right)\left\{\frac{\pi}{2}\left(\frac{\tilde{\varepsilon}-\tilde{\mu}_l}{\tilde{W}} - i\right) + \pm\left[\Psi^{(0)}\left(\frac{1}{2} + i\frac{\tilde{\mu}_l - \tilde{\varepsilon}}{2\pi}\right) - \Psi^{(0)}\left(\frac{1}{2} + \frac{\tilde{W}}{2\pi}\right)\right]\right\},$
$\dfrac{a_2^{\sigma 0/2\sigma}(\tilde{\varepsilon})}{(\Gamma/2\pi)}$	$\displaystyle\sum_l \kappa_l L\left(\tilde{E}_{20} - \tilde{\varepsilon}, \tilde{W}, l\right)\left\{\frac{\pi}{2}\left(\frac{\tilde{\varepsilon}+\tilde{\mu}_l - \tilde{E}_{20}}{\tilde{W}} - i\right) + \pm\left[\Psi^{(0)}\left(\frac{1}{2} + i\frac{\tilde{E}_{20} - \tilde{\mu}_l - \tilde{\varepsilon}}{2\pi}\right) - \Psi^{(0)}\left(\frac{1}{2} + \frac{\tilde{W}}{2\pi}\right)\right]\right\},$
$\dfrac{a_{3/4}^{\sigma 0/2\sigma}(\tilde{\varepsilon})}{(\Gamma/2\pi)}$	$\displaystyle\sum_l \kappa_l L\left(\tilde{\varepsilon} \mp \tilde{E}_{\sigma\sigma'}, \tilde{W}, l\right)\left\{\frac{\pi}{2}\left(\frac{\tilde{\varepsilon}-\tilde{\mu}_l \mp \tilde{E}_{\sigma\sigma'}}{\tilde{W}} - i\right) + \mp\left[\Psi^{(0)}\left(\frac{1}{2} + i\frac{\tilde{\mu}_l - \tilde{\varepsilon} \pm \tilde{E}_{\sigma\sigma'}}{2\pi}\right) - \Psi^{(0)}\left(\frac{1}{2} + \frac{\tilde{W}}{2\pi}\right)\right]\right\},$

Table 2.3: Analytic expressions of the elements of the dressing Nucleus.

Coulomb interaction a finite cut-off must be retained. The role of such a cut-off is played by the bandwidth (W) we have introduced in the leads density of states (Eq.(1.70)). For this reason in the following we will treat *independently* the case of *infinite Coulomb repulsion* between the electrons in the dot ($U \to \infty$) and the case of *finite repulsion* ($U \ll W$) that will allow us to perform the infinite bandwidth limit.

2.1.1 The DSO in the case of infinite Coulomb repulsion

In order to simplify the global picture let us consider firstly the limit of very strong interaction between the electrons in the dot ($U \to \infty$). In this limit the second electron is never allowed to tunnel into the dot since it is energetically too expensive, i.e. the state with two electrons in the dot ($|2\rangle$) is forbidden and the Fock space of the dot is restricted to $\mathcal{H}_\odot = \{|0\rangle, |\uparrow\rangle, |\downarrow\rangle\}$. This approximation is supposed to be a good one, considering the stability diagram in Fig.1.5, in the region around the charge degeneracy point between the state $|0\rangle$ and $|1\rangle$ or, in the presence of a finite magnetic field, $|0\rangle$ and $\min\{|\uparrow\rangle, |\downarrow\rangle\}$.
Mathematically, in order to perform the limit of infinite Coulomb repulsion we have to consider $E_{20} > W$ and retain a finite cut-off W. It is not hard to see from the second line of Tab.2.3 that $a_2^{\sigma 0/2\sigma} \to 0$ for $U \to \infty$, since $E_{20} \to \infty$. The same is for the rate $\Gamma^+_{l,2\sigma} \to 0$ (Eq.(2.3b)), since $E_{20} \to \infty$ and $\sum_k a_k^{2\sigma}(\varepsilon)$ is finite, as we were expecting because of the aforementioned considerations about the conservation of the energy. Thus, in this case, we need to compute only $\Sigma^{\sigma 0}(\varepsilon)$ that, using Tab.2.3, reads:

$$\Sigma^{\sigma 0}(\tilde{\varepsilon}) = \Gamma \sum_{l=\mathrm{L,R}} \frac{\kappa_l}{2\pi} L\left(\tilde{\varepsilon}, \tilde{W}\right) \left[\frac{3}{2}\pi\left(\frac{\tilde{\varepsilon}}{\tilde{W}} - i\right) + \right.$$
$$\left. - \Psi^{(0)}\left(\frac{1}{2} + i\frac{\tilde{\mu}_l - \tilde{\varepsilon} + \tilde{E}_{\sigma\bar{\sigma}}}{2\pi}\right) + \Psi^{(0)}\left(\frac{1}{2} + \frac{\tilde{W}}{2\pi}\right)\right]. \quad (2.4)$$

Here $\Psi^{(0)}(z)$ is the digamma function we have introduced in App.A.5 (see Eq.(A.30)) and we have approximated

$$L(\varepsilon - E_{\sigma\bar{\sigma}}, W, l) \simeq \frac{W^2}{\varepsilon^2 + W^2} \stackrel{\text{def}}{=} L(\varepsilon, W). \quad (2.5)$$

This approximation is suitable in case $W \gg E_{\sigma\bar{\sigma}}, \mu_l$ that it is usually referred as the large bandwidth limit in the literature. Moreover we have adopted the following notation: $\tilde{X} \stackrel{\text{def}}{=} X\beta$.
Unfortunately, in this case, $\Sigma^{\sigma 0}$ is not finite if $W \to \infty$. However we can keep it large compared to the other energy scales. In this limit and considering the spin symmetric case ($E_\uparrow = E_\downarrow = E_1$), it is possible to recast the equation

of the current in the following integral form:

$$I_l = \kappa_l \kappa_{\bar{l}} \frac{\Gamma e}{\hbar} \int_{-\infty}^{+\infty} d\varepsilon \left[f_l^+(\varepsilon) - f_{\bar{l}}^+(\varepsilon) \right] L(\varepsilon, W) A(\varepsilon), \tag{2.6}$$

where we introduced the total spectral function or tunnelling density of states (TDOS)

$$A(\varepsilon) = -\frac{\langle N_{\mathrm{h}} \rangle}{\pi} \frac{\Sigma_{\mathrm{I}}^{10}(\varepsilon)}{\left(\varepsilon - E_{10} - \Sigma_{\mathrm{R}}^{10}(\varepsilon)\right)^2 + \left(\Sigma_{\mathrm{I}}^{10}(\varepsilon)\right)^2}, \tag{2.7}$$

that is the sum of the spectral functions per spin species $A(\varepsilon) = \sum_\sigma A_\sigma(\varepsilon)$ and $\Sigma_{\mathrm{R}}^{10}(\Sigma_{\mathrm{I}}^{10})$ is the real(imaginary) part of the self-energy. Here we used $\langle N_{\mathrm{h}} \rangle = 2\rho_0^0 + \rho_\uparrow^\uparrow + \rho_\downarrow^\downarrow$. As we will see in Sect.3.2, it is always possible to rewrite the current as an integral function of the TDOS as in Eq.(2.6). Moreover in such Section we will show that the TDOS in Eq.(2.7) is a function of the so-called grater and lesser correlation functions.

Zero bias anomaly and scaling behaviour Eq.(2.7) gives us the opportunity for the first time in this thesis to deal with a complex many-body resonance. Indeed the spectral function in Eq.(2.7) presents a resonance whenever the equation

$$\mathsf{Re}\left\{\varepsilon - E_{10} - \Sigma^{10}(\varepsilon)\right\} = 0 \tag{2.8}$$

is satisfied or close to be fulfilled ($\mathsf{Re}\left\{\varepsilon - E_{10} - \Sigma^{10}(\varepsilon)\right\} \simeq 0$).

A resonance can be found at $\varepsilon \simeq E_{10}$ that gives the position of the Coulomb blockade peak (in literature it is often called also Hubbard peak). Notice that in the limit $\Gamma \to 0$ the spectral function tend to be proportional to a delta function centred around $\varepsilon = E_{10}$. Thus this peak it is present also in the absence of the self-energy, i.e. in the second order approximation as we have already seen in Sect.1.2.3 studying the conductance and the current. Indeed as we will see in the following the current and the spectral function are closely related.

Another purely many-body resonance can be found at $\varepsilon \simeq \mu_l$ if $T \ll \Gamma$[1] and $\mu_0 - E_{10} > n\Gamma$, where $n \geq 2$[2]. This is indeed a many-body resonance because it relies completely on the presence of the self-energy in Eq.(2.8), i.e. as $\Gamma \to 0$ this is not any more a solution of such an equation and the corresponding resonance dies out. This is the manifestation of the Kondo

[1] We will better quantify the suitable temperature regime to manifest this many-body resonance later on.

[2] In literature there is no consensus on the numerical pre-factor n. As we will see, the best way to check if the dot is tuned in the localised moment regime is to check whether the linear conductance is universal as a function of the temperature normalised to the Kondo temperature.

effect we discussed in the introduction of the thesis. Indeed if the dot is tuned in the localised regime ($\mu_0 - E_{10} > n\Gamma$) $\rho_1^1 \simeq 1$ and considering temperatures from the intermediate ($\Gamma \simeq k_\mathrm{B}T$) to the strong coupling regimes ($k_\mathrm{B}T \to 0$) the electrons in the leads screen the spin of the dot electron [22] forming a spin singlet Kondo resonance at $\varepsilon \simeq \mu_l$. Thus, in the case of an Anderson quantum dot, the role of the magnetic impurity is played by the dot itself if tuned in the proper regime. Since the DSO is the lowest order approximation that captures the effects of a self-energy, the DSO is capable to describe a zero bias anomaly as we will see in detail.

From the TDOS and the expression of the self-energy we can extract the exponential dependence (i.e. up to a pre factor) of the so-called *Kondo temperature* (T_K) [22] through the parameters of the system. The Kondo temperature is the most basic energy scale that characterises the correlated Kondo state. The energy associate to it ($k_\mathrm{B}T_\mathrm{K}$) can be seen as the bounding energy of the Kondo state. As we will see in the following, if one considers energy scales $k_\mathrm{B}T, eV, \mu_\mathrm{B}B \gg k_\mathrm{B}T_\mathrm{K}$ one destroys the Kondo bound state and correspondingly the transport properties show a strong suppression.

Let us now study the properties of this zero bias anomaly in the DSO approximation. In order to capture the system parameters dependence of the Kondo temperature we will search for solutions of Eq.(2.8) in the deep Kondo regime,

$$k_\mathrm{B}T \ll W, \qquad\qquad k_\mathrm{B}T \ll \Gamma \ll \mu_0 - E_{10}.$$

Because of the first assumption we can approximate $\Psi^{(0)}(1/2 + \tilde{W}/2\pi)$ with its asymptotic series:

$$\Psi^{(0)}(z) \underset{|z|\gg 1}{\sim} \log(z) - \frac{1}{2z} - \sum_{n=1}^{+\infty} \frac{B_{2n}}{2nz^{2n}}, \tag{2.9}$$

where B_{2n} are Bernoulli's numbers. Then, considering the leading order of the expansion, we find the following approximated expression for the self-energy:

$$\Sigma^{10}(\tilde{\varepsilon}) \underset{k_\mathrm{B}T\ll W}{\sim} \Gamma \sum_{l=\mathrm{L,R}} \frac{\kappa_l}{2\pi} L\left(\tilde{\varepsilon}, \tilde{W}\right) \left[\frac{3}{2}\pi\left(\frac{\tilde{\varepsilon}}{\tilde{W}} - i\right) + \right.$$
$$\left. - \Psi^{(0)}\left(\frac{1}{2} + i\frac{\tilde{\mu}_l - \tilde{\varepsilon}}{2\pi}\right) + \log\left(\frac{1}{2} + \frac{\tilde{W}}{2\pi}\right)\right].$$

Considering Eq.(2.8), in equilibrium $\mu_l = \mu_0$, for $\varepsilon = \mu_0$ and $\mu_0 \ll W$ we obtain the following equation

$$\mathrm{Re}\left\{\mu_0 - E_{10} - \Sigma^{10}(\tilde{\mu}_0)\right\} = 0. \tag{2.10}$$

Solving such an equation with respect to the temperature we find

$$k_\mathrm{B}T_\mathrm{K} \propto W e^{-2\pi\frac{\mu_0 - E_{10}}{\Gamma}}, \tag{2.11}$$

This analytic dependence is confirmed by the numerical simulations showing that the linear conductance temperature dependence is universal with respect to the ratio $T/T_{\rm K}$ [41], i.e. curves with different Kondo temperatures plotted against the ratio $T/T_{\rm K}$ collapse onto the same universal curve (Fig.2.2). This

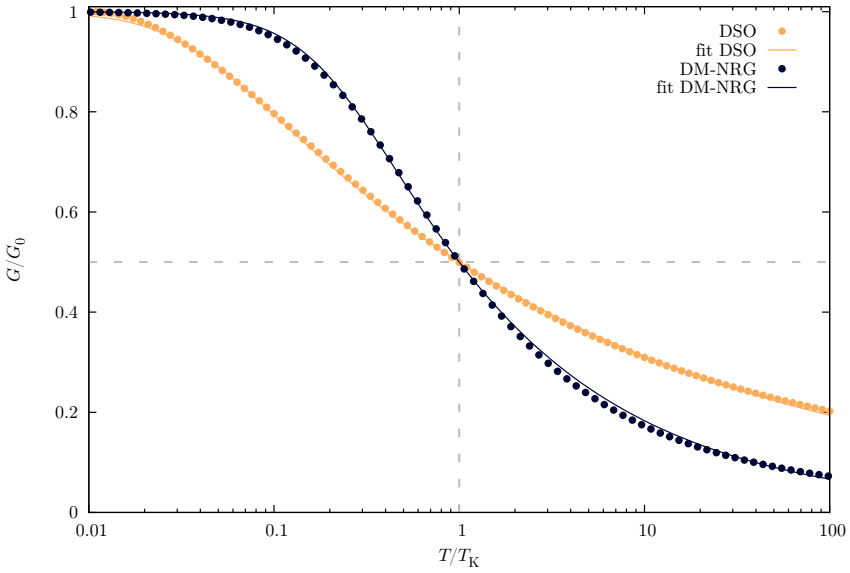

Figure 2.2: Fit (solid lines) of the DSO linear conductance (yellow circles) and DM-NRG data (dark blue circles) as a function of the temperature normalised to the corresponding $T_{\rm K}$ of each theory with the empirical curve in Eq.(2.12). Here we normalised the linear conductance with respect to the corresponding maximal values: $G_0^{\rm DSO} \simeq 0.7e^2/h$ and $G_0^{\rm DM\text{-}NRG} = 2e^2/h$. The DSO shows universality as a function of $T/T_{\rm K}$ but it does not reproduce the correct universal temperature dependence (DM-NRG curve).

is indeed one of the typical signatures of the Kondo effect.
However, as it is shown in Fig.2.2, the DSO universal curve is not the proper one and the theory breaks down for temperatures $T/T_{\rm K} < 0.01$ [41]. Because of this the DSO does not reproduce the correct unitary limit ($G_0 = 2e^2/h$) as $T \to 0$ showing a maximal value of the conductance $G_0^{\rm DSO} \simeq 0.7e^2/h$. In Fig.2.2 we present a comparison of the linear conductance obtained from the DSO theory (yellow dots) and the DM-NRG method (dark blue dots) we will present in Chap.4. We fitted in both cases the linear conductance with the empirical curve [25]

$$G(T) = G_0 \left[\left(\frac{T}{T_{\rm K}} \right)^2 \cdot \left(2^{1/s} - 1 \right) + 1 \right]^{-s}, \tag{2.12}$$

fixing $T_{\rm K}$ such that $G(T/T_{\rm K} = 1) = G_0/2$, where G_0 is the absolute maximum

in the linear conductance, reached either in the DM-NRG or in the DSO theory, and s is the only fitting parameter. The fit yields $s_{\text{DM-NRG}} = 0.22$ (compatible with the experimental results in Ref. [25]) and $s_{\text{DSO}} = 0.103 < s_{\text{DM-NRG}}/2$ showing that the DSO is not capable of reproducing the correct universal temperature dependence.
Moreover, as it was already pointed out in Ref. [41], the exponent of the Kondo temperature in Eq.(2.11) differs from the correct one ($k_{\text{B}}T_{\text{K}} \propto \exp -\pi\frac{\mu_0 - E_{10}}{\Gamma}$ [22]) by the factor 2. Interestingly the same issue was noticed also in the Resonant Tunnelling Approximation (RTA) we will present in Chap.3. These issues restrict the applicability of the DSO theory to temperatures much larger than T_{K} ($T \gg T_{\text{K}}$) since this theory captures only an onset of the Kondo resonance.
Looking carefully at Tab.2.3 one may notice that this is caused by a cancellation of the digamma functions summing up the term $a_1^{\sigma 0}(\tilde{\varepsilon})$ and $a_3^{\sigma 0}(\tilde{\varepsilon})$ in order to obtain the self-energy. Indeed, if the first term was not present at all, we would have obtained the correct exponential dependence. Thus this theory is not capable of distinguishing (apart from a sign leading to the cancellation) the contributions $a_1^{\sigma 0}(\varepsilon_1)$ and $a_3^{\sigma 0}(\varepsilon_1)$ ($\sigma = \sigma'$ for this term). In Sect.2.2 we will present an extension of the DSO that we developed in order to fix the issue of the wrong scaling exponent in the Kondo temperature.
As we will see in the next Section, even though the DSO is not the suitable theory to deal with the Kondo effect, it is capable of capturing many interesting effects beyond the perturbative theory in the intermediate coupling regime ($T \sim \Gamma$). This is due to the fact that the DSO is the lowest order approximation that captures self-energy corrections in the rates and thus in the current.

2.1.2 DSO with finite Coulomb interaction

In the case of finite U, considering the integral we have evaluated in App.A.5 to perform the ones defining the $a_k^{\sigma 0/2\sigma}(\varepsilon)$ functions (see Tab.2.3) and taking into account the large bandwidth limit

$$L(\varepsilon - E_{ij}, W, l) \simeq L(\varepsilon, W), \tag{2.13}$$

with $ij = \sigma\sigma', 20$, we find the following analytic expression for the DSO self-energy:

$$\Sigma^{\sigma 0/2\sigma}(\tilde{\varepsilon}) \simeq \Gamma \sum_{l=\text{L,R}} \frac{\kappa_l}{2\pi} L\left(\tilde{\varepsilon}, \tilde{W}\right) \left[2\pi \left(\frac{\tilde{\varepsilon}}{\tilde{W}} - i \right) + \right.$$
$$\left. \pm \Psi^{(0)}\left(\frac{1}{2} + i\frac{\tilde{E}_{20} - \tilde{\varepsilon} - \tilde{\mu}_l}{2\pi} \right) \mp \Psi^{(0)}\left(\frac{1}{2} + i\frac{\tilde{\mu}_l - \tilde{\varepsilon} \pm \tilde{E}_{\sigma\bar{\sigma}}}{2\pi} \right) \right], \tag{2.14}$$

We want to stress that, in this case, we cannot consider the limit for $U \to \infty$ because of the assumption $U \ll W$. However, it is possible to

perform analytically the infinite bandwidth limit for $\Sigma^{\sigma 0/2\sigma}(\tilde{\varepsilon})$. At this stage we have all the ingredients to obtain all the observables numerically by computing the integration that defines the rates in Eq.(2.3).
Notice that, for the *spin symmetric problem* ($E_\sigma = E_{\bar{\sigma}} = E_1$) the integral form of the current (Eqs.(1.82) and (2.3a)) can be recast in a more "user-friendly" form:

$$I_l = \kappa_l \kappa_{\bar{l}} \frac{\Gamma e}{\hbar} \int_{-\infty}^{+\infty} d\varepsilon \left[f_l^+(\varepsilon) - f_{\bar{l}}^+(\varepsilon) \right] \left(A^{10}(\varepsilon) + A^{21}(\varepsilon) \right), \tag{2.15}$$

where we have defined the components of the TDOS

$$A^{ij}(\tilde{\varepsilon}) = -\frac{1}{\pi} \frac{\left\langle N_{\mathrm{h(e)}} \right\rangle \Sigma_{\mathrm{I}}^{ij}(\varepsilon)}{\left(\varepsilon - E_{ij} + \Sigma_{\mathrm{R}}^{ij}(\varepsilon) \right)^2 + \left(\Sigma_{\mathrm{I}}^{ij}(\varepsilon) \right)^2}, \tag{2.16}$$

and $\Sigma^{ij}(\tilde{\varepsilon}) = \Sigma_{\mathrm{R}}^{ij}(\tilde{\varepsilon}) + i\Sigma_{\mathrm{I}}^{ij}(\tilde{\varepsilon})$ with $ij = 10, 21$. In Eq.(2.15) we have performed the limit $W \to \infty$ since the integral and the Self-Energies are both finite in such a limit. Physically Eq.(2.15) expresses the fact that, in case of finite Coulomb interaction, the system offers another transport channel to let the current flow with respect to the previous Section. The corresponding weights are complicated functions of the system's parameters but, in the perturbative regime ($\Gamma \ll k_{\mathrm{B}}T$), they reduce to delta functions matching specific dot's energy differences giving Eq.(1.82).

DSO results Let us analyse the conductance in the DSO approximation. In Fig.2.3 we have reported several different regimes:

1- Thermally broadened Coulomb blockade In Fig.2.3(a) $k_{\mathrm{B}}T/\Gamma = 3$: here the Coulomb blockade is mainly broadened by the temperature. Considering higher temperatures the DSO approximation tends by construction to the second order theory (see Fig.1.5). Here we have considered a much lower Coulomb interaction ($U \simeq 2$meV against $U \simeq 50$meV) than in Fig.1.5 and thus the Coulomb diamond is not fully formed yet;

2- Intermediate coupling regime In Fig.2.3(b) $k_{\mathrm{B}}T/\Gamma = 1$: here we observe a transition from a temperature to a tunnelling dominated width broadening of the Coulomb peaks (see Fig.2.4 for a bias cut). In contrast to the second order theory, the DSO is capable to capture a tunnelling induced broadening of the Coulomb blockade peaks' width ($\propto \Gamma$) and a saturation of their height. Indeed, as it is possible to notice form Fig.2.3(b) and Fig.2.4, the Coulomb Blockade peaks' height is not proportional, as in the second order theory, to $(k_{\mathrm{B}}T)^{-1}$ and it saturates to a value smaller than e^2/h before it breaks down for lower

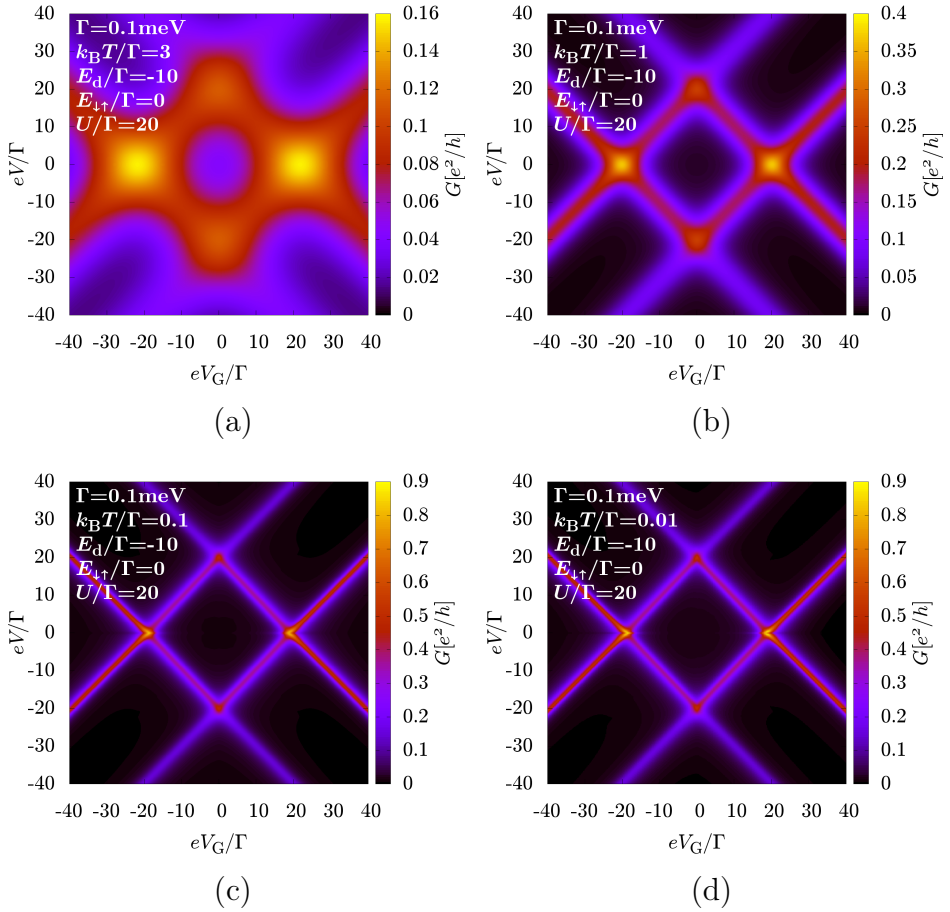

Figure 2.3: Stability diagram: differential conductance of the quantum dot in the Anderson model as a function of the gate and bias voltages.

temperatures [41].

Moreover, since the self-energy is energy dependent, the height and the width of the Coulomb blockade resonances depend on the number of states that are involved in the transition. Indeed, if we focus on the left-most charge degeneracy point ($|0\rangle \rightarrow \{|\uparrow\rangle, |\downarrow\rangle\}$), it is easy to see that the height of the Coulomb blockade resonance on the left is higher than the one on the right. On the left, by increasing the bias we switch from a dot mainly depopulated, i.e. in the singly degenerate ground state ($|0\rangle$) to a dot in a mixture of three states ($|0\rangle, |\uparrow\rangle, |\downarrow\rangle$) in the region we labelled as "D" in Fig.1.6. On the other hand, in the region on the right, in equilibrium the ground state is twice degenerate ($|\uparrow\rangle, |\downarrow\rangle$) and, increasing the bias, we get access to the same mixed state ($|0\rangle, |\uparrow\rangle, |\downarrow\rangle$). The DSO, in contrast to the second order theory, is capable to capture

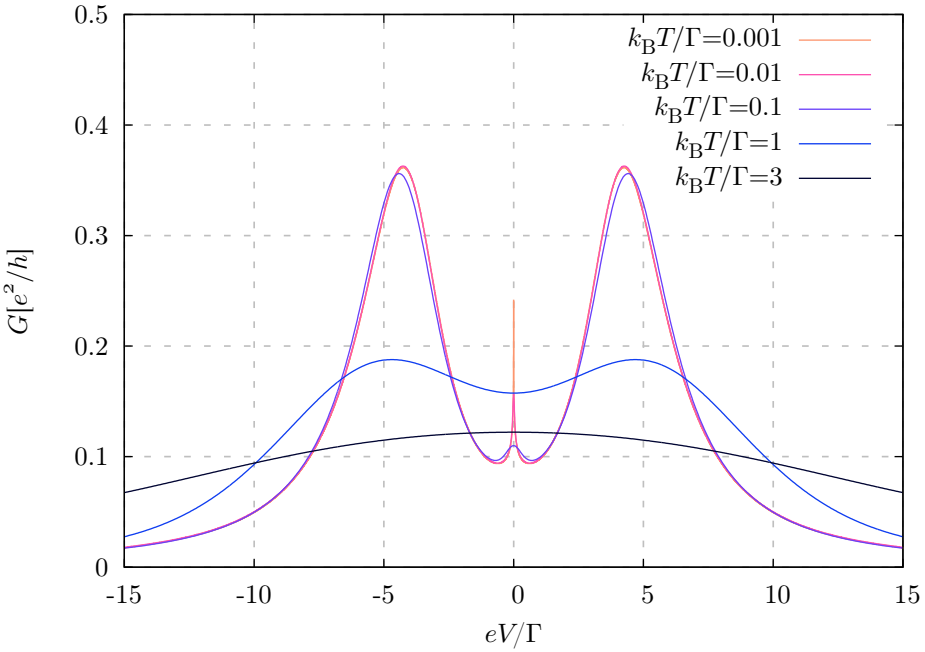

Figure 2.4: Differential conductance as a function of the applied bias in correspondence of $eV_G/\Gamma = -15$ for the same parameters as in Fig.2.3 and different temperatures (colour scale).

this difference, on the level of the conductance, due to the imaginary part of the self-energy. Moreover, as soon as one consider temperatures such that the system is in the weak coupling regime, the broadening and the height of the Coulomb blockade resonances tend to the one of the second order, i.e. they do not depend any more on the number of states involved in the transition. The mirrored picture holds true for the rightmost charge degeneracy point by particle-hole symmetry.

3- Kondo onset In Fig.2.3(c) and Fig.2.3(d) $k_BT/\Gamma = 0.1$ and $k_BT/\Gamma = 0.01$ respectively. As we lower the temperature further we notice that the Coulomb blockade peaks and heights are still consistent with respect to the above discussion. It is worth to notice that in the proximity of the charge degeneracy points, towards the one electron Coulomb valley, an on-set of a narrow "Kondo-like resonance" at zero bias (see Fig.2.4 for a bias trace of the conductance) is appearing as temperature is lowered. However its width is not the proper one since the Kondo temperature has not the right exponential dependence (see Eq.(2.11) and discussion below it). Moreover a sharp minimum is formed in correspondence of the charge degeneracy points. Interestingly, this minimum appears also

in the RTA [38] we will discuss in Chap.3. We believe that this is an artefact of the DSO due to a divergence of the self-energy in the limit $T \to 0$ in correspondence of such points. As it will become clear in the following, the regularisation of the self-energy in such a limit is a key point in the correct description of the transport properties at low temperatures.

2.1.3 Magnetic field effects

Finally we can consider the transport properties in the presence of a magnetic field. In Fig.2.5 we show the differential conductance as a function of the applied bias for different Zeeman splitting values ($E_{\downarrow\uparrow}$). It is easy to see that the zero bias anomaly splits as a function of the applied magnetic field as it should be in the Kondo effect [15, 30]. Moreover for $E_{\downarrow\uparrow} \simeq \Gamma$ the height and the width of the Coulomb blockade peaks change appreciably due to the self-energy magnetic field dependence (see Eq.(2.14)). This is in agreement with the discussion in the previous paragraph about the energy dependent broadening of the Coulomb peaks. In Fig.2.6(a) and 2.6(b) we show the DSO differential conductance for $E_{\downarrow\uparrow} = 5\Gamma$ and 10Γ respectively, while in Fig.2.6(c)-Fig.2.6(f) we present the populations (P_i, with $i \in \{ |0\rangle, |\downarrow\rangle, |\uparrow\rangle, |2\rangle \}$) for

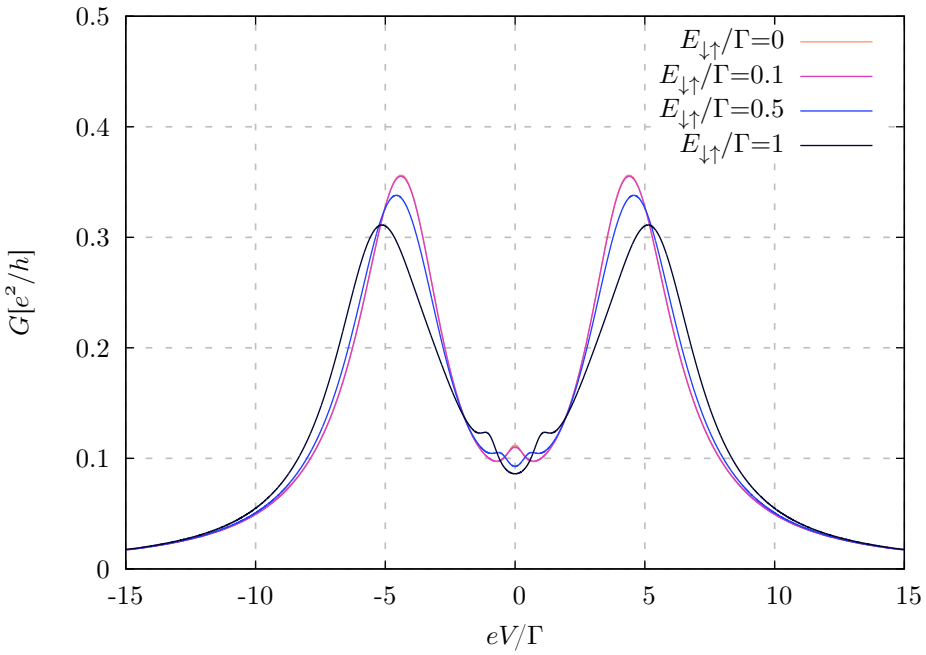

Figure 2.5: Differential conductance as a function of the applied bias in correspondence of $V_G/\Gamma = -15$ for the same parameters as in Fig.2.3c except for the applied Zeeman splitting reported in the colour scale.

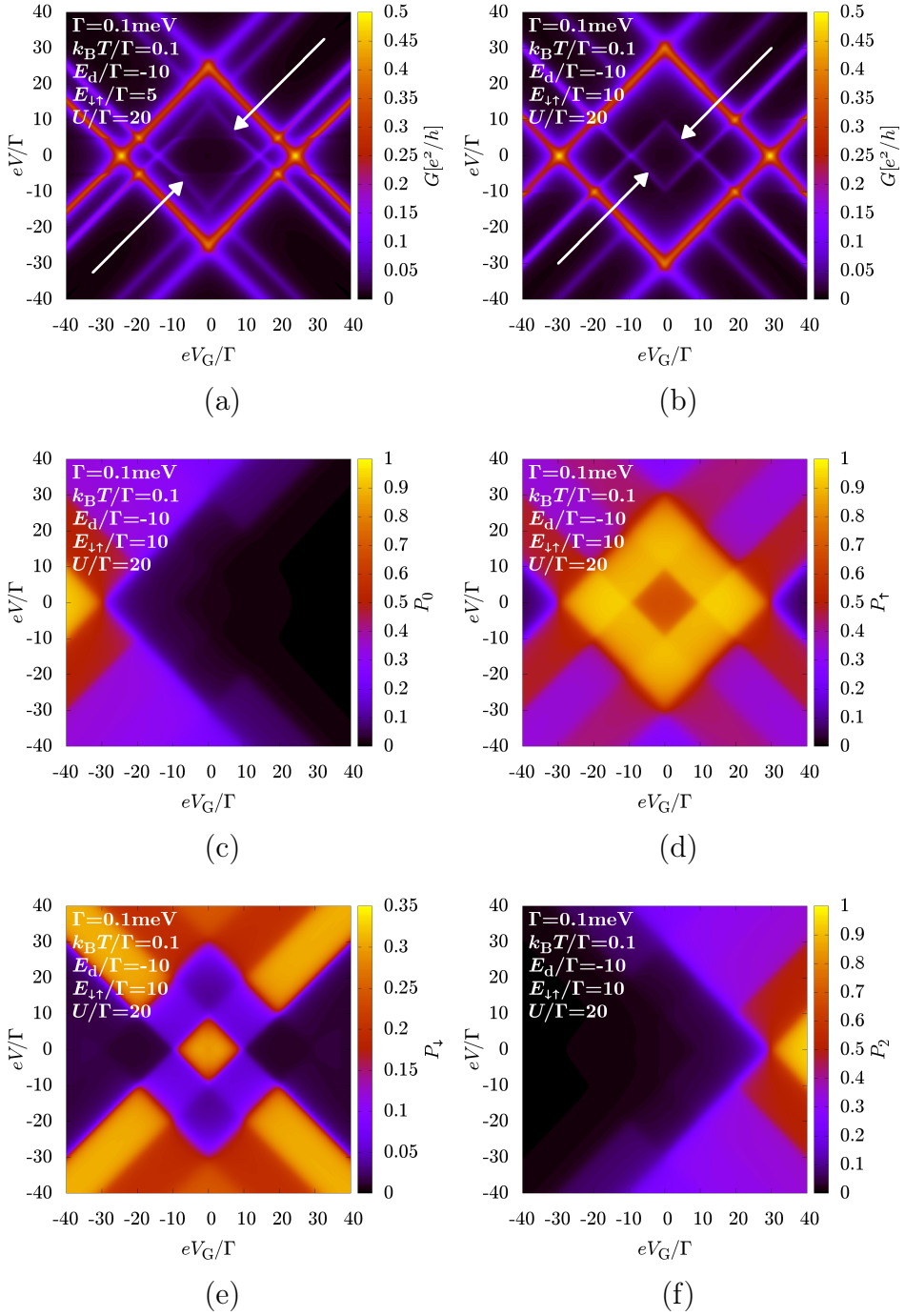

Figure 2.6: In (a) and (b) we present the differential conductance of the quantum dot as a function of the gate and bias voltages for $E_{\downarrow\uparrow} = 5\Gamma$ and 10Γ. White arrows point towards resonances in the Coulomb diamond. From (c) to (f) the populations for $E_{\downarrow\uparrow} = 10\Gamma$.

$E_{\downarrow\uparrow} = 10$. It is easy to notice that, in the case of a large Zeeman splitting, in equilibrium and for gate values such that $E_{\downarrow} > 0$ the system is mainly in the ground state configuration that is completely polarised (if $E_{\downarrow\uparrow} > 0$ the ground state is $|\uparrow\rangle$). In this limit the Coulomb blockade resonance is symmetric around the charge degeneracy points until we reach bias and gate values such that we can get access to the excited state $|\downarrow\rangle$. Then an excited state Coulomb resonance appears, pointing externally with respect to the Coulomb diamond, and the width of the Coulomb blockade resonance changes.
Unfortunately in the DSO the conductance presents a resonance towards the inner part of the Coulomb diamond (see white arrows in Fig.2.6(a) and 2.6(b)). As we will see in Chap.3, discussing the RTA, this resonance is an artefact. It arises due to the fact that in the DSO some fourth order co-tunnelling processes are missing, i.e. we consider only bubbles in the Nucleus of the dressing. This causes an artificially large correction to the excited state population [48] in the middle of the Coulomb diamond where we have $P_{\downarrow} \simeq P_{\uparrow}$. We will deal with this issue in Chap.3 where we will introduce the so-called *vertex corrections* that will allow us to take into account exactly all the fourth order processes.

2.2 Dressing the nucleus of the DSO (DDSO)

In order to improve the DSO theory there are mainly two "orthogonal" ways. The first one is to work on the *Nucleus of the dressing* in such a way that the resulting self-energy is a better approximation of the exact one; the second one is to keep the same self-energy and to include those diagrams with crossing fermion lines that we have neglected so far. In this Section we will address the first one. We shall *dress the Nucleus* $\mathcal{N}$ in Eq.(2.1) in order to heal some of the DSO artefacts regarding the scaling exponents in the Kondo temperature and in the universal linear conductance temperature dependence (see Sect.2.1.1). Indeed, at this point, it should be clear that dressing the Nucleus means actually to dress the self-energy in the DSO. The latter option will be considered in Chap.3 by presenting the RTA. Since the RTA shares the same self-energy of the DSO, this will not heal any artefact concerning the Kondo scaling exponents.

2.2.1 Dressing of the self-energy

In this Section we will consider only the Anderson model in the case of infinite Coulomb repulsion since, in this case, we need to consider only the rates $\Gamma^{\pm}_{l,\sigma 0}$ as in Sect.2.1.1. Moreover we will restrict ourselves to the spin symmetric case ($\bar{E}_{\uparrow} = \bar{E}_{\downarrow} = \bar{E}_1$ and $\bar{\alpha}_{l,\sigma} = \bar{\alpha}_{l,\bar{\sigma}} = \bar{\alpha}_{l,1}$) such that $\Gamma^{\pm}_{l,\uparrow 0} = \Gamma^{\pm}_{l,\downarrow 0} = \Gamma^{\pm}_{l,10}$.
To improve on the wrong exponents in the conductance and on the Kondo temperature T_{K}, non-perturbative corrections to the DSO are required. Considering a *dressing of the diagrams that determine the self-energy* it is natural

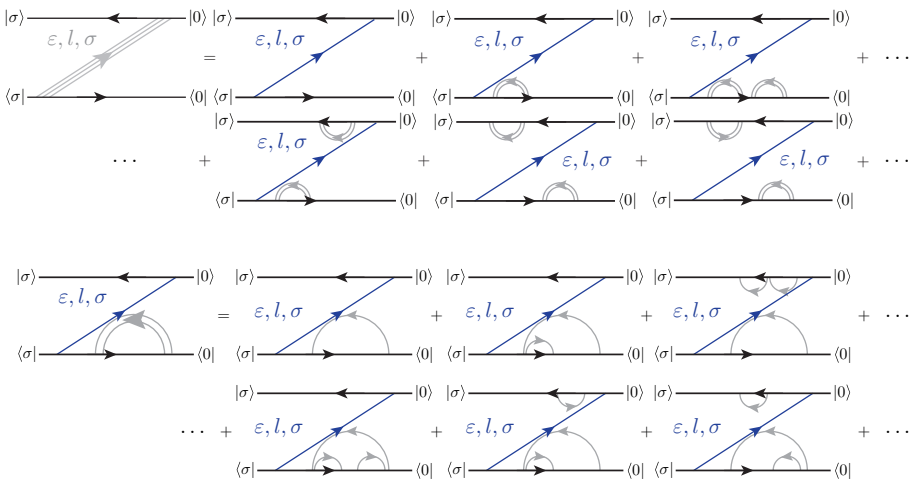

Figure 2.7: Example of a typical diagram included in the calculation of the rates in the DDSO theory. In blue we depicted the main fermion line, whereas in grey the dressing bubbles.

to focus on "dressed bubbles" as new elements of the Nucleus of the so-called Dressed-DSO (DDSO):

$$\mathcal{N}_{\mathrm{DDSO}} = \left\{ \right.$$

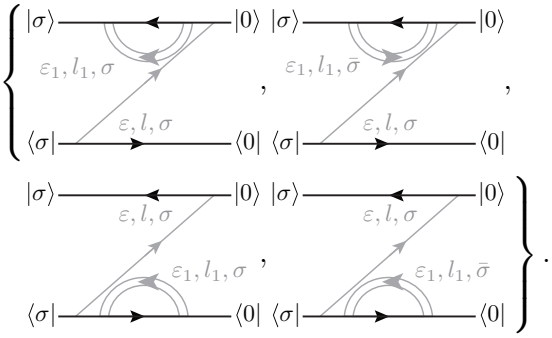

$$\left. \right\}. \tag{2.17}$$

As it is shown in Fig.2.7 we consider "dressed bubbles" between the tunnelling events defining the main (blue) fermion line. In the dressed bubbles we consider up to two simultaneous excitations. I.e., if we consider a vertical line cutting a dressed diagram, this has up to three intersections per vertical cut, as it is shown in the bottom panel of Fig.2.7. Hence, in the DDSO the elements of $\mathcal{N}_{\mathrm{DDSO}}$ are themselves the result of the sum of a series. In the following we will refer to $\mathcal{N}_{\mathrm{DDSO}}$ as the *Nucleus of the first dressing*. Thus, as it is explained in App.A.4.3, we let the dimension of $\mathcal{N}_{\mathrm{DDSO}}$ tend to infinity. The elements of the Nucleus $\mathcal{N}_{\mathrm{DDSO}}$ are non perturbative in the coupling energy E_{T}, since they are themselves dressed by other tunnelling events that we will identify as the elements of the *second dressing*. Following the prescription in App.A.4.3, fixing the order of the second dressing to one (i.e. we are considering only bubbles in the second dressing), we can write

symbolically

$$\Gamma^{\pm}_{l,\sigma 0} = \sum_{\mathbf{k},l}$$

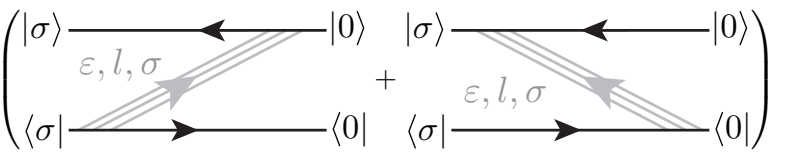

$$= \frac{2\Gamma}{h}\kappa_l \mathsf{Re}\left\{ i \lim_{\eta\to 0} \int_{-\infty}^{+\infty} d\varepsilon \, \frac{f_l^{\pm}(\varepsilon)\, L(\varepsilon, W, l)}{\varepsilon - E_{\sigma 0} + i\eta - \Sigma^{\sigma 0}_{\mathrm{DDSO}}(\varepsilon, \Gamma)} \right\}, \tag{2.18}$$

where

$$\Sigma^{\sigma 0}_{\mathrm{DDSO}}(\varepsilon, \Gamma) = \sum_{i=1}^{4} a_i^{\sigma 0}(\varepsilon, \Gamma), \tag{2.19}$$

is a complex function of the energy, as it was in the DSO; additionally now it depends non trivially on the coupling Γ because of the new corrections to the DSO, i.e. $\Sigma^{\sigma 0}_{\mathrm{DDSO}}(\varepsilon, \Gamma)$ is not a second order approximation of the real self-energy as in the DSO but it is a function of the variable Γ. These corrections come into play through the dressed elements of $\mathcal{N}_{\mathrm{DDSO}}$:

$$\tilde{a}_1^{\sigma 0}(\varepsilon) = \sum_{l_1} \int_{-\infty}^{+\infty} d\varepsilon_1 \, \frac{\bar{\alpha}_{l_1,\sigma}(\varepsilon_1)\, f^{-}_{l_1}(\varepsilon_1)}{\varepsilon - \varepsilon_1 + i\eta - B_1^{\sigma 0}(\varepsilon, \varepsilon_1)} \tag{2.20a}$$

$$\tilde{a}_2^{\sigma 0}(\varepsilon) = \sum_{l_1} \int_{-\infty}^{+\infty} d\varepsilon_1 \, \frac{\bar{\alpha}_{l_1,\bar{\sigma}}(\varepsilon_1)\, f^{+}_{l_1}(\varepsilon_1)}{\varepsilon + \varepsilon_1 - E_{20} + i\eta - B_2^{\sigma 0}(\varepsilon, \varepsilon_1)} \tag{2.20b}$$

$$\tilde{a}_{3(4)}^{\sigma 0}(\varepsilon) = \sum_{l_1} \int_{-\infty}^{+\infty} d\varepsilon_1 \, \frac{\bar{\alpha}_{l_1,\sigma'}(\varepsilon_1)\, f^{+}_{l_1}(\varepsilon_1)}{\varepsilon - \varepsilon_1 + i\eta - B_{3(4)}^{\sigma 0}(\varepsilon, \varepsilon_1)}, \tag{2.20c}$$

where we grouped the $\tilde{a}_{3(4)}^{\sigma 0}(\varepsilon)$ in the last line for $\sigma' = \sigma\,(\bar{\sigma})$ correspondingly. Moreover we have introduced the $B_i^{\sigma 0}(\varepsilon, \varepsilon_1)$ terms. In general they depend on two fermionic energies and on the parameters of the system but only linearly on the coupling strength Γ. As it is possible to notice in Eqs.(2.20) the analytic form of the $\tilde{a}_i^{\sigma 0}(\varepsilon)$ functions tends to the one of the DSO ($a_i^{\sigma 0}(\varepsilon)$) if we let $\Gamma \to 0$ in the corresponding expressions since $B_i^{\sigma 0}(\varepsilon, \varepsilon_1) \to 0$ in this limit. This is indeed the effect of dressing the Nucleus of the DSO and the corrections to the DSO are entirely captured through the $B_i^{\sigma 0}(\varepsilon, \varepsilon_1)$ functions. Their analytic expression is captured through the set of *Nuclei of the second dressing* ($\{\, \mathcal{N}^i_{\mathrm{2nd}},\, 1 \le i \le 4 \,\}$). Indeed, for every $\tilde{a}_i^{\sigma 0}$ function, we have to

specify a Nucleus of the second dressing

$$\mathcal{N}^{1}_{\text{2nd}} = \left\{ \quad , \quad \right\}, \tag{2.21a}$$

$$\mathcal{N}^{2}_{\text{2nd}} = \left\{ \quad , \quad \right\}, \tag{2.21b}$$

$$\mathcal{N}^{3(4)}_{\text{2nd}} = \left\{ \quad , \quad \right\}, \tag{2.21c}$$

where we dropped the fermionic lines labels for shortness in the notation reporting the dot's quantum number after the corresponding vertex. In Eq.(2.21a) and Eq.(2.21b) we grouped the diagrams with respect to the spin index (σ_1) in $\mathcal{N}^{1}_{\text{2nd}}$ and $\mathcal{N}^{2}_{\text{2nd}}$. Moreover, in Eq.(2.21c), we gathered the Nuclei $\mathcal{N}^{3(4)}_{\text{2nd}}$ corresponding respectively to $\sigma_1 = \sigma(\bar{\sigma})$. Thus, in each Nucleus, we have four dressing diagrams that are recombined within the external vertexes of the main DSO bubble as in Fig.2.7. In total we would have to introduce sixteen complex functions $B^{\sigma 0}_{i,j}$ with $i \in \{1, \dots, 4\}$ and $j \in \{1, \dots, 4\}$ such that

$$B^{\sigma 0}_{i}(\varepsilon, \varepsilon_1) = \sum_{j=1}^{4} B^{\sigma 0}_{i,j}(\varepsilon, \varepsilon_1), \tag{2.22}$$

where $B^{\sigma 0}_{i,j}(\varepsilon, \varepsilon_1)$ is the j-th element of the i-th Nucleus of the second dressing. From here on we identify the functions $B^{\sigma 0}_{1,1(2)}$ with analytical contribution according to the first diagram in Eq.(2.21a), $B^{\sigma 0}_{1,3(4)}$ with the second diagram considering respectively $\sigma_1 = \uparrow$ ($\downarrow$). We used the same convention for the functions $B^{\sigma 0}_{2,j}$ in Eq.(2.21b). Finally the functions $B^{\sigma 0}_{3(4),j}$ corresponds to the diagrams in $\mathcal{N}^{3(4)}_{\text{2nd}}$ in Eq.(2.21c).

2.2.2 DDSO in the case of infinite Coulomb interaction

Considering the strongly interacting limit ($U \to \infty$) and the spin symmetric case ($\bar{E}_\uparrow = \bar{E}_\downarrow = \bar{E}_1$ and $\bar{\alpha}_{l,\uparrow} = \bar{\alpha}_{l,\downarrow} = \bar{\alpha}_{l_2,1}$), we can immediately realise that

Diagram	Integral form
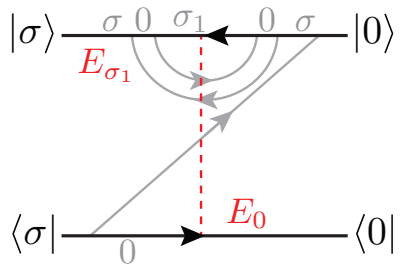	$B^{\sigma 0}_{1,1}(\varepsilon,\varepsilon_1) = B^{\sigma 0}_{1,2}(\varepsilon,\varepsilon_1) = \sum_{l_2} \int_{-\infty}^{+\infty} d\varepsilon_2 \frac{\bar{\alpha}_{l_2,1}(\varepsilon_2) f^{+}_{l_2}(\varepsilon_2)}{\varepsilon_2 - \varepsilon_1 + \varepsilon - E_{10} + i\eta}$
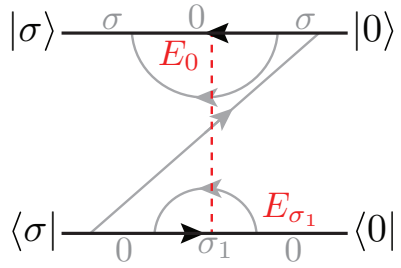	$B^{\sigma 0}_{1,3}(\varepsilon,\varepsilon_1) = B^{\sigma 0}_{1,4}(\varepsilon,\varepsilon_1) = \sum_{l_2} \int_{-\infty}^{+\infty} d\varepsilon_2 \frac{\bar{\alpha}_{l_2,1}(\varepsilon_2) f^{+}_{l_2}(\varepsilon_2)}{\varepsilon - \varepsilon_1 - \varepsilon_2 - E_{01} + i\eta}$
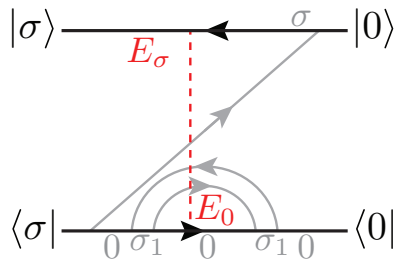	$B^{\sigma 0}_{3,1}(\varepsilon,\varepsilon_1) = B^{\sigma 0}_{4,1}(\varepsilon,\varepsilon_1) = \sum_{l_2} \int_{-\infty}^{+\infty} d\varepsilon_2 \frac{\bar{\alpha}_{l_2,1}(\varepsilon_2) f^{-}_{l_2}(\varepsilon_2)}{\varepsilon - \varepsilon_1 + \varepsilon_2 - E_{10} + i\eta}$
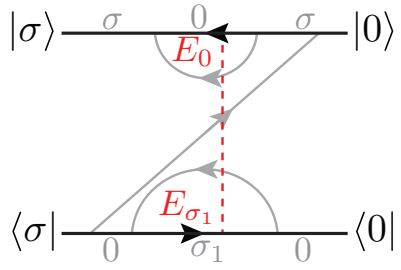	$B^{\sigma 0}_{3,3}(\varepsilon,\varepsilon_1) = B^{\sigma 0}_{4,3}(\varepsilon,\varepsilon_1) = \sum_{l_2} \int_{-\infty}^{+\infty} d\varepsilon_2 \frac{\bar{\alpha}_{l_2,1}(\varepsilon_2) f^{-}_{l_2}(\varepsilon_2)}{\varepsilon - \varepsilon_1 - \varepsilon_2 - E_{01} + i\eta}$

Table 2.4: Summary table of the integral contribution related to the elements in the Nuclei of the second dressing $\mathcal{N}^{i}_{2\text{nd}}$ with $i \in \{1,\dots,4\}$: on the left we show the diagram with the cut (red dashed line) that determines the denominator of the integral expression on the right.

$\frac{b^{\sigma 0}_{1,1(2)}(\tilde{\varepsilon},\tilde{\varepsilon}_1)}{(\Gamma/2\pi)}$	$\sum_l \kappa_l L\left(\tilde{\varepsilon}_1-\tilde{\varepsilon}+\tilde{E}_{10},\tilde{W},l\right)$ $\left\{-\frac{\pi}{2}\left(\frac{\tilde{\varepsilon}_1-\tilde{\varepsilon}+\tilde{E}_{10}-\tilde{\mu}_l}{\tilde{W}}+i\right)+\right.$ $\left.-\left[\Psi^{(0)}\left(\frac{1}{2}+\frac{\tilde{W}}{2\pi}\right)-\Psi^{(0)}\left(\frac{1}{2}+i\frac{\tilde{\varepsilon}_1-\tilde{\varepsilon}+\tilde{E}_{10}-\tilde{\mu}_l}{2\pi}\right)\right]\right\},$
$\frac{b^{\sigma 0}_{1,3(4)}(\tilde{\varepsilon},\tilde{\varepsilon}_1)}{(\Gamma/2\pi)}$	$\sum_l \kappa_l L\left(\tilde{\varepsilon}-\tilde{\varepsilon}_1-\tilde{E}_{01},\tilde{W},l\right)$ $\left\{-\frac{\pi}{2}\left(\frac{\tilde{\varepsilon}_1-\tilde{\varepsilon}-\tilde{E}_{01}+\tilde{\mu}_l}{\tilde{W}}+i\right)+\right.$ $\left.+\left[\Psi^{(0)}\left(\frac{1}{2}+\frac{\tilde{W}}{2\pi}\right)-\Psi^{(0)}\left(\frac{1}{2}+i\frac{\tilde{\varepsilon}_1-\tilde{\varepsilon}+\tilde{E}_{01}-\tilde{\mu}_l}{2\pi}\right)\right]\right\},$
$\frac{b^{\sigma 0}_{3(4),1}(\tilde{\varepsilon},\tilde{\varepsilon}_1)}{(\Gamma/2\pi)}$	$\sum_l \kappa_l L\left(\tilde{\varepsilon}_1-\tilde{\varepsilon}+\tilde{E}_{10},\tilde{W},l\right)$ $\left\{-\frac{\pi}{2}\left(\frac{\tilde{\varepsilon}_1-\tilde{\varepsilon}+\tilde{E}_{10}-\tilde{\mu}_l}{\tilde{W}}+i\right)+\right.$ $\left.+\left[\Psi^{(0)}\left(\frac{1}{2}+\frac{\tilde{W}}{2\pi}\right)-\Psi^{(0)}\left(\frac{1}{2}+i\frac{\tilde{\varepsilon}_1-\tilde{\varepsilon}+\tilde{E}_{10}-\tilde{\mu}_l}{2\pi}\right)\right]\right\},$
$\frac{b^{\sigma 0}_{3(4),3}(\tilde{\varepsilon},\tilde{\varepsilon}_1)}{(\Gamma/2\pi)}$	$\sum_l \kappa_l L\left(\tilde{\varepsilon}-\tilde{\varepsilon}_1+\tilde{E}_{01},\tilde{W},l\right)$ $\left\{-\frac{\pi}{2}\left(\frac{\tilde{\varepsilon}_1-\tilde{\varepsilon}+\tilde{E}_{01}+\tilde{\mu}_l}{\tilde{W}}+i\right)+\right.$ $\left.-\left[\Psi^{(0)}\left(\frac{1}{2}+\frac{\tilde{W}}{2\pi}\right)-\Psi^{(0)}\left(\frac{1}{2}+i\frac{\tilde{\varepsilon}_1-\tilde{\varepsilon}+\tilde{E}_{01}-\tilde{\mu}_l}{2\pi}\right)\right]\right\},$

Table 2.5: Analytic expressions of the elements in the Nuclei of the second dressing $\mathcal{N}^i_{\rm 2nd}$ for the spin symmetric case.

the contribution of the diagrams involving the state with double occupancy tends to zero. Moreover the diagrams that differ up to a spin index give the same analytical expression. This simplifies considerably the problem since we know that $\tilde{a}_2^{\sigma 0}(\varepsilon) \to 0$ for $U \to \infty$ and thus we do not need to evaluate the analytical expression from $\mathcal{N}^2_{\text{2nd}}$. Moreover $B^{\sigma 0}_{3(4),2}(\varepsilon, \varepsilon_1)$ and $B^{\sigma 0}_{3(4),4}(\varepsilon, \varepsilon_1)$ both tend to zero in such a limit. Taking into account all these considerations we need to extract only eight contributions whose analytical contributions coincide with respect to the flip of the spin σ_1. In Tab.2.4 we show their integral forms and in Tab.2.5 the corresponding analytical expression obtained according to Sect.A.5. In Tab.2.5 it is possible to notice that the only difference between the functions $b^{\sigma 0}_{1,1(2)}(\tilde{\varepsilon}, \tilde{\varepsilon}_1)$ and $b^{\sigma 0}_{3(4),1}(\tilde{\varepsilon}, \tilde{\varepsilon}_1)$ is a sign in front of the digamma functions. The same holds true for $b^{\sigma 0}_{3(4),1}(\tilde{\varepsilon}, \tilde{\varepsilon}_1)$ with respect to $b^{\sigma 0}_{3(4),3}(\tilde{\varepsilon}, \tilde{\varepsilon}_1)$. This sign difference will be crucial in the following. Having evaluated the elements of the second dressing, in the wide bandwidth limit it is straightforward to obtain

$$B_1^{10}(\tilde{\varepsilon}, \tilde{\varepsilon}_1) = \Gamma \sum_{l=\text{L,R}} \frac{\kappa_l}{\pi} L\left(\tilde{\varepsilon}_1 - \tilde{\varepsilon}, \tilde{W}\right) \left[-\pi \left(\frac{\tilde{\varepsilon}_1 - \tilde{\varepsilon}}{\tilde{W}} + i \right) + \right.$$
$$\left. + \Psi^{(0)}\left(\frac{1}{2} + i \frac{\tilde{\varepsilon}_1 - \tilde{\varepsilon} + \tilde{E}_{10} - \tilde{\mu}_l}{2\pi} \right) - \Psi^{(0)}\left(\frac{1}{2} + i \frac{\tilde{\varepsilon}_1 - \tilde{\varepsilon} - \tilde{E}_{10} + \tilde{\mu}_l}{2\pi} \right) \right], \tag{2.23}$$

and analogously

$$B_{3(4)}^{10}(\tilde{\varepsilon}, \tilde{\varepsilon}_1) = \Gamma \sum_{l=\text{L,R}} \frac{\kappa_l}{2\pi} L\left(\tilde{\varepsilon}_1 - \tilde{\varepsilon}, \tilde{W}\right) \left[-\pi \left(\frac{\tilde{\varepsilon}_1 - \tilde{\varepsilon}}{\tilde{W}} + i \right) + \right.$$
$$\left. - \Psi^{(0)}\left(\frac{1}{2} + i \frac{\tilde{\varepsilon}_1 - \tilde{\varepsilon} + \tilde{E}_{10} - \tilde{\mu}_l}{2\pi} \right) + \Psi^{(0)}\left(\frac{1}{2} + i \frac{\tilde{\varepsilon}_1 - \tilde{\varepsilon} - \tilde{E}_{10} + \tilde{\mu}_l}{2\pi} \right) \right]. \tag{2.24}$$

Notice the strong similarity of the terms $B_1^{10}(\tilde{\varepsilon}, \tilde{\varepsilon}_1)$ and $B_{3(4)}^{10}(\tilde{\varepsilon}, \tilde{\varepsilon}_1)$ due to the aforementioned observation.
Having an integral expression expression for the self-energy (Eq.(2.19) and Eq.(2.20)) and for the rate (Eq.(2.18)) we can, using Eqs.(1.78) and (1.81), address the conductance of the system.

2.2.3 DDSO linear and differential conductance

Linear conductance In Fig.2.8 we compare the linear conductance in the DDSO theory as a function of the ratio T/T_{K}, for different E_{d} values and $eV_{\text{G}} = 0$, with the DSO and DM-NRG numerical results. As it is discussed in detail in App.B it is possible, by finding an approximation of the corrections

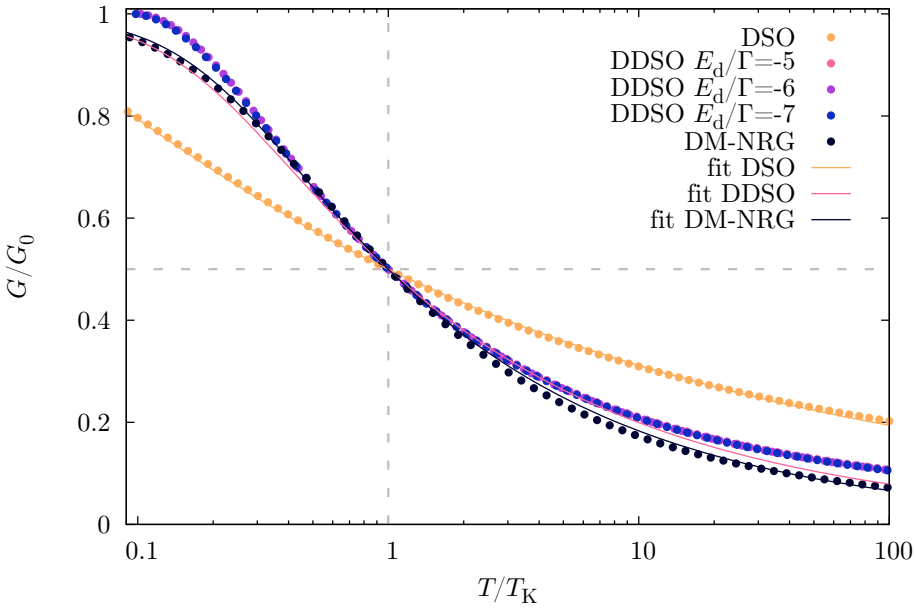

Figure 2.8: Fit (solid lines) of the DDSO linear conductance (from pink to blue circles) and DM-NRG data (black circles) as a function of the temperature normalised to the T_K of the corresponding theory with the empirical curve in Eq.(2.12). Here we reported the DSO universal curve (yellow dots) and its corresponding fit (yellow solid line) for a comparison. The DDSO data are presented for different E_d values choosing $eV_G = 0$ ($E_1 = -E_d$ and $\mu_0 = 0$), showing that the linear conductance is universal with respect to T/T_K. Here we normalised the linear conductance with respect to the corresponding maximal values: $G_0^{DSO} \simeq 0.7e^2/h$, $G_0^{DDSO} \simeq 0.73e^2/h$ and $G_0^{DM\text{-}NRG} = 2e^2/h$.

to the DSO in Eqs.(2.23) and (2.24), to extract analytically the exponential dependence of the Kondo temperature in the DDSO theory. Following the aforementioned argument in the DDSO theory we obtain

$$k_B T_K \propto \sqrt{W\Gamma} e^{-\pi \frac{\mu_0 - E_{10}}{\Gamma}}. \tag{2.25}$$

Comparing Eq.(2.25) and Eq.(2.11) we see that in the DDSO theory the proper exponential dependence is finally reproduced [22, 49]. *The DDSO theory is indeed the lowest dressing approximation that reproduces the proper Kondo temperature exponential dependence.* As we showed in App.B this is entirely due to the correction $B_1^{10}(\tilde{\varepsilon}, \tilde{\varepsilon}_1)$ that regularises the dressed $\tilde{a}_1^{10}(\tilde{\varepsilon})$ (Eq.(2.20a)) contribution to the Self-energy as $T \to 0$. Unfortunately the $\tilde{a}_{3(4)}^{10}(\tilde{\varepsilon})$ are still not regular as $T \to 0$ and thus the theory breaks down as $T/T_K \leq 0.1$. The argument in App.B is supported numerically by the

results in Fig.2.8. Indeed focusing con the DDSO numerical data in Fig.2.8 we can see that, as in the DSO theory, we obtained a universal behaviour of the linear conductance as a function of T/T_{K} for different values of E_{d} and $eV_{\mathrm{G}} = 0$. Here, fixing the Kondo temperature in such a way that $G(T/T_{\mathrm{K}} = 1) = G_0^{\mathrm{DDSO}}/2$, we found numerically

$$k_{\mathrm{B}}T_{\mathrm{K}}^{\mathrm{DDSO}} = 3.4\sqrt{W\Gamma}e^{-\pi\frac{\mu_0 - E_{10}}{\Gamma}}, \tag{2.26}$$

where the numerical pre-factor does not depend on the level position $E_{\mathrm{d}} = \mu_0 - E_{10}$. Please notice that $T_{\mathrm{K}}\left(E_{\mathrm{d}} = -5\Gamma\right)/T_{\mathrm{K}}\left(E_{\mathrm{d}} = -7\Gamma\right) \simeq 500$ and thus the values of the Kondo temperature are very different for distinct curves. Despite that the corresponding curves collapse onto the same universal temperature dependence. Moreover, in Fig.2.8, it is possible to notice that the DDSO universal curve is much closer to the DM-NRG one compared to the DSO. Indeed, fitting the DDSO numerical data with the empirical curve in Eq.(2.12), we obtained $s_{\mathrm{DDSO}} = 0.207 \pm 0.004$ that is much closer to the DM-NRG one ($s_{\text{DM-NRG}} = 0.22$), even if the DDSO numerical data do not adapt perfectly to the aforementioned empirical curve. In the DDSO we have that $s_{\mathrm{DDSO}} \simeq 2s_{\mathrm{DSO}} < s_{\text{DM-NRG}}$. This is in agreement with the analytical argument we presented in App.B in which we concluded that the DDSO linear conductance dependence on temperature is much stronger compared to the DSO one.
Of course comparing the two universal curves a significant difference is appreciable and thus we believe that much effort is still needed. We believe that the main issue here is the regularisation of the corrections $\tilde{a}^{10}_{3(4)}\left(\tilde{\varepsilon}\right)$ that in the DDSO are still not well behaved functions as $T \to 0$. However the DDSO shows the right path to be followed in order to obtain a proper description of the Kondo effect and possibly the correct zero temperature limit of the transport properties of the system.

Differential conductance In Fig.2.9 we show the differential conductance as a function of $eV/k_{\mathrm{B}}T_{\mathrm{K}}^{\mathrm{DDSO}}$ for $E_{\mathrm{d}}/\Gamma = -5$ and -6. It is easy to see that the differential conductance is universal with respect to this ratio too. Moreover we found $G\left(eV/k_{\mathrm{B}}T_{\mathrm{K}}^{\mathrm{DDSO}}\right)/G\left(0\right) \simeq 2/3 \pm 7\%$ as it was previously noticed in Refs. [50] and [29]. We can consider the whole stability diagram as a function of the gate and bias voltages in Fig.2.11(a) and 2.11(b). Here, since we considered the large Coulomb repulsion limit, we have only one charge degeneracy point and two perpendicular Coulomb blockade resonances. As in the DSO theory the Coulomb blockade resonance widths becomes proportional to the coupling energy Γ (see Fig.2.10), as we decrease the temperature. Furthermore, as we consider the *Kondo cross-over regime*, the Kondo peak is much more pronounced than in the DSO. This is due to the fact that in the DDSO the Kondo temperature is much larger than in the DSO for the same parameter set. In addition the linear conductance universal

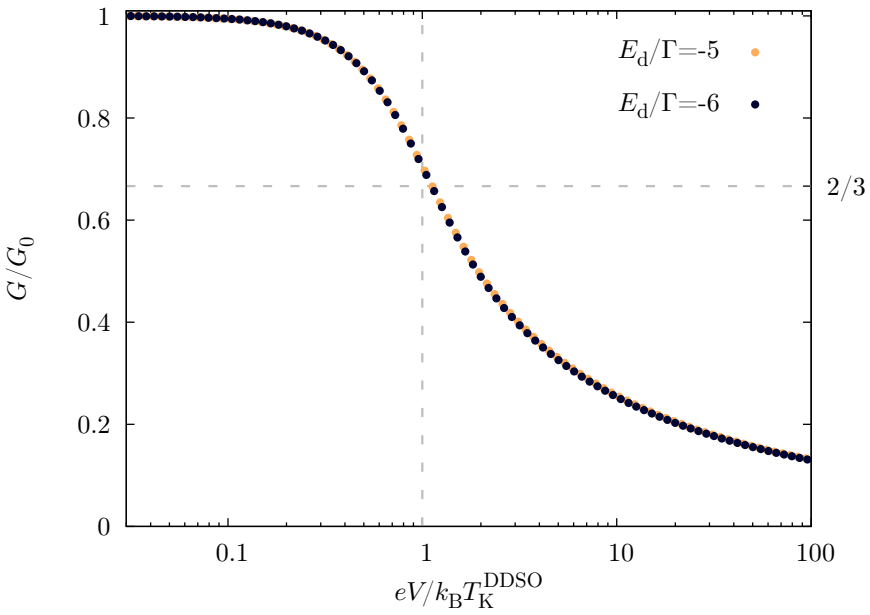

Figure 2.9: DDSO differential conductance for $k_BT/k_BT_K^{DDSO} \simeq 0.23$, $E_d/\Gamma = -5, -6$ in correspondence of $eV_G = 0$ ($E_{10} = E_d$ and $\mu_0 = 0$). The differential conductance is universal with respect to T/T_K^{DDSO}. Here we normalised the linear conductance with respect to the corresponding maximal values: $G_0^{DDSO}(E_d = -5\Gamma) \simeq 0.64e^2/h$ and $G_0^{DDSO}(E_d = -6\Gamma) \simeq 0.63e^2/h$.

curve grows faster than in the DSO as a function of the temperature.
It is important to notice that the DDSO theory is not artefact-free. Since the self energy of the DDSO is still not regular as $T \to 0$ a sharp minimum in correspondence of the charge degeneracy point appears as in the DSO. Moreover a sharp maximum appears in the so-called empty orbital regime in equilibrium, i.e. in the Coulomb valley with zero electrons. This is a new artefact that was not present in the DSO. The origin of such a peak can be traced back to the presence of a peak in the spectral function at the Fermi level in such a regime. This artefact is of the same nature of the one in the Non Crossing Approximation [49] (NCA) studied in Ref. [51]. In this paper the authors argued that this artefact is due to the fact that in the NCA the so-called vertex corrections are neglected. Since the vertex corrections are neglected in the DDSO too, in order to solve this issue and to include all the fourth order co-tunnelling processes we turn now our discussion to the inclusion of the vertex correction in the theory.

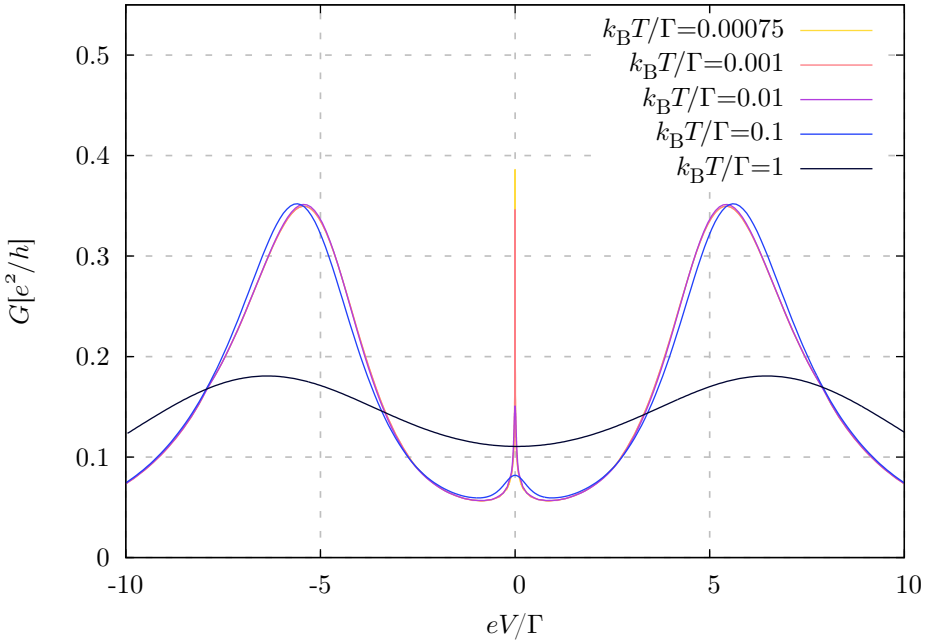

Figure 2.10: Differential conductance as a function of the applied bias for the same parameters as in Fig.2.3, in correspondence of $eV_G = 0$ and different temperatures (colour scale).

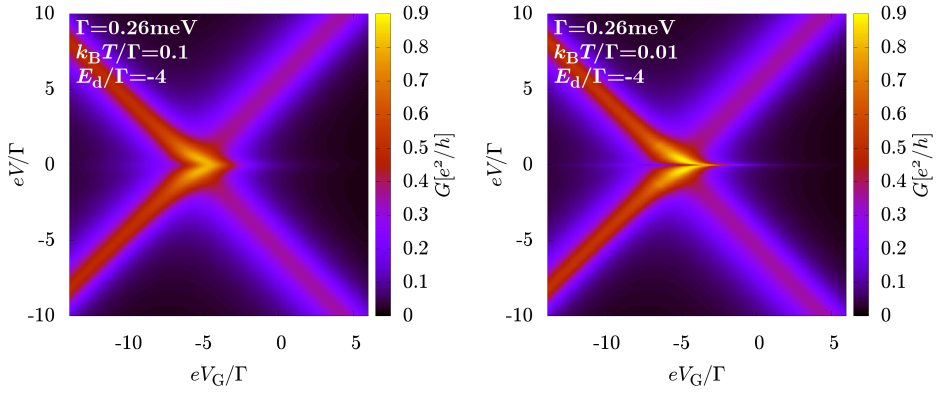

Figure 2.11: Anderson quantum dot differential conductance in the DDSO approximation as a function of the bias and gate voltages. In (a) $k_BT/\Gamma = 0.1$ and in (b) $k_BT/\Gamma = 0.01$.

CHAPTER 3

The Resonant tunnelling approximation (RTA)

In this Chapter we will present the Resonant tunnelling approximation as it was developed in Ref. [43, 44] for the metallic island and in Ref. [38, 45] for a small quantum dot with large levels spacing. Here we will follow Refs. [38] and [47], in the case of purely electronic baths, in order to include the so-called vertex corrections in the transport theory and capture completely the fourth order co-tunnelling processes. In Sect.3.1 we will introduce the general expression of the master equation, in Sect.3.2 the current and the Green functions associated to the dot operators and in Sect.3.3 we will present the two most basic blocks of diagrams in the RTA. In Sect.3.4 we will apply this formalism to a specific quantum dot model: a single level with M spin-like spices.

3.1 Master equation

Exact master equation As we have already seen for the second order, the DSO and the DDSO theories, in order to obtain the transport properties of the system, we have to obtain a master equation in terms of the rates. In contrast to the DSO and the DDSO, the RTA takes into account all the fourth order co-tunnelling processes. For this reason *we cannot "dress" the second order rates* as in the DSO and the DDSO theories in Sects.2.1 and 2.2. Instead in this Section we will obtain a formally general and exact master equation. Consequently we will apply it to a specific system with certain approximations.
As we already showed in Eq.(1.58b), we can express the time evolution of the RDM through the reduced propagator $\Pi^{b,a}_{b',a'}(t,t_0)$ from the initial time

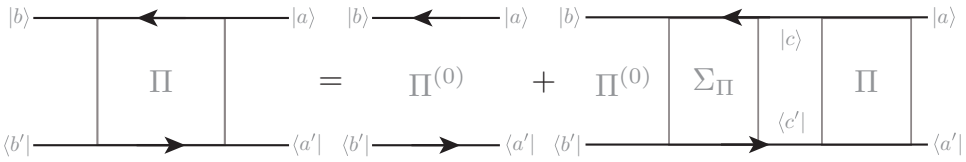

Figure 3.1: Diagrammatic representation of the iteration process defining the propagator.

t_0 to the final one t as

$$\rho^{b}_{b'}(t) = \sum_{a,a'} \Pi^{b,a}_{b',a'}(t,t_0)\,\rho^{a}_{a'}(t_0)\,, \tag{3.1}$$

Diagrammatically the propagator is the sum of all the diagrams for initial $|a\rangle, |a'\rangle$ and final $|b\rangle, |b'\rangle$ states. These states belong to the Hilbert of the quantum dot $\mathcal{H}_{\odot}$. So far no specification of the Hilbert space of the dot is needed, the formalism is general and independent on the specific dot Hilbert space choice. The propagator may be defined through a Dyson equation as we depicted in Fig.3.1. In Fig.3.1 we introduced the self-energy $\Sigma_{\Pi}{}^{b,c}_{b',c'}(t_2,t_1)$ for the propagator $\Pi^{b,a}_{a',b'}(t_0,t)$. Considering such a diagrammatic expression for every initial and final states, using the time space diagrammatic rules in Appendix A of Ref. [38], we can obtain an iterative equation for the propagator in the style of the Dyson equation

$$\begin{aligned}\Pi^{b,a}_{b',a'}(t,t_0) &= {\Pi^{(0)}}^{b}_{b'}(t,t_0)\,\delta_{a,a'}\delta_{b,b'} + \\ &+ \sum_{c,c'} \int_{t_0}^{t} dt_2 \int_{t_0}^{t_2} dt_1\, {\Pi^{(0)}}^{b}_{b'}(t,t_2)\,\Sigma_{\Pi}{}^{b,c}_{b',c'}(t_2,t_1)\,\Pi^{c,a}_{c',a'}(t_1,t_0)\,,\end{aligned} \tag{3.2}$$

where we wrote the extremes and the order of the integrations in a convenient form for the following derivation. Furthermore the free propagator matrix elements read

$${\Pi^{(0)}}^{b}_{b'}(t-t_0) = \exp\left(-iE_{bb'}(t-t_0)/\hbar\right). \tag{3.3}$$

Thus multiplying both sides of Eq.(3.2) by $\rho^{a}_{a'}(t_0)$, summing with respect to the a, a'-indexes, considering the derivative with respect to the time t and taking into account Eq.(3.1) we have

$$\dot{\rho}^{b}_{b'}(t) + \frac{i}{\hbar}E_{bb'}\rho^{b}_{b'}(t) = \sum_{c,c'} \int_{t_0}^{t} dt_1\, \Sigma_{\Pi}{}^{b,c}_{b',c'}(t,t_1)\,\rho^{c}_{c'}(t_1)\,. \tag{3.4}$$

As it is stated in Ref. [38], *this is a formally exact and general master equation for the dot RDM*: so far we did not need any assumption neither for the initial state of the RDM nor for $\Sigma_{\Pi}{}^{b,c}_{b',c'}(t,t_1)$.

Stationary ME in the case of a diagonal initial condition Despite its generality, Eq.(3.4) is merely formal and difficult to handle in practice. For this reason it is often assumed in literature that the density matrix is prepared in a diagonal state at the initial time t_0

$$\rho^a_{a'}(t_0) = \delta_{a,a'}\rho^a_a(t_0) \stackrel{\text{def}}{=} \rho_a(t_0).$$

As we have already discussed in Sect.1.1.4, for the particle number and spin conserving Anderson model, this implies that the RDM is always diagonal for all times $t > t_0$. Considering this assumption in Eq.(3.4) we have

$$\dot{\rho}_b(t) = \sum_a \int_{t_0}^{t} dt_1\, \Sigma_{\Pi b,a}(t,t_1)\,\rho_a(t_1), \tag{3.5}$$

where we defined $\Sigma_{\Pi b,a}(t,t_1) = \Sigma^{b,a}_{\Pi\, b,a}(t,t_1)\,\delta_{a',a}\delta_{b',b}$. Thus setting $t_0 = 0$, considering the Laplace transform of Eq.(3.5) in the stationary limit ($\lambda \to 0$) and exploiting the final value theorem, as we already showed in Sect.1.1.4, we have

$$\sum_a \Sigma^{\infty}_{\Pi\, b,a}\rho^{\infty}_a = 0, \tag{3.6}$$

where we defined the stationary Laplace transformed self-energy and populations respectively

$$\Sigma^{\infty}_{\Pi\, b,a} = \lim_{\lambda\to 0} \mathscr{L}\left\{\Sigma_{\Pi b,a}(\tau)\right\}(\lambda) \tag{3.7a}$$

$$\rho^{\infty}_a = \lim_{\lambda\to 0} \lambda\rho_a(\lambda) = \lim_{t\to+\infty} \rho_a(t). \tag{3.7b}$$

In Eq.(3.7a) we performed the Laplace transform with respect to the time difference since, in case of time translationally invariant systems as our system in the stationary limit, $\Sigma_{\Pi b,a}(t,t_1) = \Sigma_{\Pi b,a}(t-t_1)$. The matrix elements $\Sigma^{\infty}_{\Pi\, b,a}$ may be computed with our diagrammatic rules in App.A.3 and, as we have already seen in Sect.1.2, they are real since they are always composed of hermitian conjugated terms. As it is discussed in App.A.6 the self-energy obeys the following sum rule [38]

$$\sum_b \Sigma_{\Pi b,a}(\lambda) = 0. \tag{3.8}$$

Considering the inverse Laplace transform of $\Sigma_{\Pi b,a}(\lambda)$ in Eq.(3.8),

$$\sum_b \Sigma_{\Pi b,a}(t-t_1) = 0,$$

one finds out that the physical meaning of Eq.(3.8) is actually the RDM trace conservation (see Eq.(3.5)), i.e. given an initial RDM whose trace is one we have $\sum_b \rho_b(t) = 1$ for any $t > t_0$.

3.2 Current and Green functions

In this Section we will consider the thermal average of dot operators as

$$\left\langle \hat{A}_{\mathrm{H}}(t) \right\rangle = \mathsf{Tr}\left\{ \hat{\rho}(t_0)\, \hat{A}_{\mathrm{H}}(t) \right\}, \tag{3.9a}$$

$$\left\langle \hat{A}_{\mathrm{H}}(t_1)\, \hat{B}_{\mathrm{H}}(t_2) \right\rangle = \mathsf{Tr}\left\{ \hat{\rho}(t_0)\, \hat{A}_{\mathrm{H}}(t_1)\, \hat{B}_{\mathrm{H}}(t_2) \right\}, \tag{3.9b}$$

where we introduced the Heisenberg picture $\hat{X}_{\mathrm{H}}(t) = \hat{U}^{\dagger}(t,t_0)\, \hat{X}(t_0) \hat{U}(t,t_0)$ and $\hat{U}(t,t_0)$ is the full time evolution operator as in Sect.1.1.4. It fruitful to distinguish in the diagrammatic language between *internal vertexes*, coming from the expansion of the time evolution operators and *external vertexes* corresponding to the $\hat{A}$ and $\hat{B}$ operators. Having this distinction in mind, to evaluate the current flowing out of the l-lead we have to consider Eq.(3.9a) with $\hat{A}_{\mathrm{H}}(t) = \hat{d}^{\dagger}_{\sigma,\mathrm{H}}(t)\, \hat{c}_{l,\sigma,\mathbf{k},\mathrm{H}}(t)$ and the hermitian conjugated term:

$$I_l(t) = \mathsf{Tr}\left\{ \hat{I}_{l,\mathrm{H}}(t)\, \hat{\rho}(t_0) \right\} = \mathsf{Tr}\left\{ \hat{U}^{\dagger}_{\mathrm{I}}(t,t_0)\, \hat{I}_{l,\mathrm{I}}(t)\, \hat{U}_{\mathrm{I}}(t,t_0)\, \hat{\rho}(t_0) \right\} = \tag{3.10a}$$

$$= -i\frac{e}{\hbar} \sum_{\sigma,\mathbf{k}} T_{l,\sigma,\mathbf{k}} \mathsf{Tr}\left\{ \hat{\rho}(t_0)\, \hat{\mathsf{T}}_{\mathrm{K}} e^{-i\int_{\mathrm{K}} \frac{d\tau}{\hbar} \hat{H}_{\mathrm{T,I}}(\tau)} \hat{d}^{\dagger}_{\sigma,\mathrm{I}}(t)\, \hat{c}_{l,\sigma,\mathbf{k},\mathrm{I}}(t) \right\} + \text{h.c.} =$$

$$= -i\frac{e}{\hbar} \sum_{\sigma,\mathbf{k}} T_{l,\sigma,\mathbf{k}} \sum_{a,a',b,b'} \rho^{a}_{a'}(t_0)\, \mathsf{Tr}_{\mathrm{RS}}\Bigg\{ \hat{\rho}_{\mathrm{RS}}(t_0) \tag{3.10b}$$

$$\left\langle a'(t_0) \left| \hat{\mathsf{T}}^{(-)} \exp\left(i\int_{t_0}^{t} d\tau \hat{H}_{\mathrm{T,I}}(\tau)/\hbar \right) \right| b'(t) \right\rangle \left\langle b'(t) \left| \hat{d}^{\dagger}_{\sigma} \right| b(t) \right\rangle$$

$$\hat{c}_{l,\sigma,\mathbf{k}} \left\langle b(t) \left| \hat{\mathsf{T}}^{(+)} \exp\left(-i\int_{t_0}^{t} d\tau \hat{H}_{\mathrm{T,I}}(\tau)/\hbar \right) \right| a(t_0) \right\rangle \Bigg\} + \text{h.c.} =,$$

$$= e \sum_{a,a',b,b'} \left(\Pi^{l,-}_{\mathrm{I}} \right)^{b\ ,a}_{b',a'} (t,t_0)\, \rho^{a}_{a'}(t_0) \tag{3.10c}$$

$$= -e \sum_{a,a',b,b'} \left(\Pi^{l,+}_{\mathrm{I}} \right)^{b\ ,a}_{b',a'} (t,t_0)\, \rho^{a}_{a'}(t_0) \tag{3.10d}$$

where we introduced the Keldysh time ordering operator $\hat{\mathsf{T}}_{\mathrm{K}}$ and we wrote the integral on the Keldysh contour in such a way that the time evolution operator propagates the states forward in time, on the upper contour, from t_0 to t and backward, on the lower contour, from t to t_0 as we wrote explicitly in Eq.(3.10b). Moreover in Eq.(3.10c) we defined the reduced propagators for the current in the l-lead $\Pi^{l,\pm}_{\mathrm{I}}(t,t_0)$. In Eq.(3.10b) it is easy to see that actually these reduced propagators are composed of only one subclass of processes contained in the propagator $\Pi(t,t_0)$ (see Eq.(1.58b)). Here indeed

we defined $\Pi_{\mathrm{I}}^{l,-}(t,t_0)(\Pi_{\mathrm{I}}^{l,+}(t,t_0))$ as the propagator with the latest incoming tunnelling event on the upper(lower) Keldysh contour or outgoing on the lower(upper) one. This can be readily seen expanding the time(anti-time) ordered evolution operators in Eq.(1.58b) and match all the terms with the expansions from Eqs.(3.10c) and (3.10d).
Thus, repeating the same steps as in Sect.3.1, we have

$$I_l(t) = -e\frac{\mathrm{d}}{\mathrm{d}t}\left\langle \hat{N}_{l,\mathrm{H}}(t)\right\rangle = e\sum_{a,b}\int_{t_0}^{t} dt_1 \Sigma_{\Pi_{b,a}}^{l,-}(t,t_1)\,\rho_a(t_1) = \tag{3.11a}$$

$$= -e\sum_{a,b}\int_{t_0}^{t} dt_1 \Sigma_{\Pi_{b,a}}^{l,+}(t,t_1)\,\rho_a(t_1)\,, \tag{3.11b}$$

where $\Sigma_{\Pi_{b,a}}^{l,-}(\Sigma_{\Pi_{b,a}}^{l,+})$ is the self-energy of the $\Pi_{\mathrm{I}}^{-,l}(\Pi_{\mathrm{I}}^{l,+})$ propagator. Moreover we have

$$\Sigma_{\Pi b,a}(t,t_1) = \sum_{l=\mathrm{L,R}}\left[\Sigma_{\Pi_{b,a}}^{l,-}(t,t_1) + \Sigma_{\Pi_{b,a}}^{l,+}(t,t_1)\right], \tag{3.12}$$

where $\Sigma_{\Pi_{b,a}}^{l,-}(\Sigma_{\Pi_{b,a}}^{l,+})$ describes processes with the leftmost incoming vertex on the upper(lower) Keldysh contour or outgoing on the lower(upper) one (hermitian conjugated terms). They represent the total contribution to the current rate. In contrast to the rates we defined in Sect.1.2 these are sum of many particles tunnelling events. Considering the Laplace transform of Eqs.(3.11) we have straightforwardly

$$I_l^{\infty} = e\sum_{a,b}\Sigma_{\Pi_{b,a}}^{l,-}\rho_a^{\infty} \tag{3.13a}$$

$$= -e\sum_{a,b}\Sigma_{\Pi_{b,a}}^{l,+}\rho_a^{\infty}, \tag{3.13b}$$

where we defined the stationary current $I_l^{\infty} = \lim_{\lambda\to 0}\lambda\mathscr{L}\{I_l(t)\}(\lambda)$ and $\Sigma_{\Pi_{b,a}}^{l,\pm} = \mathscr{L}\left\{\Sigma_{\Pi_{b,a}}^{l,\pm}(t-t_1)\right\}(\lambda=0)$. The components $\Sigma_{\Pi_{b,a}}^{l,\pm}$ can be calculated with our diagrammatic rules for the current Kernel in Sect.1.1.5. Indeed, considering for example $\Sigma_{\Pi_{b,a}}^{l,-}$, we can depict Eq.(3.13a) diagrammatically as

follows

$$I_l^{\infty} = e \sum_{a,b,c} \left(\right. \quad - \quad \left. \right) \rho_a^{\infty} =$$

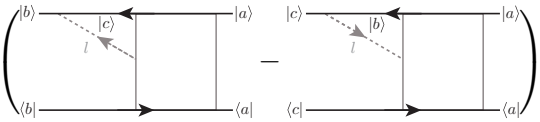

$$= e \sum_{a,b,c} \left(\right. \quad + \quad \left. \right) \rho_a^{\infty} =$$

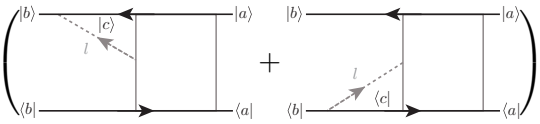

$$= e \sum_{a,b,c} 2\mathrm{Re} \left\{ \right. \left. \right\} \rho_a^{\infty}, \tag{3.14}$$

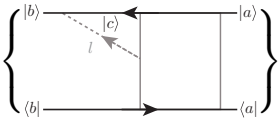

where we used the fact that if we switch the leftmost vertex from the upper to the lower contour preserving all the other characteristic of the diagram yields a minus sign multiplication and we recognized that the diagrams are hermitian conjugated in the second line (assuming from the beginning that the grey boxes in the first term and in the second one are hermitian conjugated in all the steps). Moreover in Eq.(3.14) we depicted explicitly only the external vertex, i.e. the leftmost at time t, depicting implicitly the internal ones in the grey square box. Eq.(3.14) shows that $\Sigma_{\Pi_{b,a}}^{l,-}$ and, analogously, $\Sigma_{\Pi_{b,a}}^{l,+}$ are real. Thus our procedure will always yield a real current I_l^{∞}.
Let us stress that Eqs.(3.6) and (3.13) represent a *complete general transport theory*, i.e. both the current and the populations of the system can be obtained from such equations provided that the aforementioned total rates are known. Nevertheless it is worth to link this language to the well established language of the Green functions. For this reason, in the following we will turn our discussion to the calculation of the so-called Green functions of the system.

Green functions The so-called greater(lesser) Green function [52] of the dot operators can be considered choosing $\hat{A}_{\mathrm{H}}(t) = -i\hat{d}_{\sigma,\mathrm{H}}(t)/\hbar (\hat{A}_{\mathrm{H}}(t) = i\hat{d}_{\sigma,\mathrm{H}}^{\dagger}(t))$ and $\hat{B}_{\mathrm{H}}(t') = \hat{d}_{\sigma,\mathrm{H}}^{\dagger}(t') (\hat{B}_{\mathrm{H}}(t') = \hat{d}_{\sigma,\mathrm{H}}(t'))$ in Eq.(3.9) correspondingly:

$$G_{\sigma}^{>}\left(t,t'\right) = -\frac{i}{\hbar}\left\langle \hat{d}_{\sigma,\mathrm{H}}\left(t\right)\hat{d}_{\sigma,\mathrm{H}}^{\dagger}\left(t'\right)\right\rangle, \tag{3.15a}$$

$$G_{\sigma}^{<}\left(t,t'\right) = \frac{i}{\hbar}\left\langle \hat{d}_{\sigma,\mathrm{H}}^{\dagger}\left(t'\right)\hat{d}_{\sigma,\mathrm{H}}\left(t\right)\right\rangle. \tag{3.15b}$$

They are not related to each other since we are considering the dot out-of-equilibrium. Nevertheless in the stationary limit, when the system is time-translational invariant by definition, they depend only on the time difference $G^{>(<)}\left(t,t'\right) = G^{>(<)}\left(t-t'\right)$. Thus we can consider the Fourier

transform of such functions

$$G_\sigma^{>}(\varepsilon) = \int_{-\infty}^{+\infty} d\tau e^{i\frac{\varepsilon\tau}{\hbar}} G_\sigma^{>}(\tau) = \int_{0}^{+\infty} d\tau \left[e^{i\frac{\varepsilon\tau}{\hbar}} G_\sigma^{>}(\tau,0) + e^{-i\frac{\varepsilon\tau}{\hbar}} G_\sigma^{>}(0,\tau) \right], \tag{3.16a}$$

$$G_\sigma^{<}(\varepsilon) = \int_{-\infty}^{+\infty} d\tau e^{i\frac{\varepsilon\tau}{\hbar}} G_\sigma^{<}(\tau) = \int_{0}^{+\infty} d\tau \left[e^{i\frac{\varepsilon\tau}{\hbar}} G_\sigma^{<}(\tau,0) + e^{-i\frac{\varepsilon\tau}{\hbar}} G_\sigma^{<}(0,\tau) \right]. \tag{3.16b}$$

In order to compute these Green functions it is useful to rewrite Eqs.(3.16) as follows

$$G_\sigma^{>}(\varepsilon) = 2i\mathsf{Im}\left\{ \int_{0}^{+\infty} d\tau e^{i\frac{\varepsilon\tau}{\hbar}} G_\sigma^{>}(\tau,0) \right\}, \tag{3.17a}$$

$$G_\sigma^{<}(\varepsilon) = 2i\mathsf{Im}\left\{ \int_{0}^{+\infty} d\tau e^{i\frac{\varepsilon\tau}{\hbar}} G_\sigma^{<}(\tau,0) \right\}, \tag{3.17b}$$

where we used the following relations

$$G_\sigma^{>}(0,\tau) = -\left[G_\sigma^{>}(\tau,0)\right]^*, \qquad G_\sigma^{<}(0,\tau) = -\left[G_\sigma^{<}(\tau,0)\right]^*.$$

They can be demonstrated using $\mathsf{Tr}\{\hat{A}\} = \mathsf{Tr}\{\hat{A}^{\mathrm{t}}\}$ and the hermiticity of the density matrix. Repeating the same procedure we adopted to obtain the diagrammatic representation of the current in the previous paragraph, for the case of two external vertexes (see Eq.(3.9b)), we can obtain a pictorial representation of the Green functions in Eq.(3.17),

$$G_\sigma^{>}(\varepsilon) = -2i\hbar\mathsf{Re}\left\{ \sum_{a,b} \right.$$

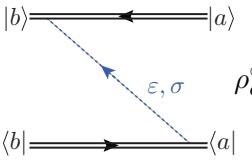

$$\left. \rho_a^\infty \right\}, \tag{3.18a}$$

$$G_\sigma^{<}(\varepsilon) = \quad 2i\hbar\mathsf{Re}\left\{ \sum_{a,b} \right.$$

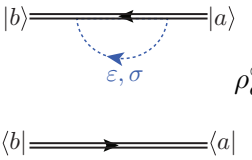

$$\left. \rho_a^\infty \right\}. \tag{3.18b}$$

In Eq.(3.18) we depicted only the external vertexes and we indicated the full time propagation with double lines along the Keldysh contours. We will consider explicitly the internal ones in Sect.3.4. We can extract the contribution of the corresponding diagram using our diagrammatic rules for the current Kernel where the number of vertexes q on the lower contour has

to be counted with respect to internal vertexes, disregarding the external ones. Moreover, since the external vertexes have no paired creation(annihilation) operator of the leads electrons, in the corresponding diagrammatic rules we have to disregard the Fermi function, the energy $\bar{\alpha}_{l,\sigma}(\varepsilon)$ and the integration with respect to the energy ε of the blue dashed fermion line that connects the two external vertexes. For this reason the unit of measure of the diagram for a Green function are $\left[\mathrm{eV}^{-2}\mathrm{sec}^{-1}\right]$ instead of the usual $\left[\mathrm{sec}^{-1}\right]$ for the rates diagrams.
It is not difficult to see, comparing the diagrammatic expression for the current and the one for the Green functions (Eqs.(3.18)), that they have the same structure. Indeed the leftmost external vertex can be contracted throughout a tunnelling line to the lower or to the upper Keldysh contour recovering immediately the same kind of diagrams defining the Green functions in Eq.(3.18). This means that we can rewrite the current in terms of the quantum dot Green functions

$$I_l^{\infty} = 2e\mathrm{Re}\left\{ \sum_{a,b} \right.$$

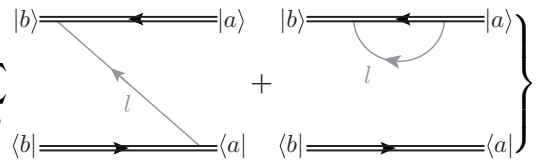

$$\left.\right\}$$

$$= 2e\sum_{\sigma}\int_{-\infty}^{+\infty} d\varepsilon \left[\gamma_{l,\sigma}^{+}(\varepsilon)\,\mathrm{Re}\left\{ \sum_{a,b} \right.\right.$$

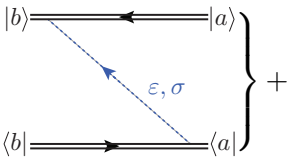

$$\left.\left. -\gamma_{l,\sigma}^{-}(\varepsilon)\,\mathrm{Re}\left\{ \sum_{a,b} \right.\right.\right.$$

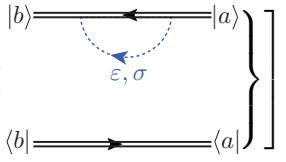

$$\left.\left.\right\}\right]$$

$$= \frac{ie}{\hbar}\sum_{\sigma}\int_{-\infty}^{+\infty} d\varepsilon \left[\gamma_{l,\sigma}^{+}(\varepsilon)\,G_{\sigma}^{>}(\varepsilon) + \gamma_{l,\sigma}^{-}(\varepsilon)\,G_{\sigma}^{<}(\varepsilon)\right], \tag{3.19}$$

where we introduced $\gamma_{l,\sigma}^{\pm}(\varepsilon) = \bar{\alpha}_{l,\sigma}(\varepsilon)\, f_l^{\pm}(\varepsilon)$. Here we adopted the same convention for the current diagrams we introduced above for the Green functions ones, i.e. we reported the full time propagation with double lines along the Keldysh contours. Eq.(3.19) is a powerful expression indicating that, in an interacting system, the knowledge of the greater and lesser Green functions gives full access to its transport characteristics. Such an expression was actually already obtained in Refs. [53–57] exploiting diverse formalisms. Assuming that the density of states energy dependence in the leads is the same up to a constant multiplicative factor $\bar{\alpha}_{\sigma,l}(\varepsilon)/\bar{\alpha}_{\sigma,\bar{l}}(\varepsilon) = \kappa_l$, i.e. we assume proportional coupling to the leads, we can recast it in the more

familiar form [55–57]

$$I_l^{\infty} = -\frac{e}{\hbar}\sum_{\sigma}\int_{-\infty}^{+\infty} d\varepsilon\, \frac{\Gamma_{l,\sigma}(\varepsilon)\,\Gamma_{\bar{l},\sigma}(\varepsilon)}{\Gamma_{l,\sigma}(\varepsilon)+\Gamma_{\bar{l},\sigma}(\varepsilon)} A_{\sigma}(\varepsilon)\left[f_{\bar{l}}^{+}(\varepsilon)-f_{l}^{+}(\varepsilon)\right], \tag{3.20}$$

just adding to Eq.(3.19) $I_l^{\infty}+I_{\bar{l}}^{\infty}=0$ and exploiting the proportional coupling assumption. In Eq.(3.20) we introduced $\Gamma_{l,\sigma}(\varepsilon)=2\pi\bar{\alpha}_{l,\sigma}(\varepsilon)$ and the spectral function [52]

$$A_{\sigma}(\varepsilon)=\frac{G_{\sigma}^{<}(\varepsilon)-G_{\sigma}^{>}(\varepsilon)}{2\pi i}. \tag{3.21}$$

So far we have developed a general formalism, now we turn our discussion to the implementation of this machinery to a specific model and with certain approximations.

3.3 Intermezzo: building block diagrams in the RTA

In order to proceed further we need to introduce the most basic blocks for the diagrammatic representation of the time evolution in the RTA. Since in the RTA one takes into account all the diagrams such that we have at most two intersections per vertical cut we need to introduce two fundamental blocks of diagrams [47]:

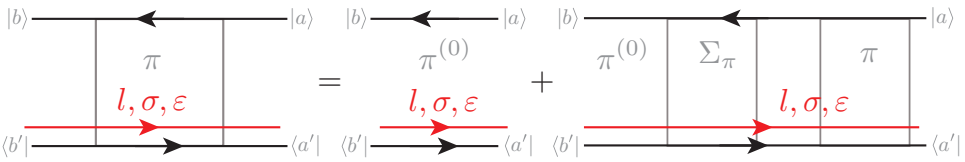

Figure 3.2: Diagrammatic iterative definition of the propagation ($\pi(\varepsilon)$) in parallel to a fermion line (red line).

1- Propagation in parallel to another tunnelling line The propagator $\pi_{b',a'}^{b,a}(\varepsilon)$ in Fig.3.2 represents the time evolution while in parallel a fermion line runs from left to right; the diagram with a parallel fermion line running from right to left ($\pi^{*}{}_{b,a}^{b',a'}(\varepsilon)$) is related to it by the mirror rule. The fermion line running parallel to the propagation due to $\pi(\varepsilon)$ will not be involved with its tunnelling events, i.e. $\pi(\varepsilon)$ "dresses" the main fermion line depicted in red in Fig.3.2. It is easy to see that this kind of diagrams were already included in the DSO and DDSO theories. As we will see, the self-energy $\Sigma_{\pi}(\varepsilon)$ will be the same as in the DSO. Indeed, as the main propagator Π, also π can be expressed through a Dyson equation (Fig.3.2). In matrix notation we can write

$$\pi(\varepsilon)=\pi^{(0)}(\varepsilon)+\pi^{(0)}(\varepsilon)\,\Sigma_{\pi}(\varepsilon)\,\pi(\varepsilon), \tag{3.22}$$

where, using the diagrammatic rules in the energy space, we have

$$\pi^{(0)}{}^{a}_{a'}(\varepsilon) = \frac{1}{\varepsilon - E_{aa'} + i\eta}\delta_{ab}\delta_{a'b'}.$$

Here, in analogy to $\Sigma_{\Pi}(\varepsilon)$, $\Sigma_{\pi}(\varepsilon)$ is the self-energy of the $\pi(\varepsilon)$ propagator. Eq.(3.22) can be solved, provided that the inversion operation is allowed, yielding

$$\pi(\varepsilon) = \left\{ \left[\pi^{(0)}(\varepsilon) \right]^{-1} - \Sigma_{\pi}(\varepsilon) \right\}^{-1}. \tag{3.23}$$

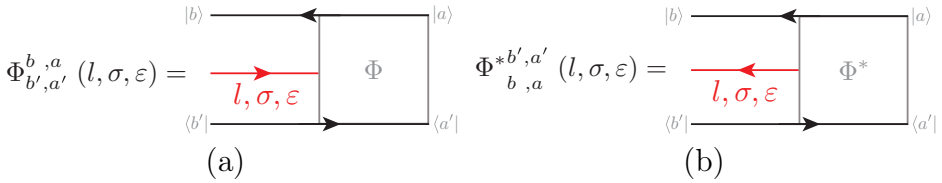

Figure 3.3: Diagrammatic representation of the propagation Φ in (a) and Φ^* in (b) involving an open incoming(outgoing) tunnelling line (red solid line). The two diagrams are related by the mirror rule.

2- Propagation involving an open tunnelling line The irreducible diagram $\Phi^{b,a}_{b',a'}(l,\sigma,\varepsilon)$ ($\Phi^{*b',a'}_{b,a}(l,\sigma,\varepsilon)$) in Fig.3.3(a)(Fig.3.3(b)) has an open incoming(outgoing) tunnelling line carrying the lead (l), spin (σ) and energy (ε) indexes of the lead electrons. Furthermore $\Phi^{b,a}_{b',a'}(l,\sigma,\varepsilon)$ and ($\Phi^{*b',a'}_{b,a}(l,\sigma,\varepsilon)$) are related by the mirror rule, i.e. they are hermitian conjugated, as it is possible to appreciate in Fig.3.3(a) and 3.3(b). The incoming(outgoing) tunnelling line will be involved in the tunnelling processes included in $\Phi^{b,a}_{b',a'}(l,\sigma,\varepsilon)$ ($\Phi^{*b',a'}_{b,a}(l,\sigma,\varepsilon)$) and thus there will be a vertex defining the beginning of this tunnelling line included in the processes described by this diagram. For this reason one may argue that the so-called vertex corrections are included in this diagram. Indeed $\Phi^{b,a}_{b',a'}(l,\sigma,\varepsilon)$ transform a bare vertex, that is the simplest way to define the beginning of a fermion line, in a much richer structure of tunnelling events, i.e. it "dresses" the bare vertex with a fixed structure defined by an iterative equations for $\Phi^{b,a}_{b',a'}(l,\sigma,\varepsilon)$. As we will see in detail in the next Section, only the first step of the iteration defining this diagrams was included in the DSO and DDSO theories, i.e. $\Phi^{b,a}_{b',a'}(l,\sigma,\varepsilon)$ in the previous Sections was just a bare vertex times the contribution deriving from the main fermion line and its dressing $\pi(\varepsilon)$.

We have now all the formal ingredients to study the transport properties within the RTA. In the following we shall see the effects due to the inclusion of the vertex corrections on the transport properties of the system.

3.4 RTA in the case of strong interactions

So far we have developed a general formalism to deal with the transport properties of a quantum dot. In this Section we will show an application of this general formalism to the case of a strongly interacting quantum dot ($U \to \infty$). We will thus forbid the double occupation in the quantum dot. Indeed as we have already seen in the previous Chapter, in the strong interacting limit the states with double occupancy do not contribute since their corresponding total rates scales as $1/U$. Let us stress that it is possible to develop the RTA also for the case with finite Coulomb interaction but the strongly interacting limit simplifies considerably the discussion and it shows already the essence of the RTA theory. Thus, having all these consideration in mind, in this Section we will focus on two cases:

M **degenerate one particle levels:** $\mathcal{H}^1_\odot = \{ |0\rangle, |1\rangle, \ldots, |M\rangle \}$. In this case the Hamiltonian of the dot reads

$$\hat{H}_\odot = \sum_{\sigma=1,\ldots,M} (E_\sigma - e k_{\mathrm{G}} V_{\mathrm{G}})\, \hat{d}^\dagger_\sigma \hat{d}_\sigma + U \sum_{\sigma>\sigma'} \hat{d}^\dagger_\sigma \hat{d}_\sigma \hat{d}^\dagger_{\sigma'} \hat{d}_{\sigma'}, \tag{3.24}$$

$M = 2$ **non degenerate one particle levels:** $\mathcal{H}^2_\odot = \{ |0\rangle, |1\rangle, |2\rangle \}$. In this case the Hamiltonian in Eq.(3.24) reduces to the one in Eq.(1.16).

3.4.1 RTA transport equations

In order to get access to the transport characteristics of the system let us consider Eqs.(3.13) and (3.6). In the non degenerate case with $M = 2$, i.e. considering $\mathcal{H}^2_\odot$, the master equation reads

$$\boldsymbol{\Sigma}^\infty_\Pi . \boldsymbol{\rho}^\infty = \mathbb{0} \quad \Rightarrow \quad \begin{cases} \Sigma^\infty_{\Pi\, 0,0}\rho^\infty_0 + \sum_\sigma \Sigma^\infty_{\Pi\, 0,\sigma}\rho^\infty_\sigma = \mathbb{0}_0, \\ \Sigma^\infty_{\Pi\, \sigma_1,0}\rho^\infty_0 + \sum_\sigma \Sigma^\infty_{\Pi\, \sigma_1,\sigma}\rho^\infty_{\sigma_1} = \mathbb{0}_{\sigma_1}, \end{cases} \tag{3.25}$$

where the linear system of equations is singular because of the sum-rule in Eq.(3.8) that guarantees the total probability conservation (see App.A.6). For $E_\uparrow \neq E_\downarrow$ the rank of the matrix $\boldsymbol{\Sigma}^\infty_\Pi$ is two and, assuming an initial density matrix such that $\sum_a \rho_a(t_0) = 1$, we substitute the $\sigma = \downarrow$ equation with the condition represented by this sum-rule: $\sum_a \rho^\infty_a = 1$[1]. The solution

[1] Alternatively we could have searched for a vector in the Null-space of the matrix $\boldsymbol{\Sigma}^\infty_\Pi$ and then normalize the solution (the dimension of the Null-space for $E_\uparrow \neq E_\downarrow$ is one).

of the corresponding linear system of equations,

$$\mathbf{M}.\boldsymbol{\rho}^{\infty} = \begin{pmatrix} \Sigma^{\infty}_{\Pi\,0,0} & \Sigma^{\infty}_{\Pi\,0,\uparrow} & \Sigma^{\infty}_{\Pi\,0,\downarrow} \\ \Sigma^{\infty}_{\Pi\,\uparrow,0} & \Sigma^{\infty}_{\Pi\,\uparrow,\uparrow} & \Sigma^{\infty}_{\Pi\,\uparrow,\downarrow} \\ 1 & 1 & 1 \end{pmatrix} \cdot \begin{pmatrix} \rho^{\infty}_{0} \\ \rho^{\infty}_{\uparrow} \\ \rho^{\infty}_{\downarrow} \end{pmatrix} = \begin{pmatrix} 0 \\ 0 \\ 1 \end{pmatrix},$$

yields the stationary populations as a function of the total rates

$$\begin{pmatrix} \rho^{\infty}_{0} \\ \rho^{\infty}_{\uparrow} \\ \rho^{\infty}_{\downarrow} \end{pmatrix} = \frac{1}{\det \mathbf{M}} \begin{pmatrix} \Sigma^{\infty}_{\Pi\,\uparrow,\downarrow}\Sigma^{\infty}_{\Pi\,0,\uparrow} - \Sigma^{\infty}_{\Pi\,0,\downarrow}\Sigma^{\infty}_{\Pi\,\uparrow,\uparrow} \\ \Sigma^{\infty}_{\Pi\,\uparrow,0}\Sigma^{\infty}_{\Pi\,0,\downarrow} - \Sigma^{\infty}_{\Pi\,0,0}\Sigma^{\infty}_{\Pi\,\uparrow,\downarrow} \\ \Sigma^{\infty}_{\Pi\,0,0}\Sigma^{\infty}_{\Pi\,\uparrow,\uparrow} - \Sigma^{\infty}_{\Pi\,\uparrow,0}\Sigma^{\infty}_{\Pi\,0,\uparrow} \end{pmatrix}. \tag{3.26}$$

Please notice that $\det \mathbf{M} = 0$ if $E_{\uparrow} = E_{\downarrow}$ since the second and the third column must be equal in case no spin dependence is left. We have thus to treat separately the degenerate case. Considering the Hilbert space $\mathcal{H}^{1}_{\odot}$ in the degenerate case we have $\rho^{\infty}_{\sigma} = \rho^{\infty}_{\sigma_1}$ for $\sigma, \sigma_1 \in \{\, 1, \ldots, M \,\}$ and thus

$$\begin{cases} \Sigma^{\infty}_{\Pi\,0,0}\rho^{\infty}_{0} + M\Sigma^{\infty}_{\Pi\,0,1}\rho^{\infty}_{1} = 0, \\ \rho^{\infty}_{0} + M\rho^{\infty}_{1} = 1. \end{cases} \tag{3.27}$$

Hence we find the following stationary populations

$$\begin{pmatrix} \rho^{\infty}_{0} \\ \rho^{\infty}_{1} \end{pmatrix} = \begin{pmatrix} \frac{\Sigma^{\infty}_{\Pi\,0,1}}{\Sigma^{\infty}_{\Pi\,0,1} - \Sigma^{\infty}_{\Pi\,0,0}} \\ \frac{1-\rho^{\infty}_{0}}{M} \end{pmatrix}, \tag{3.28}$$

where $\Sigma^{\infty}_{\Pi\,0,1} - \Sigma^{\infty}_{\Pi\,0,0} \neq 0$ as we will see in the following. Let us now consider the current flowing out of the l-lead in Eq.(3.13). In order to compute it we need also the stationary populations. Thus it is convenient to evaluate the total rates $\Sigma_{\Pi}{}^{l,\pm}_{b,a}$. Using our diagrammatic rules for the current Kernel we obtain

$$\Sigma_{\Pi}{}^{l,-}_{0,a} = 0, \tag{3.29a}$$

$$\Sigma_{\Pi}{}^{l,-}_{\sigma,a} = 2\mathsf{Re}\left\{ \right. \quad = -2\mathsf{Im}\left\{ \int_{-\infty}^{+\infty} \frac{d\varepsilon}{\hbar} \Phi^{\sigma,a}_{0,a}(\varepsilon, l, \sigma) \right\}, \tag{3.29b}$$

$$\Sigma_{\Pi}{}^{l,+}_{0,a} = 2\mathsf{Re}\left\{ \right. \quad = 2\mathsf{Im}\left\{ \sum_{\sigma} \int_{-\infty}^{+\infty} \frac{d\varepsilon}{\hbar} \Phi^{\sigma,a}_{0,a}(\varepsilon, l, \sigma) \right\}, \tag{3.29c}$$

$$\Sigma_{\Pi}{}^{l,+}_{\sigma,a} = 0, \tag{3.29d}$$

where $\sigma \in \{1,\dots,M\}$, $a \in \{0,1,\dots,M\}$ and $\Phi^{\sigma,a}_{0,a}(\varepsilon,l,\sigma)$ corresponds to the diagrams we introduced in Sect.3.3. Moreover we adopted the convection of inserting the Fermi function and the energy $\bar{\alpha}_{l,\sigma}(\varepsilon)$ corresponding to a specific fermion line in the diagram showing the generating vertex, i.e. the Fermi functions of the diagrams in Eqs.(3.29) are included in the $\Phi^{\sigma,a}_{0,a}(\varepsilon,l,\sigma)$ functions. Eqs.(3.29) give full access to the populations and the current in the RTA theory and no approximation was considered so far, i.e. we just specified some Hilbert space of the quantum dot. However these equation are still formal since we did not specify yet neither the diagrammatic form nor the functional dependence of the $\Phi^{\sigma,a}_{0,a}(\varepsilon,l,\sigma)$ functions. In order to proceed further we have to fix the approximation within which we will work. As we already mentioned, in the RTA, one considers all the diagrams such that, considering a vertical cut, we meet up to two fermion lines. Having this in mind we write:

$\Phi^{\sigma,a}_{0,a}(\varepsilon,l,\sigma) =$ 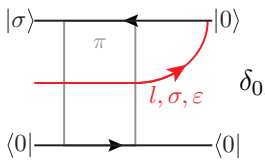 $\delta_{0,a} +$ 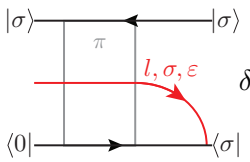 $\delta_{\sigma,a} +$ (3.30a)

$+ \sum_{l',\sigma',\varepsilon'}$ 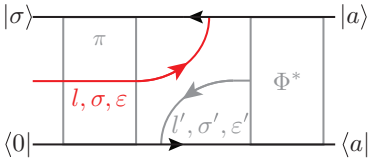 $+ \sum_{l',\varepsilon'}$ 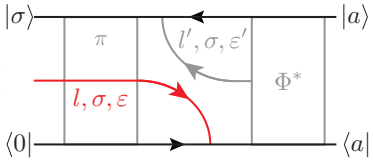 $=$

$$= \pi^{\sigma\sigma}_{00}(\varepsilon)\left[\gamma^{+}_{l}(\varepsilon)\,\delta_{0,a} - \gamma^{-}_{l}(\varepsilon)\,\delta_{\sigma,a} + \right. \tag{3.30b}$$

$$\left. -\gamma^{+}_{l}(\varepsilon)\sum_{l',\sigma'}\int_{-\infty}^{+\infty} d\varepsilon' \frac{\Phi^{*\sigma',a}_{0,a}(l',\varepsilon',\sigma')}{\varepsilon-\varepsilon'+E_{\sigma'\sigma}+i\eta} - \gamma^{-}_{l}(\varepsilon)\sum_{l'}\int_{-\infty}^{+\infty} d\varepsilon' \frac{\Phi^{*\sigma,a}_{0,a}(l',\varepsilon',\sigma)}{\varepsilon-\varepsilon'+i\eta}\right],$$

where we used the diagrammatic rules to extract the analytic expression in Eq.(3.30b) and we dropped the spin-like dependence in the tunnelling matrix elements, i.e. $\gamma^{\pm}_{l}(\varepsilon) = \gamma^{\pm}_{l,\sigma}(\varepsilon)$ for $\sigma \in \{1,\dots,M\}$. In the Eqs.(3.30) it is easy to realise that the $\Phi^{\sigma,a}_{0,a}(\varepsilon,l,\sigma)$ functions are defined iteratively. In order to fully characterise them, we have to specify also the matrix elements $\pi^{\sigma\sigma}_{00}(\varepsilon)$ of the propagator. Since in the RTA only diagrams with at most two simultaneous excitations are retained, in the self-energy matrix elements $\Sigma_{\pi\,00}^{\sigma\sigma}(\varepsilon)$ we can consider processes composed of at most one tunnelling line. Thus $\Sigma_{\pi\,00}^{\sigma\sigma}(\varepsilon)$ is composed of the following processes

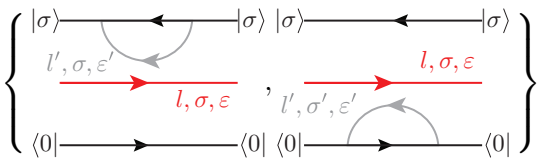 (3.31)

where $\sigma' \in \{1, \ldots, M\}$. In the case $M = 2$, these are the same diagrams (Tab.2.1) we found in the DSO theory considering strong Coulomb interactions (Sect.2.1.1). Thus the self-energy in the RTA for $M = 2$ and strong interactions is the same one we have found in the DSO: $\Sigma^{\sigma\sigma}_{\pi 00}(\varepsilon) = \Sigma^{\sigma 0}(\varepsilon)$ (in Eq.(2.4)). In the M-times degenerate case the self-energy reads

$$\Sigma^{11}_{\pi 00}(\varepsilon) = \int_{-\infty}^{+\infty} d\varepsilon' \frac{\gamma(\varepsilon')}{\varepsilon - \varepsilon' + i\eta} = \Gamma \sum_{l=\mathrm{L,R}} \frac{\kappa_l}{2\pi} \left[\left(\frac{\tilde{\varepsilon}}{\tilde{W}} - i \right) \cdot (M+1) \frac{\pi}{2} + \right.$$
$$\left. + (M-1) \left(\Psi^{(0)} \left(\frac{1}{2} + \frac{\tilde{W}}{2\pi} \right) - \Psi^{(0)} \left(\frac{1}{2} + i \frac{\tilde{\mu}_l - \tilde{\varepsilon}}{2\pi} \right) \right) \right] L(\tilde{\varepsilon}, \tilde{W}), \quad (3.32a)$$

where we introduced $\gamma(\varepsilon) = M\gamma^+(\varepsilon) + \gamma^-(\varepsilon)$, $\gamma^{\pm}(\varepsilon) = \sum_{l=\mathrm{L,R}} \gamma^{\pm}_l(\varepsilon)$ and we set $\sigma = 1$ since no spin dependence is left. Moreover we used the diagrammatic rules in App.A.4 to extract the integral form of the self-energy and we have performed the integration as in App.A.5.
We want to stress that the only approximation in the RTA is the consideration of tunnelling processes such that we have up to two simultaneous excitations. The definition of the self-energy $\Sigma^{\sigma\sigma}_{\pi 00}(\varepsilon)$ is just consistent with this approximation and it does not involve any further approximation.
Considering the components $a = 0, \sigma_1$ of Eq.(3.30b) we have in general two systems (Eqs.(3.33a) and (3.33b)) of linear integral coupled equations whose kernel is singular in the integration domain as $\eta \to 0$:

$$\Phi^{\sigma,0}_{0,0}(\varepsilon, l, \sigma) = \pi^{\sigma\sigma}_{00}(\varepsilon) \left[\gamma^+_l(\varepsilon) + \right. \quad (3.33a)$$
$$\left. - \gamma^+_l(\varepsilon) \sum_{l',\sigma'} \int_{-\infty}^{+\infty} d\varepsilon' \frac{\Phi^{*\sigma',0}_{0,0}(l', \varepsilon', \sigma')}{\varepsilon - \varepsilon' + E_{\sigma'\sigma} + i\eta} - \gamma^-_l(\varepsilon) \sum_{l'} \int_{-\infty}^{+\infty} d\varepsilon' \frac{\Phi^{*\sigma,0}_{0,0}(l', \varepsilon', \sigma)}{\varepsilon - \varepsilon' + i\eta} \right],$$

$$\Phi^{\sigma,\sigma_1}_{0,\sigma_1}(\varepsilon, l, \sigma) = \pi^{\sigma\sigma}_{00}(\varepsilon) \left[- \gamma^-_l(\varepsilon) \delta_{\sigma,\sigma_1} + \right. \quad (3.33b)$$
$$\left. - \gamma^+_l(\varepsilon) \sum_{l',\sigma'} \int_{-\infty}^{+\infty} d\varepsilon' \frac{\Phi^{*\sigma',\sigma_1}_{0,\sigma_1}(l', \varepsilon', \sigma')}{\varepsilon - \varepsilon' + E_{\sigma'\sigma} + i\eta} - \gamma^-_l(\varepsilon) \sum_{l'} \int_{-\infty}^{+\infty} d\varepsilon' \frac{\Phi^{*\sigma,\sigma_1}_{0,\sigma_1}(l', \varepsilon', \sigma)}{\varepsilon - \varepsilon' + i\eta} \right].$$

In Eq.(3.33a) it is clear that $\Phi^{\sigma,0}_{0,0}(\varepsilon, l, \sigma)$ couples to all the $M-1$ components $\Phi^{\sigma',0}_{0,0}(\varepsilon, l, \sigma)$, with $\sigma' \neq \sigma$, through the first term in the second line of Eq.(3.33a). Analogously $\Phi^{\sigma,\sigma_1}_{0,\sigma_1}(\varepsilon, l, \sigma)$ couples to the $M-1$ terms $\Phi^{\sigma',\sigma_1}_{0,\sigma_1}(\varepsilon, l, \sigma)$ with $\sigma' \neq \sigma$. Moreover no coupling is present between the Φ-functions with different initial states (rightmost indexes). Remarkably the

only difference in the equations for the Φ-functions with different initial sates is the inhomogeneous term. This will be a useful observation for the numerical solution of such system of equations. At this point if we knew the solution of the integral systems of equations in Eqs.(3.33a) and (3.33b) we would be able to describe the transport properties of the system. Unfortunately the analytical solution of such equations is known only in the degenerate case [38, 47], i.e. $E_\sigma = E_{\sigma_1}$ for $\sigma, \sigma_1 \in \{ 1, \dots, M \}$. In the following we turn our discussion to the analytical solution of such equations in the degenerate case and the numerical one in the non-degenerate one.

Solution of the RTA integral equations (degenerate case) In order to solve the integral system of coupled equations in Eqs.(3.33) for the degenerate case $E_\sigma = E_1$ with $\sigma \in \{ 1, \dots, M \}$, it is useful to introduce

$$\Phi^{+}(\varepsilon) = \sum_{l} \Phi^{\sigma,0}_{0,0}(\varepsilon, l, \sigma) \qquad \Phi^{-}(\varepsilon) = \sum_{l,\sigma} \Phi^{\sigma,\sigma_1}_{0,\sigma_1}(\varepsilon, l, \sigma). \tag{3.34}$$

In Eq.(3.34) we dropped the σ dependence in the $\Phi^{\pm}$-functions since, considering the Eq.(3.33a), it is easy to check that, if $E_\sigma = E_1$, the equations for $\Phi^{\sigma,0}_{0,0}(\varepsilon, l, \sigma)$ with different σ-indexes coincide. Thus the functions $\Phi^{\sigma,0}_{0,0}(\varepsilon, l, \sigma)$ coincide too. The same is true for $\sum_\sigma \Phi^{\sigma,\sigma_1}_{0,\sigma_1}(\varepsilon, l, \sigma)$, where we had to consider a linear combination because of the inhomogeneous term in Eq.(3.33b). Hence, in the following, we consider

$$\Phi^{\pm}(\varepsilon) = \pi^{1,1}_{0,0}(\varepsilon) \left[\pm\gamma^{\pm}(\varepsilon) - \gamma(\varepsilon) \int_{-\infty}^{+\infty} d\varepsilon' \frac{\Phi^{*\pm}(\varepsilon')}{\varepsilon - \varepsilon' + i\eta} \right], \tag{3.35}$$

where we introduced $\pi^{1,1}_{0,0}(\varepsilon) = \pi^{\sigma,\sigma}_{0,0}(\varepsilon)$ since the propagator is σ-independent too. In contrast to Eq.(3.33), where we have to consider a system of coupled integral equations, in Eq.(3.35), exploiting the fact that the system is highly symmetric, we have to solve a single equation to obtain the $\Phi^{\pm}$-functions. Notice that if we would have considered $\sum_{\sigma_1} \Phi^{\sigma,\sigma_1}_{0,\sigma_1}(\varepsilon, l, \sigma)$ instead of $\sum_\sigma \Phi^{\sigma,\sigma_1}_{0,\sigma_1}(\varepsilon, l, \sigma)$ we would have obtained the same equation for $\Phi^{-}(\varepsilon)$ as in Eq.(3.35). Thus $\Phi^{-}(\varepsilon) = \sum_{\sigma_1} \Phi^{\sigma,\sigma_1}_{0,\sigma_1}(\varepsilon, l, \sigma) = \sum_\sigma \Phi^{\sigma,\sigma_1}_{0,\sigma_1}(\varepsilon, l, \sigma)$ because we are considering the degenerate case.
As it is explained in detail in App.A.7, solving Eq.(3.35), the imaginary part of $\Phi^{\pm}(\varepsilon)$ reads

$$\mathrm{Im}\left\{\Phi^{\pm}(\varepsilon)\right\} = \mp\pi\gamma(\varepsilon) \frac{\lambda^{\pm}}{\lambda} \left\| \pi^{1,1}_{0,0}(\varepsilon) \right\|^2, \tag{3.36}$$

where we defined

$$\lambda^{\pm} = \int_{-\infty}^{+\infty} d\varepsilon\, \gamma^{\pm}(\varepsilon) \left\| \pi^{1,1}_{0,0}(\varepsilon) \right\|^2, \qquad \lambda = \int_{-\infty}^{+\infty} d\varepsilon \left\| \pi^{1,1}_{0,0}(\varepsilon) \right\|^2.$$

Thus the Self-Energies for the propagator $\Pi(\varepsilon)$ read

$$\Sigma^{\infty}_{\Pi\,0,0} = -2\pi M\frac{\lambda^{+}}{\lambda}, \qquad \Sigma^{\infty}_{\Pi\,0,1} = 2\pi\frac{\lambda^{-}}{\lambda}, \tag{3.37}$$

where

$$\lambda^{+}M+\lambda^{-} = \int_{-\infty}^{+\infty} d\varepsilon\,\gamma(\varepsilon)\left\|\pi^{1,1}_{0,0}(\varepsilon)\right\|^{2} = \int_{-\infty}^{+\infty} d\varepsilon\,\mathsf{Im}\left\{\pi^{1,1}_{0,0}(\varepsilon)\right\}/\pi = 1.$$

Moreover, considering Eq.(3.28), the stationary populations are easily obtained

$$\rho^{\infty}_{0} = \lambda^{-}, \qquad \rho^{\infty}_{1} = \lambda^{+}. \tag{3.38}$$

Here it is worth to notice that the system in Eq.(3.28) is never singular since $\Sigma^{\infty}_{\Pi\,0,1} - \Sigma^{\infty}_{\Pi\,0,0} = 2\pi/\lambda \neq 0$. Despite the fact that the $\lambda^{\pm}$ and λ functions are energy independent and with this respect constant, they do depend on the parameters of the system. Thus one has to take care of the integration defining such terms for every set of parameters. Indeed the $\lambda^{\pm}$ functions directly define the populations of the system as it is stated in Eqs.(3.38).
In general the knowledge of the total rates $\Sigma^{\infty}_{\Pi\,b,a}$ is not enough to obtain the current flowing out of the l-lead using Eq.(3.13), indeed we would need its components $\Sigma^{l,-}_{\Pi b,a}$ or $\Sigma^{l,+}_{\Pi b,a}$. Fortunately it will turn out that the Green functions $G^{>(<)}_{\sigma}(\varepsilon)$ can be expressed entirely as a function of the $\Phi^{\pm}$-functions. Then we can use Eq.(3.20) to address the current of the system. For this reason we turn now our discussion to the evaluation of the Green functions in the degenerate case.

Green functions for the M-degenerate case In the RTA, the correlation functions of the system can be depicted diagrammatically (see Sect.3.2) as follows

$$G^{>}_{\sigma}(\varepsilon) = -2i\hbar\mathsf{Re}\left\{\right.$$

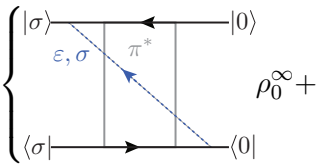

$$\rho^{\infty}_{0} +$$

$$+\sum_{\varepsilon',\sigma',l',a}$$

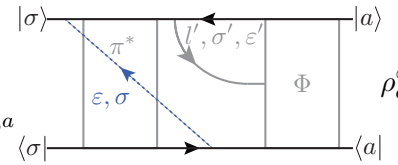

$$\left.\rho^{\infty}_{a}\right\} =$$

$$= 2i\mathsf{Im}\left\{\pi^{\sigma,\sigma}_{0,0}(\varepsilon)\left[\rho^{\infty}_{0} - \sum_{\sigma',l',a}\int_{-\infty}^{+\infty} d\varepsilon'\,\frac{\Phi^{*\sigma',a}_{0\ ,a}(l',\sigma',\varepsilon')}{\varepsilon-\varepsilon'+E_{\sigma'\sigma}+i\eta}\rho^{\infty}_{a}\right]\right\}, \tag{3.39}$$

whereas the lesser Green function reads

$$G_{\sigma}^{<}(\varepsilon) = 2i\hbar\mathsf{Re}\left\{ \right. \quad \rho_{\sigma}^{\infty} + \tag{3.40}$$

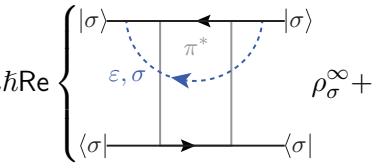

$$+ \sum_{\varepsilon', l', a}$$

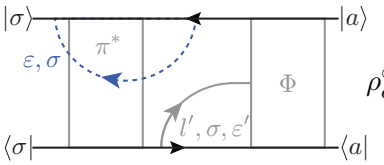

$$\rho_{a}^{\infty} \left. \right\}$$

$$= -2i\mathsf{Im}\left\{ \pi_{0,0}^{\sigma,\sigma}(\varepsilon) \left[\rho_{\sigma}^{\infty} + \sum_{l',a} \int_{-\infty}^{+\infty} d\varepsilon' \, \frac{\Phi_{0,a}^{*\sigma,a}(l', \sigma, \varepsilon')}{\varepsilon - \varepsilon' + i\eta} \rho_{a}^{\infty} \right] \right\}.$$

Here we used the diagrammatic rules in Sect.3.2 to extract the integral form of the correlation functions. It is easy to see that, if $E_{\sigma} = E_{\sigma'}$ for $\sigma, \sigma' \in \{ 1, \ldots, M \}$ we can recast Eqs.(3.39) and (3.40) in a much simpler form

$$G_{1}^{>}(\varepsilon) = 2i\mathsf{Im}\left\{ \pi_{0,0}^{1,1}(\varepsilon) \left[\rho_{0}^{\infty} - M \int_{-\infty}^{+\infty} d\varepsilon' \frac{\rho_{0}^{\infty}\Phi^{+*}(\varepsilon') + \rho_{1}^{\infty}\Phi^{-*}(\varepsilon')}{\varepsilon - \varepsilon' + i\eta} \right], \right\} \tag{3.41a}$$

$$G_{1}^{<}(\varepsilon) = -2i\mathsf{Im}\left\{ \pi_{0,0}^{1,1}(\varepsilon) \left[\rho_{1}^{\infty} + \int_{-\infty}^{+\infty} d\varepsilon' \frac{\rho_{0}^{\infty}\Phi^{+*}(\varepsilon') + \rho_{1}^{\infty}\Phi^{-*}(\varepsilon')}{\varepsilon - \varepsilon' + i\eta} \right]. \right\} \tag{3.41b}$$

where we fixed the spin-like index $\sigma = 1$ since we are considering the degenerate case. As we already mentioned, Eqs.(3.41) show that the Green functions of the system are completely determined by the $\Phi^{\pm}$-functions. Now we can use the Eqs.(3.35) to compute the integration in Eqs.(3.41) finally yielding the analytical form of the correlation functions

$$G_{1}^{>}(\varepsilon) = -2\pi i \left\| \pi_{0,0}^{1,1}(\varepsilon) \right\|^{2} \gamma^{-}(\varepsilon), \tag{3.42a}$$

$$G_{1}^{<}(\varepsilon) = \quad 2\pi i \left\| \pi_{0,0}^{1,1}(\varepsilon) \right\|^{2} \gamma^{+}(\varepsilon), \tag{3.42b}$$

Moreover the spectral function of the system reads

$$A_{1}(\varepsilon) = \frac{1}{\pi} \frac{\Gamma/2}{\left[\varepsilon - E_{10} - \mathsf{Re}\left\{ \Sigma_{\pi_{0,0}^{1,1}}(\varepsilon) \right\} \right]^{2} + \left[\mathsf{Im}\left\{ \Sigma_{\pi_{0,0}^{1,1}}(\varepsilon) \right\} \right]^{2}}, \tag{3.43}$$

i.e. as we already noticed in the DSO and DDSO the real part of the self-energy is responsible for the energy level position renormalization, whereas its

imaginary part defines the broadening of the Lorentzian-like shaped spectral function. As it was noticed in Ref. [47], $\int d\varepsilon\, A(\varepsilon) = \lambda^- + \lambda^+ = \rho_0^\infty + \rho_1^\infty$. Thus for $M > 1$ the integral of the spectral function is not equal to 1 since we are missing a factor $(M-1)\lambda^+$. This is an artefact of the RTA that considers up to two simultaneous excitations away from the diagonal state of the density matrix but unfortunately for $M > 1$ higher order simultaneous excitations cannot be disregarded. Interestingly for $M = 1$ one recovers the exact Breit-Wigner spectral function. Considering Eqs.(3.43) and (3.32) for $M = 1$, in the large bandwidth limit, we have

$$A_1(\varepsilon, M=1) = \frac{1}{\pi} \frac{\Gamma/2}{(\varepsilon - E_{10})^2 + (\Gamma/2)^2}. \tag{3.44}$$

This shows that for the single level model the RTA is an exact theory and it is capable to describe the transport properties of the system in every transport regimes. As it was noticed in Refs. [47] and [58] this is due to a cancellation of higher order diagrams in the single level case ($M = 1$).
Having the analytical form of the spectral function we can study the transport properties of the system within the RTA. However before we turn our discussion to a brief description of the numerical strategy we adopted to solve the RTA system of integral equations in the non degenerate case.

Solution of the RTA integral equations (non-degenerate case) We solved the Eqs.(3.33) for $\eta \to 0$, in the non-degenerate case, numerically mapping the systems of linear integral equations into a system of linear equations. Indeed it is always possible to map a linear system of integral equations in a linear system of equations where the unknown variables are the unknown functions evaluated on some energy grid of points [59]. In our case the situation is slightly more sophisticated since the Kernel is singular on the integration path in the limit $\eta \to 0$. In Ref. [60], K. Atkinson demonstrated that, considering a linear or higher order interpolation of the unknown functions, the resulting matrix elements are well behaved and increasing the number of sampling points in the energy space, the interpolated functions finally converge to the real unknown function. We have adapted the discussion in Ref. [60] to the case of an open path of integration as we have in our case. We stress that this method works for an arbitrary number M of one particle levels. Moreover it would work also for finite Coulomb interaction taking into account the states with double occupancy. However, since the size of the linear system of equations is proportional to the number of one particle levels, the computational costs to obtain the functions $\Phi_{0,a}^{\sigma,a}(\varepsilon)$ increases considerably (as M^3 if we use the LU-decomposition to solve the linear system) increasing M. For this reason we considered the simplest case with $M = 2$ in the next Section.

3.4.2 RTA conductance and populations

In this Section we present the RTA transport properties using the theory we have developed in the previous Section. Let us first of all consider the dependence of the Kondo temperature through the parameters of the system. Considering the self-energy for the M-degenerate case in Eq.(3.32) and extracting the exponential dependence of the Kondo temperature using Eq.(2.10) we have

$$k_{\rm B}T_{\rm K}^{\rm RTA} \propto We^{-2\pi\frac{\mu_0-E_{10}}{(M-1)\Gamma}}. \tag{3.45}$$

In the case $M = 2$ we recover the same exponential dependence of the Kondo temperature we found in the DSO (Eq.(2.11)). This is because in the strongly interacting limit, the DSO self-energy coincides with the RTA one. Moreover, in Eq.(3.45), it is interesting to notice that the wrong scaling exponent is due, as in the DSO, to a cancellation between two contributions in the self-energy leading to the wrong $(M-1)$ prefactor in the denominator of the exponent. In the following we will focus on the case $M = 2$ to be able to compare with the results form the previous Chapter.
In Fig.3.4 we show the RTA linear conductance as a function of the temper-

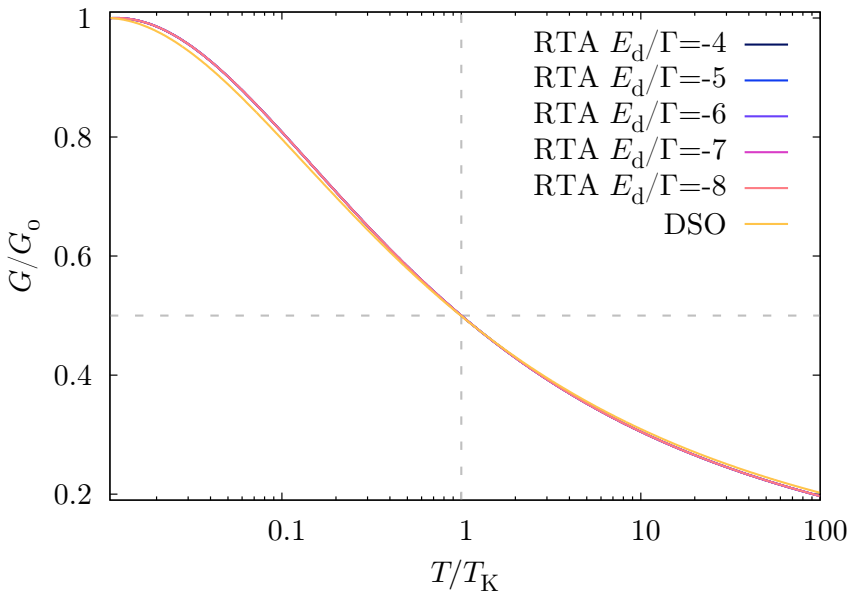

Figure 3.4: Comparison of the linear conductance in the RTA (from black to pink solid lines) and DSO (yellow solid line) theories as a function of the temperature normalised to the corresponding $T_{\rm K}$ of each theory. Each curve is normalised to its corresponding maximum: $G_0^{\rm RTA} \simeq 1e^2/h$ and $G_0^{\rm DSO} \simeq 0.7e^2/h$. The RTA data are presented for different values of the level position $E_{\rm d}$ keeping the gate constant to $V_{\rm G} = 0$.

ature normalised to the Kondo one (Eq.(3.45)), fixing the pre-factor as in Chap.2. It is easy to see that the linear conductance is universal varying the position of the energy level $E_{\rm d}$. Moreover, as it was noticed in Ref. [41], the RTA and DSO universal curves normalised to their corresponding absolute maximum are very similar due to the fact that the two theories share the same self-energy in the strongly interacting case. Differently from the DSO the linear and differential conductance in the RTA never breaks down [41]. Instead for temperatures $T/T_{\rm K}^{\rm RTA} < 0.01$ the linear conductance tends to zero because the divergence in the real part of the self-energy imposes an unphysical diverging correction to the level position $E_{\rm d}$. Thus the first effect of the inclusion of the vertex corrections in the theory is the solution of the break down of the conductance, though they do not solve the issue of an unphysically large real part of the self-energy as the temperature tends to zero.

In Fig.3.5a we present the RTA differential conductance as a function of the applied gate and bias voltages in the degenerate case. In this case we exploited Eq.(3.20) and the analytical form of the RTA spectral function in Eq.(3.43) to address the current flowing out of the l-lead and thus we computed numerically the conductance. In contrast, in Fig.3.5b we considered a finite Zeeman splitting $E_{\uparrow\downarrow} \neq 0$. In this case, as we have mentioned previously, no analytical solution is available. Thus we performed the limit $\eta \to 0$ and we solved numerically the RTA systems of linear coupled integral equations in the Eqs.(3.33). The solution of such systems yields twelve complex functions $\Phi_{0,a}^{\sigma,a}(\varepsilon, l, \sigma)$ for $\sigma = \uparrow, \downarrow = 1, 2$, $a \in \{0, \uparrow, \downarrow\}$ and $l = {\rm L}, {\rm R}$. Then we integrated the imaginary part of these functions to obtain the total rates in Eq.(3.29) and it is thus straightforward to first evaluate the populations in Eq.(3.26) and then the stationary current in Eq.(3.13). Finally, differentiating numerically the current, one obtains the differential conductance as we show in Fig.3.5b. As in the DSO, in the RTA the widths of the Coulomb blockade resonances saturate, as the temperature is lowered in the regime $k_{\rm B}T/\Gamma < 1$, to a value proportional to Γ, the proportionality coefficient depending on the gate voltage since the imaginary part of the self-energy is energy dependent. The height of these resonances saturates too, its maximal value being approximately $G_0 \simeq 1e^2/h$, as we already noticed in Fig.3.4. Thus the vertex corrections come into play in the degenerate case correcting the absolute height of the Coulomb blockade peaks.

Moreover, as we consider a Zeeman splitting, an excited state resonance in the conductance appears in Fig.3.5a at a bias voltage $eV \simeq E_{\uparrow\downarrow}$ as in the DSO. However, in contrast to the DSO, this resonance does not extend in the one electron Coulomb valley (on the right of the charge degeneracy point). Instead we observe in Fig.3.5f and 3.5d that the system is in the ground state ($|\downarrow\rangle$) for bias voltages $eV < E_{\uparrow\downarrow}$. For bias voltages $eV = E_{\uparrow\downarrow}$ and gate voltages in the one electron Coulomb valley, a co-tunnelling resonance appears parallel to the gate axis. This is consistent with the co-tunnelling analysis for the

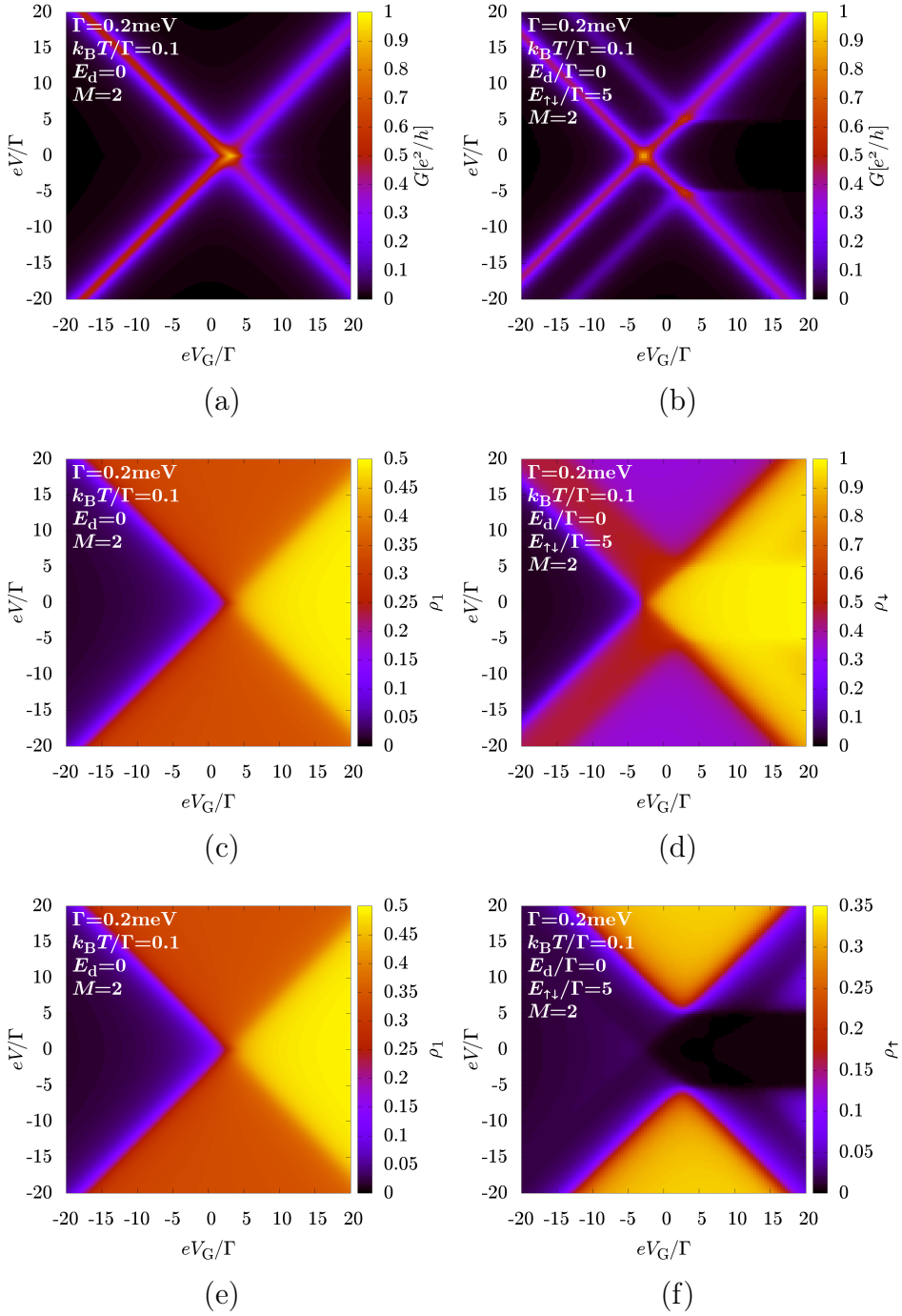

Figure 3.5: (a) and (b) RTA differential conductance as a function of the applied bias and gate voltages, while from (c) to (f) we show the populations of the quantum dot. In (a), (c) and (e) $E_{\uparrow\downarrow} = 0$, whereas in (b), (d) and (f) $E_{\uparrow\downarrow}/\Gamma = 5$. We considered a value of the leads bandwidth $W/\Gamma = 5000$.

perturbative regime in Ref. [48]. Indeed, as we mentioned many times at this point, in the RTA all the fourth order co-tunnelling processes are included and thus the RTA reduces itself naturally to the perturbative analysis in Ref. [48]. Thus the RTA is capable to describe both the non perturbative saturation effects of the Coulomb blockade widths and heights and the perturbative co-tunnelling effects in the intermediate regime $k_{\mathrm{B}}T/\Gamma < 1$. Unfortunately it is not capable, sharing the same self-energy of the DSO, to reproduce the correct scaling exponent in the Kondo temperature.

3.5 Conclusion

We conclude with this Section the first part of this thesis about the transport analysis of quantum dot systems within the RDM framework. In Chap.1 we introduced the general RDM formalism and we gave an exemplary application within the second order approximation for the electron tunnelling across an Anderson quantum dot. In Chap.2 we extended the RDM framework to the non perturbative regime ($k_{\mathrm{B}}T \simeq \Gamma$) with the so-called DSO approximation and we proposed a prescription to heal the issue of the wrong scaling exponent in the Kondo temperature with the DDSO approximation. Such a theory is capable to take into account some of the three particle simultaneous excitations away from the diagonal condition of the RDM but it does not capture all the fourth order co-tunnelling processes and more in general it does not take into account the so-called vertex corrections. Then we turned our discussion to the inclusion of the vertex corrections in the theory within the RTA in Chap.3. As we discussed in the present Chapter, in the RTA, the DSO artefacts in the presence of the magnetic field are completely solved and all the fourth order co-tunnelling processes are taken into account systematically. However the inclusion of the vertex corrections does not solve the issue of the wrong scaling exponent in the Kondo temperature leaving unchanged the DSO self-energy analytical form in the strongly interacting case. In order to solve this issue and improve consistently the RTA, one should include the vertex corrections in the self-energy of the $\pi(\varepsilon)$ propagator and accordingly "dress" its processes, i.e. one should include all the three simultaneous excitations away from the diagonal condition of the density matrix. However, being already highly computationally demanding the numerical solution of the RTA equations in the non degenerate case, this seems to be an highly intricate purpose from the pure numerical point of view.
To conclude, much work is still needed, both from the analytical and numerical point of view, to find a computationally valuable and efficient way to describe non perturbative transport features within the RDM framework, especially the ones concerning the Kondo effect.

Part II

Transport properties of a carbon nanotube quantum dot: a DM-NRG study

CHAPTER 4

DM-NRG study of the Kondo effect in a carbon nanotube

In the present Chapter we will consider the linear transport across a carbon nanotube (CNT) quantum dot within the Density Matrix-Numerical Renormalization Group (DM-NRG) scheme. The Chapter is organised as follows: in Sect.4.1 we give a brief and qualitative overview on the CNT based quantum dots and the rich physics one gains access to studying them, in Sect.4.2 we present our model Hamiltonian for CNTs and we briefly analyse its symmetries, in Sect.4.3 we present our results for the linear transport properties of such a system, in Sect.4.4 we study the behaviour of the Kondo temperature with respect to the underlying symmetries of the Hamiltonian. In Sect.4.5 we include the effects of a finite magnetic field in our analysis. Finally in Sect.4.6 we will present a comparison of the theory studied in the previous Sections with experimental results obtained in the group of Jean-Pierre Cleuziou in Grenoble.
Parts of this Chapter have been published in cooperation with Cătălin Paşcu Moca, Gergely Zaránd and Milena Grifoni in Ref. [61]

4.1 Introduction and motivation

As we mentioned in the introduction and in the previous Chapters, the Kondo effect [22] is a hallmark of strongly correlated electron physics. Its observation in quantum dot set-ups is ubiquitous and, as we shall see in the following, reveals precious information on the underlying symmetries of the quantum dot system and on the corresponding degeneracies of its spectrum.

Specifically, the physics of CNT based quantum dots is very rich since electrons in CNTs possess a spin and a pseudo-spin degree (see Sect.4.2.2) of freedom [62]. The latter originates from the presence of two inequivalent

Dirac points (usually labelled with K and K') in the underlying graphene hexagonal lattice (see Fig.4.1). As we will see in detail in Sect.4.2.2 such pseudo-spin degree of freedom is the generalisation of the spin one in a CNT. Indeed it is possible to define such pseudo-spin in the CNT diagonalised basis using the generators of the SU(2) Lie algebra (see Sect.4.2.2).

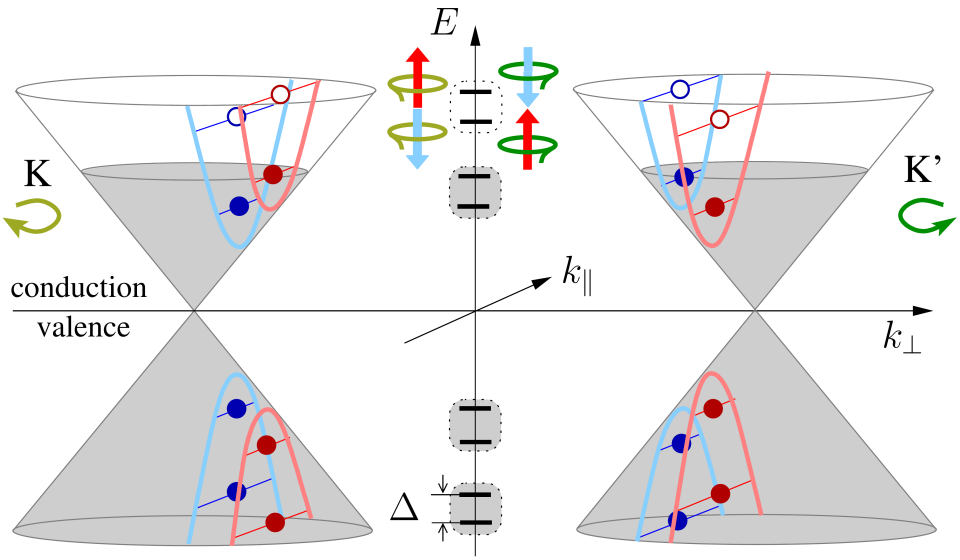

Figure 4.1: Sketch of the dispersion relation in a graphene sheet as a function of the parallel ($k_\parallel$) and perpendicular ($k_\perp$) momentum with respect to the CNT axis. In light blue and pink we show the hyperbolic 1-D dispersion relation in a CNT deriving from the imposition of the periodic boundary conditions on $k_\perp$. Finally we show the discrete levels the levels of the CNT based quantum dot obtained imposing the open boundary conditions on $k_\parallel$. Here we considered the general situation in which the CNT quantum dot states are split by an energy Δ. Adapted from Ref. [63].

Since CNTs are rolled up sheets of graphene, the physics associated to them is closely related to the graphene dispersion relation. In Fig.4.1 we sketch such a dispersion relation as a function of the parallel $k_\parallel$ and perpendicular $k_\perp$ (with respect to the CNT axis) momenta. This dispersion relation can be readily derived from the aforementioned hexagonal structure of the graphene [13, 64]. It is easy to notice the aforementioned Dirac cones. By rolling up the graphene sheet and thus imposing periodic boundary conditions on $k_\perp$ (transverse quantization) one obtains the hyperbolic one dimensional (1-D) dispersion relation of a CNT. Depending on the specific way the graphene is rolled up, one may obtain a gapless dispersion relation and thus a metallic CNT (cutting the Dirac cones exactly at the K, K' points). Otherwise one has a gapped dispersion relation (see light blue and pink solid curves in Fig.4.1 considering $\Delta = 0$) and thus a semi-conducting

CNT[1].

Including a curvature enhanced spin-orbit interaction (SOI) [65] results in the splitting of the states in the same valley, i.e. belonging either to the Dirac cone centred in K or K', and different spin values (see light blue and pink solid curves in Fig.4.1). Such an interaction is magnetic field independent and it is due to relativistic and curvature effects. Thus the energy spectrum results in a set of doublets each containing a couple of electrons with opposite spin and valley momenta.

Furthermore in CNT based quantum dots also the quantization of $k_{\parallel}$ (longitudinal quantization) is important, since the CNT length is finite. This leads to the discrete energy spectrum we sketched in Fig.4.1 on the energy axis. It is thus evident that the CNT based quantum dot, the energy levels organise themselves in "shells" with different longitudinal momenta that can accommodate up to four electrons. Such shells are typically well separated in energy due to the longitudinal quantization.

Let us now consider the CNT in the absence of the spin-orbit interaction. As we will see in detail in Sect.4.2.2 and App.C, in this limit the CNT Hamiltonian is invariant under time-reversal (see Sect.4.2.1) and pseudo-spin reversal (see Sect.4.2.2) symmetries. Thus a quadruplet of degenerate levels is associated with a given longitudinal momentum (see Fig.4.1 if the light blue and pink solid curves coincide). In this case, the four-fold degeneracy may lead to the occurrence of the so called SU(4)-Kondo effect at low temperatures [66–70]. In order to see this exotic Kondo resonance it is important, however, that both spin and pseudo-spin quantum numbers are conserved during tunnelling, as a mixing of these degrees of freedom can result in a more conventional SU(2) Kondo effect [71]. For CNTs devices where parts of the tube act as leads (see Fig.4.2), such a situation can be realised, and the peculiar features associated to the presence of both spin and valley degrees of freedom can be probed in finite magnetic fields [69, 72].

In a more realistic description of a CNT though, pseudo-spin symmetry breaking contributions, like SOI or valley mixing due to scattering off the boundaries [73, 74] or to disorder [75], should be included. As a consequence, the fourfold degeneracy is broken and, for a given value of the longitudinal momentum, the spectrum of an isolated CNT quantum dot consists of two pairs of degenerate Kramers pairs, with splitting provided by the combined effects of SOI and valley mixing [76]. In this situation, upon increasing the SOI strength or the valley mixing, a crossover from the SU(4)-Kondo state involving both Kramers pairs, to the more standard SU(2) Kondo regime is expected [77–79].

Despite the considerable amount of experiments reporting Kondo behaviour in CNTs, [69, 72, 79–85], the combined effect of SOI, valley mixing and the impact of applied magnetic fields on the SU(4) to SU(2) crossover

[1] If such a gap is large the CNT may be considered insulating.

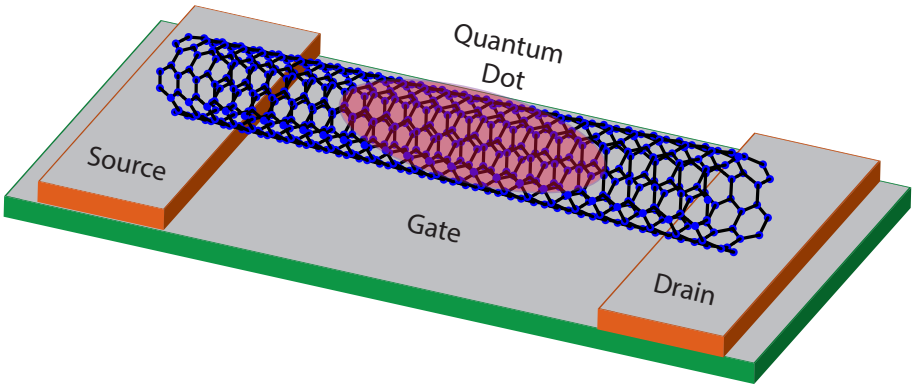

Figure 4.2: Sketch of the set-up. The CNT is coupled to two external contacts, source and drain. The quantum dot formed in the CNT is indicated by the shaded area. The electrostatic state of the dot is capacitively controlled by a back-gate.

have only been addressed within a field theoretical effective Keldysh action approach [79]. A numerically exact investigation of the highly intricate crossover is thus very desirable.

4.2 Theoretical framework

In this Chapter we study the dynamical and linear transport properties of CNT-based Kondo quantum dots by means of the DM-NRG method [36, 77, 86, 87]. We firstly focus on the SU(4) to SU(2) crossover induced by finite SOI and valley mixing, then we study the influence of magnetic fields parallel or perpendicular to the CNT axis.

4.2.1 Model Hamiltonian

Having in mind all the considerations in the previous Section, the set-up we consider consists of a CNT quantum dot coupled to two external leads (see the sketch in Fig.4.2). We focus on a single shell and correspondingly we describe the CNT by an extended Anderson impurity model [22, 76], consisting of a pair of interacting Kramers doublets. We denote by E_j the energies of the four levels ($j = \{1, 2, 3, 4\}$), and by $\hat{N}_j = \hat{d}_j^\dagger \hat{d}_j$ their occupation. In what follows, we shall refer to this basis as the Kramers basis (see Fig.4.3(a)). Each of the four levels can accommodate one electron and, with a good approximation, these electrons interact with each other through a strong and level-independent on-site interaction U. In this basis, the CNT Hamiltonian

takes the form

$$\hat{H}_{\mathrm{CNT}} = \sum_{j=1}^{4} E_j \, \hat{N}_j + U \sum_{j<j'}^{4} \hat{N}_j \, \hat{N}_{j'} \, . \tag{4.1}$$

In the absence of the spin-orbit interaction and valley mixing, $\Delta_{\mathrm{SO}} = 0$ and $\Delta_{\mathrm{KK'}} = 0$, the CNT Hamiltonian is invariant under time-reversal and valley-reversal [62]. These operations are represented by the two anti-unitary operators

$$\hat{\mathcal{T}} = \kappa \left(\hat{d}_2^\dagger \hat{d}_1 + \hat{d}_4^\dagger \hat{d}_3 - \mathrm{h.c.} \right) , \tag{4.2a}$$

$$\hat{\mathcal{P}} = \kappa \left(\hat{d}_4^\dagger \hat{d}_1 - \hat{d}_3^\dagger \hat{d}_2 - \mathrm{h.c.} \right) , \tag{4.2b}$$

respectively [79]. They yield a fourfold degenerate spectrum of the CNT, $E_j \equiv E_{\mathrm{d}}$. Correspondingly, the CNT Hamiltonian is SU(4) invariant (see Sect.4.2.2). Moreover we capture the effects of a an applied gate voltage tuning the on-site energy E_{d}. In what follows, we shall label states such that $(1,2)$ and $(3,4)$ form Kramers pairs, while $(1,4)$ and $(2,3)$ are pairs associated with the $\hat{\mathcal{P}}$ symmetry. Notice that a third unitary operator $\hat{\mathcal{C}} = \hat{\mathcal{P}} \cdot \hat{\mathcal{T}}^{-1}$ linking the remaining pairs $(1,3)$ and $(2,4)$ can also be constructed from $\hat{\mathcal{T}}$ and $\hat{\mathcal{P}}$ (see Fig.4.3(b)). It reads

$$\hat{\mathcal{C}} = \hat{d}_1^\dagger \hat{d}_3 + \hat{d}_2^\dagger \hat{d}_4 + \mathrm{h.c.} \, . \tag{4.3}$$

A finite $\Delta = \sqrt{\Delta_{\mathrm{SO}}^2 + \Delta_{\mathrm{KK'}}^2}$, breaks the $\hat{\mathcal{P}}$ symmetry and, correspondingly, also the SU(4) symmetry (see Sect.4.2.2). Since time-reversal symmetry is preserved, the on-site energies remain twofold degenerate, $E_1 = E_2 = E_{\mathrm{d}} + \Delta/2$ and $E_3 = E_4 = E_{\mathrm{d}} - \Delta/2$ (see Fig.4.3(a)). Notice that a finite Δ plays the same role as a magnetic field on the $\mathcal{P}$ - and $\mathcal{C}$-pairs, such that conjugation relations among energy levels exist: $E_1(\Delta) = E_4(-\Delta)$, and similarly for the other couples. In a CNT, with a good approximation, each nanotube level couples to independent channels in the leads, and their tunnel coupling can thus be described by the Hamiltonian

$$\hat{H}_{\mathrm{T}} = \sum_j T_j \sqrt{\rho_0} \int_{-W}^{W} d\varepsilon \, \hat{a}_{\varepsilon j}^\dagger \hat{d}_j + \mathrm{h.c.} \, . \tag{4.4}$$

Here, instead of the original left/right operators $\hat{c}_{\varepsilon j,\mathrm{L/R}}^\dagger$ for the leads, we introduced the symmetric and antisymmetric combinations

$$\begin{pmatrix} \hat{a}_{\varepsilon j} \\ \hat{b}_{\varepsilon j} \end{pmatrix} = \begin{pmatrix} \cos\gamma_j & \sin\gamma_j \\ -\sin\gamma_j & \cos\gamma_j \end{pmatrix} \begin{pmatrix} \hat{c}_{\varepsilon j,\mathrm{L}} \\ \hat{c}_{\varepsilon j,\mathrm{R}} \end{pmatrix} ,$$

the corresponding effective tunnelling amplitude $T_j \equiv \sqrt{T_{j,\mathrm{L}}^2 + T_{j,\mathrm{R}}^2}$ and asymmetry parameter $\gamma_j \equiv \arctan\left(T_{j,\mathrm{R}}/T_{j,\mathrm{L}}\right)$. Moreover, in Eq.(4.4), we

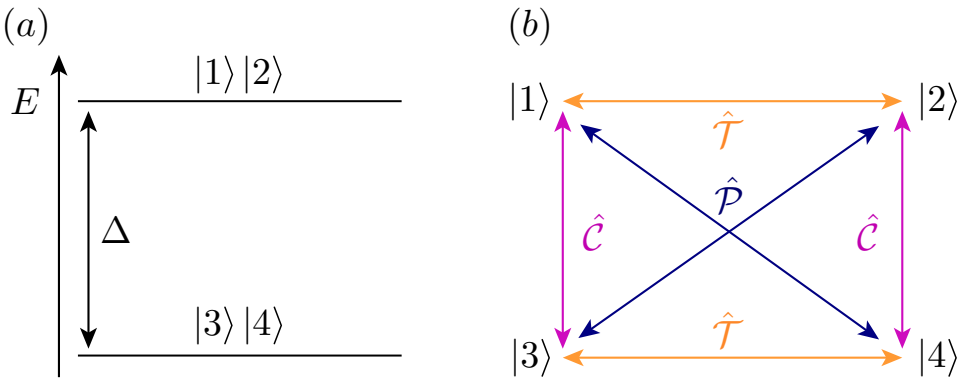

Figure 4.3: a) Energy level scheme involving two Kramers doublets separated by the energy Δ. (b) Connection among the energy levels established by the symmetry operations $\hat{\mathcal{T}}$, $\hat{\mathcal{P}}$ and $\hat{\mathcal{C}}$.

assumed energy independent tunnelling matrix elements as in the previous Chapters. In Eq.(4.4) we have chosen to write the tunnelling Hamiltonian directly in the energy space. The leads are assumed to be non-interacting with a constant density of states per flavour $\rho(\varepsilon) = \rho_0 = 1/2W$, and a bandwidth $2W$. They are described by the Hamiltonian[2]

$$\hat{H}_{\rm RS} = \sum_j \int_{-W}^{W} d\varepsilon\, \varepsilon \left(\hat{a}^\dagger_{\varepsilon j} \hat{a}_{\varepsilon j} + \hat{b}^\dagger_{\varepsilon j} \hat{b}_{\varepsilon j} \right). \tag{4.5}$$

Notice that only the $\hat{a}_{\varepsilon j}$ channel couples to the dot, while channel $\hat{b}_{\varepsilon j}$ remains completely decoupled in equilibrium. The total Hamiltonian

$$\hat{H} = \hat{H}_{\rm CNT} + \hat{H}_{\rm T} + \hat{H}_{\rm RS} \tag{4.6}$$

captures the essential physics of our set-up and, under equilibrium conditions, can be solved using Wilson NRG method [36] (see App.D for a brief discussion on the NRG procedure).

4.2.2 Global symmetries

Let us now discuss the continuous symmetries of the Hamiltonian Eq.(4.6). These symmetries are extremely useful, since they allow for an efficient numerical treatment of the problem. Throughout this Chapter, we shall focus on the simplest but physically relevant case of

$$T_j \equiv T, \qquad\qquad \gamma_j \equiv \gamma\,.$$

[2] Quasiparticle operators are normalized to satisfy $\{\hat{a}_{\varepsilon j}, \hat{a}_{\varepsilon' j'}\} = \delta(\varepsilon - \varepsilon')\,\delta_{jj'}$.

In this case, for $\Delta = 0$, the total SU(4) pseudo-spin operator

$$\hat{\mathbf{J}}^{\mathrm{SU(4)}} = \frac{1}{2}\sum_{j,j'=1}^{4}\left(\hat{d}_j^{\dagger}\boldsymbol{\lambda}_{jj'}\hat{d}_{j'} + \int d\varepsilon\ \hat{a}_{\varepsilon j}^{\dagger}\boldsymbol{\lambda}_{jj'}\hat{a}_{\varepsilon j'}\right) \tag{4.7}$$

commutes with the Hamiltonian in Eq.(4.6), and the SU(4) symmetrical Anderson model [70] is recovered. The $\boldsymbol{\lambda}$ vector above denotes the 15 generalized Gell-Mann matrices or some other set of matrices defining the SU(4) representation, and the operators Eq.(4.7) satisfy the SU(4) Lie algebra [88]. Finite inter-valley scattering or spin-orbit field implies $\Delta \neq 0$, and break the SU(4) symmetry down to SU(2) $\otimes$ SU(2). The latter are generated by the usual SU(2) pseudo-spin operators

$$\hat{\mathbf{J}}_{\kappa} = \frac{1}{2}\sum_{j,j'\in\kappa}\left(\hat{d}_j^{\dagger}\boldsymbol{\sigma}_{jj'}\hat{d}_{j'} + \int d\varepsilon\ \hat{a}_{\varepsilon j}^{\dagger}\boldsymbol{\sigma}_{jj'}\hat{a}_{\varepsilon j'}\right), \tag{4.8}$$

acting on the two Kramers doublets $\kappa = (1,2)$ and $\kappa = (3,4)$ (see Fig. 4.3). Here, $\boldsymbol{\sigma} = (\sigma_x, \sigma_y, \sigma_z)$ is the regular vector of the Pauli matrices. In addition to these SU(2) symmetries, the total charge is also conserved in each Kramers "channel"

$$\hat{Q}_{\kappa} = \frac{1}{2}\sum_{j\in\kappa}\left(\hat{d}_j^{\dagger}\,\hat{d}_j - 1/2 + \int d\varepsilon\ :\hat{a}_{\varepsilon j}^{\dagger}\hat{a}_{\varepsilon j}:\right), \tag{4.9}$$

with $:\ldots:$ referring to normal ordering.

4.3 Transport properties

In this Section we present the results for the spectral functions $A_j(\varepsilon)$ of the operators $\hat{d}_j^{\dagger}$ and evaluate the conductance across the dot under equilibrium conditions. The linear conductance can be computed directly within the NRG and is related to the equilibrium spectral function of the operators $\hat{d}_j^{\dagger}$. It reads

$$G(T) = \frac{e^2}{\hbar}\sum_j \alpha_j\Gamma_j \int_{-\infty}^{+\infty} d\varepsilon \left(-\frac{\partial f\,(\varepsilon,T)}{\partial\varepsilon}\right) A_j\,(\varepsilon)\,, \tag{4.10}$$

with $\Gamma_j = 2\pi T_j^2\rho_0$ the usual broadening parameter[3], and the asymmetry pre-factor $\alpha_j = \tan\gamma_j/\left(1+\tan\gamma_j\right)^2$, which depends on the source and drain couplings and is in general smaller than one. In Eq.(4.10) is the Fermi-Dirac distribution function and $A_j\,(\varepsilon)$ denotes the equilibrium spectral function of the j-th dot level,

$$A_j\,(\varepsilon) = -\frac{1}{\pi}\mathsf{Im}\left\{G_{j,j}^{\mathrm{R}}\,(\varepsilon)\right\}, \tag{4.11}$$

[3]Notice that in Ref. [61] $\Gamma_j' = \pi T_j^2\rho_0$ was introduced instead of the Γ_j we consider in this thesis.

where $G^{\mathrm{R}}_{j,j}(\varepsilon)$ is the Fourier transform of the retarded Green function

$$G^{\mathrm{R}}_{j,j}(t) = -\frac{i}{\hbar}\Theta(t)\left\langle\left\{\hat{d}_{j,\mathrm{H}}(t), \hat{d}^{\dagger}_{j,\mathrm{H}}(0)\right\}\right\rangle = \Theta(t)\left[G^{>}_{j}(t,0) - G^{<}_{j}(t,0)\right].$$

To compute $A_j(\varepsilon)$, we used the open-access *Budapest DM-NRG* code [89], that explicitly uses the symmetries of the system. As discussed above, for $\Delta = 0$ the system exhibits SU(4) symmetry. Therefore, by tuning the parameter Δ from 0 to some large value $\Delta \gg W$, for a singly occupied longitudinal level, we can follow the crossover from the the SU(4)-Kondo fixed point to the SU(2) $\otimes$ SU(2) one. In the next two subsections we shall study the manifestation of the crossover at the level of the spectral functions and of the linear conductance, respectively.

4.3.1 Spectral functions

The impact of the splitting Δ on the Kondo resonance is demonstrated in Fig.4.4a and 4.4b, where we display the total spectral function, $A_{\mathrm{tot}}(\varepsilon) = \sum_j A_j(\varepsilon)$, for two specific values of E_{d} and a relatively large ratio $U/\Gamma = 25$. For $\Delta = 0$ the occupation of the CNT levels is controlled by the 'dimensionless gate voltage', $N_{\mathrm{G}} = (-E_{\mathrm{d}} + U/2 + \Delta)/(U + \Delta/2)$, taking on integer values $N_{\mathrm{G}} = k = 1, 2, 3$ just in the middle of the Coulomb blockade valleys with k particles on the CNT.

Fig.4.4a displays the crossover from the SU(4) to the SU(2) regime for the case $N_{\mathrm{G}} = 1$ and several values of Δ. By particle-hole symmetry, the spectral functions for $N_{\mathrm{G}} = 3$ are the mirror images of the $N_{\mathrm{G}} = 1$ spectral functions, and we do not discuss them in detail. In the limit $\Delta = 0$, an SU(4) Kondo resonance arises due to quantum fluctuations of the ground state quadruplet. As expected [22], this resonance is pinned asymmetrically to the Fermi level, $\varepsilon = 0$. As soon as the splitting Δ becomes comparable to $T_{\mathrm{K}}^{\mathrm{SU(4)}}$ (extracted form the half width at half maximum of $A_{\mathrm{tot}}(\varepsilon)$), the spectral function maximum lowers and tends to be symmetrical around the Fermi energy. At the same time, two satellite peaks emerge at approximately $\pm\Delta$. These satellite peaks correspond to "electron-hole" excitations between the two Kramers pairs depicted in Fig.4.3. Notice that the value of the spectral function does not change at the Fermi energy as the SU(4) resonance gradually turns into a symmetrical SU(2) Kondo resonance. This implies, according to Eq.(4.10), that for $N_{\mathrm{G}} = 1$ the $T = 0$ temperature conductance is not suppressed by breaking the SU(4) symmetry[66, 67, 70, 71, 78]. However, as shown in the inset, the Kondo temperature is strongly reduced for $\Delta \gg T_K^{\mathrm{SU(4)}}$.

The situation is dramatically different for $N_{\mathrm{G}} = 2$ ($E_{\mathrm{d}} = -3U/2$). At this value of E_{d} there are two electrons on the CNT longitudinal shell. The Hamiltonian exhibits electron-hole symmetry, and the total spectral function is symmetrical for any value of Δ. As a consequence of the Friedel sum rule [90], the value of $A_{\mathrm{tot}}(\varepsilon = 0)$ is twice as large as it was for $N_{\mathrm{G}} = 1$.

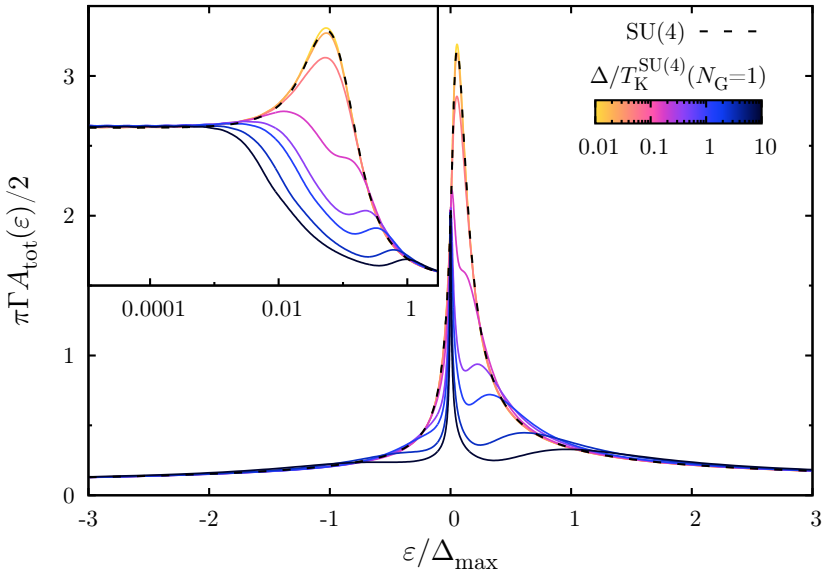

(a)

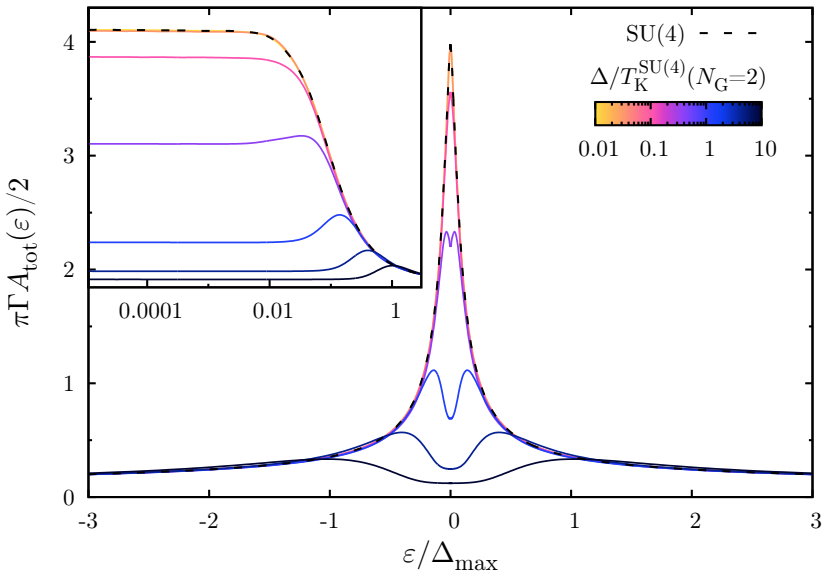

(b)

Figure 4.4: (a) and (b) the $T = 0$ temperature total spectral function $A_{\rm tot}(\varepsilon)$ as a function of the energy for different values of Δ. The colour scale is in units of $T_{\rm K}^{\rm SU(4)} = T_{\rm K}(\Delta = 0)$, where in (a) $T_{\rm K}^{\rm SU(4)} \simeq 0.000215\Gamma$ and the other parameters were fixed to $U = W$, $E_{\rm d} = -U/2$ ($N_{\rm G} = 1$), $\Gamma = U/25$. In (b) $E_{\rm d} = -3U/2$ ($N_{\rm G} = 2$) and $T_{\rm K}^{\rm SU(4)} \simeq 0.000155\Gamma$. The remaining parameters are the same as in (a). Insets: The evolution of the Kondo peak for different values of Δ in logarithmic scale.

For $N_G = 2$, however, a splitting $\Delta \gg T_K^{SU(4)}$ eliminates the ground state degeneracy of the isolated CNT, completely suppresses the Kondo resonance, and leads to the emergence of a 'pseudogap' of width $\sim \Delta$ in $A_{tot}(\varepsilon)$.

4.3.2 Linear conductance

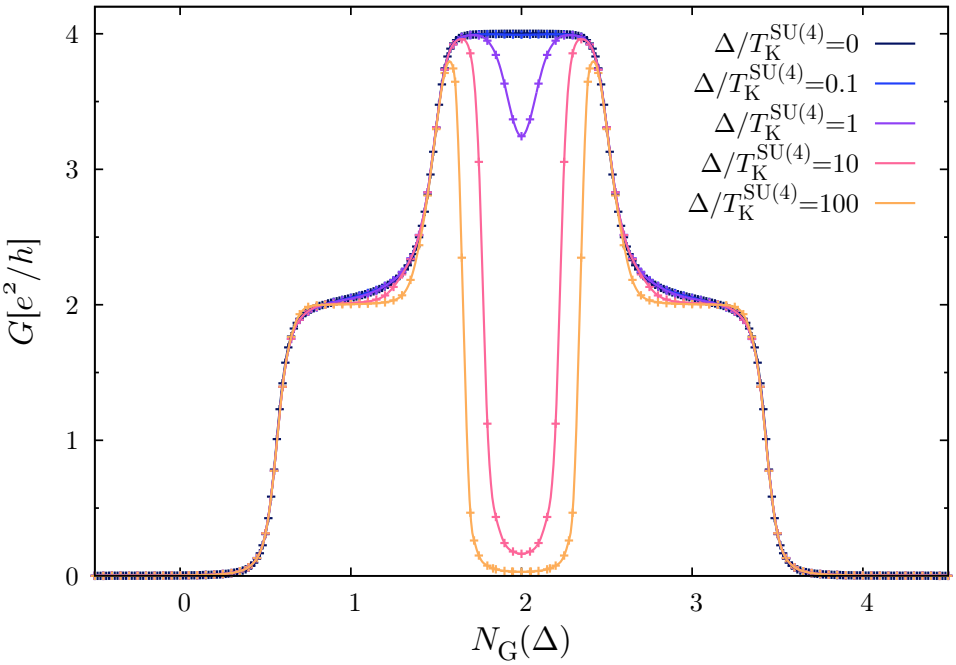

Figure 4.5: Linear conductance as a function of N_G for different values of the splitting Δ ($T_K^{SU(4)} = T_K(\Delta = 0, N_G = 1) = 0.000215\Gamma$). The parameters are $U = W$, $\Gamma = U/25$ and $T = 0$.

The crossover features in the spectral function are also reflected in transport characteristics. In Fig.4.5, we present the $T = 0$ temperature linear conductance as a function of N_G for several values of the splitting Δ. Similar to the spectral function, as a manifestation of the two electron SU(4)-Kondo state, the linear conductance also acquires its maximal value at the particle-hole symmetric point $N_G = 2$ in the SU(4) symmetrical case, $\Delta = 0$ [78]. This large conductance is, however, sensitive to Δ and is quickly suppressed for $\Delta \gg T_K^{SU(4)}$, as a consequence of the pseudogap appearing in the spectral function.

In contrast, for $N_G = 1$ and $N_G = 3$ a large Δ does not destroy the conductance at $T = 0$ temperature, which remains close to $2e^2/h$. Notice, however, that the origin of the conductance is different in the limits $\Delta = 0$ and $\Delta \gg T_K^{SU(4)}$. In the SU(4) limit, $\Delta \to 0$, incident conduction electrons pass through the quantum dot with probability 1/2 in all four channels. In

contrast, for $\Delta \to \infty$ the two empty levels and the corresponding channels do not conduct at all, while the other two have a perfect, unitary conductance due to the residual SU(2) Kondo effect. Since in these channels electrons pass through the dot with probability one, in this $\Delta \to \infty$ limit the linear conductance becomes noiseless [22]. Similar results for the dependence of the linear conductance on Δ and the applied gate have been obtained in Ref. [78] (see dashed curves in Fig. 4 therein).

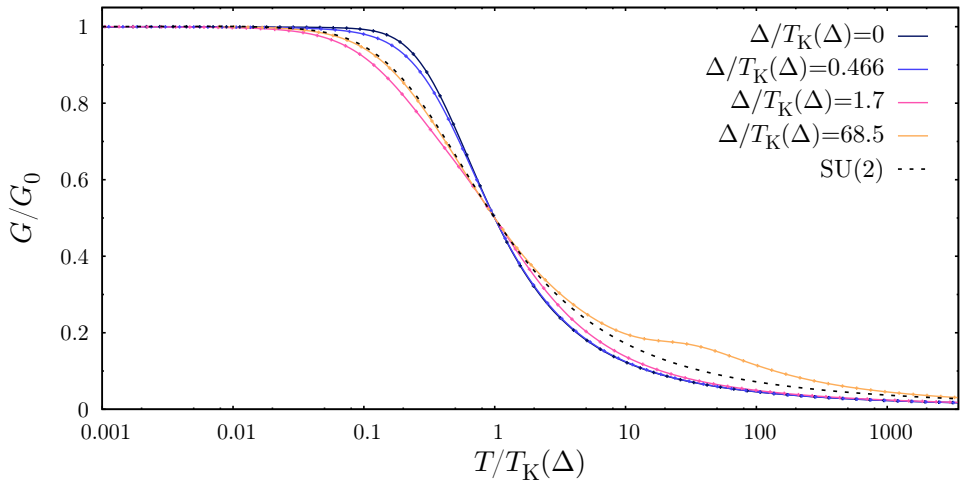

Figure 4.6: DM-NRG linear conductance as a function of T/T_K for different values of the splitting Δ. The parameters are as in (a) except for $E_d = -U/2$. Here $T_K(\Delta)$ stands for $T_K^{HCM}(\Delta)$ defined in the main text.

Another useful way to visualise the crossover between the SU(4) and SU(2) regimes is to consider the temperature dependence of the linear conductance, shown for $N_G = 1$ in Fig.4.6. To explore universal scaling, we have rescaled the temperature by the Kondo temperature $T_K^{HCM}(\Delta)$, defined as the temperature at which the conductance is reduced to half of its $T = 0$ temperature value [22]. For Δ much smaller than $T_K^{HCM}(\Delta)$, conductance curves show SU(4) universality and lie on the top of each other. As soon as Δ becomes comparable with $T_K^{HCM}(\Delta)$, however, universality is lost, the Kondo temperature lowers and a peak emerges at approximately Δ. For very large values of $\Delta/T_K^{HCM}(\Delta)$, the curves become universal again, but they now follow a simple SU(2)-scaling. The two universal curves for $\Delta = 0$ and $\Delta > U$ are associated with the SU(4) and SU(2) fixed points, and can be derived from the corresponding Kondo models (see App.E for further details).

4.4 Kondo temperature

As we have already discussed in Chap.2 for the pure SU(2) case, the Kondo temperature fully characterises the Kondo correlated state. In contrast to

the previous Chapters, where we extracted the Kondo temperature in the asymmetric case ($U \to \infty$ and $E_{\rm d} \neq U/2$) close to the first Coulomb peak, here we will study the behaviour of the Kondo temperature as a function of the symmetry breaking parameter Δ in the middle of the Coulomb diamonds with $N_{\rm G} \approx 1$ and $N_{\rm G} \approx 3$.

Indeed, studying the spectral function and the linear conductance as a function of the splitting Δ, we have already realised that for $N_{\rm G} \approx 1$ and $N_{\rm G} \approx 3$ the Kondo temperature is dramatically suppressed for large Kramers pair splittings $\Delta > T_{\rm K}^{\rm SU(4)}$ (e.g. see the spectral function Kondo peak width in Figs.4.4). This suppressed SU(2) Kondo temperature, $T_{\rm K}^{\rm SU(2)}$, can be estimated by carrying out a two-step RG procedure [91].

Considering $N_{\rm G} \approx 1$ and $N_{\rm G} \approx 3$ the extended Anderson Hamiltonian can be mapped onto the simpler spin exchange Hamiltonian [31, 52] of the form $\hat{H}_{\rm int} = J\,\mathbf{S}\cdot\mathbf{s}$, describing the interaction of a magnetic moment $\mathbf{S}$ at the origin with the local spin density $\mathbf{s}$ of the conduction electrons, with $J > 0$ an anti-ferromagnetic exchange coupling. Here the symmetry of the exchange Hamiltonian plays a crucial role and affects the Kondo temperature. The SU(N)-Kondo model [92], in particular, [4] yields a Kondo temperature $T_{\rm K}^{\rm SU(N)} \approx W\, e^{-2/N\rho_0 J}$, implying that a larger N appreciably enhances $T_{\rm K}$. This behaviour can be obtained by carrying out a renormalization group analysis for the effective exchange coupling (vertex functions) describing scattering processes at energy ϵ . To leading logarithmic order, the dimensionless effective exchange coupling, $j(\epsilon) \equiv \rho_0 J_{\rm eff}$, satisfies the RG equation

$$\frac{{\rm d}j}{{\rm d}x} = \frac{N}{2}\, j^2, \tag{4.12}$$

with $x = \ln(W/\epsilon)$ the scaling parameter, and diverges logarithmically at the Kondo scale $\epsilon = T_{\rm K}^{\rm SU(N)}$.[5]

Let us now focus on the Kondo regime ($\Gamma \ll U$) of a CNT quantum dot with $N_{\rm G} = 1$ electrons trapped inside a shell. In this regime, assuming further $\Delta \ll U$, the interaction of the electrons with the nanotube can be described by an exchange Hamiltonian of almost perfect SU(4) symmetry [70]. The structure of the vertex function (effective exchange amplitude), however, depends on the energy of the electrons scattered. Electrons of very high energy, $\epsilon \gg \Delta$, can induce transitions between all four levels, and experience an SU(4) exchange process. Correspondingly their scattering amplitude satisfies Eq.(4.12) with $N = 4$. Electrons of energy $\epsilon \ll \Delta$, however, can only flip the states within the lower Kramers doublet, and their scattering amplitude obeys Eq.(4.12) with $N = 2$. Matching the $N = 2$ and $N = 4$

[4] The SU(N) Hamiltonian is defined in terms of an N-fold degenerate level as $\hat{H}_{\rm int} = (J/2)\,\hat{X}$, with $\hat{X}$ the exchange operator.

[5] Both ϵ and W can be considered as scaling variables here.

solutions of Eq.(4.12) at $x = \ln(W/\Delta)$ we thus obtain

$$j(\epsilon < \Delta) = \frac{1}{\ln\left[\epsilon\ \Delta/\left(T_K^{\mathrm{SU(4)}}\right)^2\right]}\ .$$

The energy where the perturbative RG breaks down can be identified as the Kondo temperature T_{K}, and it is expressed as

$$T_{\mathrm{K}}\left(\Delta\right) \propto \frac{U^2}{\Delta}\, e^{-1/j}, \tag{4.13}$$

predicting a $\sim 1/\Delta$ decay of the Kondo temperature for $\Delta < U$. Notice that in this expression, we replaced the bandwidth by U, which serves as an upper cutoff for spin exchange processes within the Anderson model.

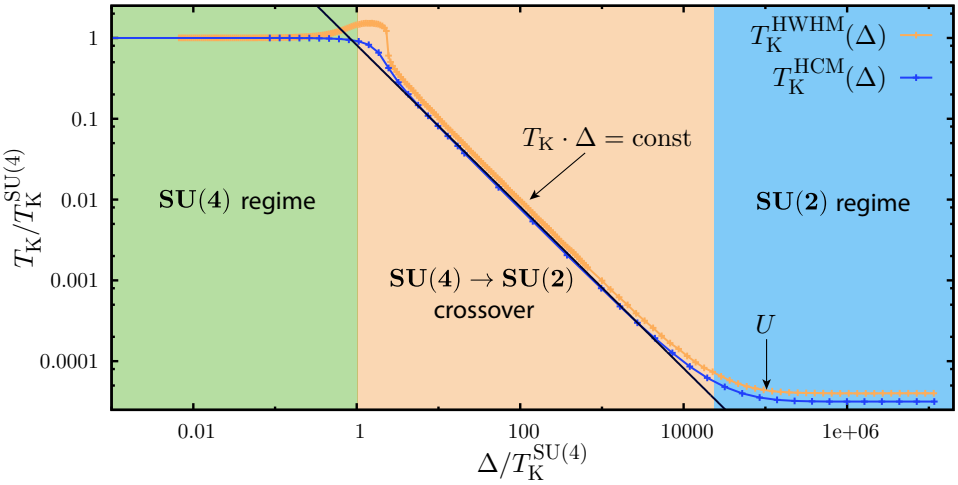

Figure 4.7: Evolution of the Kondo temperature as a function of Δ. The Kondo temperature was extracted from the NRG data in two different ways: *i*) as the half width at half maximum of the total spectral function (HWHM), *ii*) half conductance maximum (HCM). The other parameters were fixed to: $U = W$, $E_{\mathrm{d}} = -U/2$ ($N_{\mathrm{G}} = 1$), $\Gamma = U/25$ and $T = 0$.

As we now demonstrate, the analytical expression Eq.(4.13) is in good agreement with our NRG calculations. The definition of T_{K} is not unique, we have therefore extracted it from the NRG data in two different ways: in addition to the half conductance scale $T_{\mathrm{K}}^{\mathrm{HCM}}(\Delta)$ defined earlier, we also introduced the Kondo scale $T_{\mathrm{K}}^{\mathrm{HWHM}}(\Delta)$ as the half width at half maximum of the spectral function for the $\hat{d}_j$ operators. Both Kondo temperatures are shown in Fig.4.7, where three regimes can be delineated: For $\Delta < T_{\mathrm{K}}^{\mathrm{SU(4)}}$, the system is governed by SU(4) physics, and T_{K} agrees with the SU(4) Kondo temperature. This is followed by a 'crossover region', $T_{\mathrm{K}}^{\mathrm{SU(4)}} < \Delta < U$,

where an SU(4) → SU(2) crossover takes place as a function of temperature or energy, but below Δ an SU(2) Kondo state emerges with a suppressed Kondo temperature given by Eq.(4.13). Finally, for $\Delta > U$ only one Kramers doublet remains active, and an SU(2) Kondo behaviour appears at all scales with a T_K independent of Δ.
Having analysed the crossover for the SU(4) → SU(2) Kondo effect due to finite SOI or valley mixing we turn now our discussion to the inclusion of a finite magnetic field.

4.5 Magneto-transport properties

A finite magnetic field turns out to be crucial to disentangle the effects of SOI and valley mixing [79]. As shown below, both the spectral function and the linear conductance display qualitatively different features depending on the direction of the applied magnetic field. In finite magnetic field the $N_G = 1$ (centre of the first Coulomb valley) condition becomes $E_d = -U/2 - (E_4(B_\parallel) + E_3(B_\parallel))/2$, whereas $N_G = 2$ (particle-hole symmetric point) remains $E_d = -3U/2$.

4.5.1 Parallel magnetic field

Spectrum The energy levels of the CNT Hamiltonian, Eq.(4.1), easily follow from the discussion in App.C. They read

$$E_{1,4} = E_d + \frac{1}{2} g_s B_\parallel \pm \frac{1}{2}\sqrt{\Delta_{KK'}^2 + \left(\Delta_{SO} + 2g_{orb}B_\parallel\right)^2}, \tag{4.14a}$$

$$E_{2,3} = E_d - \frac{1}{2} g_s B_\parallel \pm \frac{1}{2}\sqrt{\Delta_{KK'}^2 + \left(\Delta_{SO} - 2g_{orb}B_\parallel\right)^2}, \tag{4.14b}$$

where $g_s(g_{orb})$ is the Landé spin(orbital) g-factor and $B_\parallel$ the amplitude of the parallel magnetic field.

The resulting spectrum for occupancies with $N = 1, 2, 3$ of the CNT is shown in Fig.4.8. It is interesting to notice the crossing of the states $|3\rangle$ and $|4\rangle$ in the sector $N = 1$ (circles in Fig.4.8(c)). It can occur if

$$\frac{|\Delta_{KK'}|}{|\Delta_{SO}|} < \sqrt{\frac{4g_{orb}^2}{g_s^2} - 1}, \tag{4.15}$$

at a magnetic field value given by

$$B_s = \sqrt{\frac{\Delta_{SO}^2}{g_s^2} - \frac{\Delta_{KK'}^2}{4g_{orb}^2 - g_s^2}}. \tag{4.16}$$

Thus, the ground states in the one-particle sector of the Hilbert space switch from $|4\rangle$ to $|3\rangle$ for $B_\parallel > B_s$. Moreover, an avoided crossing occurs at

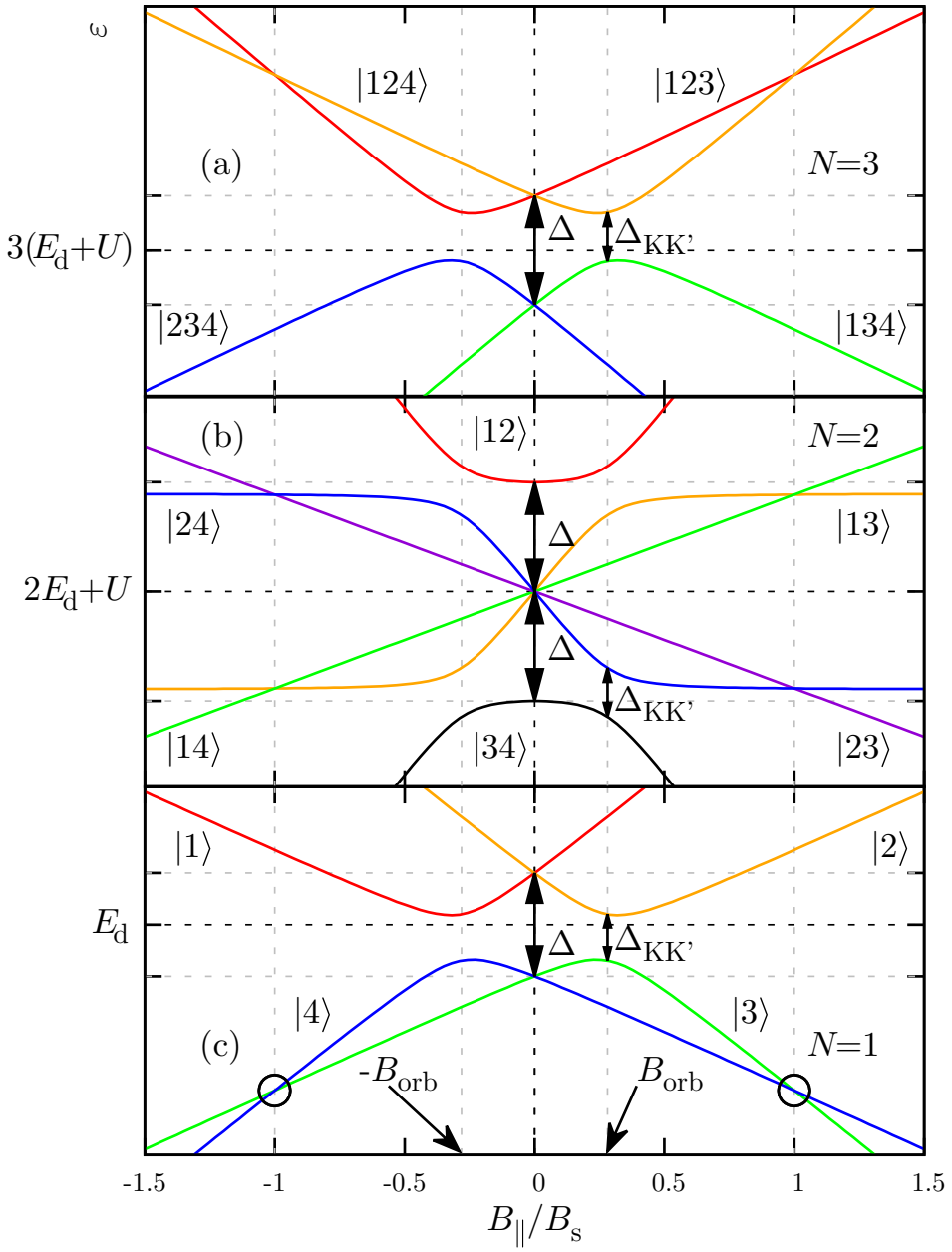

Figure 4.8: Parallel magnetic field dependence of the energy levels for (a) $N = 3$, (b) $N = 2$ and (c) $N = 1$ Hilbert space sectors. Black circles indicate ground-state levels crossing. The parameters are $U = W$, $\Gamma = 0.04W$, $E_d = -U/2$, $g_s = 2$, $g_{orb} = 1.83g_s$ and $\Delta_{KK'} = \Delta_{SO}/2 = 2.5\Gamma$. They are chosen such that the inequality Eq.(4.15) is fulfilled.

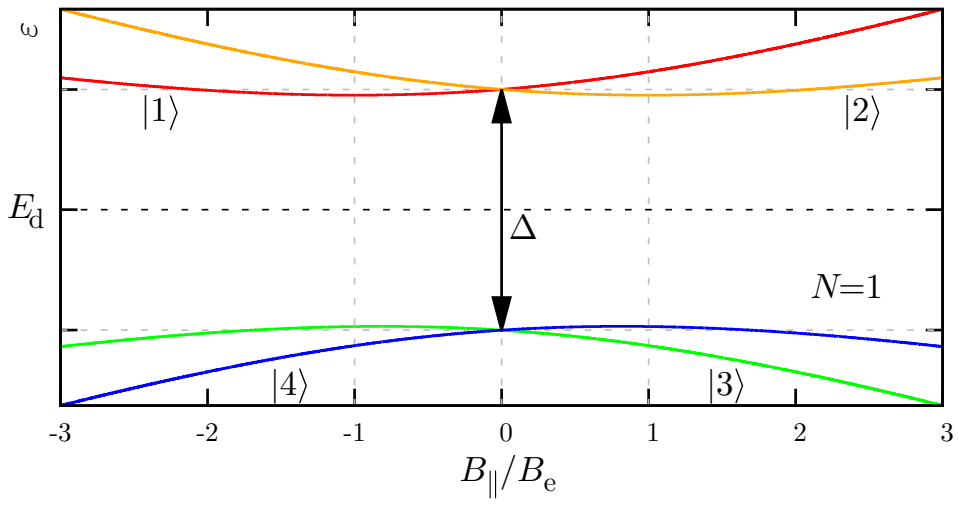

Figure 4.9: Evolution of the single particle energy levels in parallel magnetic field. The parameters are $\Gamma = 0.04W$, $U = W$, $E_d = -U/2$, $\Delta_{SO} = 2.5\Gamma$, $g_s = 2$, $g_{orb} = 1.83 g_s$ and $\Delta_{KK'} = 10\Delta_{SO}\sqrt{4g_{orb}^2/g_s^2 - 1}$. For this choice of parameters the inequality Eq.(4.15) is not satisfied and no level crossing is possible at finite magnetic field. Here, $B_e > 0$ corresponds to the value of $B_\parallel$ such that the state $|2\rangle$ shows a minimum.

$B_\parallel = B_{orb} = \Delta_{SO}/(2g_{orb})$. If Eq.(4.15) is not satisfied, the crossing of the two states in the $N = 1$ sector cannot be achieved, as it is shown in Fig.4.9.

Focusing on the $N = 2$ sector of the Hilbert space (see Fig.4.8(b)), one notices that again an avoided crossing occurs at $B_{orb} = \Delta_{SO}/2g_{orb}$, which becomes an exact crossing for $\Delta_{KK'} = 0$. In this special case the two states $|34\rangle$ and $|24\rangle$ are degenerate. Finally, no ground state crossing is observed for $N = 3$ (see Fig.4.8(a)).

Using these considerations, we can build up the ground state configuration of the system as a function of the applied parallel magnetic field and of the orbital energy E_d (see Fig.4.10a). By inspecting where a crossing occurs (dashed lines in Fig.4.10a), it is possible to capture the so-called "Kondo revivals" [78], where the Kondo effect is restored for some specific values of the applied magnetic field. As Fig.4.10a reveals, revivals are expected around $B_\parallel = B_{orb}$ for $\Delta_{KK'} \simeq 0$ in the $N = 2$ valley, and around $B_\parallel = B_s$, if the inequality Eq.(4.15) is fulfilled, in the $N = 1$ valley.

This ground-state analysis was for the first time performed in Ref. [78] (see Sec. IV) where the effects of a finite SOI splitting were investigated. In our work we also include a finite valley mixing which, as shown in Fig.4.9, can preclude a crossing and thus, as demonstrated below, a Kondo revival. These considerations are reflected in the behaviour of the spectral function and of the linear conductance.

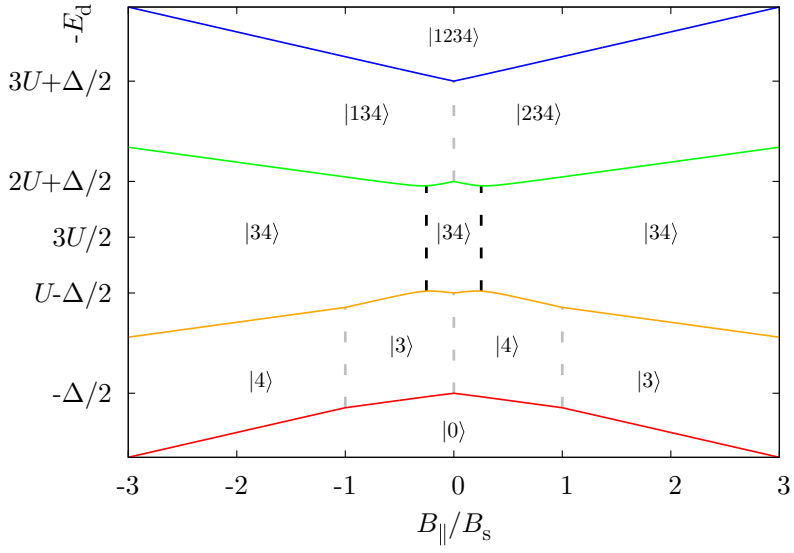

(a)

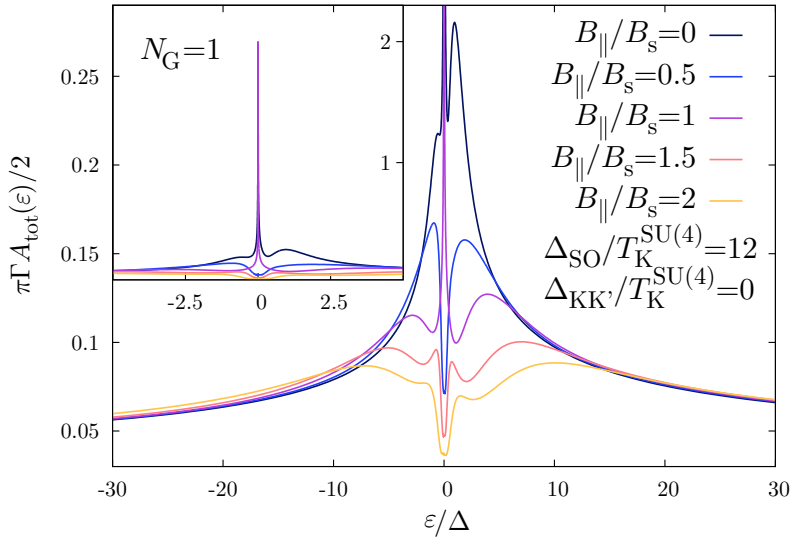

(b)

Figure 4.10: (a) Ground state configuration as a function of the energy E_d and the applied parallel magnetic field. Grey dashed lines indicate degeneracies. The black dashed line indicates $B_\parallel = B_{orb}$. Parameters are, as in Fig.4.8, $U = W$, $\Gamma = 0.04W$, $E_d = -U/2$, $g_s = 2$, $g_{orb} = 1.83g_s$ and $\Delta_{KK'} = \Delta_{SO}/2 = 2.5\Gamma$. (b) close-up image of the spectral function as a function of the frequency for $\Delta_{KK'} = 0$ and several values of the parallel magnetic field in the middle of the Coulomb valley with $N_G = 1$ at $T = 0$. Inset: Full spectral function. The unitary limit is reached for $B_\parallel = 0$ while the full Kondo revival is obtained at $B_\parallel = B_s$.

Spectral function The spectral function is shown for several values of the parallel magnetic field in Fig.4.10b. In the absence of the magnetic field (black curve) it shows a Kondo peak at the Fermi level and two satellite peaks located at $\varepsilon \simeq \pm\Delta = \pm(E_{1(2)}(0) - E_{3(4)}(0))$. As we switch on the magnetic field, the Kondo peak lowers and then splits into two resonances located at $\varepsilon \simeq \pm(E_3(B_\parallel) - E_4(B_\parallel))$, due to processes representing quantum fluctuations within the lowest Kramers pair. Increasing the magnetic field, the peaks merge again into one at $B_\parallel = B_s$ (violet curve) and the spectral function recovers the unitary value at $\varepsilon = 0$ (see inset of Fig.4.10b). For larger values of $B_\parallel$ the Kondo peak splits again. Regarding the satellite peaks, they lower, broaden and shift towards higher energies. We find that at $B_\parallel = B_s$ the leftmost one is due to a resonance in the third and fourth components ($A_3(\varepsilon) = A_4(\varepsilon)$, $E_3 = E_4$ for $B_\parallel = B_s$) of the spectral function. On the other hand, the rightmost peak has an internal substructure being the sum of a maximum in the first, $A_1(\varepsilon)$, and second, $A_2(\varepsilon)$, components. Increasing furthermore the magnetic field ($B_\parallel > B_s$) the satellites peaks lower and broaden, the leftmost being determined essentially by the component corresponding to the ground state, $A_3(\varepsilon)$. Despite the fact that the energy separation, $E_2(B_\parallel) - E_1(B_\parallel)$, of the excited states $|1\rangle$ and $|2\rangle$ is monotonically increasing, the total spectral function does not show a split of the corresponding resonances in this range of investigated parallel magnetic field values ($0 \leq B_\parallel \leq 2B_s$ with $B_s \simeq 90T_K(\Delta)$). Our results on the impact of a parallel magnetic field on the spectral function of a CNT are consistent with the NRG analysis performed in Ref. [71] when $\Delta_{SO} = \Delta_{KK'} = 0$.

Linear Conductance In Fig.4.11 we show the linear conductance of the system as a function of the applied parallel magnetic field and for a fixed ratio of $\Delta/T_K^{SU(4)} \simeq 12$. In Fig.4.11(a) the conductance shows, as expected, the Kondo revival at $B_\parallel = B_s$. Moreover, the width of the Kondo peak is proportional to $T_K(\Delta)$. By increasing the valley mixing term $\Delta_{KK'}$ the resonance shifts towards $B_\parallel = 0$ and, in case $\Delta_{KK'}/\Delta_{SO}$ does not fulfil Eq.(4.15), the Kondo revival disappears (black solid line).

In the $N_G = 2$ valley, Fig.4.11(b), the valley mixing term acts slightly differently. For $\Delta_{KK'} = 0$ the SU(4)-Kondo effect in $B_\parallel = 0$ is essentially suppressed for this set of parameters ($\Delta/T_K^{SU(4)} \simeq 12$) and hence a Kondo peak is present only at $B_\parallel = B_{orb}$. Switching on the valley mixing, since B_{orb} is not $\Delta_{KK'}$ dependent, results in the suppression of this resonance without any shift. We notice that Kondo revivals have indeed been seen in experiments on CNT-dots in parallel fields [76].

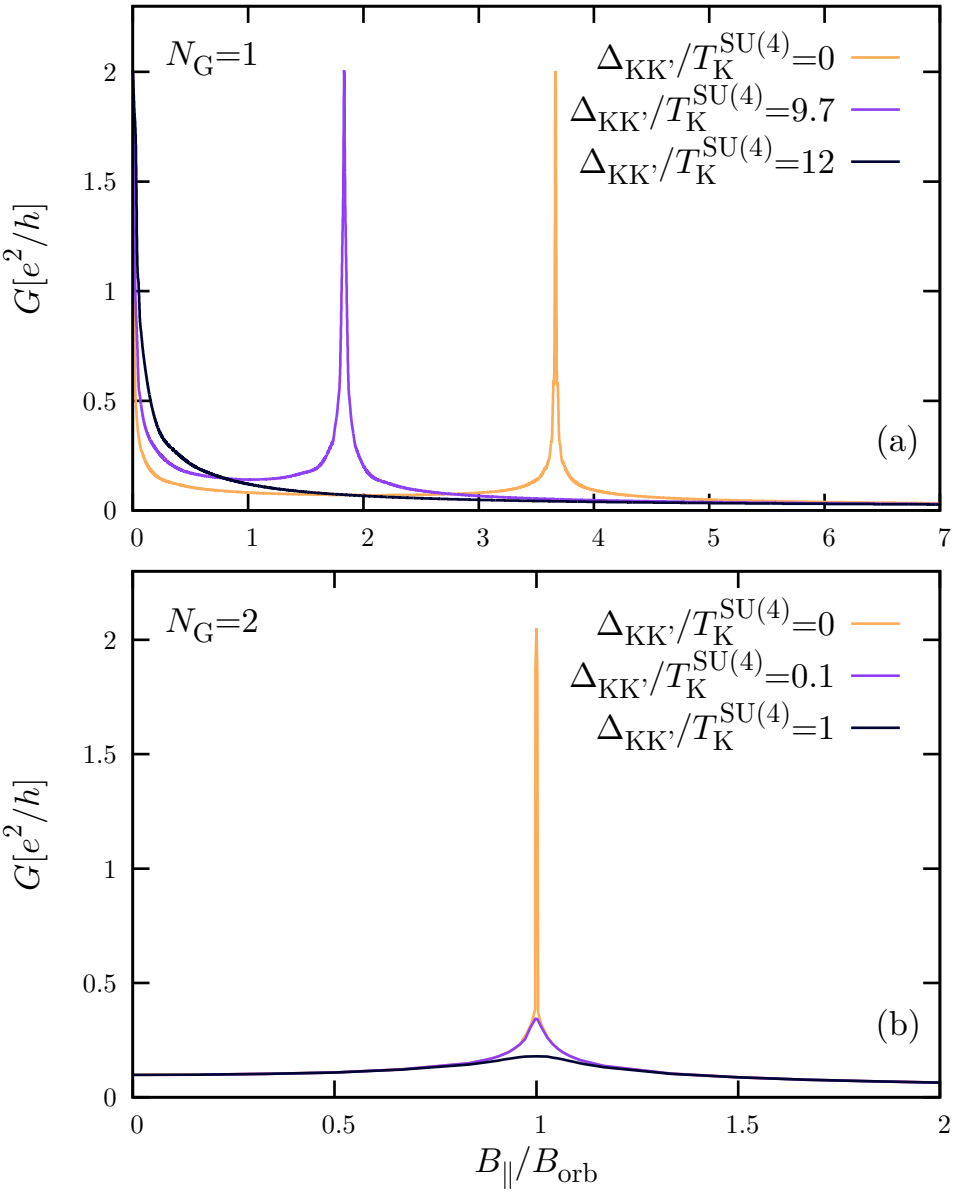

Figure 4.11: Linear conductance as a function of the parallel magnetic field (a) in the middle of the Coulomb valley, $N_G = 1$, and (b) at the particle-hole symmetric point, $N_G = 2$ at $T = 0$. Δ_{SO} and $\Delta_{KK'}$ were varied such that $\Delta/T_K^{SU(4)}$ remained constant.

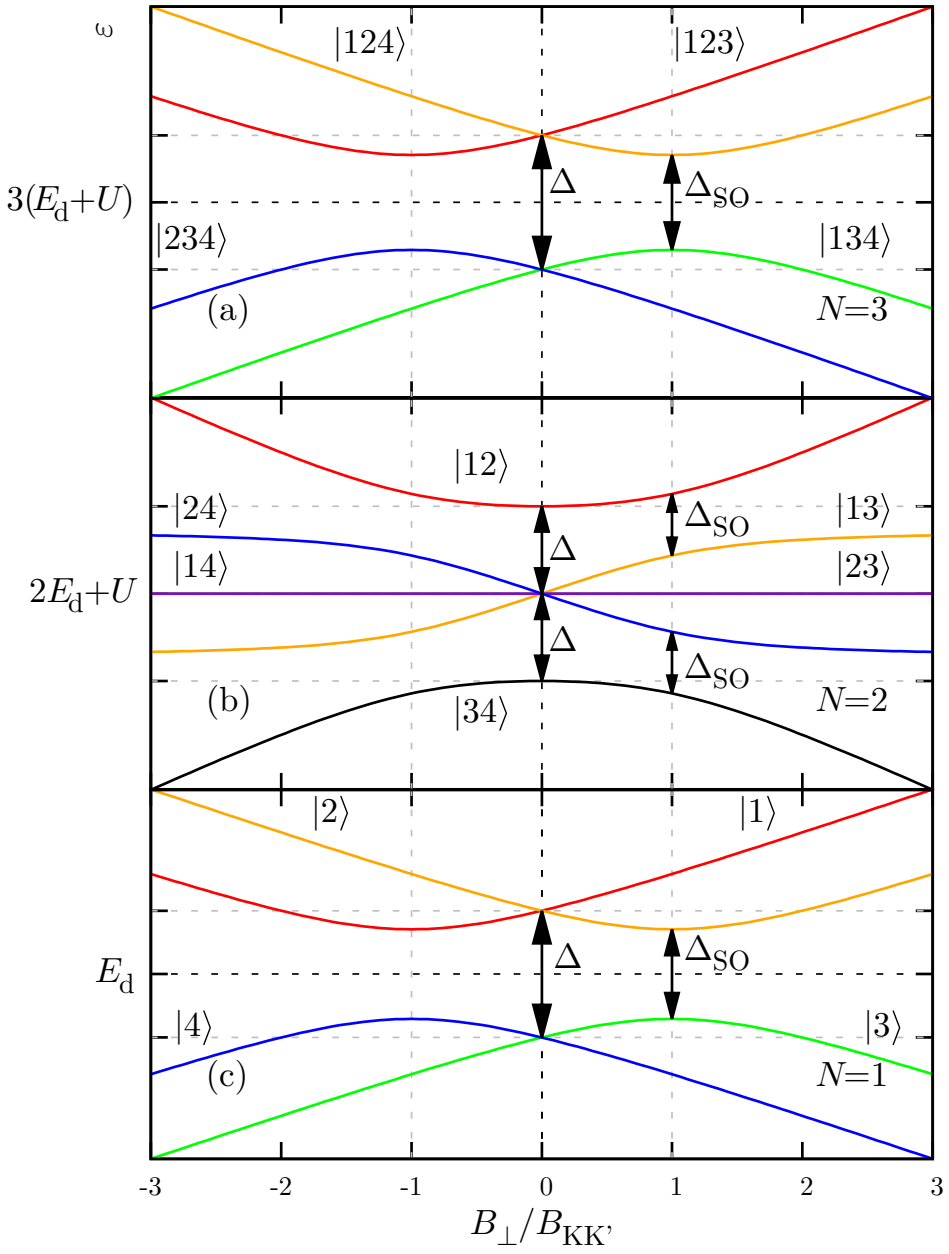

Figure 4.12: Perpendicular magnetic field dependence of the energy levels for (a) $N = 3$, (b) $N = 2$ and (c) $N = 1$ particle number.

4.5.2 Perpendicular magnetic field

Spectrum A magnetic field perpendicular to the CNT axis couples only to the spin degree of freedom. As it follows from App.C, the energy levels of the CNT Hamiltonian Eq.(4.1) in the presence of a perpendicular magnetic field read

$$E_{1,4} = E_{\rm d} \pm \frac{1}{2}\sqrt{\Delta_{\rm SO}^2 + (\Delta_{\rm KK'} + g_{\rm s}B_\perp)^2}, \tag{4.17a}$$

$$E_{2,3} = E_{\rm d} \pm \frac{1}{2}\sqrt{\Delta_{\rm SO}^2 + (\Delta_{\rm KK'} - g_{\rm s}B_\perp)^2}, \tag{4.17b}$$

where $B_\perp$ is the amplitude of the perpendicular magnetic field. The corresponding spectrum is shown in Fig.4.12. It shows clear qualitative differences with respect to the parallel case. For example, no ground state crossing is observed for $N = 1$ and $N = 3$: the distance between the lowest energy levels first increases and then saturates to the valley mixing strength $\Delta_{\rm KK'}$. An avoided crossing between excited states occurs for $B_\perp = \pm B_{\rm KK'}$, where $B_{\rm KK'} = \Delta_{\rm KK'}/g_{\rm s}$. On the other hand, in the $N = 2$ sector, the avoided crossing at $B_\perp = \pm B_{\rm KK'}$ is between the ground state $|34\rangle$ and the state $|24\rangle$. Hence an exact crossing occurs for $\Delta_{\rm SO} = 0$. Comparing Fig.4.12 and 4.8 we indeed see that the SOI and the valley mixing exchange their role switching from parallel to perpendicular magnetic fields. Following the same argument of the previous Section, this revels that the Kondo revival can be achieved only in the $N_{\rm G} = 2$ valley for $B_\perp = B_{\rm KK'}$.

Spectral function We analyse the behaviour of the total spectral function at $N_{\rm G} = 1$ for several values of the perpendicular magnetic field in Fig.4.13. Since the Kondo revival is not possible in the first valley, the Kondo peak monotonically splits into two sub-peaks located at $\varepsilon = \pm(E_3(B_\perp) - E_4(B_\perp))$. Furthermore, two satellite peaks are visible. The rightmost resonance is the sum of two peaks in $A_1(\varepsilon)$ and $A_2(\varepsilon)$, whereas the leftmost one is essentially determined by the fourth component, $A_4(\varepsilon)$, corresponding to the ground state level. As in the parallel case, no splitting of the satellites is observed in the investigated magnetic field range. For $B_\perp \geq B_{\rm KK'}/2$ the central Kondo peaks merge with the lateral satellites.

Linear conductance In Fig.4.14 we show the linear conductance as a function of the applied perpendicular magnetic field. Since we consider a large Kramers splitting value, the SU(4) Kondo effect is almost completely suppressed at zero magnetic field. On the other hand, a perfect Kondo revival is obtained only if $\Delta_{\rm SO} = 0$ at $B_\perp = B_{\rm KK'}$. However, for $\Delta_{\rm SO} \neq 0$, the Kondo resonance is suppressed because the degeneracy between the sates $|34\rangle$ and $|24\rangle$ is lifted and the fluctuations of the quantum numbers referring to these states become energetically unfavourable.

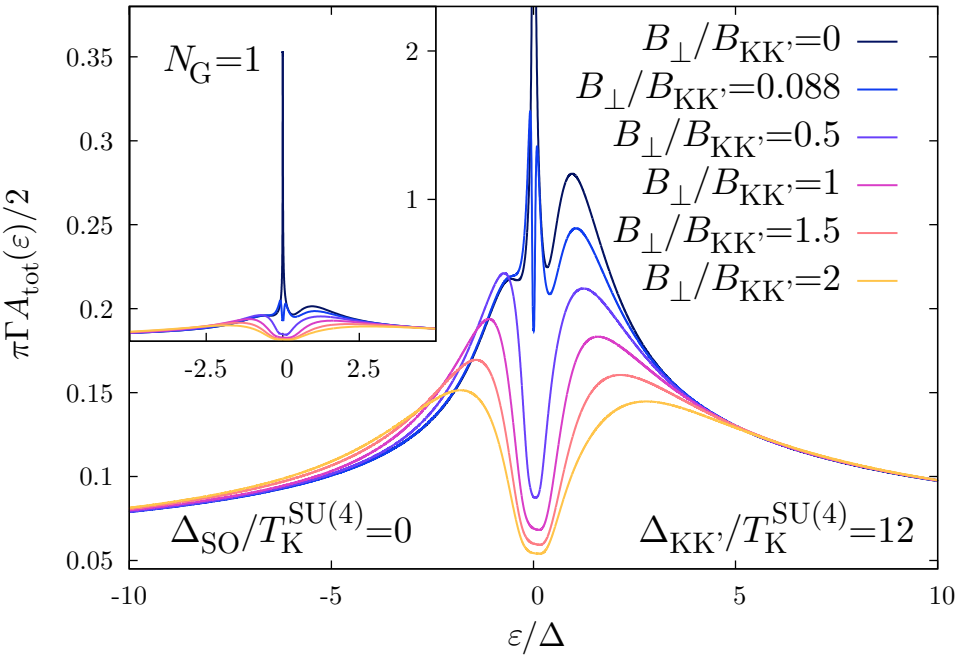

Figure 4.13: Close-up structure of the total spectral function as a function of the frequency for several values of the perpendicular magnetic field, for $N_G = 1$ and $T = 0$. Inset: Full spectral function, showing that the unitary limit is only obtained for $B_\perp = 0$.

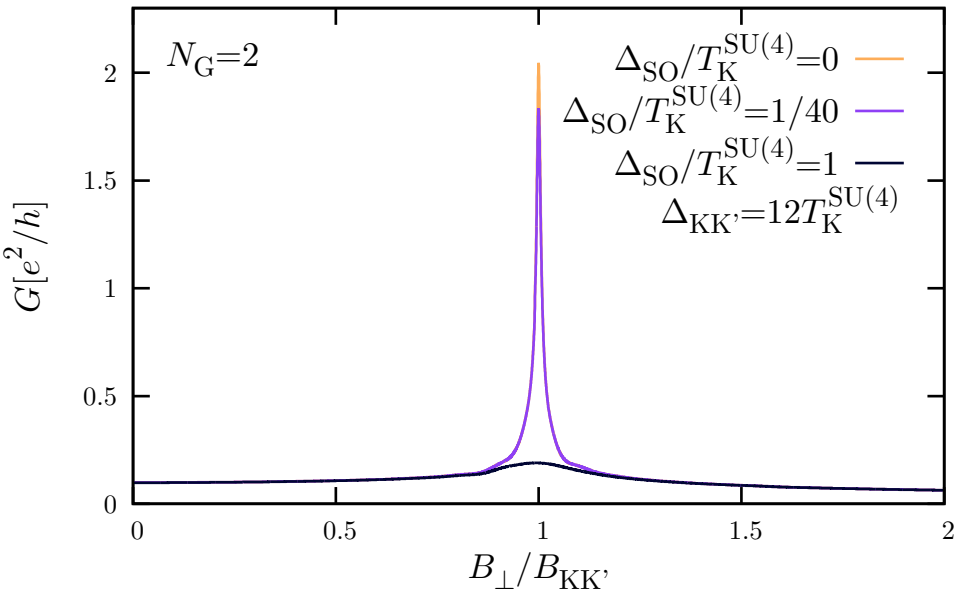

Figure 4.14: Linear conductance as a function of the perpendicular magnetic field at the particle-hole symmetric point, $N_G = 2$ at $T = 0$.

4.6 Application: description of an experiment

Parts of this Section have been accepted for publication in Nature communications in cooperation with Michael Niklas, Sergey Smirnov, Magdalena Margańska, Ngoc-Viet Nguyen, Wolfgang Wernsdorfer, Jean-Pierre Cleuziou and Milena Grifoni in Ref. [63].

In this Section we present the results we computed to describe a CNT quantum dot realised in Grenoble by the group of Jean-Pierre Cleuziou[63, 84]. The device under study (see Fig.4.15) consists of a semiconducting CNT, grown in-situ on top of two platinum contacts, used as normal metal source and drain leads (for the details of the device fabrication see Ref. [84]). The CNT junction is suspended over an electrostatic gate and can be modelled as a single semiconducting quantum dot of size imposed by the contact separation ($\approx$ 200 nm).

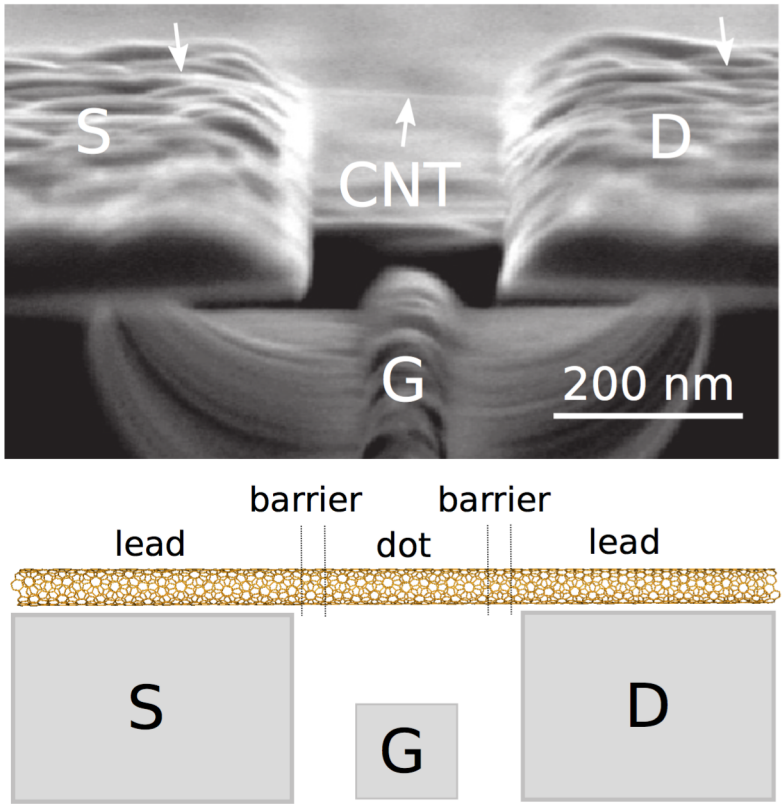

Figure 4.15: (upper panel) Scanning electron microscopy of the CNT based quantum dot. (lower panel) Sketch of the experimental set-up. Adapted form Ref. [63].

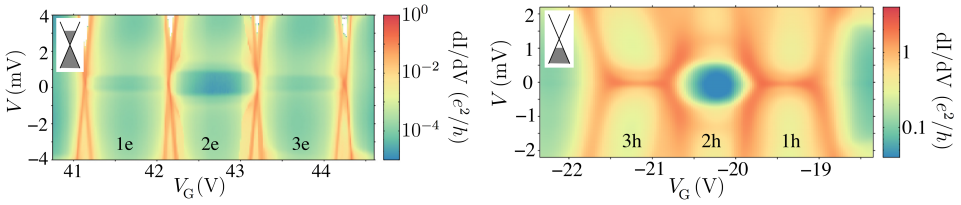

Figure 4.16: (a) and (b) experimentally measured differential conductance of a CNT based quantum dot as a function of the applied gate and bias voltages. In (a) we have the weak coupling regime in the electron side whereas in (b) the strong coupling regime in the hole one. Adapted from [63].

The measurements we show in Figs.4.16 were performed at a mixing chamber temperature of about $T_{\text{exp}} = 30$ mK. This value sets a lower bound to the actual electronic temperature and it is the one we considered in our simulations to reproduce the linear conductance gate dependence. As it is possible to appreciate in Figs.4.16, it is experimentally possible to measure the conductance dependence of such a system as a function of the applied bias and gate voltages. This results in a four fold pattern swiping the gate from positive gate values (Fig.4.16a), in the so called electron regime, to negative ones, in the hole regime (Fig.4.16b). Here we report only two shells but actually it is experimentally possible to measure this four fold pattern for several shells continuously as a function of the gate (see for example Fig.1(b) in Ref. [84]). In Figs.4.16 we labelled the Coulomb valleys either with the number of holes in the specific shell in Fig.4.16b or considering the number of electrons in the shell in Fig.4.16a.

In the electron regime the CNT is charged with extra electrons by means of a positive gate values and the coupling to the leads decreases increasing the gate voltage. In contrast, in the hole one the CNT is depleted and the coupling to the leads increases lowering the gate voltage. For this reason, the conductance shows very different features in the two different regimes in Figs.4.16. In Fig.4.16a the transport characteristics are dominated by the sequential and co-tunneling tunnelling features because the ratio $U/\Gamma \gg 1$ and the Kondo temperature is much lower than the device one. In this regime, the Coulomb blockade features are clearly visible and co-tunnelling steps are present in the middle of the Coulomb diamonds. They are of the same nature of the ones we obtained with the RTA in Sect.3.4.2. Notice that the temperature is such that $\Gamma \simeq k_{\text{B}}T \gg k_{\text{B}}T_{\text{K}}$ and thus the results in Fig.4.16a were actually obtained in the intermediate coupling regime where the Coulomb blockade peak widths are Γ-broadened and their heights are actually determined also by the energy of coupling to the leads. In contrast, in Fig.4.16b it is easy to notice the presence of Kondo ridges in the 3-h and

1-h Coulomb valleys. Here we are clearly in a Kondo correlated regime. In the following we shall quantify this statement by means of a DM-NRG study of the zero bias trace from Fig.4.16b.

DM-NRG study of the Kondo correlated regime In the following let us focus on the zero bias trace of the conductance from Fig.4.16b. For this specific CNT shell let us evaluate the linear conductance of the system as a function of the applied gate in order to find the best set of parameters to describe such a zero bias trace.

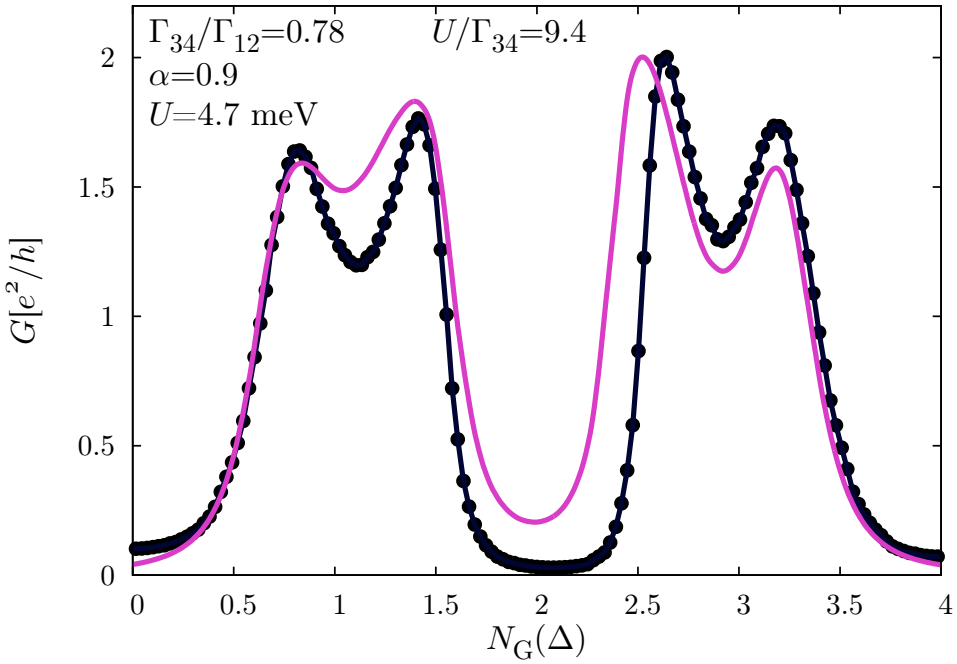

Figure 4.17: (Purple solid lines) DM-NRG linear conductance as a function of the dimensionless gate N_G and (Black bullets) experimentally measured linear conductance. In order to compute the linear conductance we imposed in our simulations $T = 30$mK being this the experimentally measured temperature of the chamber containing the CNT quantum dot.

In Fig.4.17 we compare the experimentally measured linear conductance (black bullets) with the DM-NRG one (purple solid lines) computed for the set of parameters we reported in the picture. As it is possible to notice in Fig.4.17 there is an appreciable asymmetry between the Coulomb peaks corresponding to $N_G \simeq 0.5, 1.5$ and the ones with $N_G \simeq 2.5, 3.5$. In order to reproduce such a feature we choose $\Gamma_1 = \Gamma_2 = \Gamma_{12}$ different with respect to $\Gamma_3 = \Gamma_4 = \Gamma_{34}$, being their ratio $\Gamma_{34}/\Gamma_{12} = 0.78$. In this way we could capture such an asymmetry in the conductance and we could still exploit the $SU(2) \otimes SU(2)$ Kramers spin symmetries to compute the linear conductance. Moreover we

imposed an asymmetry between the left and right leads such that $\alpha_j \equiv \alpha$ and $\alpha = 0.9$, where we assumed for simplicity that this asymmetry is the same among the Kramers levels. This in practice fixes the absolute value of the highest Coulomb blockade peak that in our case is the one in $N_G \simeq 2.5$.

Here we have found qualitative agreement with the experimental data, where the main discrepancies are the absolute value of the conductance in the $N_G = 2$ valley and the position of the Coulomb blockade peak in $N_G \simeq 2.5$. We traced back the reason of these discrepancies to the absence in our model of the so-called exchange interaction. Indeed such an interaction would weaken furthermore the residual SU(4) Kondo effect in the $N_G = 2$ Coulomb valley, lowering the absolute value of the conductance in this point, and it would correct the position of the $N_G = 2.5$ Coulomb peak. Unfortunately, the inclusion of this kind of interaction, beyond the extended Anderson impurity model, is theoretically possible but in practice of very difficult implementation. Indeed such an interaction would remove the SU(2) $\otimes$ SU(2) Kramers spin symmetries making computationally extremely expensive the description of the linear conductance as a function of the applied gate. For this reason we had to neglect this effect and the best result we could achieve is the one we present in Fig.4.17.

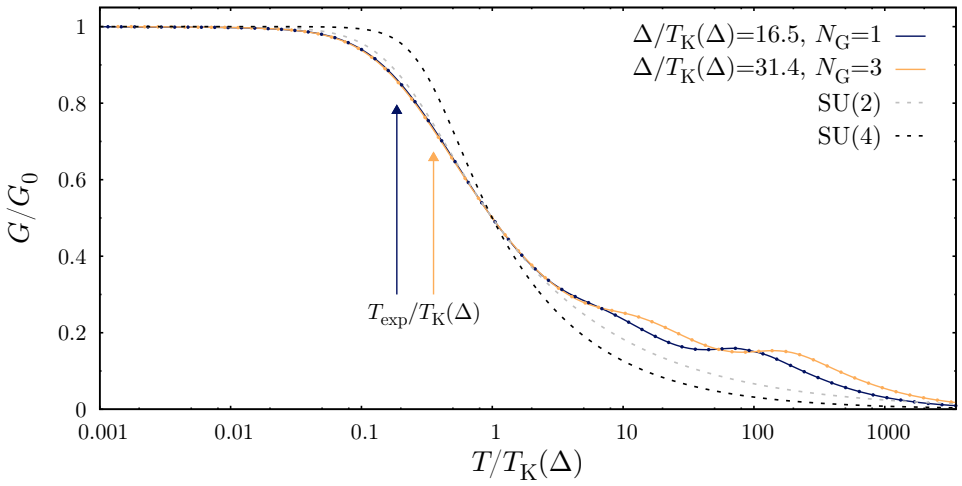

Figure 4.18: Linear conductance as a function of the temperature normalised to the Kondo one in $N_G = 1$ (blue solid line) and $N_G = 3$ (yellow solid line). We reported also the SU(2) (black dashed line) and SU(4) Kondo universal curves for a comparison.

Having set the best set of parameters, we computed the linear conductance as a function of the temperature in $N_G = 1$ and $N_G = 3$ (see Fig.4.18). Indeed, in this way, it is possible to quantitatively study the regime in which the experiment was performed. In Fig.4.18 it is easy to see that, for this set of parameters, the linear conductance temperature dependence is

approximately universal until about $T \simeq T_{\mathrm{K}}(\Delta)$ according to the SU(2) Kondo universal curve (grey dashed curve) in both Coulomb valleys. Despite this universality feature the Kondo temperatures extracted in $N_{\mathrm{G}} = 1$ and $N_{\mathrm{G}} = 3$ are different $\left(T_{\mathrm{K}}\left(\Delta, N_{\mathrm{G}} = 1\right)/T_{\mathrm{K}}\left(\Delta, N_{\mathrm{G}} = 3\right) = 1.9\right)$ since we considered $\Gamma_{12} \neq \Gamma_{34}$. In Fig.4.18 we indicated the ratios of the experimental and the Kondo temperatures with the blue and yellow arrows. It is easy to see that in this shell the experiment was performed in the so-called Kondo crossover regime. This is consistent with the fact that in Fig.4.17 the linear conductance shows two minima in $N_{\mathrm{G}} \simeq 1$ and $N_{\mathrm{G}} \simeq 3$. If we were in the strong coupling regime these minima would be absent and the conductance would have been flat around some maximal value fixed by the asymmetries in the left and right leads and between Γ_{12} and Γ_{34}. Having studied the Kondo correlations strength from the linear conductance point of view, let us now consider such correlations from the thermodynamical point of view. For this reason we turn our discussion to the computation of the so-called CNT added entropy in the next Section.

4.6.1 CNT added entropy

A deeper insight on the Kondo correlations can be gained considering the CNT added entropy and the specific heat (see Fig.4.19). According to Refs. [93–95], we define the CNT added entropy as $S_{\mathrm{CNT}}(T) = S(T) - S_{\mathrm{RS}}(T)$, where

$$S(T) = -\frac{\partial}{\partial T}\Omega(T) = k_{\mathrm{B}} \ln\left(\mathcal{Z}(T)\right) + \frac{\left\langle \hat{H} \right\rangle}{T}, \tag{4.18a}$$

$$S_{\mathrm{RS}}(T) = -\frac{\partial}{\partial T}\Omega_{\mathrm{RS}}(T) = k_{\mathrm{B}} \ln\left(\mathcal{Z}_{\mathrm{RS}}(T)\right) + \frac{\left\langle \hat{H}_{\mathrm{RS}} \right\rangle}{T}, \tag{4.18b}$$

are the entropy of the total system evaluated considering the full Hamiltonian in Eq.(4.6) and the entropy evaluated considering only the leads Hamiltonian in Eq.(4.5) correspondingly. Moreover in Eq.(4.18) we introduced the grand-canonical partition functions $\mathcal{Z} = \mathsf{Tr}\left\{\exp(-\beta\hat{H})\right\}$, $\mathcal{Z}_{\mathrm{RS}} = \mathsf{Tr}\left\{\exp(-\beta\hat{H}_{\mathrm{RS}})\right\}$ and the corresponding thermodynamic potentials $\Omega(T) = -k_{\mathrm{B}}T\ln(\mathcal{Z})$, $\Omega_{\mathrm{RS}}(T) = -k_{\mathrm{B}}T\ln(\mathcal{Z}_{\mathrm{RS}})$. Finally we define the CNT added specific heat $C_{\mathrm{CNT}}(T) = C(T) - C_{\mathrm{RS}}(T)$, where

$$C(T) = T\frac{\partial}{\partial T}S(T) = k_{\mathrm{B}}\beta^2 \left\langle \left(\hat{H} - \left\langle \hat{H} \right\rangle\right)^2 \right\rangle, \tag{4.19a}$$

$$C_{\mathrm{RS}}(T) = T\frac{\partial}{\partial T}S_{\mathrm{RS}}(T) = k_{\mathrm{B}}\beta^2 \left\langle \left(\hat{H}_{\mathrm{RS}} - \left\langle \hat{H}_{\mathrm{RS}} \right\rangle\right)^2 \right\rangle, \tag{4.19b}$$

are the total and leads specific heat respectively. The thermodynamic properties of the system can be computed directly within the NRG scheme, as it is explained in detail in Refs. [93–96] for the single impurity Anderson model.

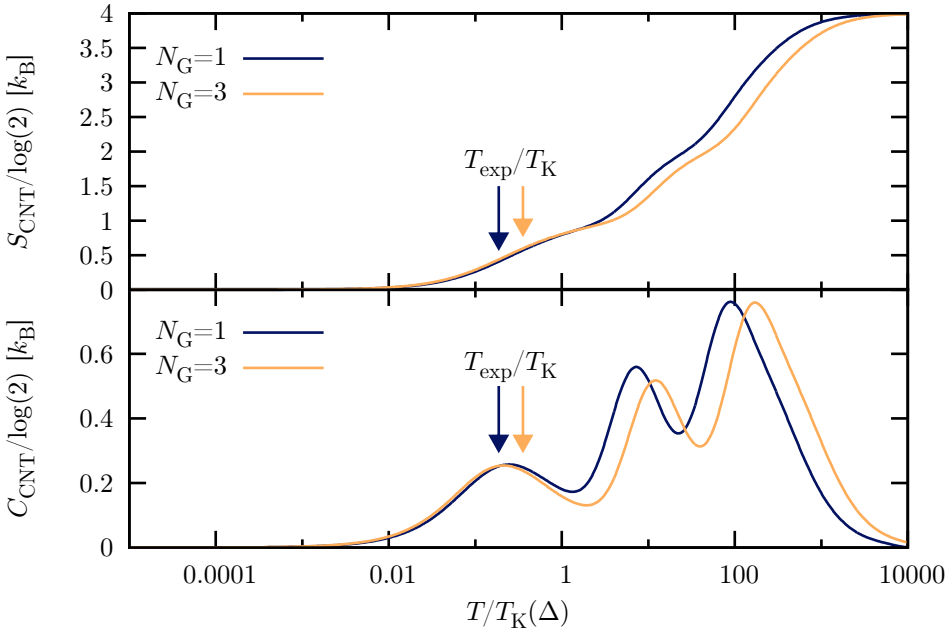

Figure 4.19: (Upper plot) impurity entropy in $N_G = 1$ (blue solid line) and in $N_G = 3$ (yellow solid line) as a function of the temperature normalised to the Kondo one. (Lower plot) the same as in the upper plot for the impurity specific heat.

Minima in the CNT added specific heat are clearly resolved in correspondence of the shoulders in S_{CNT} in Fig.4.19. Here we retained a constant number of multiplets $N_{kept} = 8192$ (fixing the initial discarding iteration to $m = 2$) and averaged the results, according to Refs. [97–99], over $N_z = 4$ simulations with $z = 1/4, 1/2, 3/4, 1$ and the discretisation parameter $\Lambda = 5$. It is easy to see that at hight temperature the CNT entropy approaches the value $k_B \ln(16) = k_B \ln(d)$, where $d = 16$ is the dimensionality of the CNT Hilbert space. In this regime all the states of the CNT are available through thermal excitations and thus the entropy is the maximal one for such a system. In contrast, as $T \to 0$, the entropy tends to zero signalling that all the CNT degrees of freedom are screened due to the Kondo effect, i.e. the ground state is a singlet and the system is fully ordered in such a state. As we consider intermediate temperatures we can notice the formations of plateaux at the dot excitation energies whose heights corresponds to $\ln(\sum_i^n d_i)$, where n is the number of thermally available states and d_i is the degeneracy of the corresponding states. In our case these plateaux are shoulders since, for the parameters of the experiment, there is not a clear separation of the energy scales. However we can clearly see a shoulder whose height corresponds to $k_B \ln(2)$, signalling the "melting down" of the Kondo

state, i.e. getting access to the lower Kramers pair, and another one whose height corresponds to $k_B 2\ln(2)$, signalling the thermal excitation of the upper Kramers pair. Moreover, in Fig.4.19, we can notice that the Entropy and the specific heat are universal with respect to the ratio $T/T_K(\Delta)$. Please notice that $T_K(\Delta, N_G = 1)/T_K(\Delta, N_G = 3) = 1.9$ and thus the two curves are clearly separated if we do not normalise the temperature to the Kondo one. Form this analysis we can deduce that (see arrows in Fig.4.19) the experiment is in the regime in which the Kondo state is formed or about to be formed, i.e., consistently with respect to the behaviour of the linear conductance as a function of the temperature, we are in the cross-over regime.

4.7 Conclusion

In the second part of this thesis, we have investigated the transport and spectral properties of CNTs based quantum dots in the Kondo regime. In order to do that, we have constructed a model that, for the sake of simplicity, assumes spin and valley quantum number conservation during tunnelling processes, but accounts for the combined effects of spin-orbit interaction, valley mixing, electron-electron interaction, U, and finite magnetic field.

First, we carried out a detailed study of the cross-over between the SU(4) and SU(2)-Kondo regime by analysing the dependence of the spectral functions and the linear conductance on the Kramers pair splitting, Δ. We have shown by means of DM-NRG computations, in particular, that in the Kondo regime of a singly occupied CNT longitudinal mode a universal SU(4) conductance is displayed for $\Delta < T_K^{SU(4)}$, while for $\Delta \gg T_K^{SU(4)}$ the conductance and the spectral functions display characteristic SU(2) behaviour with a strongly reduced Kondo temperature. In the intermediate regime $T_K^{SU(4)} \ll \Delta \ll U$ we observed a $1/\Delta$ dependence of the Kondo temperature. This behaviour can be explained in terms of simple scaling arguments, and is also in agreement with exact Bethe Ansatz results obtained in case of infinitely strong Coulomb repulsion [100, 101].

Then, we analysed the magnetic field dependence of the linear conductance and the spectral function, both in fields parallel and perpendicular to the CNT axis. Along the lines of Ref. [78], we derived the necessary conditions to observe the Kondo revival, while extending our analysis to finite valley mixing values ($\Delta_{KK'} \neq 0$) and to the case of perpendicular magnetic fields. We showed that in both parallel and perpendicular fields, the total spectral function of the system shows a four peak structure (two for the absorption and two for the emission processes). We showed that in the case of odd occupancy of a CNT shell, a large enough $\Delta_{KK'}$ can prevent the occurrence of a Kondo revival in parallel field; in perpendicular fields no revival is expected. Kondo revivals have indeed so far been observed experimentally only for parallel magnetic fields [76, 79]. In case of a perpendicular magnetic field, the outer

peaks can merge with those of the split Kondo resonance, thereby leading to a two-peak structure (one for absorption and one for emission processes) for large magnetic field values compared to the SU(4)-Kondo temperature and $B_\perp > B_{\mathrm{KK'}}/2$.

Finally we used our model Hamiltonian to describe the measured linear transport characteristics in a real device fabricated in Grenoble by the group of Jean-Pierre Cleuziou. To this purpose we focused on a specific shell of the CNT quantum dot. Here we could achieve qualitative agreement with the experimental data. We could not achieve quantitative agreement because the inclusion of the so-called exchange interaction revealed to be computationally too challenging. Having found the set of parameters that describes at best the characteristics of the measured linear conductance, we investigated the regime in which the experiment was conducted studying the linear conductance and CNT added entropy temperature dependences. From this analysis we concluded that, at the experimentally measured temperature, the Kondo state was formed or about to be formed.

APPENDIX A

Transport properties via the Reduced Density Matrix

In this Appendix we want to deal with all the demonstrations and the technical details we have judged too lengthy for the main text but that are particularly important for a deep understanding of the theory we have presented in Chap.1, Chap.2 and 3. In particular we will explicitly derive (Sect.A.1) the time dependence of the Kernel super-operator (Eq.(1.48)), we will show explicitly how the diagrammatic rules work (Sect.A.3.1) and how they could be used to push the theory beyond the "standard" perturbative theories (Sect.A.4). In Sect.A.5 we will compute a recurrent integration occurring in evaluating the rates and the elements of the dressing. Finally in Sects.A.6 and A.7 we will focus on the proof of important identities related to the RTA theory we presented in Chap.3. In particular we will prove the propagator sum rule in Eq.(3.8) (Sect.A.6) and we will solve the RTA system of integral equations in the M-times degenerate case in Eq.(3.35) (Sect.A.7).

A.1 Time dependence of the Kernel super-operator

In this Section we want to demonstrate that the Kernel super-operator ($\hat{\mathcal{K}}^{(2)}(\tau_1,\tau_0)$), for time independent perturbations, evolves exclusively according to the time difference

$$\hat{\mathcal{K}}^{(2)}(\tau_1,\tau_0) = \hat{\mathcal{K}}^{(2)}(\tau_1-\tau_0)\,. \tag{A.1}$$

To this purpose we have to express the Liouville super-operator (Eq.(1.24)) in terms of the creation and annihilation operators of the dot and the leads (Eq.(1.14)). Let us consider Eq.(1.44),

$$\hat{\mathcal{K}}^{(2)}_{\mathrm{I}}(\tau_1,\tau_0)\,\hat{\rho}_{\odot,\mathrm{I}}(\tau_0) = -\mathsf{Tr}_{\mathrm{RS}}\left\{\hat{\mathcal{L}}_{\mathrm{T,I}}(\tau_1)\,\hat{\mathcal{L}}_{\mathrm{T,I}}(\tau_0)\,\hat{\rho}_{\odot,\mathrm{I}}(\tau_0)\otimes\hat{\rho}_{\mathrm{RS}}(t_0)\right\}. \tag{A.2}$$

Expressing the commutators in terms of $\hat{D}^{p}_{\mathrm{I},i,\mathbf{j}}$ and $\hat{C}^{p}_{\mathrm{I},i,\mathbf{j}}$ (from Eqs.(1.61)), exploiting that $\left\{\hat{D}^{p}_{\mathrm{I},i,\mathbf{j}}, \hat{C}^{p_1}_{\mathrm{I},i_1,\mathbf{j}_1}\right\} = 0$ and considering the trace over the leads degrees of freedom we obtain:

$$\begin{aligned}\hat{\mathcal{K}}^{(2)}_{\mathrm{I}}(\tau_1,\tau_0)\,\hat{\rho}_{\odot,\mathrm{I}}(\tau_0) = \\ = \sum_{\mathbf{j}_1,p}\Bigg\{ \left[\hat{D}^{p}_{\mathrm{I},1,\mathbf{j}_1}, \hat{\rho}_{\odot,\mathrm{I}}(\tau_0)\,\hat{D}^{\bar{p}}_{\mathrm{I},0,\mathbf{j}_1}\right]\left\langle \hat{C}^{p}_{\mathrm{I},0,\mathbf{j}_1}\hat{C}^{\bar{p}}_{\mathrm{I},1,\mathbf{j}_1}(t)\right\rangle_{\mathrm{RS}} + \\ - \left[\hat{D}^{p}_{\mathrm{I},1,\mathbf{j}_1}, \hat{D}^{\bar{p}}_{\mathrm{I},0,\mathbf{j}_1}\hat{\rho}_{\odot,\mathrm{I}}(\tau_0)\right]\left\langle \hat{C}^{\bar{p}}_{\mathrm{I},1,\mathbf{j}_1}\hat{C}^{p}_{\mathrm{I},0,\mathbf{j}_1}\right\rangle_{\mathrm{RS}}\Bigg\}. \end{aligned} \tag{A.3}$$

Moreover, in order to achieve the form of Eq.(A.3), we have used the Wick theorem fixing the type of creation or annihilation operators in the trace of the leads. In order to further develop the expression of the Kernel we have to make some considerations about *correlation functions* in Eq.(A.3):

$$\left\langle \hat{C}^{\bar{p}}_{\mathrm{I},\mathbf{j}_1,1}\hat{C}^{p}_{\mathrm{I},\mathbf{j}_1,0}\right\rangle_{\mathrm{RS}} = \left\langle \hat{U}^{\dagger}_0(\tau_1,t_0)\,\hat{C}^{\bar{p}}_{\mathbf{j}_1}\hat{U}_0(\tau_1,t_0)\,\hat{U}^{\dagger}_0(\tau_0,t_0)\,\hat{C}^{p}_{\mathbf{j}_1}\hat{U}_0(\tau_0,t_0)\right\rangle_{\mathrm{RS}}, \tag{A.4a}$$

$$\left\langle \hat{C}^{p}_{\mathrm{I},\mathbf{j}_1,0}\hat{C}^{\bar{p}}_{\mathrm{I},\mathbf{j}_1,1}\right\rangle_{\mathrm{RS}} = \left\langle \hat{U}^{\dagger}_0(\tau_0,t_0)\,\hat{C}^{p}_{\mathbf{j}_1}\hat{U}_0(\tau_0,t_0)\,\hat{U}^{\dagger}_0(\tau_1,t_0)\,\hat{C}^{\bar{p}}_{\mathbf{j}_1}\hat{U}_0(\tau_1,t_0)\right\rangle_{\mathrm{RS}}. \tag{A.4b}$$

Using the cyclic property of the trace, the hypothesis of non evolution of $\hat{\rho}_{\mathrm{RS}}$,

$$\left[\hat{\rho}_{\mathrm{RS}}, \hat{U}_{\mathrm{RS}}(\tau_i,t_0)\right] = 0, \tag{A.5}$$

and

$$\hat{U}_0(\tau_1,t_0)\,\hat{U}^{\dagger}_0(\tau_0,t_0) = \hat{U}_0(\tau_1,\tau_0), \tag{A.6}$$

we can recast them in the following form

$$\left\langle \hat{C}^{\bar{p}}_{\mathrm{I},\mathbf{j},1}\hat{C}^{p}_{\mathrm{I},\mathbf{j},0}\right\rangle_{\mathrm{RS}} = \left\langle \hat{U}^{\dagger}_0(\tau_1,\tau_0)\,\hat{C}^{\bar{p}}_{\mathbf{j}}\hat{U}_0(\tau_1,\tau_0)\,\hat{C}^{p}_{\mathbf{j}}\right\rangle_{\mathrm{RS}} \overset{\mathrm{def}}{=} \left\langle \hat{C}^{\bar{p}}_{\mathrm{I},\mathbf{j}}(\tau_1-\tau_0)\,\hat{C}^{p}_{\mathbf{j}}\right\rangle_{\mathrm{RS}}, \tag{A.7a}$$

$$\left\langle \hat{C}^{p}_{\mathrm{I},\mathbf{j},0}\hat{C}^{\bar{p}}_{\mathrm{I},\mathbf{j},1}\right\rangle_{\mathrm{RS}} = \left\langle \hat{C}^{p}_{\mathbf{j}}\hat{U}_0(\tau_1,\tau_0)\,\hat{C}^{\bar{p}}_{\mathbf{j}}\hat{U}^{\dagger}_0(\tau_1,\tau_0)\right\rangle_{\mathrm{RS}} \overset{\mathrm{def}}{=} \left\langle \hat{C}^{p}_{\mathbf{j}}\hat{C}^{\bar{p}}_{\mathrm{I},\mathbf{j}}(\tau_1-\tau_0)\right\rangle_{\mathrm{RS}}. \tag{A.7b}$$

Eqs.(A.7) demonstrates that the correlation functions are stationary: they depend only on the time difference. Considering Eq.(A.3), in order to complete our demonstration we have to switch from the interaction picture to the Schrödinger one also for the density matrix and the dot's creation and annihilation operators. We can achieve this purpose using Eq.(1.47), then

substituting into it the expression of the Kernel of Eq.(A.3) and, exploiting Eq.(1.61a) and Eq.(A.6), we find:

$$\begin{aligned}\hat{\mathcal{K}}^{(2)}(\tau_1,\tau_0)\,\hat{\rho}_{\odot}(\tau_0) &= \\ &= \sum_{\mathbf{i},p}\Bigg\{\left[\hat{D}^{p}_{\mathbf{i}},\hat{U}_0(\tau_1,\tau_0)\,\hat{\rho}_{\odot}(\tau_0)\,\hat{D}^{\bar{p}}_{\mathbf{i}}\hat{U}_0^{\dagger}(\tau_1,\tau_0)\right]\left\langle \hat{C}^{p}_{\mathbf{i}}\hat{C}^{\bar{p}}_{\mathrm{I},\mathbf{i}}(\tau_1-\tau_0)\right\rangle_{\mathrm{RS}} + \\ &- \left[\hat{D}^{p}_{\mathbf{i}},\hat{U}_0(\tau_1,\tau_0)\,\hat{D}^{\bar{p}}_{\mathbf{i}}\hat{\rho}_{\odot}(\tau_0)\,\hat{U}_0^{\dagger}(\tau_1,\tau_0)\right]\left\langle \hat{C}^{\bar{p}}_{\mathrm{I},\mathbf{i}}(\tau_1-\tau_0)\,\hat{C}^{p}_{\mathbf{i}}\right\rangle_{\mathrm{RS}}\Bigg\} = \\ &\overset{\mathrm{def}}{=} \hat{\mathcal{K}}^{(2)}(\tau_1-\tau_0)\,\hat{\rho}_{\odot}(\tau_0)\,. \end{aligned} \tag{A.8}$$

This demonstrates our postulate (Eq.(A.1)) since $\hat{U}_0(\tau_1,\tau_1)$ depends only on the time difference $\tau_1-\tau_0$.

A.2 Straightforward calculation of the Kernel component

In this appendix we want to show how to evaluate the Kernel components without the use of the diagrammatic rules (App.A.3). This will be of support for these rules, showing that the two methods coincide, and will further clarify that the Kernel super-operator evolves only ruled by the time difference as we have demonstrated in App.A.1.

Diagonal elements Let us consider the Kernel element $\left(\hat{\mathcal{K}}^{(2)}\right)^{2,2}_{2,2}$. Then, from Eq.(1.66), we have to evaluate

$$\left(\hat{\mathcal{K}}^{(2)}\right)^{2,2}_{2,2} = \lim_{\lambda\to 0}\int_0^{+\infty} d\tau'\, e^{-\lambda\tau'}\langle 2|\hat{\mathcal{K}}^{(2)}_{\mathrm{I}}(t,t-\tau')\left[|2\rangle\,\langle 2|\right]|2\rangle\,.$$

Since the exponential in Eq.(1.66) depends on the energy differences $E_b-E_{b'}$ and $E_a-E_{a'}$, in case of the populations they cancel out. Because the final and initial state coincide we can deduce that, up to the second order, only diagrams composed of "bubbles" can contribute to this Kernel element. Therefore, from Tab.1.1, we can directly write the non zero contributions:

$$\left(\hat{\mathcal{K}}^{(2)}\right)^{2,2}_{2,2} = \sum_{\mathbf{k}_1,l_1,\sigma_1}\left(\;\right) \tag{A.9}$$

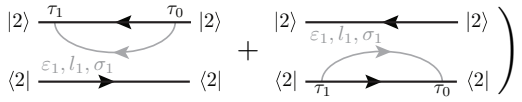

$$\begin{aligned} &= -\sum_{\mathbf{k}_1,l_1,\sigma_1}\lim_{\lambda\to 0}\int_0^{+\infty} d\tau'\, e^{-\lambda\tau'}\left\langle \hat{C}^{-}_{\mathrm{I},1,\mathbf{j}_1}\hat{C}^{+}_{\mathrm{I},0,\mathbf{j}_1}\right\rangle_{\mathrm{RS}} \\ &\qquad \langle 2|\,\hat{D}^{+}_{\mathrm{I},1,\mathbf{j}_1}\,|\sigma_1\rangle\,\langle\sigma_1|\,\hat{D}^{-}_{\mathrm{I},0,\mathbf{j}_1}\,|2\rangle + \mathrm{h.c.}, \end{aligned}$$

where $\tau' = \tau_1 - \tau_0 = t - \tau$ and $\varepsilon_1 = \varepsilon_1(\mathbf{k}_1)$. Here we have neglected diagrams that bring the dot in the state $|3\rangle$ and then come back to the state $|2\rangle$ because in the Anderson model this state is not available. Then, using Eq.(1.67), we find

$$\left(\hat{\mathcal{K}}^{(2)}\right)_{2,2}^{2,2} = -\frac{1}{\hbar^2}\lim_{\eta\to 0}\sum_{l,\sigma}\int_{-\infty}^{+\infty} d\varepsilon\, \bar{\alpha}_{l,\sigma}(\varepsilon)\, f_l^-(\varepsilon)\int_0^{+\infty} d\tau' e^{\frac{i}{\hbar}(E_2 - E_\sigma - \varepsilon + i\eta)\tau'} + \text{h.c.}$$

$$= -\frac{i}{\hbar}\lim_{\eta\to 0}\sum_{l,\sigma}\int_{-\infty}^{+\infty}\frac{\bar{\alpha}_{l,\sigma}(\varepsilon)\, f_l^-(\varepsilon)}{-\varepsilon + E_2 - E_\sigma + i\eta}\, d\varepsilon + \text{h.c.}, \tag{A.10}$$

where we have defined $\eta = \hbar\lambda$. As expected we have no dependence on the time "t". For future convenience let us recast the integral in the previous expression in terms of the bare Fermi function $f^+(\varepsilon) = f(\varepsilon) = (1+e^{\varepsilon})^{-1}$ and $f^-(\varepsilon) = 1 - f(\varepsilon)$,

$$\int_{-\infty}^{\infty} d\varepsilon \frac{f_l^p(\varepsilon)}{d\varepsilon - A + i\eta} L(\varepsilon, W, l) = \int_{-\infty}^{\infty} d\varepsilon \frac{f^p[\beta(\varepsilon - \mu_l)]}{d\varepsilon - A + i\eta} L(\varepsilon, W, l) =$$

$$= \int_{-\infty}^{\infty} \frac{d\tilde{\varepsilon}}{\beta} \frac{f^p(\tilde{\varepsilon}) L(\tilde{\varepsilon}, \tilde{W})}{d(\tilde{\varepsilon}\beta^{-1} + \mu_l) - A + i\eta} = \int_{-\infty}^{\infty} d\tilde{\varepsilon} \frac{f^p(\tilde{\varepsilon}) L(\tilde{\varepsilon}, \tilde{W})}{d(\tilde{\varepsilon} + \tilde{\mu}_l - \tilde{A}') + i\tilde{\eta}} =$$

$$= \int_{-\infty}^{\infty} d\tilde{\varepsilon} \frac{f^p(\tilde{\varepsilon})}{d(\tilde{\varepsilon} - \beta\bar{\mu}_l^{i,j}) + i\tilde{\eta}} L(\tilde{\varepsilon}, \tilde{W})$$

where $d = \pm 1$, $\tilde{W} = W\beta$, $\tilde{\mu}_l = \mu_l\beta$, $\tilde{\eta} = \eta\beta$ and $\bar{\mu}_l^{i,j}$ is the chemical potential of the l-lead shifted by the energy difference $E_i - E_j$:

$$\bar{\mu}_l^{i,j} = E_i - E_j - \mu_l.$$

Moreover we have introduced $L(\tilde{\varepsilon}, \tilde{W}) = \tilde{W}^2/(\tilde{\varepsilon}^2 + \tilde{W}^2)$. This suggests us to consider the function

$$Y_d^p\left(\bar{\mu}_l^{i,j}\right) \stackrel{\text{def}}{=} -\frac{i}{\hbar}\lim_{\tilde{\eta}\to 0}\int_{-\infty}^{+\infty} d\tilde{\varepsilon}\frac{f^p(\tilde{\varepsilon})}{d\left(\tilde{\varepsilon} - \beta\bar{\mu}_l^{i,j}\right) + i\tilde{\eta}} L(\tilde{\varepsilon}, \tilde{W}), \tag{A.11}$$

that allows us to recast the element of the Kernel we are evaluating as

$$\left(\hat{\mathcal{K}}^{(2)}\right)_{2,2}^{2,2} = \sum_{l,\sigma}\|T_{l,\sigma}\|^2 \rho_{l,\sigma} Y_+^+\left(\bar{\mu}_l^{\sigma,2}\right) + \text{h.c.}$$

$$= 2\sum_{l,\sigma}\|T_{l,\sigma}\|^2 \rho_{l,\sigma}\mathsf{Re}\left\{Y_+^+\left(\bar{\mu}_l^{\sigma,2}\right)\right\}. \tag{A.12}$$

In App.A.5 we will deal with the evaluation of the integral in Eq.(A.11). In the end it is a complex function of the real variable $\bar{\mu}_l^{i,j}$ and it captures the energy dependence of the Kernel components.

At this stage it is only important to notice that the energy dependence is of the form

$$-\frac{i}{\hbar}\int_{-\infty}^{+\infty} d\tilde{\varepsilon}\,\frac{f_l^p(\tilde{\varepsilon})}{\Delta},$$

where the denominator Δ comes from the exponential ($e^{\frac{i}{\hbar}\Delta\tau'}$) in the Laplace transform and $p \in \{+,-\}$ depends on the element of the Kernel super-operator we consider, as it is easy to understand from Tab.1.1.

Non-diagonal elements In this paragraph we want to demonstrate that, as we have shown in general in App.A.1, also for non-diagonal elements of the Kernel, the time dependence is still $\tau' = \tau_1 - \tau_0$. Let us consider

$$\left(\hat{\mathcal{K}}^{(2)}\right)^{2,\sigma}_{\bar{\sigma},0} = \sum_{\mathbf{k},l}$$

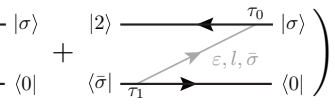

$$= \sum_{\mathbf{k},l} \lim_{\lambda\to 0} \int_0^{+\infty} e^{-\lambda\tau'} e^{-\frac{i}{\hbar}E_\sigma\tau'} e^{-\frac{i}{\hbar}U\tau_1} \left\langle \hat{C}^-_{\mathrm{I},0,\mathbf{j}} \hat{C}^+_{\mathrm{I},1,\mathbf{j}} \right\rangle_{\mathrm{RS}} \cdot$$

$$\cdot \langle 2|\, \hat{D}^+_{\mathrm{I},1,\mathbf{j}}\, |\sigma\rangle \langle 0|\, \hat{D}^-_{\mathrm{I},0,\mathbf{j}}\, |\bar{\sigma}\rangle\, d\tau' + \text{h.c.}, \quad \text{(A.13)}$$

where $U = E_2 - \sum_\sigma E_\sigma$ is the interaction energy (Eq.(1.17)).
Since $\left\langle \hat{C}^-_{\mathrm{I},0,\mathbf{j}} \hat{C}^+_{\mathrm{I},1,\mathbf{j}} \right\rangle_{\mathrm{RS}}$ depends only on the time difference we have only to check if the time evolution of the operators $\hat{D}^+_{\mathrm{I},1,\mathbf{j}}$ and $\hat{D}^-_{\mathrm{I},0,\mathbf{j}}$ cancel out the residue dependence on t. Considering only the time dependent exponentials, using Eq.(1.67), we have

$$e^{-\lambda\tau'} e^{-\frac{i}{\hbar}E_\sigma\tau'} e^{-\frac{i}{\hbar}U\tau_1} e^{\frac{i}{\hbar}(E_2-E_\sigma)\tau_1} e^{-\frac{i}{\hbar}E_{\bar{\sigma}}\tau_0} = e^{\frac{i}{\hbar}(E_{\bar{\sigma}}-E_\sigma)\tau'} e^{-\lambda\tau'}. \quad \text{(A.14)}$$

Since this is the whole time dependence in Eq.(A.13), Eq.(A.14) completes our statement.

A.3 Diagrammatic rules

In this Section we will deal with the diagrammatic rules we have anticipated in Sect.1.1.5. These diagrammatic rules were previously introduced in Refs. [38, 40, 47]. We will show briefly (Sect.A.3.1) that the diagrammatic rules give straightforwardly the right contributions we would obtain by calculating the Kernel elements (see App.A.2). Moreover in the next Section (Sect.A.4) we will develop, through the language of the diagrams, a method to "dress" the main fermion line through "blocks" of tunnelling events.

A.3.1 "Standard" diagrammatics

As explained in Sect.1.1.5 there is a one-to-one correspondence between the diagrams in the time domain and the Laplace transform of the Kernel components. In the following we will list all the steps we have to follow to obtain the right contribution. At the same time we will give an example, by applying these rules to $\left(\hat{\mathcal{K}}^{(2)}\right)^{2,2}_{2,2}$, in order to convince furthermore the reader.

1- Labels and their meaning In a process of the $2n$-th order in the tunnelling Hamiltonian, in which *n-fermion lines* ($1 \leq i \leq n$) are involved, every fermion line has to be labelled with *three parameters* (see Tab.1.1):

- ε_i: the energy of the lead particle exchanged in the i-th process;
- l_i: the index of the lead involved in the i-th process;
- σ_i: the spin of the tunnelling particle.

Assign to each time interval on the contours the energy corresponding to the state ;

2- Extract the right denominators Since every fermion line is bound by two vertexes, we have $2n$ of them labelled with τ_i : ($\tau_{2n-1} = t, \ldots, \tau_0 = \tau$) along the contours. In each time interval ($\tau_{j+1} \geq \tau' \geq \tau_j$, $0 \leq j \leq 2n-2$) we have to perform a vertical cut (red line):

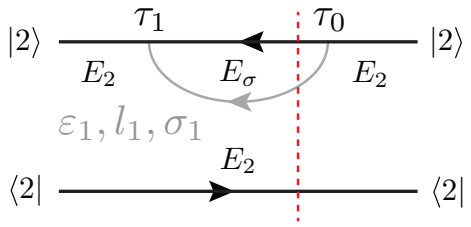

For every cut we can obtain a denominator A_i: for *each intersection* we have to add to the denominator A_i the energy (E_i) of each line that the vertical cut meet. If the fermion line, or the contour, join the cut from the *left* we have to add the energy with a *positive sign*, otherwise, if it comes form the *right*, with a *negative* sign. In our example we have only one denominator A_0 and it reads:

$$A_0 = E_2 - \varepsilon_1 - E_\sigma.$$

3- Selecting the type of process For every fermion line we have to define a sign p_i which is fixed by the type of process: if it represents an *in-tunnelling* process $p_i = +$, if it is an *out-tunnelling* process $p_i = -$. In

general if the vertexes are on the same contour and the fermion line has the same direction of the contour then $p_i = -$; otherwise, if it has the opposite direction with respect to the contour, $p_i = +$. If the two vertexes lie on different contours it is the other way round. For our diagram it holds

$$p_0 = -.$$

4- Determine the sign of the contribution We use and integer q to impose the sign of the Kernel element: it is equal to the number of vertexes on the lower contour plus the number of crossings of fermion lines. In our case:

$$q = 0.$$

Integral form of the Kernel element Considering the Laplace transform of Eq.(1.67), the integral contribution of a specific diagram reads

$$(-1)^{q+1} \frac{i}{\hbar} \lim_{\eta \to 0} \prod_{i=1}^{n} \int_{-\infty}^{+\infty} d\varepsilon_i \, \bar{\alpha}_{l_i,\sigma_i}(\varepsilon_i) \, f_{l_i}^{p_i}(\varepsilon_i) \prod_{j=0}^{2n-2} \frac{1}{A_j + i\eta}. \tag{A.15}$$

Substituting all the parameters for our second order diagram we have

$$-\frac{i}{\hbar} \lim_{\eta \to 0} \int_{-\infty}^{+\infty} d\varepsilon \, \bar{\alpha}_{l,\sigma}(\varepsilon) \frac{f_l^-(\varepsilon)}{-\varepsilon + E_2 - E_\sigma + i\eta},$$

This is exactly what we have obtained in Eq.(A.10) (first term, the second one is the hermitian conjugated) without exploiting these diagrammatic rules.

For the interested reader a deeper explanation of these rules can be found in Ref. [40] Appendix A.

A.4 Dressing fermion lines via blocks of tunnelling events

In this Section we want to mathematically deduce "*new diagrammatic rules*" for straightforwardly obtaining the integral contribution of diagrams formed by a main fermion line, contributing to transport, "dressed" with several tunnelling events that will capture spin and charge quantum fluctuations in the dot. In particular we will derive the analytical contribution of the the sum of all the possible combinations of a set ($\mathcal{N}$) of diagrams we have called "*Nucleus of the dressing*". The *dimension* (N) of this set is the *number of distinct, irreducible and contour state conserving diagrams we have chosen to dress the main fermion line.* In this Appendix the dimension of the Nucleus will not be fixed in order to keep the theory as much general as possible.

A.4.1 Dressing of the main fermion line

Let us study, in the first place, the i-th element of the Nucleus (see Figs.A.1). We have defined a Nucleus ($\mathcal{N}_{\pm}$) for each main fermion line we dress. Moreover the i-th element of this set, with $1 \leq i \leq N$, is specified by *the order (n) of such dressing element*, that is the number of fermion lines, excluded the main one, within τ_1 and τ_{2n}.

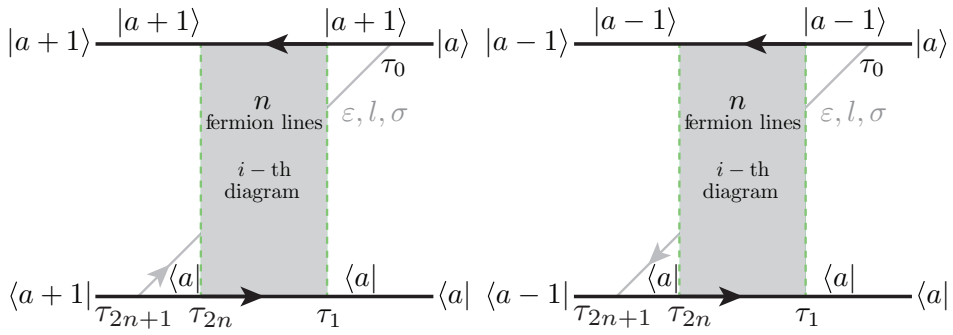

(a) Forward pointing diagram (b) Backward pointing diagram

Figure A.1: (a) i-th element of the Nucleus ($\mathcal{N}_+$) of the dressing with $2n$ tunnelling events within the interval $\tau_{2n} \geq \tau \geq \tau_1$: forward pointing main fermion line. (b) The same as in (a) with a backward pointing main fermion line (i-th element of $\mathcal{N}_-$).

Let us focus on the dressing of the forward main fermion line (nucleus $\mathcal{N}_+$). Our strategy in the following will consist in considering the most general diagram we can form using the processes we have included in the Nucleus and to find the corresponding integral form. Then we will sum up over all the possible combinations of the diagrams in $\mathcal{N}_+$. At the end we will extract from this procedure, the afore-mentioned "new diagrammatic rules".

Let us consider m blocks of the species i_j with $j \in \{\, 0, \ldots, m-1 \,\}$ and $i_j \in \{\, 1, \ldots, N \,\}$, i.e. the index i selects a block in the Nucleus and the index j its position along the time line in the diagram as we depicted in Fig.A.2. It is worth to notice that, since every element of the Nucleus (grey regions) conserves the state on the single contour the number of vertexes on the (lower)upper-contour has to be even, within τ_1 and τ_{2nm}. Furthermore the directions of the fermion lines have to be such that we create as many particles on the single contour as much we destroy them. Because the dressing is of the order n in E_{T} the j-th element of the dressing is delimited, independent of the i-type, by the vertexes lying in $\tau_{2(j+1)n}$ and τ_{2jn+1}. As we will see in detail in the following, fixing $\{\, i_j,\, 0 \leq j \leq m \,\}$ and changing the order of the elements does not change the analytic contribution of the total diagram. This will be of importance counting how many diagrams give the same contribution

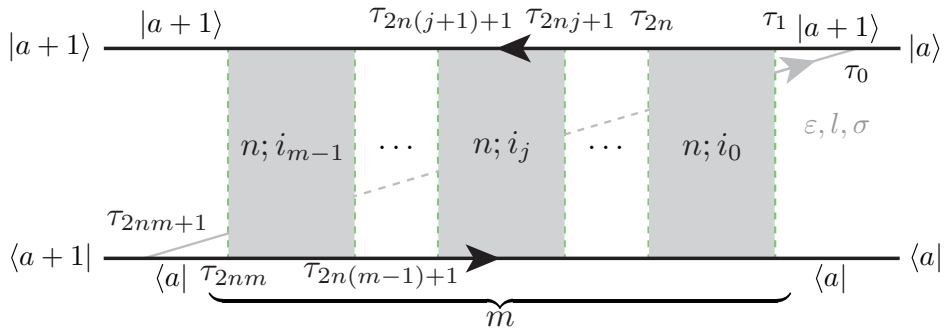

Figure A.2: Generic diagram composed of a main fermion line (grey) dressed with m blocks of the order n (grey regions delimited with light-green dashed lines). We have reported the time delimiters for every process $n; i_j$ and the states at the beginning of the dressing and at the end of it.

in order to properly sum the series of them. As we will prove in the next paragraph this procedure will lead to a geometric series that we can sum and obtain an analytical form of the "dressed" diagram (see Eq.(A.20)).

Extracting the integral form of the dressed diagram (proof) At this stage of the discussion we use the diagrammatic rules developed in App.A.3 to deduce the contribution of the diagram shown in Fig.A.2. Since the number of vertexes in the j-th grey region is even, the total number of vertexes on the lower contour (including the vertex from the main fermion line) is always odd ($2r+1$, $r \in \mathbb{N}$). Then, using the fourth rule in App.A.3 we have

$$q = 1 + 2r + n_{\text{int}}^{\text{tot}}, \qquad n_{\text{int}}^{\text{tot}} = \sum_{j=0}^{m-1} n_{\text{int}}^{j},$$

where n_{int}^{j} is the total number of intersections between fermion lines in the j-th grey block. Furthermore, since we have $nm+1$ fermion lines we have to define:

$$\boldsymbol{\varepsilon} = (\varepsilon, \varepsilon_1, \ldots, \varepsilon_{n_1 n}), \qquad \mathbf{l} = (l, l_1, \ldots, l_{nm}),$$
$$\boldsymbol{\sigma} = (\sigma, \sigma_1, \ldots, \sigma_{nm}), \qquad \mathbf{p} = (p = +, p_1, \ldots, p_{nm}).$$

Here we have shown the direction of the first fermion line since it is fixed. Moreover, having $2(nm+1) = 2n_{\text{ord}}$ different vertexes τ_j (n_{ord} is the order in E_{T} of the total diagram), we have to perform $2(nm+1)-1$ vertical cuts identifying as well $2(nm+1)-1$ denominators A_j. Since we have m distinct blocks from $\mathcal{N}_+$ we have

$$\underbrace{m-1}_{\text{intervals between } n_1 \text{ blocks}} + \overbrace{2}^{\text{first and last interval}}$$

intervals with equal denominators. Using the second rule of App.A.3, this denominator can be easily identified as

$$A_0 = \varepsilon - E_{a+1,a}.$$

Then the integral contribution of the generic dressed diagram in Fig.A.2 reads

$$\frac{i}{\hbar}\lim_{\eta\to 0}\prod_{i=1}^{nm}\int_{-\infty}^{+\infty} d\varepsilon \left[\frac{\bar{\alpha}_{l,\sigma}(\varepsilon) f_l^+(\varepsilon)}{(\varepsilon - E_{a+1,a} + i\eta)^{m+1}} \right.$$
$$\left. (-1)^{2+2r+n_{\text{int}}^i}\int_{-\infty}^{+\infty} d\varepsilon_i\, \bar{\alpha}_{l_i,\sigma_i}(\varepsilon_i) f_{l_i}^{p_i}(\varepsilon_i) \prod_{j=1}^{(2n-1)m}\frac{1}{A_j + i\eta}\right],$$

where we want to stress that A_j depends, in general, on $\boldsymbol{\varepsilon}$, since the generic element of $\mathcal{N}_+$ is of the order n and we have an additionally the main fermion line. This implies that, in the worst case, we have m factorized integrals in n dimensions as follows

$$\frac{i}{\hbar}\lim_{\eta\to 0}\int_{-\infty}^{+\infty} d\varepsilon \frac{\bar{\alpha}_{l,\sigma}(\varepsilon) f_l^+(\varepsilon)}{(\varepsilon - E_{a+1,a} + i\eta)^{m+1}}\prod_{i=1}^{m} a_i(\varepsilon), \tag{A.16}$$

having defined the integral form of the i-th element of the Nucleus as

$$a_i(\varepsilon) = (-1)^{n_{\text{int}}^i}\sum_{l_1,\ldots,l_n}\cdot$$
$$\int_{-\infty}^{+\infty} d\varepsilon_1\ldots d\varepsilon_n \prod_{j=1}^{2n-1}\frac{\bar{\alpha}_{l_1,\sigma_1}(\varepsilon_1) f_{l_1}^{p_1^i}(\varepsilon_1)\ldots\bar{\alpha}_{l_n,\sigma_n}(\varepsilon_n) f_{l_n}^{p_n^i}(\varepsilon_n)}{A_j^i + i\eta}. \tag{A.17}$$

Here we have re-organized the $\mathbf{p}$ vector in a $(m\times n)$ matrix p_j^i. For example it is always possible to change $\varepsilon_i \leftrightarrow \varepsilon_j$ (since they are "dumb" variables of integration) in such a way that $p_j^i = (\mathbf{p})_{(i-1)n+j}$. Moreover we have introduced A_j^i, where $1 \le i \le m$ indicates the element of the Nucleus, whereas $0 \le j \le 2n-1$ corresponds to the position of the vertical cut. Let us consider Eq.(A.16). Since the Nucleus of the dressing has N elements we have only N independent $a_i(\varepsilon)$ along the timeline. This means that we can recast Eq.(A.16) as follows:

$$\frac{i}{\hbar}\lim_{\eta\to 0}\int_{-\infty}^{+\infty} d\varepsilon \frac{\bar{\alpha}_{l,\sigma}(\varepsilon) f_l^+(\varepsilon)}{(\varepsilon - E_{a+1,a} + i\eta)^{m+1}}\prod_{i=1}^{N} a_i^{m_i}(\varepsilon),$$

where $0 \le m_i \le N$ is the number of times the i-th element of the Nucleus appears in the generic diagram in Fig.A.2. Eventually $m_i = 0$ if the i-th

process does not appear. For the following notice that

$$\sum_{i=1}^{N} m_i = m. \tag{A.18}$$

Having obtained the integral form of the generic term of the series we are interested in, we sum all the possible combinations of diagrams with a forward pointing fermion line dressed with processes of order n, symbolically we write:

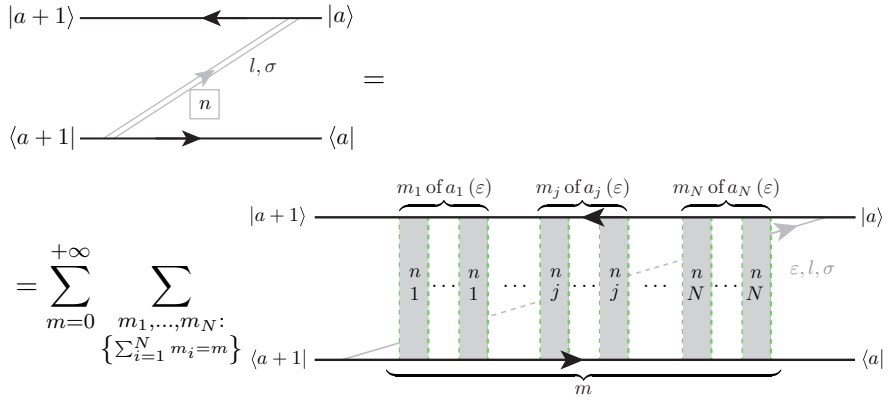

$$= \sum_{m=0}^{+\infty} \sum_{\substack{m_1,\ldots,m_N: \\ \left\{\sum_{i=1}^{N} m_i = m\right\}}} \frac{i}{\hbar} \lim_{\eta\to 0} \int_{-\infty}^{+\infty} d\varepsilon \, \frac{\bar{\alpha}_{l,\sigma}(\varepsilon) f_l^+(\varepsilon)}{(\varepsilon - E_{a+1,a} + i\eta)^{m+1}} \prod_{i=1}^{N} a_i^{m_i}(\varepsilon). \tag{A.19}$$

Here we have indicated the sum of the series of the dressed diagram with processes of the order n with the diagram reported in the first line. It is worth to stress that in the time interval within the first two vertexes (analogously for the two last vertexes) we have one intersection per vertical cut, while in between the second and the third we can have from one up to $n+1$ intersections per vertical cut. As indicated in the first line in Eq.(A.19) of the two fermion line has to be counted up to n times in order to reproduce the same result. In the future n will be omitted only in the simplest case in which we dress the main fermion line with processes composed of only one fermion line. Let us rewrite the sum with respect to the $m_1, \ldots, m_N$ indexes in a more computational way:

$$\sum_{\substack{m_1,\ldots,m_N: \\ \left\{\sum_{i=1}^{N} m_i = m\right\}}} \prod_{i=1}^{N} a_i^{m_i}(\varepsilon) = \sum_{m_1=0}^{m} \sum_{m_2=0}^{m-m_1} \cdots \sum_{m_{N-1}=0}^{m-\sum_{i=1}^{N-1} m_i} \Bigg[C\left(m_1, m_2, \ldots, m - \sum_{i=1}^{N-1} m_i\right) \prod_{i=1}^{N} a_i^{m_i}(\varepsilon) \Bigg],$$

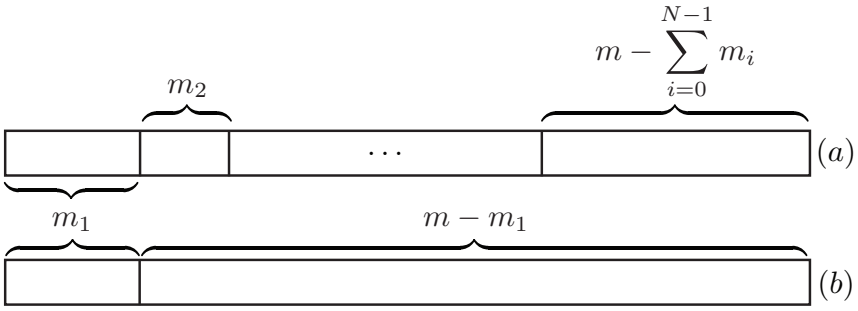

Figure A.3: Sketch of a string of length m divided in $m_1, \ldots, m_N$ sub-strings.

where we have defined the function $C\left(m_1, m_2, \ldots, m - \sum_{i=1}^{N} m_i\right)$ that counts all the possible combinations to obtain a string $a_1^{m_1} \ldots a_N^{m_N}$. This function, from the combinatorics theory, is the *multinomial coefficient*: $\binom{m}{m_1,\ldots,m_N}$. We can figure this out considering, as already mentioned, a string of length m divided in $m_1, \ldots, m_N$ sub-strings (Fig.A.3(a)). Let us focus on the first subdivision: m_1 and $m - m_1$ (see Fig.A.3(b)). We have m_1 possible ways to choose the position for the first $a_1(\varepsilon)$ function, in the sub-string of length $m - m_1$, $m_1 - 1$ for the second and so on until $m - m_1 + 1$ for the last one we can place. Then there are $m!/(m - m_1)!$ different possible strings divided in such a way. To this number we have to subtract the different ways of ordering the string of length m_1, it reads:

$$\frac{m!}{(m - m_1)! m_1!} \stackrel{\text{def}}{=} \binom{m}{m_1}.$$

Iterating this argument for all the subdivision $m_1, \ldots, m_N$ and gathering all the possibilities we get:

$$C\left(m_1, \ldots, m - \sum_{i=1}^{N-1} m_i\right) = \binom{m}{m_1}\binom{m - m_1}{m_2} \ldots \binom{m - \sum_{i=1}^{N-1} m_i}{m_N} \stackrel{\text{def}}{=} \binom{m}{m_1, \ldots, m - \sum_{i=1}^{N-1} m_i}.$$

Then from Eq.(A.19), using the *multinomial theorem*,

$$\sum_{m_1=0}^{m} \sum_{m_2=0}^{m-m_1} \cdots \sum_{m_{N-1}=0}^{m-\sum_{i=1}^{N-1} m_i} \left[\binom{m}{m_1, \ldots, m_1 - \sum_{i=1}^{N-1} m_i} \prod_{i=1}^{N-1} a_i^{m_i}(\varepsilon) \cdot \cdot a_N^{m - \sum_{i=1}^{N-1} m_i}(\varepsilon) \right] = \left(\sum_{i=1}^{N} a_i(\varepsilon) \right)^m.$$

Thus we have

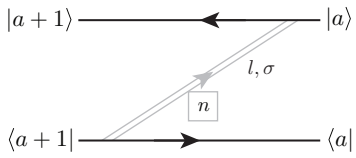

$$= \tag{A.20}$$

$$= \sum_{m=0}^{+\infty} \frac{i}{\hbar} \lim_{\eta\to 0} \int_{-\infty}^{+\infty} d\varepsilon \, \frac{\bar{\alpha}_{l,\sigma}(\varepsilon) f_l^+(\varepsilon)}{(\varepsilon - E_{a+1,a} + i\eta)^{m+1}} \left(\sum_{i=1}^{N} a_i(\varepsilon) \right)^m$$

$$= \frac{i}{\hbar} \lim_{\eta\to 0} \int_{-\infty}^{+\infty} d\varepsilon \, \frac{\bar{\alpha}_{l,\sigma}(\varepsilon) f_l^+(\varepsilon)}{\varepsilon - E_{a+1,a} + i\eta - \sum_{i=1}^{N} a_i(\varepsilon)}.$$

Here we have summed up the geometric series assuming it converges. A detailed discussion about its convergence can be found in Ref. [41].

A.4.2 Diagrammatic rules for dressed diagrams

Eq.(A.20) allows us to extract new diagrammatic rules. Indeed, in order to deduce the integral form of a dressed diagram, we can simply consider the following steps:

1- Nucleus of the dressing. For each fermion line we want to dress, choose:

- **a-** the number (N);
- **b-** the order (n);
- **c-** the type;

of elements in the Nucleus. The set of diagrams we have chosen unequivocally define the Nucleus of the dressing:

$\mathcal{N}(n) =$ 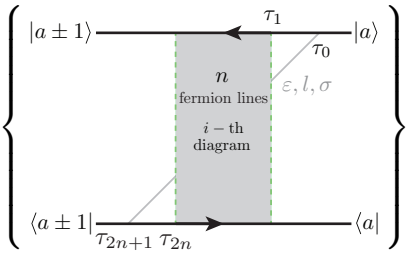 with $1 \leq i \leq N$,

where we explicitly reported the Nucleus dependence on the order (n) of its elements.

2- Role of the main fermion line. Take in consideration the *main fermion line* we are dressing. Define the energies on the corresponding contour within τ_0 and τ_1 or, equivalently, τ_{2n} and τ_{2n+1}. Perform a vertical cut

in the time interval within τ_0 and τ_1. Determine the sign p_0 and the denominator A_0 with the same rules we have presented in the "standard diagrammatic rules". Then it reads:

$$p_0 = \begin{cases} +, & \text{forward pointing} \\ -, & \text{backward pointing} \end{cases} \qquad A_0 = E_a - E_{a\mp1} \pm \varepsilon.$$

The leading integral form concerning the dressed diagram reads:

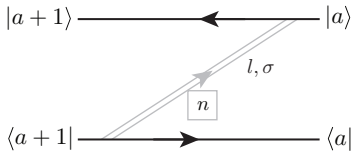

$$= \frac{i}{\hbar} \lim_{\eta\to 0} \int_{-\infty}^{+\infty} d\varepsilon \, \frac{\bar{\alpha}_{l,\sigma}(\varepsilon) f_l^{p_0}(\varepsilon)}{A_0(\varepsilon) + i\eta - \sum_{i=1}^{N} a_i(\varepsilon)}. \tag{A.21}$$

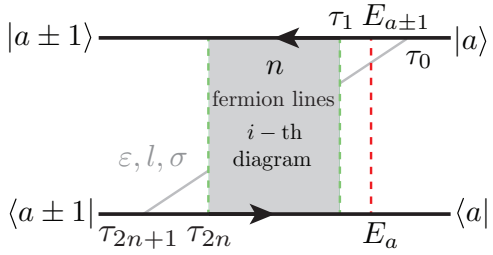

3- Role of the dressing $a_i(\varepsilon)$. Having defined the order n of the process in the Nucleus of the dressing we have to introduce ε_i, l_i and σ_i, with $1 \le i \le n$. Moreover we have to extract for each $a_i(\varepsilon)$ (then for each diagram in the Nucleus) $(2n-1)\cdot N$ denominators A_j^i, where $i:\ 1 \le i \le N$ is the index of the diagram, whereas $j:\ 1 \le j \le 2n-1$ is the index of the vertical cut along the time-line. Then fixing n_{int}^i equal to the number of intersections between the fermion lines in the i-th diagram, as we have just demonstrated, the corresponding integral form reads:

$$a_i(\varepsilon) = (-1)^{n_{\text{int}}^i} \cdot \sum_{l_1,\ldots,l_n} \int_{-\infty}^{+\infty} d\varepsilon_1 \ldots d\varepsilon_n \prod_{j=1}^{2n-1} \frac{\bar{\alpha}_{l_1,\sigma_1}(\varepsilon_1) f_{l_1}^{p_1^i}(\varepsilon_1) \ldots \bar{\alpha}_{l_n,\sigma_n}(\varepsilon_n) f_{l_{n_2}}^{p_n^i}(\varepsilon_n)}{A_j^i + i\eta}. \tag{A.22}$$

The simplest example of dressing a main fermion line with processes of the second order with respect to E_{T} ($n=1$) is the DSO approximation presented in Sect.2.1.

A.4.3 Second dressing of the main fermion line

Since the theory we developed in the previous Section is completely general with respect to the dressing order n of each element in $\mathcal{N}(n)$, nothing forbids us to consider elements from Nuclei $\mathcal{N}(n)$ with different n, recombine them and sum over infinite contributions. This yields an effectively dressed form of the Nucleus.

At this point it should be clear to the reader that we can repeat the same steps in Sect.A.4.1 for the elements $a_i(\varepsilon)$ to obtain their dressed version $\tilde{a}_i(\varepsilon)$.

To this purpose we have first of all to choose the elements $a_i(\varepsilon)$ we want to dress. In the following we will fix them to the one in Eq.(2.1) and address the corresponding dressed set of functions $\{\tilde{a}_i(\varepsilon), 1 \leq i \leq 4\}$ as *the Nucleus of the first dressing* ($\mathcal{N}_{1\text{st}}$). Notice that even thought the Nucleus of the first dressing contains four elements, they are dressed and thus its dimension is not finite any more. Furthermore we will address the sets of elements $\{b_{i,j}(\varepsilon), 1 \leq j \leq N^i_{2\text{nd}}\}$ dressing the elements $a_i(\varepsilon)$ in $\mathcal{N}_{1\text{st}}$ as the *Nucleus of the second dressing.*

In the following we will fix the element of the Kernel we are dressing ($K^{\sigma,0}_{\sigma,0}$) even if the procedure is completely general and it is possible to consider and arbitrary element of the Kernel.

Thus we will adopt the following prescription:

1- Contribution of the main fermion line The contribution of the main fermion line is unaltered. Determine the denominator A_0 and the the sign p_0 as in the "standard diagrammatics", the leading integral form reads as in Eq.(A.21):

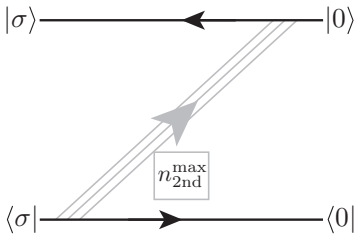

$$= \frac{i}{\hbar} \lim_{\eta \to 0} \int_{-\infty}^{+\infty} d\varepsilon \, \frac{\bar{\alpha}_{l,\sigma}(\varepsilon) f_l^{p_0}(\varepsilon)}{A_0(\varepsilon) + i\eta - \sum_{i=1}^{4} \tilde{a}_i(\varepsilon)}.$$

2- Analytic form of the elements $\tilde{a}_i(\varepsilon)$ in $\mathcal{N}_{1\text{st}}$ For each element ($\tilde{a}_i(\varepsilon)$) in the Nucleus of the first dressing $\mathcal{N}_{1\text{st}}$ choose:

a- the number ($N^i_{2\text{nd}}$);

b- the order ($n^i_{2\text{nd}}$);

c- the type (kind of process);

of diagrams dressing the corresponding $\tilde{a}_i(\varepsilon)$ with $i \in \{1,2,3,4\}$ in this case. Here $n^{\max}_{2\text{nd}}$ is the largest $n^i_{2\text{nd}}$. This defines a set of Nuclei

$\{\mathcal{N}^i_{\rm 2nd}\}$ of the second dressing that in this case reads

$$\mathcal{N}^1_{\rm 2nd} = \left\{ \quad \text{with } 1 \le j \le N^1_{\rm 2nd} \right.$$

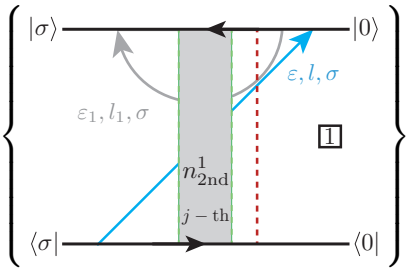

$$\mathcal{N}^2_{\rm 2nd} = \left\{ \quad \text{with } 1 \le j \le N^2_{\rm 2nd} \right.$$

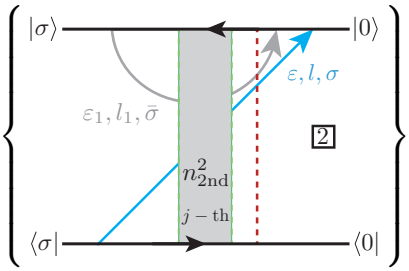

$$\mathcal{N}^{3(4)}_{\rm 2nd} = \left\{ \quad \text{with } 1 \le j \le N^{3(4)}_{\rm 2nd} \right.$$

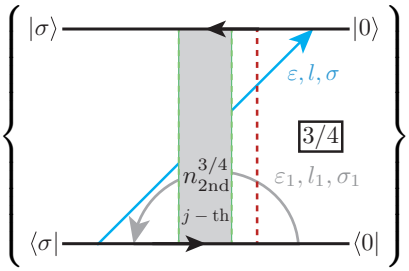

where we depicted in light-blue the main fermion line, in grey the one from the Nucleus of the first dressing and the grey shaded area represents the tunnelling events dressing the elements in $\mathcal{N}_{\rm 1st}$. We reported the index corresponding to the element of $\mathcal{N}_{\rm 1st}$ in a squared box. Notice that we grouped the Nuclei for the functions $a_{3(4)}(\varepsilon)$ in the last row. From the above diagrams it is possible to extract the integral expression of the elements in $\mathcal{N}_{\rm 1st}$:

$$\tilde{a}_i(\varepsilon) = \sum_{l_1} \int_{-\infty}^{+\infty} d\varepsilon_1 \, \frac{\bar{\alpha}_{l_1,\sigma_1}(\varepsilon_1)\, f^{p_1}_{l_1}(\varepsilon_1)}{A_1(\varepsilon,\varepsilon_1) + i\eta - \sum_{j=1}^{N^i_{\rm 2nd}} b_{i,j}(\varepsilon,\varepsilon_1)} \tag{A.23}$$

where $A_1(\varepsilon,\varepsilon_1)$ and p_1 have to be determined through the "standard diagrammatic rules" and σ_1 is fixed by the specific form of the diagram.

3- Role of the second dressing: $(b_{i,j}(\varepsilon))$ Having defined the elements in the Nuclei of the second dressing and thus their order $n^i_{\rm 2nd}$ and shapes we can determine the contribution of the j-th element in the i-th

Nucleus $\mathcal{N}^i_{\text{2nd}}$ according to

$$b_{i,j}(\varepsilon) = (-1)^{n^{i,j}_{\text{int}}} \cdot \sum_{l_1,\ldots,l_{n_2}} \int_{-\infty}^{+\infty} d\varepsilon \ldots d\varepsilon_{n_4+1} \prod_{k=1}^{2n_4-1} \frac{\bar{\alpha}_{l_2,\sigma_2}(\varepsilon) f^{p^{i,j}_2}_{l_2}(\varepsilon) \ldots \bar{\alpha}_{l_{n+1},\sigma_{n+1}}(\varepsilon_{n+1}) f^{p^{i,j}_{n+1}}_{l_{n+1}}(\varepsilon_{n+1})}{A^{i,j}_k + i\eta}. \quad \text{(A.24)}$$

where the denominators $A^{i,j}_k$ and the signs $p^{i,j}_2, \ldots, p^{i,j}_{n_2+1}$ have to be determined with the standard diagrammatic rules as usual.

An application of this extension of the theory can be found in Sect.2.2.

A.5 Energy dependence of the second order rates: $Y^p_d(\bar{\mu}^{i,j}_l)$

In this Section we will deal with the calculation of the analytical function $Y^p_d(\bar{\mu}^{i,j}_l)$, we have defined in App.A.5. This is of crucial importance, as we have shown in Sect.2.1, for the identification of the rates. To this purpose let us notice that

$$Y^p_d\left(\bar{\mu}^{i,j}_l\right) = Y^{pd}_+\left(d\bar{\mu}^{i,j}_l\right),$$

which allows us to consider the following (see Eq.(A.11)) integral:

$$Y^{pd}_+\left(\tilde{\mu}^{i,j}_l\right) = -\frac{i}{\hbar} \lim_{\tilde{\eta}\to 0} \int_{-\infty}^{+\infty} d\tilde{\varepsilon} \frac{f^{pd}(\tilde{\varepsilon})}{\tilde{\varepsilon} - \tilde{\mu}^{i,j}_l + i\tilde{\eta}} L\left(\tilde{\varepsilon}, \tilde{W}\right), \quad \text{(A.25)}$$

where $\tilde{\mu}^{i,j}_l = d\beta\bar{\mu}^{i,j}_l$. Here the convergence of the integral is ensured by the Lorentzian cut-off in the density of states (see Eq.(1.70)). We choose to perform this integration using the residue theorem and choosing the following complex function:

$$\xi(z) = \frac{f^{pd}(z)}{z - \tilde{\mu}^{i,j}_l + i\tilde{\eta}} L\left(z, \tilde{W}\right). \quad \text{(A.26)}$$

In Tab.A.1 we have shown the poles of this function: in the first column we have reported the function to which it corresponds the pole, in the second the position of the pole and in the third the residue of the $\xi(z)$ function. In order to perform the integration we have chosen the path ($\bar{\gamma} = C^+_R + C^+_\varepsilon + \gamma_R$) indicated in Fig.A.4. We have divided it in a semi-circle of radius R (C^+_R), that we will send to infinity, a semi-circle of radius ϵ (C^+_ε), that we use to regularize the pole in $z = \tilde{\mu}^{i,j}_l$ (having performed the limit for $\tilde{\eta} \to 0$), and a

Function	Pole position	Residuum
$f^{pd}(z)$	$z = i2\pi\left(k+\frac{1}{2}\right),\ k\in\mathbb{Z}$	$-dp\frac{L\left[i2\pi\left(k+\frac{1}{2}\right),\tilde{W}\right]}{i2\pi\left(k+\frac{1}{2}\right)-\tilde{\mu}_l^{i,j}+i\tilde{\eta}}$
$L\left(z,\tilde{W}\right)$	$z=\pm iW$	$\mp i\frac{\tilde{W}}{2}\cdot\frac{f^{pd}\left(\pm i\tilde{W}\right)}{i\left(\pm\tilde{W}+\tilde{\eta}\right)-\tilde{\mu}_l^{i,j}}$
$\frac{1}{z-\tilde{\mu}_l^{i,j}+i\tilde{\eta}}$	$z=\tilde{\mu}_l^{i,j}-i\tilde{\eta}$	$f^{dp}\left(\tilde{\mu}_l^{i,j}-i\tilde{\eta}\right)L\left(\tilde{\mu}_l^{i,j}-i\tilde{\eta},\tilde{W}\right)$

Table A.1: Poles of the function $\xi(z)$.

straight line along the real axis from $-R$ to R (γ_R):

$$\lim_{\tilde{\eta}\to 0}\left[\lim_{R\to\infty}\lim_{\epsilon\to 0}\left(\int_{-R}^{\tilde{\mu}_l^{i,j}-\epsilon}\frac{f^{pd}(x)\,L\left(x,\tilde{W}\right)}{x-\tilde{\mu}_l^{i,j}+i\tilde{\eta}}\,dx+\int_{\tilde{\mu}_l^{i,j}+\epsilon}^{R}\frac{f^{pd}(x)\,L\left(x,\tilde{W}\right)}{x-\tilde{\mu}_l^{i,j}+i\tilde{\eta}}\,dx\right)+\right.$$
$$\left.+\lim_{R\to\infty}\int_0^{\pi}\frac{f^{pd}\left(Re^{i\theta}\right)L\left(Re^{i\theta},\tilde{W}\right)}{Re^{i\theta}-\tilde{\mu}_l^{i,j}+i\tilde{\eta}}Re^{i\theta}i\,d\theta\right]+$$
$$+\lim_{\epsilon\to 0}\int_{\pi}^{0}f^{pd}\left(\tilde{\mu}_l^{i,j}+\epsilon e^{i\theta}\right)L\left(\tilde{\mu}_l^{i,j}+\epsilon e^{i\theta},\tilde{W}\right)i\,d\theta. \quad \text{(A.27)}$$

It's not difficult to demonstrate that the second term in Eq.(A.27) vanishes in the limit of $R\to\infty$, for every angle θ, because of the Lorentzian cut-off. It's worth to notice that, since we have to perform the limit for $\tilde{\eta}\to 0$, the number of poles in the superior ($y>0$) half complex plane and in the inferior one ($y<0$) is equal. Moreover the values of the residues is such that if we have chosen the path formed by the semicircle lying in the inferior semi-plane (C_R^-), the result wouldn't change because the change of sign in the residues is compensated by the sign due to the clockwise order of integration. This is a further "consistency check" to be taken into account. Considering the first term in Eq.(A.27), we can recognize the definition of the principal value integral that allows us to recast the real and imaginary part of our integral

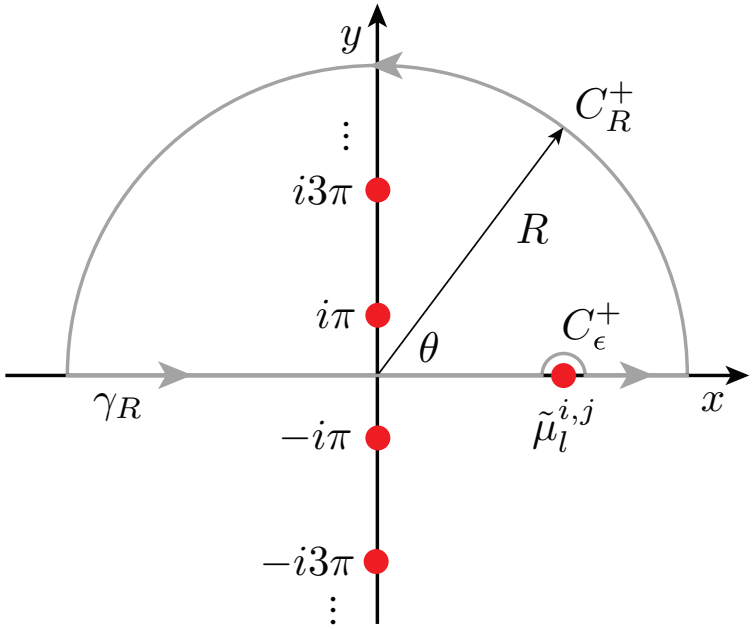

Figure A.4: Scheme of the complex plane for the function $\xi(z)$: we have reported the poles in red and the path we have chosen in grey.

as:

$$\mathsf{Re}\left\{\lim_{\tilde{\eta}\to 0}\int_{\tilde{\gamma}}\frac{f^{pd}(z)\,L\left(z,\tilde{W}\right)}{z-\tilde{\mu}_l^{i,j}+i\tilde{\eta}}\,dz\right\}\overset{\text{def}}{=}\fint\frac{f^{pd}(z)\,L\left(z,\tilde{W}\right)}{z-\tilde{\mu}_l^{i,j}}\,dz,$$

$$\mathsf{Im}\left\{\lim_{\tilde{\eta}\to 0}\int_{\tilde{\gamma}}\frac{f^{pd}(z)\,L\left(z,\tilde{W}\right)}{z-\tilde{\mu}_l^{i,j}+i\tilde{\eta}}\,dz\right\}=-\pi f^{pd}\left(\tilde{\mu}_l^{i,j}\right)L\left(\tilde{\mu}_l^{i,j},\tilde{W}\right),$$

where in the real part of the integration we indicated the principal value prescription ($\fint$). It is important to stress that the sign of the imaginary part is fixed by the physics. Indeed, since $t>0$, $\lambda>0$ in the Laplace transform of the Kernel super-operator and then also $\tilde{\eta}>0$. This imposes that the pole of the denominator of $\xi(z)$ is in the inferior half plane and then it has to be avoided and not included in the chosen path (otherwise it would have contributed with the sign $+$)[1]. In order to perform the principal value integration we use the residue theorem and, taking into account Tab.A.1, we

[1]One can also include the pole in the path but, consequently, he has also to subtract the value of the pole he has added artificially.

obtain:

$$\mathsf{Re}\left\{\lim_{\tilde{\eta}\to 0}\int_{\bar{\gamma}}\frac{f^{pd}\left(z\right)L\left(z,\tilde{W}\right)}{z-\tilde{\mu}_l^{i,j}+i\tilde{\eta}}\,dz\right\}=$$
$$=-\mathsf{Re}\left\{2\pi i\left[dp\sum_{k=0}^{+\infty}\frac{L\left(i\omega_k,\tilde{W}\right)}{i\omega_k-\tilde{\mu}_l^{i,j}}+\frac{f^{pd}\left(i\tilde{W}\right)}{i\tilde{W}-\tilde{\mu}_l^{i,j}}\left(\frac{i\tilde{W}}{2}\right)\right]\right\}, \quad \text{(A.28)}$$

where $\omega_k=(2k+1)\,\pi$. We can recast this result in a more "user-friendly" form using the two following identities

$$f^{dp}\left(i\tilde{W}\right)=\frac{1-idp\tan\left(\frac{\tilde{W}}{2}\right)}{2},$$
$$\frac{L\left(i\omega_k,\tilde{W}\right)}{i\omega_k-\tilde{\mu}_l^{i,j}}=iL\left(\tilde{\mu}_l^{i,j},\tilde{W}\right)\left[\frac{1}{2}\left(\frac{1-i\frac{\tilde{\mu}_l^{i,j}}{\tilde{W}}}{\omega_k-\tilde{W}}+\frac{1+i\frac{\tilde{\mu}_l^{i,j}}{\tilde{W}}}{\omega_k-\tilde{W}}\right)-\frac{1}{\omega_k+i\tilde{\mu}_l^{i,j}}\right],$$

where in order to demonstrate the second identity we have used the partial fraction decomposition. Then inserting these equations in Eq.(A.28) and taking the real value we obtain:

$$\mathsf{Re}\left\{\lim_{\tilde{\eta}\to 0}\int_{\bar{\gamma}}\frac{f^{pd}\left(z\right)L\left(z,\tilde{W}\right)}{z-\tilde{\mu}_l^{i,j}+i\tilde{\eta}}\,dz\right\}=$$
$$=L\left(\tilde{\mu}_l^{i,j},\tilde{W}\right)\left\{\sum_{k=0}^{+\infty}dp\left[\frac{\pi}{\omega_k-\tilde{W}}+\frac{\pi}{\omega_k+\tilde{W}}-\mathsf{Re}\left\{\frac{2\pi}{\omega_k+i\tilde{\mu}_l^{i,j}}\right\}\right]+\right.$$
$$\left.-\frac{\pi}{2}\left[\frac{\tilde{\mu}_l^{i,j}}{\tilde{W}}+dp\tan\left(\frac{\tilde{W}}{2}\right)\right]\right\}$$
$$=\left\{dp\left[\frac{1}{2}\sum_{k=0}^{+\infty}\left(\frac{1}{k+\frac{1}{2}-\frac{\tilde{W}}{2\pi}}+\frac{1}{k+\frac{1}{2}+\frac{\tilde{W}}{2\pi}}-2\mathsf{Re}\left\{\frac{1}{k+\frac{1}{2}+i\frac{\tilde{\mu}_l^{i,j}}{2\pi}}\right\}\right)+\right.\right.$$
$$\left.\left.-\frac{\pi}{2}\tan\left(\frac{\tilde{W}}{2}\right)\right]-\frac{\pi\tilde{\mu}_l^{i,j}}{2\tilde{W}}\right\}L\left(\tilde{\mu}_l^{i,j},\tilde{W}\right). \quad \text{(A.29)}$$

Here it's convenient to introduce the *digamma-function* [102]

$$\Psi^{(0)}\left(z\right)=-\frac{1}{z}+\sum_{n=1}^{+\infty}\left[\log\left(1+\frac{1}{n}\right)-\frac{1}{n+z}\right], \quad \text{(A.30)}$$

for which the following identity holds true:

$$\Psi^{(0)}\left(\frac{1}{2}+x\right)-\Psi^{(0)}\left(\frac{1}{2}-x\right)=\pi\tan\left(\pi x\right). \quad \text{(A.31)}$$

Notice that $z \in \mathbb{C}$, whereas, in Eq.(A.31), $x \in \mathbb{R}$. Then, recognizing the digamma function in the last line of Eq.(A.29), we can recast it in a more compact form as follows:

$$\mathsf{Re}\left\{\lim_{\tilde{\eta}\to 0}\int_{\bar{\gamma}} \frac{f^{pd}(z)\, L\left(z,\tilde{W}\right)}{z-\tilde{\mu}_l^{i,j}+i\tilde{\eta}}\, dz\right\} = -L\left(\tilde{\mu}_l^{i,j},\tilde{W}\right)\cdot$$
$$\cdot\left\{\frac{\pi\tilde{\mu}_l^{i,j}}{2\tilde{W}} + pd\left[\Psi^{(0)}\left(\frac{1}{2}+\frac{\tilde{W}}{2\pi}\right) - \mathsf{Re}\left\{\Psi^{(0)}\left(\frac{1}{2}+i\frac{\tilde{\mu}_l^{i,j}}{2\pi}\right)\right\}\right]\right\}. \quad \text{(A.32)}$$

Because as $\tilde{\mu}_l^{i,j}/\tilde{W} \ll 1$,

$$L\left(\tilde{\mu}_l^{i,j},\tilde{W}\right) \simeq 1+\mathcal{O}\left(\frac{\tilde{\mu}_l^{i,j}}{\tilde{W}}\right), \qquad \frac{\tilde{\mu}_l^{i,j}}{2\tilde{W}} \simeq 0+\mathcal{O}\left(\frac{\tilde{\mu}_l^{i,j}}{\tilde{W}}\right),$$

we can approximate the final result for the function we are interested in as:

$$Y_+^{pd}\left(\tilde{\mu}_l^{i,j}\right) \simeq -\pi f^{pd}\left(\tilde{\mu}_l^{i,j}\right) +$$
$$+ ipd\left[\Psi^{(0)}\left(\frac{1}{2}+\frac{\tilde{W}}{2\pi}\right) - \mathsf{Re}\left\{\Psi^{(0)}\left(\frac{1}{2}+i\frac{\tilde{\mu}_l^{i,j}}{2\pi}\right)\right\}\right]. \quad \text{(A.33)}$$

Here it's worth to highlight that we can find the finite bandwidth cut-off ($\tilde{W}$) only in the imaginary part of $Y_+^{pd}\left(\tilde{\mu}_l^{i,j}\right)$ (the digamma function is real if the argument is real see Eq.(A.30)). Since the *rates in the second order* are function of the real part of this function *the cut-off does not appear* in the equation for the populations and the current flowing through the dot. On the contrary this is not the case for the DSO in the limit of large Coulomb interaction ($U \to +\infty$) where the cut-off is the only remaining energy scale apart form E_σ (see Sect.2.1.1). It is useful to recast Eq.(A.33) in a more compact form. Using the following identity:

$$f^p(x) = \frac{\pi - 2p\mathsf{Im}\left\{\Psi^{(0)}\left(\frac{1}{2}+i\frac{x}{2\pi}\right)\right\}}{2\pi} \quad \text{with } x \in \mathbb{R}.$$

Eq.(A.33) without any wide bandwidth approximation reads

$$Y_+^{pd}\left(\tilde{\mu}_l^{i,j}\right) = -\frac{i}{\hbar}L(\tilde{\mu}_l^{i,j},\tilde{W})\left\{-\frac{\pi}{2}\left(\frac{\tilde{\mu}_l^{i,j}}{\tilde{W}}+i\right) +\right.$$
$$\left. - pd\left[\Psi^{(0)}\left(\frac{1}{2}+\frac{\tilde{W}}{2\pi}\right) - \Psi^{(0)}\left(\frac{1}{2}+i\frac{\tilde{\mu}_l^{i,j}}{2\pi}\right)\right]\right\}. \quad \text{(A.34)}$$

It will turn out that Eq.(A.34) is a very useful expression when considering a non-perturbative treatment of the Liouville-Von Neumann equation.

A.6 Propagator sum rule

In this Section we will deduce, with the help of the diagrammatic language, the sum-rule in Eq.(3.8) concerning the self-energy $\Sigma_{\Pi b,a}(t,t_1)$. Moreover we will discuss its implications on the current flowing out of the l-lead. To this purpose let us consider the general diagrammatic expressions for the self-energy components

$$\Sigma^{l,-}_{\Pi_{b,a}}(\lambda) = \sum_c \mathsf{Re}\left\{ \right. \tag{A.35a}$$

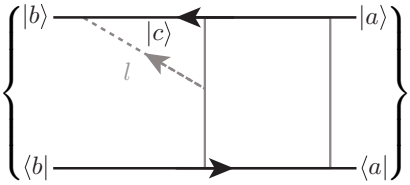

$$\left. \right\},$$

$$\Sigma^{l,+}_{\Pi_{c,a}}(\lambda) = \sum_b \mathsf{Re}\left\{ \right. \tag{A.35b}$$

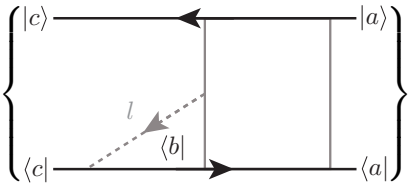

$$\left. \right\},$$

where we fixed $|b\rangle = \hat{d}^\dagger_\sigma |c\rangle$. Thus we have the following constraint on the number of particles $N(b) = N(c) + 1$. Moreover we will assume without any loss of generality that $N(c) = n$ with $n \in \mathbb{N}$. Since the states' time evolution on the Keldysh contours in Eqs.(A.35a) and (A.35b) is the same but we placed one vertex on the lower contour in Eq.(A.35b) with respect to Eq.(A.35a), using the diagrammatic rules we have

$$\sum_{\substack{b:\\ N(b)=n+1}} \Sigma^{l,-}_{\Pi_{b,a}}(\lambda) = -\sum_{\substack{c:\\ N(c)=n}} \Sigma^{l,+}_{\Pi_{c,a}}(\lambda)\,. \tag{A.36}$$

In order to further develop Eq.(A.36), we notice that in an Hilbert space composed of states with at most N particles we have

$$\Sigma^{l,-}_{\Pi_{0,a}}(\lambda) = 0, \qquad \Sigma^{l,+}_{\Pi_{N,a}}(\lambda) = 0, \tag{A.37}$$

i.e. $\hat{d}^\dagger_\sigma |N\rangle = 0$ and it does not exist any state such that $|0\rangle = \hat{d}^\dagger_\sigma |c\rangle$. Taking into account Eqs.(A.37), we consider the sum with respect to all the particle numbers in the Hilbert space of Eq.(A.36),

$$\sum_{n=0}^{N-1} \sum_{\substack{b:\\ N(b)=n+1}} \Sigma^{l,-}_{\Pi_{b,a}}(\lambda) = -\sum_{n=0}^{N-1} \sum_{\substack{c:\\ N(c)=n}} \Sigma^{l,+}_{\Pi_{c,a}}(\lambda)\,,$$

and thus

$$\sum_{n=0}^{N} \left[\sum_{\substack{b:\\ N(b)=n}} \Sigma^{l,-}_{\Pi_{b,a}}(\lambda) + \sum_{\substack{c:\\ N(c)=n}} \Sigma^{l,+}_{\Pi_{c,a}}(\lambda) \right] = \sum_b \Sigma^{l,-}_{\Pi_{b,a}}(\lambda) + \sum_c \Sigma^{l,+}_{\Pi_{c,a}}(\lambda) = 0.$$

This straightforwardly implies

$$\sum_b \Sigma_{\Pi b,a}(\lambda) = \sum_b \Sigma^{\infty}_{\Pi\, b,a} = 0,$$

as we stated in Eq.(3.8). Moreover, considering the inverse Laplace transform of $\Sigma^{l,\pm}_{\Pi b,a}(\lambda)$, we have

$$\sum_b \Sigma_{\Pi b,a}(t-t_1) = 0,$$
$$\sum_{\substack{b:\\ N(b)=n+1}} \Sigma^{l,-}_{\Pi b,a}(t-t_1) = -\sum_{\substack{c:\\ N(c)=n}} \Sigma^{l,+}_{\Pi c,a}(t-t_1).$$

Using the time space diagrammatic rules in Appendix A of Ref. [38], it turns out that these sum rules hold true in general:

$$\sum_b \Sigma_{\Pi b,a}(t,t_1) = 0, \tag{A.38a}$$
$$\sum_{\substack{b:\\ N(b)=n+1}} \Sigma^{l,-}_{\Pi b,a}(t,t_1) = -\sum_{\substack{c:\\ N(c)=n}} \Sigma^{l,+}_{\Pi c,a}(t,t_1). \tag{A.38b}$$

As we observed in Sect.3.1, Eq.(A.38a) implies the RDM trace conservation during the time evolution. Considering Eq.(3.5) we can gain more insight on these sum rules

$$-e\sum_b N(b)\dot{\rho}_b(t) = -e\sum_{a,b}\int_{t_0}^{t} dt_1 \sum_b N(b)\Sigma_{\Pi b,a}(t,t_1)\,\rho_a(t_1),$$

where we multiplied Eq.(3.5) by the charge in the state $|b\rangle$ and we summed over all the states in the Hilbert space. Using Eq.(A.38b) we obtain

$$\frac{\mathrm{d}}{\mathrm{d}t}Q(t) = \frac{\mathrm{d}}{\mathrm{d}t}\left[\sum_b -eN(b)\rho_b(t)\right] = \tag{A.39}$$
$$= -\sum_l I_l(t) = -e\sum_l\sum_{b,a}\int_{t_0}^{t} dt_1\, \Sigma^{l,-}_{\Pi b,a}(t,t_1)\,\rho_a(t_1).$$

Eq.(A.39) represents the charge conservation equation: $\dot{Q}(t) + \sum_l I_l(t) = 0$[2]. In the stationary limit, when no time dependence is left in the quantum dot charge, Eq.(A.39) yields the tunnelling current conservation condition

$$\sum_l I^{\infty}_l = 0.$$

[2]Notice that we considered the current flowing out of the l-leads in contrast to Ref. [38] where the authors evaluated the current flowing into the l-lead.

A.7 Solution of the RTA equations in the degenerate case

In this Section, along the lines of Appendix B in Ref. [38], we calculate the imaginary part of the solution of the RTA integral equations in the M-degenerate case (Eq.(3.35)). To this purpose let us consider the following equation

$$\left[\pi_{0,0}^{1,1}(\varepsilon)\right]^{-1}\Phi(\varepsilon)=h(\varepsilon)-\gamma(\varepsilon)\int_{-\infty}^{+\infty}d\varepsilon'\frac{\Phi^{*}(\varepsilon')}{\varepsilon-\varepsilon'+i\eta}, \tag{A.40}$$

whose inhomogeneous term $h(\varepsilon)$ distinguishes the solutions $\Phi^{\pm}(\varepsilon)$. Moreover in the following is fruitful to consider

$$\begin{aligned}&\mathsf{Im}\left\{\left[\pi_{0,0}^{1,1}(\varepsilon)\right]^{-1}\right\}=-\mathsf{Im}\left\{\Sigma_{\pi_{0,0}^{1,1}}(\varepsilon)\right\}\\&=\mathsf{Im}\left\{\lim_{\eta\to0}\int_{-\infty}^{+\infty}d\varepsilon'\frac{\gamma(\varepsilon)}{\varepsilon'-\varepsilon-i\eta}\right\}=\pi\gamma(\varepsilon),\end{aligned} \tag{A.41}$$

where we used the relation $\lim_{\eta\to0}\frac{1}{x-i\eta}=P(1/x)+i\pi\delta(x)$ to perform the integration. Here we indicated with $P(1/x)$ the principal value integration of $1/x$. Thus we consider the imaginary part of Eq.(A.40)

$$\left[\varepsilon-E_{10}-\mathsf{Re}\left\{\Sigma_{\pi_{0,0}^{1,1}}(\varepsilon)\right\}\right]\mathsf{Im}\left\{\Phi(\varepsilon)\right\}=\gamma(\varepsilon)\fint_{+\infty}^{-\infty}d\varepsilon'\frac{\mathsf{Im}\left\{\Phi(\varepsilon')\right\}}{\varepsilon-\varepsilon'}, \tag{A.42}$$

where the integration on the right side has to be understood as the principal value integration prescription ($\fint$). $\Sigma_{\pi_{0,0}^{1,1}}(\varepsilon)$ and $\pi_{0,0}^{1,1}(\varepsilon)$ are analytic functions in the upper half complex plane[3]and $\pi_{0,0}^{1,1}(\varepsilon)/(\varepsilon-\varepsilon')\sim1/(\|\varepsilon'\|^{2}\exp i\theta)$ as $\|\varepsilon'\|\to\infty$, thus we have

$$\lim_{\eta\to0}\int_{C}dz\frac{\pi_{0,0}^{1,1}(z)}{\omega-z+i\eta}=0\quad\Rightarrow\quad\fint_{+\infty}^{-\infty}d\varepsilon'\frac{\pi_{0,0}^{1,1}(\omega')}{\omega-\omega'}-i\pi\pi_{0,0}^{1,1}(\omega)=0, \tag{A.43}$$

where, on the left, we integrated in the upper half complex plane on a curve C as in App.A.5. Thus the propagator $\pi_{0,0}^{1,1}(\varepsilon)$ fulfils the Kramers-Kronig relations in Eq.(A.43), i.e. its real and imaginary parts are related each other.

[3]The proper analytic continuation of the self-energy $\Sigma_{\pi_{0,0}^{1,1}}(\varepsilon)$ is obtained considering Eq.(3.32). Indeed the digamma function has no poles in the upper half complex plane.

Thus the ansatz $\mathsf{Im}\left\{\Phi\left(\varepsilon\right)\right\} = c\mathsf{Im}\left\{\pi_{0,0}^{1,1}\left(\varepsilon\right)\right\}$ fulfils Eq.(A.42):

$$\left[\varepsilon - E_{10} - \mathsf{Re}\left\{\Sigma_{\pi_{0,0}^{1,1}}\left(\varepsilon\right)\right\}\right]\mathsf{Im}\left\{\Phi\left(\varepsilon\right)\right\} = c\mathsf{Re}\left\{\left[\pi_{0,0}^{1,1}\left(\omega\right)\right]^{-1}\right\}\mathsf{Im}\left\{\pi_{0,0}^{1,1}\left(\varepsilon\right)\right\} =$$

$$= \gamma\left(\varepsilon\right)\int_{+\infty}^{-\infty} d\varepsilon' \frac{\mathsf{Im}\left\{\Phi\left(\varepsilon'\right)\right\}}{\varepsilon - \varepsilon'} = -c\mathsf{Im}\left\{\left[\pi_{0,0}^{1,1}\left(\varepsilon\right)\right]^{-1}\right\}\mathsf{Re}\left\{\pi_{0,0}^{1,1}\left(\varepsilon\right)\right\}.$$

It is a matter of pure algebra to check that indeed

$$\mathsf{Re}\left\{\left[\pi_{0,0}^{1,1}\left(\omega\right)\right]^{-1}\right\}\mathsf{Im}\left\{\pi_{0,0}^{1,1}\left(\varepsilon\right)\right\} = -\mathsf{Im}\left\{\left[\pi_{0,0}^{1,1}\left(\varepsilon\right)\right]^{-1}\right\}\mathsf{Re}\left\{\pi_{0,0}^{1,1}\left(\varepsilon\right)\right\}.$$

In order to find the proportionality constant c we multiply both sides of Eq.(A.40) by $\pi_{0,0}^{1,1}\left(\varepsilon\right)/\gamma\left(\varepsilon\right)$ and we integrate it with respect to ε:

$$\int_{-\infty}^{+\infty} d\varepsilon \frac{\Phi\left(\varepsilon\right)}{\gamma\left(\varepsilon\right)} = \int_{-\infty}^{+\infty} d\varepsilon \frac{\pi_{0,0}^{1,1}\left(\varepsilon\right)}{\gamma\left(\varepsilon\right)} h(\varepsilon) - \int_{-\infty}^{+\infty} d\varepsilon \int_{-\infty}^{+\infty} d\varepsilon' \pi_{0,0}^{1,1}\left(\varepsilon\right) \frac{\Phi^*\left(\varepsilon'\right)}{\varepsilon - \varepsilon' + i\eta}. \quad \text{(A.44)}$$

Provided that we can exchange the order of integration in the second term on the right hand side of Eq.(A.44), the integration of this term yields zero contribution, since the function to be integrated $\left(\pi_{0,0}^{1,1}\left(\varepsilon\right)/\left(\varepsilon - \varepsilon' + i\eta\right)\right)$ is analytic in the upper half complex plane and it decays fast enough as $\|\varepsilon\| \to \infty$ to integrate it considering the residue theorem. Having this in mind and considering the imaginary part of Eq.(A.44) we have

$$\int_{-\infty}^{+\infty} d\varepsilon \frac{\mathsf{Im}\left\{\Phi\left(\varepsilon\right)\right\}}{\gamma\left(\varepsilon\right)} = \int_{-\infty}^{+\infty} d\varepsilon \frac{c\mathsf{Im}\left\{\pi_{0,0}^{1,1}\left(\varepsilon\right)\right\}}{\gamma\left(\varepsilon\right)} = \int_{-\infty}^{+\infty} d\varepsilon \frac{\pi_{0,0}^{1,1}\left(\varepsilon\right)}{\gamma\left(\varepsilon\right)} h(\varepsilon), \quad \text{(A.45)}$$

where in the second step we used the aforementioned ansatz. Thus, using $\mathsf{Im}\left\{\pi_{0,0}^{1,1}\left(\varepsilon\right)\right\} = -\pi\gamma\left(\varepsilon\right)\left\|\pi_{0,0}^{1,1}\left(\varepsilon\right)\right\|^2$, the proportionality constant reads

$$c = \frac{\int_{-\infty}^{+\infty} d\varepsilon \left\|\pi_{0,0}^{1,1}\left(\varepsilon\right)\right\|^2 h\left(\varepsilon\right)}{\int_{-\infty}^{+\infty} d\varepsilon \left\|\pi_{0,0}^{1,1}\left(\varepsilon\right)\right\|^2}.$$

Finally the solution we are seeking for reads

$$\Phi\left(\varepsilon\right) = -\pi\gamma\left(\varepsilon\right)\frac{\int_{-\infty}^{+\infty} d\varepsilon' \left\|\pi_{0,0}^{1,1}\left(\varepsilon'\right)\right\|^2 h\left(\varepsilon'\right)}{\int_{-\infty}^{+\infty} d\varepsilon' \left\|\pi_{0,0}^{1,1}\left(\varepsilon'\right)\right\|^2}\left\|\pi_{0,0}^{1,1}\left(\varepsilon\right)\right\|^2. \quad \text{(A.46)}$$

It is easy to see now that, fixing $h\left(\varepsilon'\right)$ to $\gamma^{\pm}\left(\varepsilon'\right)\left(1\right)$, one can introduce the constants $\lambda^{\pm}(\lambda)$ and write the solution to Eq.(3.35) as in Eq.(3.36).

APPENDIX B

DDSO corrections to the Kondo temperature

In this Appendix we want to give a qualitative argument to show that the DDSO corrections to the DSO are responsible for the correct scaling exponent in the Kondo temperature. To this purpose we will follow the prescription in Sect.2.1.1 to extract the Kondo temperature up to a numerical pre-factor. In the DDSO the situation is much more intricate since, in general, we do not have an analytical expression of the self-energy because of the $B_i^{\sigma 0}(\varepsilon, \varepsilon_1)$ functions in Eq.(2.20)[1]. For such a reason in this Appendix we first need to find some approximation of these functions that will allow us to obtain an analytical expression of the DDSO self-energy. We stress that we will consider this approximation only in this Appendix; in the results in the main text we took into account the full theory numerically. Having these considerations in mind we consider the self-energy (Eq.(2.19)) at the Fermi level $\varepsilon = \mu_0$, in equilibrium $\mu_l = \mu_0$. Thus we evaluate the DDSO corrections

[1] Even though we found an "analytic" expression, in the form of a series, of the DDSO self-energy, such an expression revealed to be not fruitful to argue about the analytic form of the Kondo temperature.

straightforwardly

$$B_1^{10}\left(\tilde{\mu}_0,\tilde{\varepsilon}_1\right)=\frac{\Gamma}{\pi}L\left(\varepsilon_1-\mu_0,W\right)\left[-\pi\left(\frac{\varepsilon_1-\mu_0}{W}+i\right)+\right. \tag{B.1a}$$
$$\left.+\Psi^{(0)}\left(\frac{1}{2}+i\frac{\tilde{\varepsilon}_1+\tilde{E}_{10}-2\tilde{\mu}_0}{2\pi}\right)-\Psi^{(0)}\left(\frac{1}{2}+i\frac{\tilde{\varepsilon}_1-\tilde{E}_{10}}{2\pi}\right)\right],$$
$$B_{3(4)}^{10}\left(\tilde{\mu}_0,\tilde{\varepsilon}_1\right)=\frac{\Gamma}{2\pi}L\left(\varepsilon_1-\mu_0,W\right)\left[-\pi\left(\frac{\varepsilon_1-\mu_0}{W}+i\right)+\right. \tag{B.1b}$$
$$\left.-\Psi^{(0)}\left(\frac{1}{2}+i\frac{\tilde{\varepsilon}_1+\tilde{E}_{10}-2\tilde{\mu}_0}{2\pi}\right)+\Psi^{(0)}\left(\frac{1}{2}+i\frac{\tilde{\varepsilon}_1-\tilde{E}_{10}}{2\pi}\right)\right].$$

In order to find a qualitatively good approximation of these functions in the Kondo regime, close to the Fermi level, we consider their Taylor expansion about $\varepsilon_1=\mu_0$ up to the zeroth order. Even though this is a crude approximation of these corrections, as we will see, it captures the essence of the full DDSO theory. Thus we have

$$B_1^{10}\left(\tilde{\mu}_0,\tilde{\mu}_0\right)=\frac{\Gamma}{\pi}\left[-i\pi+\right. \tag{B.2a}$$
$$\left.+\Psi^{(0)}\left(\frac{1}{2}-i\frac{\tilde{\mu}_0-\tilde{E}_{10}}{2\pi}\right)-\Psi^{(0)}\left(\frac{1}{2}+i\frac{\tilde{\mu}_0-\tilde{E}_{10}}{2\pi}\right)\right],$$
$$B_{3(4)}^{10}\left(\tilde{\mu}_0,\tilde{\mu}_0\right)=\frac{\Gamma}{2\pi}\left[-i\pi+\right. \tag{B.2b}$$
$$\left.-\Psi^{(0)}\left(\frac{1}{2}-i\frac{\tilde{\mu}_0-\tilde{E}_{10}}{2\pi}\right)+\Psi^{(0)}\left(\frac{1}{2}+i\frac{\tilde{\mu}_0-\tilde{E}_{10}}{2\pi}\right)\right].$$

Since in the Kondo regime $\mu_0-E_{10}\gg k_{\mathrm{B}}T$ we can approximate the digamma functions according to their asymptotic series in Eq.(2.9) obtaining

$$B_1^{10}\left(\tilde{\mu}_0,\tilde{\mu}_0\right)=2i\Gamma, \tag{B.3a}$$
$$B_{3(4)}^{10}\left(\tilde{\mu}_0,\tilde{\mu}_0\right)=0. \tag{B.3b}$$

The difference between $B_1^{10}\left(\tilde{\mu}_0,\tilde{\mu}_0\right)$ and $B_{3(4)}^{10}\left(\tilde{\mu}_0,\tilde{\mu}_0\right)$, as we mentioned in Sect.2.2 is in the signs in front of the digamma functions. For this reason we obtained a finite value for $B_1^{10}\left(\tilde{\mu}_0,\tilde{\mu}_0\right)$, whereas $B_{3(4)}^{10}\left(\tilde{\mu}_0,\tilde{\mu}_0\right)\to 0$. This is crucial in the following since, approximating $B_i^{10}\left(\tilde{\mu}_0,\tilde{\varepsilon}_1\right)\simeq B_i^{10}\left(\tilde{\mu}_0,\tilde{\mu}_0\right)$ with $i\in\{\,1,3,4\,\}$, we can perform analytically the integration defining the

elements in $\mathcal{N}_{\text{DDSO}}$ (see Eq.(2.20)) obtaining straightforwardly

$$\frac{a_1^{10}(\mu_0)}{(\Gamma/2\pi)} = i\frac{\pi}{2} - \Psi^{(0)}\left(\frac{1}{2}+\frac{\tilde{\Gamma}}{\pi}\right) + \Psi^{(0)}\left(\frac{1}{2}+\frac{\tilde{W}}{2\pi}\right), \tag{B.4a}$$

$$\frac{a_{3(4)}^{10}(\mu_0)}{(\Gamma/\pi)} = i\frac{\pi}{2} + \Psi^{(0)}\left(\frac{1}{2}\right) - \Psi^{(0)}\left(\frac{1}{2}+\frac{\tilde{W}}{2\pi}\right). \tag{B.4b}$$

It is worth to notice that the element $a_1^{10}(\varepsilon)$ of $\mathcal{N}_{\text{DDSO}}$ is completely regular as $T \to 0$, whereas the $a_{3(4)}^{10}(\varepsilon)$ are still divergent in this limit. This is the direct consequence of the Eqs.(B.3). We can see that the DDSO, in contrast to to the DSO, is capable of distinguishing between the two processes. However it is not precise enough to obtain the proper zero temperature limit. We have now all the ingredients to write the Self-energy as

$$\Sigma_{\text{DDSO}}^{10}(\mu_0) = \frac{\Gamma}{2\pi}\left[-\frac{3}{2}\pi i + \Psi^{(0)}\left(\frac{1}{2}+\frac{\tilde{\Gamma}}{\pi}\right) + \Psi^{(0)}\left(\frac{1}{2}+\frac{\tilde{W}}{2\pi}\right) - 2\Psi^{(0)}\left(\frac{1}{2}\right)\right].$$

Thus, considering Eqs.(2.19) and (2.10), in the limits $\tilde{\Gamma}, \tilde{W} \gg 1$ we find

$$\mu_0 - E_{10} - \frac{\Gamma}{2\pi}\log\left(\frac{\Gamma W}{2\left(\pi k_{\text{B}} T\right)^2}\right) = 0. \tag{B.5}$$

Solving such equation with respect to the temperature we obtain

$$k_{\text{B}}T = \frac{1}{\pi}\sqrt{\frac{\Gamma W}{2}}e^{-\pi\frac{\mu_0 - E_{10}}{\Gamma}},$$

and thus the Kondo temperature in the DDSO theory results

$$k_{\text{B}}T_{\text{K}} \propto \sqrt{\Gamma W}e^{-\pi\frac{\mu_0 - E_{10}}{\Gamma}}. \tag{B.6}$$

Hence in the DDSO the exponent presents the proper dependence on the ratio $(\mu_0 - E_{10})/\Gamma$ [22, 49]. Moreover also the energy dependent pre-factor is now in agreement with the usual formula of the Kondo temperature of the infinite-U Anderson model in Ref. [49] with degeneracy $N = 2$[2].
The Kondo temperature analytic dependence we extracted in Eq.(B.6) is confirmed by the numerical analysis in Sect.2.2, showing the universality of the linear conductance as a function of T/T_{K} for different gate voltages fixing the proportionality constant to be the same for all the gate values.
Moreover already from Eq.(B.5) one can expect that the linear conductance temperature dependence in the DDSO is much stronger,

$$\text{Re}\left\{\Sigma_{\text{DDSO}}^{10}\right\}/\Gamma \propto \log\left(\frac{W\Gamma}{(k_{\text{B}}T)^2}\right),$$

[2]Notice that in literature it is often introduced $\Gamma' = \Gamma/2$ instead of our definition of the coupling constant Γ.

with respect to the DSO one

$$\mathsf{Re}\left\{\Sigma^{10}_{\mathrm{DSO}}\right\}/\Gamma \propto \log\left(\frac{W}{k_{\mathrm{B}}T}\right).$$

Indeed, as it is discussed in Sect.2.2, the DDSO fits the empirical curve in Eq.(2.12) with an exponent ($s_{\mathrm{DDSO}} \simeq 0.2$) almost twice larger than the DSO one ($s_{\mathrm{DSO}} \simeq 0.1$).

APPENDIX C

Orthogonal transformations

In this Appendix we present the construction of the Hamiltonian introduced in Eq.(4.1) in the Kramers basis from an underlying Anderson model that takes into account the carbon nanotube structure [73, 79]. In the absence of the valley mixing and spin-orbit interaction, the basis set $\{|K',\uparrow\rangle, |K',\downarrow\rangle, |K,\uparrow\rangle, |K,\downarrow\rangle\}$, indexed by the valley and spin quantum numbers, is orthogonal. When $\Delta \neq 0$ this is no longer true, and it is suitable to adopt instead the bonding (anti-bonding) representation $\{|a,\uparrow\rangle, |b,\uparrow\rangle, |a,\downarrow\rangle, |b,\downarrow\rangle\}$, which can be constructed as

$$|a,\sigma\rangle = \hat{d}^{\dagger}_{+,\sigma}|0\rangle = \frac{|K',\sigma\rangle + |K,\sigma\rangle}{\sqrt{2}}, \tag{C.1a}$$

$$|b,\sigma\rangle = \hat{d}^{\dagger}_{-,\sigma}|0\rangle = \frac{|K',\sigma\rangle - |K,\sigma\rangle}{\sqrt{2}}, \tag{C.1b}$$

In this basis the CNT Hamiltonian consists of several terms

$$\begin{aligned}\hat{H}_{\mathrm{CNT}} &= \hat{H}^{(0)}_{\mathrm{CNT}} + \hat{H}_{e-e} + \hat{H}_{\mathrm{B}} \\ &= \hat{H}_{\mathrm{d}} + \hat{H}_{\mathrm{KK'}} + \hat{H}_{\mathrm{SO}} + \hat{H}_{e-e} + \hat{H}_{\mathrm{B}},\end{aligned} \tag{C.2}$$

where $\hat{H}_{\mathrm{d}}$ is the SU(4) invariant component and E_{d} the orbital energy which can be tuned through the applied gate voltage. Explicitly,

$$\hat{H}_{\mathrm{d}} = E_{\mathrm{d}} \sum_{i,\sigma=\pm} \hat{d}^{\dagger}_{i,\sigma}\hat{d}_{i,\sigma}\,. \tag{C.3}$$

We add to the pure SU(4) term, respectively, the valley mixing (Eq.(C.4a)) and the SOI (Eq.(C.4b)) components:

$$\hat{H}_{\mathrm{KK'}} = \frac{\Delta_{\mathrm{KK'}}}{2} \sum_{i,\sigma=\pm} i\hat{d}^{\dagger}_{i,\sigma}\hat{d}_{i,\sigma}, \tag{C.4a}$$

$$\hat{H}_{\mathrm{SO}} = \frac{\Delta_{\mathrm{SO}}}{2} \sum_{i,\sigma=\pm} \sigma\hat{d}^{\dagger}_{-i,\sigma}\hat{d}_{i,\sigma}. \tag{C.4b}$$

Notice that in the bonding/anti-bonding basis the valley mixing effect translates in an energy difference between the bonding and anti-bonding states [73]. On the other hand, the SOI (due to curvature effects and relativistic correction to the CNT Hamiltonian) is off-diagonal.
The fourth term in Eq.(C.2) describes the electron-electron interaction with U associated to the charging energy of the dot

$$\hat{H}_{e-e} = \frac{U}{2} \sum_{i\neq i_1=\pm} \sum_{\sigma,\sigma_1=\pm} \hat{d}^{\dagger}_{i,\sigma}\hat{d}_{i,\sigma}\hat{d}^{\dagger}_{i_1,\sigma_1}\hat{d}_{i_1,\sigma_1}. \tag{C.5}$$

The external magnetic field enters through the last term in Eq.(C.2)).

Spectrum for zero magnetic field The single particle Hamiltonian in Eq.(C.2) can be diagonalized by a unitary transformation, and the new orthogonal basis is the Kramers basis $\{|1\rangle, |4\rangle, |2\rangle, |3\rangle\}$ used throughout of the present work. The unitary operator is

$$\mathcal{U} = \begin{pmatrix} \cos(\theta) & \sin(\theta) & 0 & 0 \\ -\sin(\theta) & \cos(\theta) & 0 & 0 \\ 0 & 0 & \cos(\theta) & -\sin(\theta) \\ 0 & 0 & \sin(\theta) & \cos(\theta) \end{pmatrix}, \tag{C.6}$$

where the angle θ is given by $\tan(2\theta) = \Delta_{\mathrm{SO}}/\Delta_{\mathrm{KK'}}$. In the diagonalized form, $\hat{H}_{\mathrm{CNT}}$ becomes the dot Hamiltonian in Eq.(4.1).
We immediately notice that, because the two blocks in Eq.(C.6) yield the same eigenvalues, two pairs of degenerate doublets arise. These are the so-called Kramer pairs that, in our notation, are the couples of states $(1,2)$ and $(3,4)$. As such, the states within each Kramers pair are related through the time reversal operator $\hat{\mathcal{T}}$ (see Eq.(4.2a)) as it is sketched in Fig.4.3. Additionally, valley reversal, governed by the anti-unitary operator $\hat{\mathcal{P}}$ (see Eq.(4.2b)), relates the couples $(1,4)$ and $(2,3)$ originating from the two sub-blocks. Finally, defining $\hat{\mathcal{C}} = \hat{\mathcal{P}} \cdot \hat{\mathcal{T}}^{-1}$ (see Eq.(4.3)), it is possible to relate the couples $(1,3)$ and $(2,4)$ to each other.

Spectrum for finite parallel magnetic field An external magnetic field parallel to the CNT axis couples to both the spin degree of freedom and the

"orbital" one. Thus, in the bonding(anti-bonding) basis, $\hat{H}_{\mathrm{B}}$ reads [79]

$$\begin{aligned}\hat{H}_{\mathrm{B}} &= \hat{H}^{\parallel}_{\mathrm{B-s}} + \hat{H}^{\parallel}_{\mathrm{B-orb}} \\ &= \frac{1}{2} g_{\mathrm{s}} B_{\parallel} \sum_{i,\sigma=\pm} \sigma \hat{d}^{\dagger}_{i,\sigma} \hat{d}_{i,\sigma} + g_{\mathrm{orb}} B_{\parallel} \sum_{i,\sigma=\pm} \hat{d}^{\dagger}_{-i,\sigma} \hat{d}_{i,\sigma},\end{aligned} \tag{C.7}$$

where $B_{\parallel}$ is the amplitude of the parallel magnetic field. Thus, the diagonalized single particle Hamiltonian is

$$\mathcal{U}^{\dagger}\left(B_{\parallel}\right)\left(\hat{H}^{(0)}_{\mathrm{CNT}} + \hat{H}_{\mathrm{B}}\right)\mathcal{U}\left(B_{\parallel}\right) = \sum_{j=1}^{4} E_j \hat{d}^{\dagger}_j \hat{d}_j \tag{C.8}$$

where

$$\mathcal{U}\left(B_{\parallel}\right) = \begin{pmatrix} \cos\left(\theta^{+}\right) & \sin\left(\theta^{+}\right) & 0 & 0 \\ -\sin\left(\theta^{+}\right) & \cos\left(\theta^{+}\right) & 0 & 0 \\ 0 & 0 & \cos\left(\theta^{-}\right) & -\sin\left(\theta^{-}\right) \\ 0 & 0 & \sin\left(\theta^{-}\right) & \cos\left(\theta^{-}\right) \end{pmatrix}.$$

Here we defined $\theta^{\pm}$ in such a way that $\tan(2\theta^{\pm}) = (\Delta_{\mathrm{SO}} \pm 2 g_{\mathrm{orb}} B_{\parallel})/\Delta_{\mathrm{KK'}}$. Notice that $\mathcal{U}\left(B_{\parallel}\right)$ posses a similar block structure as in Eq.(C.6). However, due to $\theta^{+} \neq \theta^{-}$, time reversal symmetry is broken.

Spectrum for finite perpendicular magnetic field An external magnetic field perpendicular to the CNT axis couples, differently to the parallel case, only to the spin degree of freedom [73, 79]. Its action reads

$$\hat{H}_{\mathrm{B}} = \frac{1}{2} g_{\mathrm{s}} B_{\perp} \sum_{i,\sigma=\pm} \hat{d}^{\dagger}_{i,\bar{\sigma}} \hat{d}_{i,\sigma}. \tag{C.9}$$

The transformation that diagonalizes the single particle Hamiltonian can be decomposed as a product of two orthogonal matrices:

$$\begin{aligned}\mathcal{U}\left(B_{\perp}\right) &= \mathcal{O}_1\left(B_{\perp}\right)\mathcal{O}_2\left(B_{\perp}\right), \\ \mathcal{O}_1\left(B_{\perp}\right) &= \begin{pmatrix} \cos\left(\theta^{+}\right) & \sin\left(\theta^{+}\right) & 0 & 0 \\ -\sin\left(\theta^{+}\right) & \cos\left(\theta^{+}\right) & 0 & 0 \\ 0 & 0 & \cos\left(\theta^{-}\right) & \sin\left(\theta^{-}\right) \\ 0 & 0 & -\sin\left(\theta^{-}\right) & \cos\left(\theta^{-}\right) \end{pmatrix}, \\ \mathcal{O}_2\left(B_{\perp}\right) &= \frac{1}{\sqrt{2}} \begin{pmatrix} 1 & 0 & 1 & 0 \\ 0 & 1 & 0 & -1 \\ 1 & 0 & -1 & 0 \\ 0 & 1 & 0 & 1 \end{pmatrix},\end{aligned}$$

where $\theta^{\pm}$ is such that $\tan(2\theta^{\pm}) = \Delta_{\mathrm{SO}}/(\Delta_{\mathrm{KK'}} \pm g_{\mathrm{s}} B_{\perp})$. We notice that $\mathcal{U}\left(B_{\perp}\right)$ mixes both the spin and the bonding(anti-bonding) degrees of freedom, whereas, in the previous case, $\mathcal{U}\left(B_{\parallel}\right)$ was mixing only the latter one.

APPENDIX D

Numerical renormalization group approach

In this Appendix we sketch briefly the strategy to solve the Hamiltonian in Eq.(4.6) using the numerical renormalization group approach [36]. In our work we followed the prescription introduced by Wilson for the single impurity Anderson model [93, 103]. The reader might be interested also in Ref. [104] where the NRG mapping is carried in detail for the Anderson model, being its extension to our extended Anderson model straightforward. The core of the NRG is a logarithmic discretisation of the conduction band with a parameter $\Lambda \simeq 2$, followed by a mapping of the Hamiltonian to a semi-infinite chain, the *Wilson chain*. In this way the problem can be solved perturbatively, as the hopping couplings along the chain, $t_n^j \sim \Lambda^{-n/2}$ decrease exponentially [87]. The conduction band Hamiltonian becomes

$$\hat{H}_{\text{chain}} = \sum_{j=1}^{4} \sum_{n=0}^{+\infty} t_n^j \, \hat{f}_{j,n}^{\dagger} \, \hat{f}_{j,n+1} + \text{h.c.}. \tag{D.1}$$

Here $\hat{f}_{j,n}^{\dagger}$ are the fermionic creation operators at the n-th site in the j-th channel. The impurity is sitting at site -1 and is coupled to the site $n = 0$

$$\hat{H}_{\text{T}} = T' \sum_{j=1}^{4} \hat{f}_{j,0}^{\dagger} \hat{d}_j + \text{h.c.} \tag{D.2}$$

As the dot Hamiltonian in Eq.(4.1) is not modified by this procedure, the total Hamiltonian consists now of four spinless conduction bands coupled to a complex impurity composed of the dot degrees of freedom. This procedure allows to solve the problem numerically. Indeed the mapping of the leads' Hamiltonian onto an semi-infinite chain in Eq.(D.1) permits an iterative

diagonalization of the Hamiltonian and, since the hopping couplings decrease exponentially, one is allowed to truncate the semi-infinite chain at some iteration N for which the corresponding eigenenergies are converged. For this reason, adopting this procedure, one obtains numerically exact results.

DM-NRG symmetry generators As it was immediately realised by Wilson [93] and as it is discussed in detail in Refs. [89, 105, 106], along the NRG procedure it is crucial to use the symmetries of the system in order to achieve numerically reliable results. When $\Delta = 0$, the model is SU(4) invariant, as the total Hamiltonian commutes with the SU(4)-spin operator

$$\hat{\mathbf{J}}^{\mathrm{SU(4)}} = \frac{1}{2} \sum_{n=-1}^{+\infty} \sum_{j,j'=1}^{4} \hat{f}^{\dagger}_{j,n} \boldsymbol{\lambda}_{jj'} \hat{f}_{j',n}, \tag{D.3}$$

where $\boldsymbol{\lambda} = (\lambda_1, \ldots, \lambda_{15})$ is a set of matrices defining the generators for the SU(4) algebra (generalised Gell Mann matrices [107] for example). As discussed in Sect.4.2.2, there are also two U(1) symmetries corresponding to the conservation of charge in each of the Kramers channels. In the NRG language the generators are

$$\hat{Q}_{\kappa} = \frac{1}{2} \sum_{j \in \kappa} \sum_{n=-1}^{+\infty} \left(\hat{f}^{\dagger}_{j,n} \hat{f}_{j,n} - \frac{1}{2} \right). \tag{D.4}$$

Since the generators for spin and for the charges commute among themselves, the system has a global $\mathrm{U(1)} \otimes \mathrm{U(1)} \otimes \mathrm{SU(4)}$ symmetry. The spin orbit and valley mixing perturbations, i.e. $\Delta \neq 0$, break the global symmetry down to the $\mathrm{U(1)} \otimes \mathrm{U(1)} \otimes \mathrm{SU(2)} \otimes \mathrm{SU(2)}$, generated by the charge and the SU(2)-spin operators

$$\hat{\mathbf{J}}_{\kappa} = \frac{1}{2} \sum_{n=-1}^{+\infty} \sum_{j,j' \in \kappa} \hat{f}^{\dagger}_{j,n} \boldsymbol{\sigma}_{jj'} \hat{f}_{j',n}, \tag{D.5}$$

acting on the two Kramers doublets. Here $\boldsymbol{\sigma} = (\sigma_x, \sigma_y, \sigma_z)$ is the vector of Pauli matrices.

APPENDIX E

Universality and the fixed points

We devote this Appendix to a brief analysis of the properties of the SU(2) and SU(4) limiting cases in the $N_G = 1$ valley. When $\Delta = 0$ we expect the system to be at the SU(4) fixed point. In Fig.E.1 we compare on one side, the conductance as computed with the help of Eq.(4.10) for $\Delta = 0$, with the universal curve for $G(T/T_K)$ as obtained from an underlying Kondo model with SU(4) symmetry, and we find a perfect agreement. Increasing Δ, the system flows away from the SU(4) towards the SU(2) fixed point. As the other curve in Fig.E.1 shows, for large enough values of Δ, i.e. $\Delta \gg W$, the

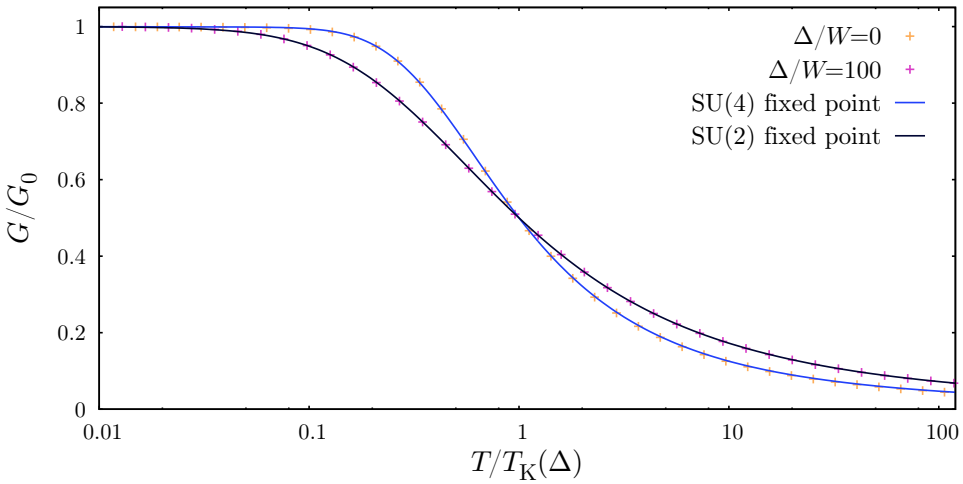

Figure E.1: Comparison between the temperature dependence of the conductance in the limits when $\Delta \to 0$ and $\Delta \to \infty$ (symbols) and the SU(2) and SU(4) universal curves for the conductance (solid lines).

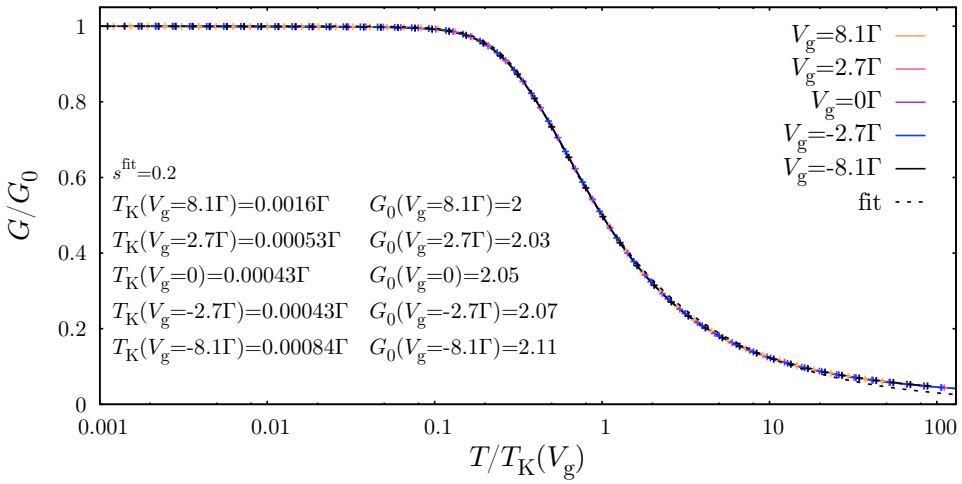

Figure E.2: Universal scaling of the conductance as a function of T/T_K for different gate voltages and comparison with the heuristical curve from Eq.(E.1) with $n = 3$. The other parameters are: $U = W$, $\Gamma = U/25$, $T = 0$, $\varepsilon_d = -U/2$ and $\Delta = 0$. Here G_0 is the unitary conductance in unit $2e^2/h$.

system has already reached the SU(2) fixed point. Recently, in Ref. [108] an heuristical analytical expression was proposed for the universal conductance, of the form

$$\frac{G\left(T/T_K\right)}{G_0} = \left(1 + \left(2^{1/s} - 1\right) \cdot \left(\frac{T}{T_K}\right)^n\right)^{-s}, \tag{E.1}$$

in order to reproduce the leading-order in the temperature expansion predicted by the conformal field theory [109, 110] for the SU(4)-Kondo Hamiltonian. In this case the leading order is predicted to be cubic, $G(T/T_K)/G_0 \simeq 1 - \alpha \cdot (T/T_K)^3 + \ldots$, with α a constant of the order ~ 1, even though the system has still a Fermi liquid character. This sets $n = 3$ in Eq.(E.1) in contrast to the case $n = 2$ for the SU(2) symmetry.

In Fig.E.2 we compare the conductance with this heuristic curve for different gate voltages. From the fits of the DM-NRG data (Fig.E.2), in the range $0 \leq T/T_K \leq 1$, we obtained a good estimate for $s = 0.202 \pm 0.002$ in agreement with Ref. [108]. The heuristic curve reproduces very well the DM-NRG results in a wide range of temperatures, $0 \leq T/T_K \leq 10$, and deviations become visible only for large enough temperatures.

Trying to fit the data for $\Delta \gg W$ in Fig.E.1 with $n = 2$ we found $s = 0.215 \pm 0.002$, in agreement with the predictions from the conformal field theory.

Acknowledgments

In this Section I would like to thank all the people that, in these three years and half, helped me in this very enriching experience and supported me in this "scientific adventure". My PhD was a very dense and intense experience both from the personal and scientific point of view.

In the first place I want to thank Milena that gave me the opportunity to work here in Regensburg. To leave abroad for almost four years is a great opportunity to widen your borders and open your mind to different way of thinking. For sure it teaches you that the world is much wider place than your very local point of view. Moreover I want to thank Milena for the time she spent with me sharing her experience and knowledge about Physics. I want to thank her also for our endless discussions about talks and her patience in trying to give a broader point of view to my presentations.

During my PhD I had also the opportunity to visit Gergely Zaránd and Cătălin Pascu Moca in the University of Budapest. I want to thank them for the knowledge they shared with me. The collaboration with them literally made me discover a new way to look at Physics. Furthermore I want to thank Pascu for our Skype discussions and the support he gave me during our work.

Concerning this project I want also to thank the system administrator of Athene Randy Rueckner. His help was very precious in running all the simulations on this cluster.

I want also to thank my co-workers that shared with me this experience. Namely I want to thank the system administrators in my group Manohar Awasthi and Benjamin Siegert that many times gave me suggestions to solve practical problems, Andrea Donarini for many interesting discussions, Magdalena Margańska to share with me her understanding about carbon nanotubes, Sebastian Pfaller, Lars Mils, Sonja Predin, Michael Kammermeier, Felix Weiner and Michael Niklas. Last but not least a big thank you to Sergey Smirnov, Alexander Lopez and Prakash Parida with whom I shared the office. It was very interesting to get in contact with very different realities from all

over the world.

Finally I want to thank the set of people I define my “family”. I want to thank my parents that supported me in this adventure and for their priceless advices. Thank you for helping me setting up here in Regensburg. Moreover I want to thank Marta that, despite the distance, has understood the importance of this experience for me and has always found a way to inspire and encourage me. Thank you for being always a constant in my days. Then I want to thank Marco for visiting me several times here in Germany. A friend that you can always count on is a priceless gift.

References

[1] Lydia L. Sohn, Leo P. Kouwenhoven, and Gerd Schön, eds. *Mesoscopic Electron Transport*. NATO ASI Series 345. Dordrecht: Springer, 1997. ISBN: 978-94-015-8839-3. DOI: 10.1007/978-94-015-8839-3.

[2] Yoseph Imry. *Introduction to Mesoscopic Physics (Mesoscopic Physics and Nanotechnology)*. Oxford University Press, 2008. ISBN: 019955269X.

[3] Yuli V. Nazarov and Yaroslav M. Blanter. *Quantum Transport: Introduction to Nanoscience*. Cambridge University Press, 2009. ISBN: 0521832462.

[4] Leo Kouwenhoven and Charles Marcus. In: *Physics World* 11 (1998), p. 35. DOI: 10.1088/2058-7058/11/6/26.

[5] L. P. Kouwenhoven, D. G. Austing, and S. Tarucha. In: *Reports on Progress in Physics* 64 (2001), p. 701. DOI: 10.1088/0034-4885/64/6/201.

[6] John W. Negele and Henri Orland. *Quantum Many-particle Systems (Advanced Books Classics)*. Perseus Books, 1998. ISBN: 0738200522.

[7] Gerald D. Mahan. *Many-Particle Physics (Physics of Solids and Liquids)*. Springer, 2000. ISBN: 0306463385.

[8] John H. Davies. *The Physics of Low-dimensional Semiconductors: An Introduction*. Cambridge University Press, 1997. ISBN: 052148491X.

[9] M. A. Kastner. In: *Rev. Mod. Phys.* 64 (1992), pp. 849–858. DOI: 10.1103/RevModPhys.64.849.

[10] Bernhard Mandl et al. In: *Nano Letters* 6 (2006), pp. 1817–1821. DOI: 10.1021/nl060452v.

[11] Yong-Joo Doh et al. In: *Nano Letters* 8 (2008), pp. 4098–4102. DOI: 10.1021/nl801454k.

[12] R. Saito, G. Dresselhaus, and M. S. Dresselhaus. *Physical Properties of Carbon Nanotubes*. Imperial College Press, 1998. ISBN: 1860942237.

[13] M. S. Dresselhaus, G. Dresselhaus, and P. Avouris. *Carbon Nanotubes: Synthesis, Structure, Properties and Applications*. Springer, 2001. ISBN: 3540410864.

[14] Jan von Delft and D.C. Ralph. In: *Physics Reports* 345 (2001), pp. 61–173. DOI: 10.1016/S0370-1573(00)00099-5.

[15] D. Goldhaber-Gordon et al. In: *Nature* 391 (1998), pp. 156–159. DOI: 10.1038/34373.

[16] Alexander W. Holleitner et al. In: *Science* 297 (2002), pp. 70–72. DOI: 10.1126/science.1071215.

[17] L. P. Kouwenhoven et al. In: *Science* 278 (1997), pp. 1788–1792. DOI: 10.1126/science.278.5344.1788.

[18] Silvano De Franceschi et al. In: *Nat Nano* 5 (2010), pp. 703–711. DOI: 10.1038/nnano.2010.173.

[19] A. Martín-Rodero and A. Levy Yeyati. In: *Advances in Physics* 60 (2011), pp. 899–958. DOI: 10.1080/00018732.2011.624266.

[20] J Barnaś and I Weymann. In: *Journal of Physics: Condensed Matter* 20 (2008), p. 423202. DOI: 10.1088/0953-8984/20/42/423202.

[21] Leo Kouwenhoven and Leonid Glazman. In: *Physics World* 14 (2001), p. 33. DOI: 10.1088/2058-7058/14/1/28.

[22] A. C. Hewson. *The Kondo Problem to Heavy Fermions*. Ed. by Cambridge University Press. Cambridge: Cambridge University Press, 1997.

[23] L. I. Glazman and M. E. Raikh. In: *JETP Lett.* 47 (1988), p. 452. URL: http://www.jetpletters.ac.ru/ps/1095/article_16538.pdf.

[24] Tai Kai Ng and Patrick A. Lee. In: *Phys. Rev. Lett.* 61 (1988), pp. 1768–1771. DOI: 10.1103/PhysRevLett.61.1768.

[25] D. Goldhaber-Gordon et al. In: *Phys. Rev. Lett.* 81 (1998), p. 5225. DOI: 10.1103/PhysRevLett.81.5225.

[26] Yang Ji et al. In: *Science* 290 (2000), pp. 779–783. DOI: 10.1126/science.290.5492.779.

[27] Jun Kondo. In: 32 (1964), pp. 37–49. DOI: 10.1143/PTP.32.37.

[28] L.I. Glazman and M. Pustilnik. "Coulomb blockade and Kondo effect in quantum dots". In: *New Directions in Mesoscopic Physics (Towards Nanoscience)*. Ed. by R. Fazio, V. F. Gantmakher, and Y. Imry. Netherlands: Springer, 2003, pp. 93–115. ISBN: 1402016654. arXiv: cond-mat/0302159.

[29] Mikhail Pletyukhov and Herbert Schoeller. In: *Phys. Rev. Lett.* 108 (2012), p. 260601. DOI: 10.1103/PhysRevLett.108.260601.

[30] A. Kogan et al. In: *Phys. Rev. Lett.* 93 (2004), p. 166602. DOI: 10.1103/PhysRevLett.93.166602.

[31] J. R. Schrieffer and P. A. Wolff. In: *Phys. Rev.* 149 (1966), pp. 491–492. DOI: 10.1103/PhysRev.149.491.

[32] Heinz-Peter Breuer and Francesco Petruccione. *The Theory of Open Quantum Systems*. Oxford University Press, 2007. ISBN: 0199213909.

[33] H. Schoeller. "Transport theory of interacting quantum dots". In: *Mesoscopic Electron Transport*. Ed. by Lydia L. Sohn, Leo P. Kouwenhoven, and Gerd Schön. NATO ASI Series 345. Dordrecht: Springer, 1997, pp. 291–330. ISBN: 978-94-015-8839-3. DOI: 10.1007/978-94-015-8839-3_8.

[34] Carsten Timm. In: *Phys. Rev. B* 77 (2008), p. 195416. DOI: 10.1103/PhysRevB.77.195416.

[35] Carsten Timm. In: *Phys. Rev. B* 83 (2011), p. 115416. DOI: 10.1103/PhysRevB.83.115416.

[36] Kenneth G. Wilson. In: *Rev. Mod. Phys.* 47 (1975), pp. 773–840. DOI: 10.1103/RevModPhys.47.773.

[37] Massimiliano Esposito, Upendra Harbola, and Shaul Mukamel. In: *Rev. Mod. Phys.* 81 (2009), pp. 1665–1702. DOI: 10.1103/RevModPhys.81.1665.

[38] Jürgen König et al. In: *Phys. Rev. B* 54 (1996), p. 16820. DOI: 10.1103/PhysRevB.54.16820.

[39] Karl Blum. *Density Matrix Theory and Applications (Springer Series on Atomic, Optical, and Plasma Physics, Vol. 64)*. Springer, 2012.

[40] Sonja Koller. "Spin phenomena and higher order effects in transport across interacting quantum-dots". PhD thesis. Universität Regensburg, 2009.

[41] Johannes Kern and Milena Grifoni. In: *The European Physical Journal B* 86 (2013), p. 384. DOI: 10.1140/epjb/e2013-40618-9.

[42] Claude Cohen-Tannoudji, Bernard Diu, and Frank Laloe. *Quantum Mechanics, Vol. 1*. Wiley, 1991.

[43] Herbert Schoeller and Gerd Schön. In: *Phys. Rev. B* 50 (1994), p. 18436. DOI: 10.1103/PhysRevB.50.18436.

[44] Herbert Schoeller and Gerd Schön. In: *Physica B: Condensed Matter* 203 (1994), pp. 423–431. DOI: http://dx.doi.org/10.1016/0921-4526(94)90091-4.

[45] Jürgen König, Herbert Schoeller, and Gerd Schön. In: *Phys. Rev. Lett.* 76 (1996), pp. 1715–1718. DOI: 10.1103/PhysRevLett.76.1715.

[46] S. Koller et al. In: *Phys. Rev. B* 82 (2010), p. 235307. DOI: 10.1103/PhysRevB.82.235307.

[47] Jürgen König. "Resonanztunnlen in mesoskopischen Systemen". MA thesis. Deutschland: Universität Karlsruhe, 1995.

[48] M. Leijnse and M. R. Wegewijs. In: *Phys. Rev. B* 78 (2008), p. 235424. DOI: 10.1103/PhysRevB.78.235424.

[49] N. E. Bickers. In: *Rev. Mod. Phys.* 59 (1987), pp. 845–939. DOI: 10.1103/RevModPhys.59.845.

[50] Andrey V. Kretinin, Hadas Shtrikman, and Diana Mahalu. In: *Phys. Rev. B* 85 (2012), p. 201301. DOI: 10.1103/PhysRevB.85.201301.

[51] T. A. Costi, J. Kroha, and P. Wölfle. In: *Phys. Rev. B* 53 (1996), pp. 1850–1865. DOI: 10.1103/PhysRevB.53.1850.

[52] Henrik Bruus and Karsten Flensberg. *Many-Body Quantum Theory in Condensed Matter Physics: An Introduction (Oxford Graduate Texts)*. Oxford University Press, 2004.

[53] C. Caroli et al. In: *Journal of Physics C: Solid State Physics* 5 (1972), p. 21. URL: http://stacks.iop.org/0022-3719/5/i=1/a=006.

[54] Selman Hershfield, John H. Davies, and John W. Wilkins. In: *Phys. Rev. Lett.* 67 (1991), pp. 3720–3723. DOI: 10.1103/PhysRevLett.67.3720.

[55] Yigal Meir and Ned S. Wingreen. In: *Phys. Rev. Lett.* 68 (1992), pp. 2512–2515. DOI: 10.1103/PhysRevLett.68.2512.

[56] Yigal Meir, Ned S. Wingreen, and Patrick A. Lee. In: *Phys. Rev. Lett.* 70 (1993), pp. 2601–2604. DOI: 10.1103/PhysRevLett.70.2601.

[57] Ned S. Wingreen and Yigal Meir. In: *Phys. Rev. B* 49 (1994), pp. 11040–11052. DOI: 10.1103/PhysRevB.49.11040.

[58] O. Karlström et al. In: *Journal of Physics A: Mathematical and Theoretical* 46 (2013), p. 065301. DOI: 10.1088/1751-8113/46/6/065301.

[59] William H. Press. *Numerical Recipes 3rd Edition: The Art of Scientific Computing*. Cambridge University Press, 2007.

[60] Kendall Atkinson. In: *SIAM J. Numer. Anal.* 9(2) (1972), pp. 284–299. DOI: 10.1137/0709028.

[61] Davide Mantelli et al. In: *Physica E: Low-dimensional Systems and Nanostructures* 77 (2016), pp. 180–190. DOI: 10.1016/j.physe.2015.11.023.

[62] Edward A. Laird et al. In: *Rev. Mod. Phys.* 87 (2015), pp. 703–764. DOI: 10.1103/RevModPhys.87.703.

[63] Michael Niklas et al. In: (2016). arXiv: 1603.00380.

[64] Michael Niklas. "Electronic spectra of ultra-clean carbon nanotubes in a magnetic field". MA thesis. Deutschland: Universität Regensburg, 2013.

[65] Tsuneya Ando. In: *Journal of the Physical Society of Japan* 69 (2000), pp. 1757–1763. DOI: 10.1143/JPSJ.69.1757.

[66] László Borda et al. In: *Phys. Rev. Lett.* 90 (2003), p. 026602. DOI: 10.1103/PhysRevLett.90.026602.

[67] Gergely Zaránd, Arne Brataas, and David Goldhaber-Gordon. In: *Solid State Communications* 126 (2003), pp. 463–466. DOI: 10.1016/S0038-1098(03)00180-7.

[68] S. Sasaki et al. In: *Phys. Rev. Lett.* 93 (2004), p. 017205. DOI: 10.1103/PhysRevLett.93.017205.

[69] Pablo Jarillo-Herrero et al. "Orbital Kondo effect in carbon nanotubes". In: *Nature* 434 (2005), pp. 484–488. DOI: 10.1038/nature03422.

[70] Manh-Soo Choi, Rosa López, and Ramón Aguado. In: *Phys. Rev. Lett.* 95 (2005), p. 067204. DOI: 10.1103/PhysRevLett.95.067204.

[71] Jong Soo Lim et al. In: *Phys. Rev. B* 74 (2006), p. 205119. DOI: 10.1103/PhysRevB.74.205119.

[72] P. Jarillo-Herrero et al. In: *Phys. Rev. Lett.* 94 (2005), p. 156802. DOI: 10.1103/PhysRevLett.94.156802.

[73] Magdalena Marganska, Piotr Chudzinski, and Milena Grifoni. In: *Phys. Rev. B* 92 (2015), p. 075433. DOI: 10.1103/PhysRevB.92.075433.

[74] W. Izumida, R. Okuyama, and R. Saito. In: *Phys. Rev. B* 91 (2015), p. 235442. DOI: 10.1103/PhysRevB.91.235442.

[75] F. Kuemmeth et al. In: *Nature* 452 (2008), pp. 448–452. DOI: 10.1038/nature06822.

[76] T. S. Jespersen et al. In: *Nat Phys* 7 (2011), pp. 348–353. DOI: 10.1038/nphys1880.

[77] Frithjof B. Anders et al. In: *Phys. Rev. Lett.* 100 (2008), p. 086809. DOI: 10.1103/PhysRevLett.100.086809.

[78] Martin R. Galpin et al. In: *Phys. Rev. B* 81 (2010), p. 075437. DOI: 10.1103/PhysRevB.81.075437.

[79] Daniel R. Schmid et al. In: *Phys. Rev. B* 91 (2015), p. 155435. DOI: 10.1103/PhysRevB.91.155435.

[80] J. Paaske et al. In: *Nat. Phys.* 2 (2006), pp. 460–464. DOI: 10.1038/nphys340.

[81] C. H. L. Quay et al. In: *Phys. Rev. B* 76 (2007), p. 245311. DOI: 10.1103/PhysRevB.76.245311.

[82] A. Makarovski et al. In: *Phys. Rev. B* 75 (2007), p. 241407. DOI: 10.1103/PhysRevB.75.241407.

[83] A. Makarovski, J. Liu, and G. Finkelstein. In: *Phys. Rev. Lett.* 99 (2007), p. 066801. DOI: 10.1103/PhysRevLett.99.066801.

[84] J. P. Cleuziou et al. In: *Phys. Rev. Lett.* 111 (2013), p. 136803. DOI: 10.1103/PhysRevLett.111.136803.

[85] K. Grove-Rasmussen et al. In: *Phys. Rev. Lett.* 108 (2012), p. 176802. DOI: 10.1103/PhysRevLett.108.176802.

[86] Walter Hofstetter. In: *Phys. Rev. Lett.* 85 (2000), pp. 1508–1511. DOI: 10.1103/PhysRevLett.85.1508.

[87] Ralf Bulla, Theo A. Costi, and Thomas Pruschke. In: *Rev. Mod. Phys.* 80 (2008), pp. 395–450. DOI: 10.1103/RevModPhys.80.395.

[88] John F. Cornwell. *Group Theory in Physics, Volume 2 (Techniques of Physics)*. Academic Press, 1986. ISBN: 0121898040.

[89] A. I. Tóth et al. In: *Phys. Rev. B* 78 (2008), p. 245109. DOI: 10.1103/PhysRevB.78.245109.

[90] David C. Langreth. In: *Phys. Rev.* 150 (1966), pp. 516–518. DOI: 10.1103/PhysRev.150.516.

[91] M. Eto. In: *AIP Conference Proceedings* 772 (2005), pp. 821–822. DOI: 10.1063/1.1994359.

[92] Assaf Carmi, Yuval Oreg, and Micha Berkooz. In: *Phys. Rev. Lett.* 106 (2011), p. 106401. DOI: 10.1103/PhysRevLett.106.106401.

[93] H. R. Krishna-murthy, J. W. Wilkins, and K. G. Wilson. In: *Phys. Rev. B* 21 (1980), pp. 1003–1043. DOI: 10.1103/PhysRevB.21.1003.

[94] L. Merker and T. A. Costi. In: *Phys. Rev. B* 86 (2012), p. 075150. DOI: 10.1103/PhysRevB.86.075150.

[95] L. Merker, A. Weichselbaum, and T. A. Costi. In: *Phys. Rev. B* 86 (2012), p. 075153. DOI: 10.1103/PhysRevB.86.075153.

[96] Piers Coleman, Erik Koch, and Eva Pavarini. *Many-Body Physics: From Kondo to Hubbard*. Forschungszentrum JĂŒlich, 2015.

[97] Wanda C. Oliveira and Luiz N. Oliveira. In: *Phys. Rev. B* 49 (1994), pp. 11986–11994. DOI: 10.1103/PhysRevB.49.11986.

[98] S. C. Costa et al. In: *Phys. Rev. B* 55 (1997), pp. 30–33. DOI: 10.1103/PhysRevB.55.30.

[99] Vivaldo L. Campo and Luiz N. Oliveira. In: *Phys. Rev. B* 72 (2005), p. 104432. DOI: 10.1103/PhysRevB.72.104432.

[100] Rui Sakano and Norio Kawakami. In: *Phys. Rev. B* 73 (2006), p. 155332. DOI: 10.1103/PhysRevB.73.155332.

[101] P. Schlottmann. In: *Phys. Rev. Lett.* 50 (1983), pp. 1697–1700. DOI: 10.1103/PhysRevLett.50.1697.

[102] Milton Abramowitz and Irene Stegun. *Handbook of Mathematical Functions with Formulas, Graphs, and Mathematical Tables*. Martino Fine Books, 2014. ISBN: 161427617X.

[103] H. R. Krishna-murthy, J. W. Wilkins, and K. G. Wilson. In: *Phys. Rev. B* 21 (1980), pp. 1044–1083. DOI: 10.1103/PhysRevB.21.1044.

[104] Michael Sindel. "Numerical Renormalization Group studies of Quantum Impurity Models in the String Coupling Limit". PhD thesis. Ludwig-Maximilians-Universität München, 2004.

[105] Alex Arne. "Non-Abelian symmetries in the Numerical Renormalization Group". MA thesis. Deutschland: Ludwig-Maximilians-Universität München, 2009.

[106] Andreas Weichselbaum. In: *Annals of Physics* 327 (2012), pp. 2972–3047. DOI: 10.1016/j.aop.2012.07.009.

[107] Maa Sbaih and Mkh Srour. In: *Electron. J. Theor. Phys.* 10.28 (2013), pp. 9–26. URL: http://ejtp.com/articles/ejtpv10i28p9.pdf.

[108] A. J. Keller et al. In: *Nat. Phys.* 10 (2014), pp. 145–150. DOI: 10.1038/nphys2844.

[109] K. Le Hur, P. Simon, and D. Loss. In: *Phys. Rev. B* 75 (2007), p. 035332. DOI: 10.1103/PhysRevB.75.035332.

[110] Christophe Mora et al. In: *Phys. Rev. B* 80 (2009), p. 155322. DOI: 10.1103/PhysRevB.80.155322.